

Study of wave run-up and overtopping with Large Eddy Simulations for overtopping wave energy converters.

Claudio Alejandro Sandoval Munoz

A dissertation submitted in partial fulfillment
of the requirements for the degree of
Doctor of Philosophy
of
University College London.

Department of Civil, Environmental and Geomatic Engineering
University College London

May 24, 2025

I, Claudio Alejandro Sandoval Munoz, confirm that the work presented in this thesis is my own. Where information has been derived from other sources, I confirm that this has been indicated in the work.

Abstract

This research studied the wave-structure interaction of monochromatic waves and slope structures. A three-dimensional numerical wave tank (Hydro3D-NWT) based on the large eddy simulation (LES) method is employed to evaluate the water surface morphology, particle kinematics, turbulent structures, flow energy and dynamic pressures. Hydro3D-NWT's performance is validated for each case studied with experimental data, analytical solutions, and well-known empirical formulas used in coastal engineering.

First, the interaction of monochromatic waves over a trapezoidal submerged structure is studied. The structure comprises a front slope, a horizontal berm, and a rear slope. Four front slope geometries are implemented. The results show that the front's geometry slope modifies the evolution of the waves over the structure, affecting the wave profile, the generation of different turbulent structures and the stability of the structure.

A sloped structure that represents an overtopping wave energy converter's run-up ramp (OWEC) is next studied. In this section, Hydro3D-NWT is validated for the first time to simulate wave breaking, run-up, overtopping and run-down. The analysis reveals that the run-down flow plays an important role in the energy dissipation over the ramp. Reducing the run-down flow moves the wave-breaking type towards collapsing and surging, less turbulent than plunging waves. This change in the breaking condition reduces the wave's curl, decreasing turbulence and speeding up the run-up flow. An improvement up to 20 % on the remaining energy in the run-up is recorded when a transition from plunging to collapsing breaking type is

achieved.

Two geometries that include a gap on the slope to deflect the run-down flow are simulated. The results show that the run-down flow is deflected with the geometries assessed; however, the overtopping is reduced, and therefore, the power available at the crest of the structure is also reduced. Based on the results, four conceptual designs of the OWEC's run-up ramp are proposed.

This study contributes to understanding the hydrodynamics of wave structure interaction. It gives insight into the process that occurs over the run-up ramp of an OWEC and proposes new alternatives to improve its efficiency. The performance of a numerical tool has been tested with complex fluid mechanics scenarios, and its ability to produce detailed data of high interest to coastal engineering has been corroborated.

Impact Statement

In today's times, there is a pressing need to develop sustainable methods for producing energy. Green technologies have been developed to harness renewable energy sources, including solar, wind, and marine energy. Wave energy (WE) stands out with worldwide wave power resources estimated at $2TW$. It has been confirmed that harvesting energy from waves is possible and can contribute to diversifying the energy mix. The challenges involved in designing devices to endure the harsh and corrosive marine environment, resist extreme conditions, and operate in remote locations have slowed the growth of this industry compared to the solar and wind industries. Developing wave energy converters (WECs) requires a detailed understanding of complex wave-structure interactions. OWECs operate onshore and can be integrated into breakwaters. Their operations lie in their ability to capture overtopping discharges. This type of WEC presents a significantly reduced cost and risk compared to offshore WEC; however, its efficiency needs to be improved. Studies have used experimental and numerical models to evaluate the effects on the device's efficiency of different geometries of the run-up ramp. They include the slope angle, curve slopes, and guiding walls. These studies have proven that the OWEC's performance can be optimised by altering the run-up ramp according to the wave conditions. No research has included a detailed analysis of the hydrodynamics process over the ramp, such as the wave breaking, run-up and run-down flows, and overtopping. All these processes contribute to energy dissipation, affecting the power available to be collected at the crest of the structure. In the present research, a Large Eddy simulation-based numerical code is employed to study the hydrodynamics involved in the interaction of waves and the run-up ramp. Results

have allowed for identifying the important role of the run-down flow in the breaking condition over the ramp, which is directly linked to the energy dissipation. It has been detected that a reduction of the run-down flow can improve the operation of an OWEC. These findings may lead to new alternatives to maximise the efficiency of OWECs, providing a fresh impulse to research and progress in the wave energy field.

Acknowledgements

First, I would like to thank my supervisor, Professor Thorsten Stoesser. Without his guidance, advice, and encouragement, completing this PhD would not have been possible. Since we first contacted by email, he has shown great interest in the research and an outstanding ability to share his knowledge and experience. He offered support and understanding during the pandemic and other difficult periods that my family and I went through.

My wife, Camila Parodi, and I share the challenge of conducting a PhD. At the end of 2019, we jumped into this adventure with our beautiful son Lucas; we knew nothing about what would come soon. During these 4.5 years, we have encountered many happy moments but also sad and difficult times. I thank Camila for her constant support, patience, and love; without her, I would probably never have embarked on this beautiful voyage. I want to thank Lucas for the many smiles and laughs he has brought to our lives; he has been a constant source of joy and pride as a father.

I want to express my gratitude to my parents, Ruth Munoz and Claudio Sandoval. They are largely responsible for the person I am, and every success in my life is theirs. To my sister and brother-in-law, Maria Jose Sandoval and Herman Elgueta, I thank them for encouraging me to pursue this study and advice.

Working at UCL and being a member of the "Hydro3D team" has allowed me to meet a brilliant group of people keen to share their knowledge with no condi-

tions. A special mention should be made to Aristos Christou and Qianyu Luo. Their help to unravel the code and suggestions to improve my work have been greatly appreciated. They will continue doing great work and contributing to the field.

Last but not least, I thank all of the members of the Civil, Environment & Geomatic Department, academic staff, researchers and administration members, who indirectly contributed to the execution of my research, and without their work, this research would be impossible.

Agradecimientos

Primero, quisiera agradecer a mi supervisor, profesor Thorsten Stoesser. Sin su guía, consejos, y estímulo, completar este PhD no habría sido posible. Desde la primera vez que nos contactamos por email, ha demostrado gran interés en mi investigación y una destacable habilidad para compartir sus conocimientos y experiencia. Durante la pandemia y otros momentos difíciles que pasamos con mi familia, él nos ofreció apoyo y entendimiento.

Mi esposa, Camila Parodi y yo compartimos el desafío de realizar un doctorado. A fines del 2019 saltamos en esta aventura con nuestro hermoso hijo Lucas; no sabíamos que se nos vendría al poco tiempo. Durante estos 4.5 años, hemos vivido muchos momentos felices, pero también otros tristes y muy difíciles. Agradezco a Camila por su apoyo constante, paciencia y amor. Si no es por ella nunca me habría embarcado en esta hermosa aventura. También quiero agradecer a Lucas por las muchas sonrisas y risas que ha traído a nuestras vidas. Él ha sido una fuente constante de alegrías y orgullo como padre.

Quiero expresar mi gratitud a mis padres, Ruth Munoz y Claudio Sandoval. Ellos son ampliamente responsables por lo que soy hoy como persona, y cada éxito en mi vida es de ellos también. A mi hermana y cuñado, María José Sandoval y Herman Elgueta, les agradezco por animarme para seguir este estudio y sus consejos.

Trabajando en UCL y como miembro del equipo "Hydro3D" me ha permitido

conocer a un grupo brillante de personas, dispuestas a compartir sus conocimientos sin condiciones. Una mención especial merecen Aristos Christou y Qianyu Luo. Su ayuda para desenredar el código y sugerencias para mejorar mi trabajo son altamente apreciadas. Con seguridad seguirán realizando un gran trabajo y contribuyendo a la ciencia.

Por último, pero no menos importante, agradezco a todos los miembros del Departamento Civil, Environment & Geomatic, académicos, investigadores y miembros de la administración, ellos contribuyeron indirectamente a la ejecución de mi investigación, y sin su trabajo, esta investigación habría sido imposible.

UCL Research Paper Declaration

Form:

Referencing the doctoral candidate's own published work(s).

1. **1. For a research manuscript that has already been published** (if not yet published, please skip to section 2):

- (a) **What is the title of the manuscript?**

Study with Large Eddy Simulations of energy dissipation due to back-wash flows in wave overtopping.

- (b) **Please include a link to or doi for the work:**

<https://doi.org/10.36688/ewtec-2023-626>

- (c) **Where was the work published?**

Proc. EWTEC, vol. 15, Sep. 2023.

- (d) **Who published the work?**

The Energy and Climate Change Division at the University of Southampton

- (e) **When was the work published?**

2nd of September 2023.

- (f) **List the manuscript's authors in the order they appear on the publication:**

Claudio Sandoval, Thorsten Stoesser.

(g) **Was the work peer reviewed?**

Yes.

(h) **Have you retained the copyright?**

No

(i) **Was an earlier form of the manuscript uploaded to a preprint server (e.g. medRxiv)? If 'Yes', please give a link or doi**

No

If 'No', please seek permission from the relevant publisher and check the box next to the below statement:

- *I acknowledge permission of the publisher named under 1d to include in this thesis portions of the publication named as included in 1c.*

2. **For multi-authored work, please give a statement of contribution covering all authors** (if single-author, please skip to section 4):

3. **In which chapter(s) of your thesis can this material be found?**

Chapter 5.

e-Signatures confirming that the information above is accurate (this form should be co-signed by the supervisor/ senior author unless this is not appropriate, e.g. if the paper was a single-author work):

Candidate: Claudio Sandoval

Date: September 2024

Supervisor/Senior Author signature (where appropriate): Thorsten Stoesser

Date: September 2024

UCL Research Paper Declaration

Form:

Referencing the doctoral candidate's own published work(s).

1. For a research manuscript prepared for publication but that has not yet been published:

(a) What is the current title of the manuscript?

The effect of surface shape on the propagation of monochromatic waves over a submerged berm.

(b) Has the manuscript been uploaded to a preprint server 'e.g. medRxiv'?

If 'Yes', please please give a link or doi:

No.

(c) Where is the work intended to be published?

Journal of Ocean Engineering and Science.

(d) List the manuscript's authors in the intended authorship order:

Claudio Sandoval, Thorsten Stoesser, Aristos Christou.

(e) Stage of publication:

Submitted, under Review.

2. For multi-authored work, please give a statement of contribution covering all authors (if single-author, please skip to section 4):

Claudio Sandoval: Programming, simulations, data analysis and paper writing.

3. In which chapter(s) of your thesis can this material be found?

Chapter 4.

e-Signatures confirming that the information above is accurate (this form should be co-signed by the supervisor/ senior author unless this is not appropriate, e.g. if the paper was a single-author work):

Candidate: Claudio Sandoval

Date: September 2024

Supervisor/Senior Author signature (where appropriate): Thorsten Stoesser

Date: September 2024

UCL Research Paper Declaration

Form:

Referencing the doctoral candidate's own published work(s).

1. For a research manuscript prepared for publication but that has not yet been published:

(a) What is the current title of the manuscript?

Effect of wave run-down on the performance of overtopping wave energy converters.

(b) Has the manuscript been uploaded to a preprint server 'e.g. medRxiv'?

If 'Yes', please please give a link or doi:

No.

(c) Where is the work intended to be published?

Renewable Energy.

(d) List the manuscript's authors in the intended authorship order:

Claudio Sandoval, Thorsten Stoesser.

(e) Stage of publication:

Submitted, under Review.

2. For multi-authored work, please give a statement of contribution covering all authors (if single-author, please skip to section 4):

Claudio Sandoval: Programming, simulations, data analysis and paper writing.

3. In which chapter(s) of your thesis can this material be found?

Chapter 5.

e-Signatures confirming that the information above is accurate (this form should be co-signed by the supervisor/ senior author unless this is not appropriate, e.g. if the paper was a single-author work):

Candidate: Claudio Sandoval

Date: September 2024

Supervisor/Senior Author signature (where appropriate): Thorsten Stoesser

Date: September 2024

Contents

Abbreviations	28
Symbols	29
1 Introduction	31
1.1 Motivation	31
1.2 Aims and objectives	35
1.3 Thesis structure	36
2 Literature Review	38
2.1 Ocean Waves	38
2.2 Wave Theory	41
2.2.1 Linear Waves	41
2.2.2 Stokes Waves	45
2.3 Wave Run-up and Overtopping	47
2.3.1 Wave Run-up	48
2.3.2 Wave Overtopping	52
2.4 Wave Energy and Power	55
2.5 World Wave Energy	57
2.5.1 Worldwide Wave Energy	57
2.5.2 Chilean Wave Energy	59
2.6 Wave energy converters	63
2.6.1 Wave Energy Converter Classification and Principles	63
2.6.2 Oscillating Water Column (OWC)	64
2.6.3 Oscillating Bodies	67

2.6.4	Overtopping Wave Energy Converters	70
2.6.5	Wave Energy Converters Comparison	74
2.7	Overtopping Wave Energy Converter Studies	76
2.7.1	Overtopping Wave Energy Converters Development	78
2.7.2	Advantages of Overtopping Wave Energy Converters	87
2.8	Conclusions	89
3	Numerical framework	92
3.1	Introduction.	92
3.2	Large Eddy Simulations	92
3.3	Hydro3D-NWT.	96
3.3.1	Domain Discretisation.	97
3.3.2	Time Fractional-step.	98
3.3.3	Sub-Grid-Scale Model.	100
3.3.4	Free-surface Capturing.	101
3.3.5	Immersed Boundary Method	104
3.3.6	Surface Tension	105
3.3.7	Waves Input and Relaxation	106
3.3.8	Code Parallelisation and Work Sequence	108
3.3.9	Conclusion.	111
4	Study of Waves and Submerged Trapezoidal Structure	112
4.1	Introduction	112
4.2	Simulations of a submerged trapezoidal structure	114
4.3	Numerical study of front slope geometry	119
4.3.1	Water surface results	120
4.3.2	Forces results	133
4.4	Conclusions	141
5	Study of Waves and Sloped Structure	144
5.1	Introduction	144
5.2	Validation	146

5.2.1	Wave overtopping validation	146
5.2.2	Wave run-up validation	154
5.2.3	Validation conclusion	158
5.3	Methodology	158
5.4	Results and discussion	161
5.5	Conclusions	175
6	Conceptual structures.	178
6.1	Simulation new geometries	179
6.1.1	Results of new geometries	179
6.1.2	Conclusions of new geometries	185
6.2	Conceptual designs	187
6.2.1	Concept 1	187
6.2.2	Concept 2	187
6.2.3	Concept 3	188
6.2.4	Concept 4	189
6.3	Conclusions	193
7	Conclusions and Further Works	195
7.1	Conclusions	195
7.2	Further Works	200
	Bibliography	202

List of Figures

2.1	Ocean waves. Figures extracted from [1]	39
2.2	Linear Waves description.	39
2.3	Water particles movement under the surface.	40
2.4	Wave breaking type and estimate ξ	41
2.5	Representation of wave profiles for different theories based on [2]. .	44
2.6	Wave theories depending on the dimensionless depth (X axis), and the dimensionless wave height (Y axis). Based on [3]	45
2.7	Wave run-up and overtopping.	48
2.8	Run-up predictions compared with the laboratory results from [4, 5]. Figure extracted from [6].	50
2.9	Dimensionless run-up results from [7] compared to Hunt's run- up formulation and visualisation of new breaker criteria. Black dots: $\xi < 3$, grey dots: $\xi > 3$. Coloured dashed lines indicate a trend according to the relative depth, d/L_0 . Data from [7].	51
2.10	Annual mean wave power density and annual mean wave direction. Land buffer shows as a coloured band by continent. Extracted from [8].	57
2.11	Wave power available and yield compared to electricity consump- tion in (GW). Data from [8]	59
2.12	Wave power in front of the Chilean coast estimated in [9]. Solid Line: 100 m. depth, Dashed line: 50 m depth.	61
2.13	Central Chile wave power resources maps P_{10} , P_{50} and P_{90} pre- sented in [10]. Extracted from [10].	62

2.14	Concentration of wave power P_{10} , P_{50} and P_{90} near the shore presented in [10]. Extracted from [10].	62
2.15	Wave energy converters classification according to: Above distance to the shore, bottom orientation to waves. Extracted from [11] . . .	64
2.16	Oscillating water column (OWC). Extracted from. Extracted from [11]	65
2.17	LIMPET cross-section and general view. Extracted from [12]	65
2.18	Mutriku plant, cross-section and general view. Extracted from [13].	66
2.19	Point Absorber CETO. Pictures ©Carnie Clean Energy.	68
2.20	Oyster WEC diagram. Pictures ©Carnie Clean Energy.	68
2.21	Pelamis WEC. Extracted from [14].	70
2.22	Overtopping wave energy converter (OWEC). Extracted from [11] .	71
2.23	Tapchan. Extracted from [15].	72
2.24	Wave Dragon.	73
2.25	OBREC device, cross-section layout and prototype.	74
2.26	Hydraulic efficiency (η_{hyd}) for various WECs.	75
2.27	Performance factor for various WECs technologies, [16].	76
2.28	Cross section of SSG presented in [17] Extracted from [17].	79
2.29	Schematic of physical model tested in [18]	81
2.30	View of test run in [19] and numerical results from [20]	83
2.31	Sketch of OWEC presented in [21]. Extracted from [21]	84
2.32	Results and models from [22].	85
2.33	Comparison of waves' overtopping between laboratory and numerical simulations in [23]. Extracted from [23]	86
2.34	Cross section geometries of run-up ramp tested in [24] and overtopping results for each geometry.	87
3.1	Turbulent Spectrum and energy cascade.	95
3.2	Uniform Staggered Cartesian grid and locations of computation of quantities.	98

3.3	Grid and Lagrangian markers. Red dots Lagrangian markers, dashed blue line surface simulated.	104
3.4	3D sketch of Hydro3D Domain including a sloped structure.	107
3.5	Hydro3D-NWT flow chart.	110
4.1	3D view of the domain and longitudinal section.	117
4.2	Water surface fluctuations at each wave gauge (WG). Solid line Hydro3D-NWT, dots laboratory data.	118
4.3	Figures a), b) and c) frequency spectrum for WG1, WG3 and WG6 respectively, experimental data [25] (red) and Hydro3D-NWT results (black). Figure d) Hydro3D-NWT wave envelope and two instantaneous water surface.	119
4.4	Wave envelopes (solid lines) and crest level difference (dashed line) compared to linear geometry. Structure not in scale, to indicate the location of the front slope, berm, and rear slope.	122
4.5	Amplitude spectrum for all cases.	124
4.6	Shoaling coefficient, $K_s = H/H_w$, variation over the front slope and berm.	125
4.7	Comparisons of the water surface elevations at different times of the simulations.	126
4.8	Water surface over structure, Concave case ($x/y=1$, $x/z=1$).	127
4.9	Velocity fields on front-slope/berm transition for concave and convex case. ($x/z = 1/1.6$).	130
4.10	Q-criterion and Y-Vorticity for the linear case.	131
4.11	Q-criterion and Y-Vorticity for concave case.	131
4.12	Q-criterion and Y-Vorticity for cubic case.	132
4.13	Q-criterion and Y-Vorticity for convex case.	132
4.14	Water surface and total and dynamic forces acting on the concave case, at $t=20.40s$. Scale $x/z = 1/2$	134

4.15	Resultant force variations for the complete structure over two wave periods. Left: resultant horizontal force F_x , Right: resultant vertical force F_z	135
4.16	Ratio of the force variation's amplitude concerning the linear case (Blue R_{ax} , red R_{az}). Left: complete structure, Right: front slope. . .	137
4.17	Instance of maximum horizontal force at the nose (left) and maximum vertical force at the nose (right) for the linear case.	137
4.18	Variation of resultant forces at the nose of the structure normalized by the the linear case for two wave periods. Left: horizontal forces F_x , Right: vertical forces F_z	138
4.19	Water surface and forces diagram for concave case, and M_y for three wave periods.	139
4.20	M_y and F_x applied in front slope for three wave periods and concave and convex cases.	140
5.1	3D and lateral view of domain	148
5.2	Section where the overtopping flow is calculated and coloured by the horizontal velocity u_i . The blue iso-surfaces represent the upper and lower boundaries of the water surface in the overtopping flow. .	149
5.3	Overtopping dimensionless discharge Q for case $ Ov_3$. Green squares experimental data from [19], Hydro3D-NWT results: red circle <i>Grid1</i> , blue square <i>Grid2</i> and black triangles <i>Grid1</i>	150
5.4	Water surface during run-up flow for 3 Grid resolution. Water surface coloured by elevation. Dark grey represents the structure. . . .	151
5.5	Sequence of wave-structure interaction case $ Ov_1$. Black dashed line from experimental results from [20]. Blue are hydro3D-NWT results, and grey structure.	153
5.6	Overtopping dimensionless discharge Q . Green squares: experimental data from [19], black triangles Hydro3D-NWT results	154
5.7	Longitudinal view run-up simulations. In dashed line limit of structure used in overtopping simulations $R_c = 0.05 m$	156

- 5.8 Lateral view of wave breaking conditions cases Ru_1 , Ru_2 , Ru_3 and Ru_4 , blue iso-surface represents the water surface, and light grey the structure 157
- 5.9 Comparison of Hydro3D-NWT's run-up results against empirical formulations. 158
- 5.10 Lateral view of structure with different freeboards (R_c), and 3D view of cross-section S where the flow's energy is quantified. 160
- 5.11 Wave breaking of cases $case1_{Ru}$ and $case1_{25}$ at selected instants in time. Blue iso-surface shows water surface and contoured horizontal velocities u 164
- 5.12 3D view of wave breaking for cases $case1_{Ru}$ and $case1_{25}$ at selected instants in time. Blue iso-surface: water surface; and iso-surface according to Q criterion contoured by vorticity magnitude. 168
- 5.13 3D view of wave breaking for cases $case4_{Ru}$ and $case4_{25}$ at selected instants in time. Blue iso-surface: water surface; and iso-surfaces of the Q criterion contoured by vorticity magnitude. 169
- 5.14 Energy distribution through section S over one wave period. KE: Kinetic energy, DPE:dynamic potential energy and TE: total energy. Solid lined: $case2_{Ru}$, dashed lines: $case2_{50}$ 170
- 5.15 Normalised energy per run-up flow (E_{sru}/E_w). Black:TE, Blue:DPE, Red:KE, Solid Line: Ru , Dashed: $R_c = 0.075$ m, Dotted: $R_c = 0.05$ m and Dash-Dot: $R_c = 0.025$ m. 171
- 5.16 Normalised cumulative energy per run-up flow (E_{sru}/E_w). Black:TE, Blue:DPE, Red:KE, Solid Line: Ru , Dashed: $R_c = 0.075$ m, Dotted: $R_c = 0.05$ m and Dash-Dot: $R_c = 0.025$ m. 172
- 5.17 Energy variation versus variation in overtopping, separate by ξ 173

5.18	Power at the crest of the structure (P_{crest}) as a function of average normalised Total energy per run-up event (TE_{sru}/TE_w). Blue squares: $R_c = 0.075$ m, Red triangles: $R_c = 0.050$ m and Green Diamonds: $R_c = 0.025$ m. Lines present the best fit for each R_c according to the symbols' colours.	174
5.19	Energy variation versus variation in overtopping.	175
6.1	3D and cross-section view of geometries <i>Geo1</i> and <i>Geo2</i>	179
6.2	Lateral view wave breaking <i>case250</i>	181
6.3	Lateral view wave breaking <i>Geo1</i>	181
6.4	Lateral view wave breaking <i>Geo2</i>	182
6.5	Lateral view run-up <i>Geo1</i>	183
6.6	Lateral view run-up <i>Geo2</i>	184
6.7	Phase average overtopping flow over the crest of the structure, normalised by the maximum flow in <i>case250</i> . Black line: <i>case250</i> , Red line: <i>Geo1</i> , Blue line: <i>Geo2</i>	185
6.8	3D and lateral views conceptual design 1.	188
6.9	3D and lateral views conceptual design 2.	189
6.10	3D and lateral views conceptual design 3.	191
6.11	3D and lateral views conceptual design 4, alternative 1.	192
6.12	3D and lateral views conceptual design 4, alternative 2.	192

List of Tables

2.1	Annual wave power resource P and output power yield ψ for selected countries, and considering a virtual Pelamis P2 wave farm, [8].	58
4.1	Study cases, front slope functions and a sketch of geometries.	120
4.2	Location where waves peak x_p , wave height (H_p) at x_p , shoaling coefficient ($K_{sp} = H_p/H_w$) at x_p , ratio compared to linear case ($r_p = H_p/H_{pL}$) at x_p	123
4.3	Average wave height (H) at $x_1 = 6.0$ m and $x_2 = 8.0$ m, average wave celerity (c_{av12}) between x_1 and x_2 and wave height ratio compare to linear case at x_2	126
4.4	Resultant maximum average forces (F_{xmax} and F_{zmax}), amplitude of force fluctuations (Fa_x and Fa_z) and ratios compared to linear case ($R_{Fx} = F_{xmax}/Fl_{xmax}$, $R_{Fz} = F_{zmax}/Fl_{zmax}$, $R_{ax} = Fa_x/Fal_x$ and $R_{az} = Fa_z/Fal_z$) for the complete structure, front slope, nose, and each case.	136
4.5	Average maximum y moment M_{ymax} in Nm , average minimum y moment M_{ymin} in Nm , Average M_y range Ra_{My} in Nm , ratios respect to Linear case R_{Mymax} , R_{Mymax} and R_{RaMy}	140
5.1	Cases used to validate overtopping discharge, wave height H_w , wave period (T), wavelength L_w , water depth in still water level d , structure freeboard R_c and slope angle α	146
5.2	Grids resolution.	147

5.3	Dimensionless overtopping discharge Q results and error E compared to experimental data.	149
5.4	Cases used to validate wave run-up, H_w , wave period (T), wave-length L_w , ξ , and slope angle	156
5.5	Study cases, wave height H_w , wave period (T), wave length L_w , freeboard R_c , Iribarren number ξ	160
5.6	Averaged normalised energy per run-up event though section S . KE_{av} : Average normalised kinetic energy; DPE_{av} : Average normalised dynamic potential energy; TE_{av} : Average normalised total energy; $VarTE_{wave}$: % variation of TE_{av} relative to run-up case; $VarTE_{ac}$: % variation of cumulative total energy relative to run-up case.	173
6.1	Cases and overtopping discharge q normalised by $case2_{50}$	185

Abbreviations

- CDS: Central differences scheme.
- CFL: Courant-Friedrichs-Lewy condition.
- DPE: Dynamic potential energy.
- IB: Immersed boundary method.
- KE: Kinetic energy.
- LES: Large Eddy Simulation.
- LCOE: Levelized cost of energy.
- LSM: Level-set method.
- OWEC: Overtopping wave energy converter.
- OWC: Oscillating water columns.
- RK: Runge-Kutta scheme.
- RM: Relaxation method.
- SGS: Sub-grid scale model.
- SWL: Still water level.
- TE: Total energy.
- WALE: Wall-Adapting Local Eddy-viscosity.
- WE: Wave energy. WEC: Wave energy converter.
- WENO: 5th order Weighted essentially non-oscillatory scheme.

Symbols

- C_w : WALE empirical constant.
- d : Water depth in still water condition (m).
- dx, dy, dz : Grid size in x, y and z direction respectively (m).
- $\delta(\phi)$: Transition function used to calculate F_i^{sf} .
- 2ε : Thickness transition zone used in LSM.
- H_w : Wave height (m) in inlet boundary.
- $H(\phi)$: Heaviside function used in LSM.
- L_w : Wave length (m) in inlet boundary.
- $\eta(t)$: Variable water depth (m).
- κ : Interface curvature used to calculate F_i^{sf} .
- f_i : Forcing calculated by IB.
- F_i^{sf} : Surface tension.
- g_i : Gravitational acceleration.
- \bar{p} : Pressure field.
- u : Velocity in x direction.
- \bar{u}_i : Instantaneous filter velocity.
- ν : Fluid kinematic viscosity.
- ν_t : Fluid viscosity calculated by SGS.
- ρ : Fluid density.
- q : Overtopping mean discharge.

- Q : Dimensionless overtopping mean discharge.
- σ : Surface tension coefficient.
- R : Relaxation method coefficient.
- R_u : Run-up (m).
- T : Wave period (s).
- τ_{ij}^{SGS} : Sub-grid scale stress tensor.
- ϕ : Distance function used in LSM to capture water surface.
- v : Velocity in y direction.
- w : Velocity in z direction.
- $\Gamma(x_r)$: Relaxation function used in RM.
- Δ : Filtered size used in WALE, defined as $(dx \cdot dy \cdot dz)$.

Chapter 1

Introduction

1.1 Motivation

Human civilisation has always needed energy for its development, from fire to cook food and work metals to combustion engines and electricity, which moves the modern world. The primary energy source has been fossil fuels such as oil, coal and natural gas, representing 80% of the total energy production today, according to the International Energy Agency (IEA). Most countries have realised the negative impact on the environment of an energy matrix based mainly on fossil sources, such as the expulsion of greenhouse gases into the atmosphere, which contributes to speeding up climate change. A worldwide consensus is that moving to a more sustainable energy matrix is necessary to reduce CO₂ emissions and their negative environmental impacts. According to the European Climate Law, European Union (EU) members have established an energy road map to become a climate-neutral economy and society by 2050. This agreement includes reducing greenhouse gas emissions by at least 55% by 2030, compared to 1990 levels, and reaching a net-zero greenhouse gas emission by 2050. To meet these objectives, developing the green energy industry is necessary. New technologies have been created in the last few decades to exploit sustainable energy sources, such as solar, wind, and marine energy. These alternatives have lower CO₂ emissions, considerably reducing their negative environmental impact. Continuous research and development of these technologies has helped to decrease their levelized cost of energy (LCO), making them a competitive

alternative to conventional fossil sources [26] and [27]. However, more research is needed to improve the efficiency and reliability of energy converters specially in less mature technologies such as marine energy (waves and tidal).

Wave energy (WE) is a promising renewable energy source with worldwide wave power resources estimated at 2 TW, [8]. Studies and projects [15], [16], have confirmed that it is possible to harvest energy from waves and that WE plants can input electricity into national grids. However, the WE industry has not grown at the speed expected from a source with such high potential. According to the International Energy Agency (IEA) report, in the 20 years from 2001 to 2021, the electricity production from marine energy, including waves and tides, grew by 86%; much less than the solar and wind industry, which reported a 2,489% and 4,745% growth, respectively, in the same period. The high risk involved in working in the sea, exposure to extreme conditions, corrosive environments, and the remoteness of the operation mean it is a high-risk investment for any enterprise. The LCOE is a standard indicator used in the energy market to evaluate the cost of generating energy by a specific method. It is estimated that WE has LCOE 2 to 3 times bigger than solar energy and 1.5 to 2 times more than offshore wind [28, 29]. Given the variety of wave energy converters (WECs), the LCOE can change significantly between each device. [29] estimated that the floating overtopping WEC Wave Dragon could have a LCOE 70%-80% lower than other alternatives like Pelamis. These values must decrease for WE to be considered a competitive energy source. This reduction can be achieved by developing the technology, lowering costs and improving the efficiency of the devices.

Another example of a delay in the WE industry can be seen in Chile. This country has over 6,000 kms of coastline exposed to some of the most energetic wave conditions in the world, which positions it as the third country with the largest WE resources [8]. However, even with these great WE resources, Chile has no WE plant. Like the EU, Chile has an energy plan to transition to a more sustainable method of energy production. This plan's goals include achieving by 2050 that at least 70% of the electricity will be produced from renewable resources, and there

is to be a reduction of 30% of CO₂ emissions by 2030. To accomplish these goals, a diverse and effective use of its green energy resources such as solar, wind, and waves on its shore will need to be made [30].

WECs can be classified as off-shore, nearshore and on-shore devices. Off-shore WE converters, like the Pelami device [16], are exposed to the highest wave energy density, which explains why these devices have attracted the most attention from developers. However, they must endure extreme conditions, making their study and deployment a risky enterprise. On-shore devices like oscillating water columns (OWC) and overtopping wave energy converters (OWECs), [16], are technologies that can be installed in existing breakwaters - a factor that facilitates their construction and maintenance, reducing their cost and risk. However, the wave energy available to collect near the shore is significantly less than in off-shore locations; however, high efficiency can overcome less energetic waves. OWC have proved their viability in the Mutriku WE plant, [31], which has delivered more than 2.8 GWh into the Spanish electricity grid since its commissioning in 2011 (reported by The Basque Energy Agency EVE). The development of OWECs is some steps behind that of OWCs. In 2015, a full-scale OWEC prototype, OBREC (overtopping breakwater wave energy converter), was built in the Naples port breakwater [32] to study the real potential of this kind of WEC. One of the most significant advantages of an OWEC is its structural simplicity; it comprises a ramp, a reservoir, a turbine, and electronics. No mobile parts (besides the turbine) are included. The performance of an OWEC in producing energy depends on its ability to capture wave overtopping volumes as high as possible, to generate enough level difference to produce energy through the turbine when the water is returned to the sea. The efficiency of an OWEC device is related to transforming the total wave energy into pure potential energy. A high scatter of the estimated hydraulic efficiency of OWECs is found in the literature, with values from 3% to nearly 30% [33], [16]. However, most of this comes from scale models, with very few taken into large-scale prototypes.

Barriers that affect the growth of the WE energy industry are the devices'

early-stage of development, uncertainties regarding the environmental impacts, and the high cost involved. OWECs can reduce these problems. Their environmental impacts can be considerably reduced when these devices are integrated into coastal defences in existing or new projects. This integration eliminates the need for a specific structure to place the device. It makes the coastal defence a hybrid system, improving material and resource efficiency. The cost of an OWEC integrated into a coastal defence is also lower than that of an off-shore or nearshore WEC; they are easily accessible for construction and maintenance, and the construction costs are shared with the coastal defence.

Four main stages can be identified in the wave-structure interaction of an OWEC: first, wave breaking; second, the run-up flow; third, the overtopping discharge; and finally, a run-down flow. Except for the overtopping, all of these processes occur over the ramp of the structure. The run-down is the remaining water that does not overtop the structure and returns to the sea by running down the slope. This flow then interacts with the incoming wave during the breaking stage. The losses during the breaking process are among the most important, and they depend on the wave conditions and geometry of the run-up ramp. Several studies have focused on optimising the OWECs run-up ramp design. The longitudinal ramp shape is studied in [34] and [24], and found that a convex shape can maximise the overtopping collected. [34] specifically found that an elliptical optimises the volume captured. [18] studied the implementation of converging lateral walls and found that with an appropriate opening angle, their implementation can improve the capture of overtopping volume in moderate wave conditions. No information was found in the literature about the energy losses related to the interaction between the incoming wave and the run-down flow.

Their operation and efficiency must be improved to make OWECs a more attractive wave energy converter, leading to a decrease in the LCOE. A better understanding of the hydrodynamics of the wave-structure interaction is required to achieve this improvement, especially in the process that occurs on the run-up ramp of an OWEC, where the more significant energy losses occur.

1.2 Aims and objectives

This research aims to study wave structure interaction that can help better understand and improve the operation of an OWEC. The study is centred on the processes that occur over the ramp of an OWC. The flows that occur after the crest of the structure, in the reservoir and through the turbine are not included here. The following objectives are defined to achieve this aim:

- Validate a suitable numerical code to simulate:
 - wave shoaling process,
 - wave breaking
 - wave run-up
 - wave overtopping.
- Study the effect of submerged structures on wave transformation.
- Simulate the interaction of monochromatic waves with a slope structure and study the hydrodynamics in the breaking, run-up, and run-down stages.
- Analyse the turbulent structures that are generated during the wave-structure interaction.
- Evaluate the effect of the run-down flow on the energy losses during the wave-structure interaction and its impact on the operational efficiency of an OWEC.
- Propose a conceptual ramp geometry that can improve the efficiency of an OWEC.

To accomplish these objectives, an open-source numerical LES-based code, Hydro3D-NWT, [35], is used to simulate the interaction of monochromatic waves with submerged and sloped structures, which aims to mimic a coastal defence and the ramp of an OWEC. In an LES, the eddies that account for most of the energy dissipation in the flow are solved in the mesh, and the eddies smaller than the grid are included by a sub-grid scale model. This characteristic allows a detailed study of the flow hydrodynamics of the wave structure interaction.

The main objective of the present research is to explore the role of the run-down flow in the energy dissipation that occurs on the ramp of an OWEC.

1.3 Thesis structure

This thesis is organised into six more chapters. A brief description of its contents is presented below.

Chapter 2, *Literature Review*: This chapter starts with a brief review of the ocean wave's mechanics and the most used theoretical and empirical formulations developed to describe shoaling, wave breaking, wave run-up, and overtopping. The following section presents research on the availability of worldwide wave energy. Section 2.6 reviews the operational principle of wave energy extraction, presents iconic WECs, and discusses their strengths and weaknesses. Section 2.7 provides a more extensive review of OWEC, including its operation parameters, studies on improving efficiency, and advantages and disadvantages. Finally, the main gaps detected in the development of OWEC are highlighted at the conclusion of this chapter.

Chapter 3, *Numerical Framework*: This chapter presents the characteristics of Large Eddy Simulations (LES) and explains why this type of numerical code is appropriate for this study. The following sections contain the numerical framework of Hydro3D-NWT, including the governing Navier-Stokes equations, the fractional-step method adopted, the level set method applied to capture the water surface, and the immersed boundary method implemented to include solid geometries in the numerical domain.

Chapter 4, *Study of Waves and Submerged Trapezoidal Structure*: This chapter studies the interaction of monochromatic waves with submerged trapezoidal structures. In the first section, Hydro3D is validated to generate monochromatic waves and the water surface transformation against the experimental results collected from the literature. The research is expanded by evaluating the effects of different geometries of the upstream side face of the submerged structure on the wave transformation, hydrodynamics, and forces against the structure.

Chapter 5, *Study of Waves and Sloped Structure*: This chapter studies the interaction of monochromatic waves with sloped structures, which aim to represent the ramp of an OWEC. Two primary processes crucial to analysing the operation of an OWEC are validated: wave run-up and wave overtopping discharge. Then, a comprehensive study of the energy flux and dissipation after the wave breaking is presented. By implementing different structures' heights and allowing wave overtopping, which consequently modifies the run-down flow, the effect of the run-down flow on energy dissipation is evaluated.

Chapter 6, *Conceptual Structures*: This chapter explores the effects of two novel geometries on the run-down flow and the power available at the crest of the structure. Numerical simulations are conducted, and their results are presented and analysed. Based on the results of the previous chapters and the present one, a series of conceptual geometries of an OWEC's ramp are introduced and discussed.

Chapter 7, *Conclusions and Further Works*: The study's main conclusions and outcomes are presented in this chapter. In addition, the following steps to expand the research's results and the improvements required to be implemented in Hydro3D to continue this investigation are presented.

Chapter 2

Literature Review

2.1 Ocean Waves

Wind-generated waves result from the interaction between air and the water's surface. The wind disturbs the water's surface, transmitting momentum and energy to the water. The alteration creates a disequilibrium of the water's mass, creating a vertical oscillation of the water's surface. The oscillation is propagated across the surface due to an interaction of gravity and inertia forces, transmitting the energy to further places. The amount of energy transferred from the air to the surface of the sea depends on the following factors:

- The wind's intensity
- The wind's duration
- The distance (fetch) where the wind blows in the same direction

Waves produced by storms in deep water travel hundreds or thousands of kilometres with minor energy loss, but as they approach shallow waters, they interact with the sea bed and shorelines, making them slow down and change shape. The wave's profile changes as the water depth reduces, its crest gets steeper until it becomes unstable and collapses. All these processes dissipate the energy transported by the waves from their origin.

Ocean waves can be classified as *sea* or *swell*. The first type is waves generated by local winds. The water surface is irregular in this condition, and several wave

periods and lengths are present, figure 2.1a. On the other hand, swells are waves generated in a remote location. The distance travelled permits the waves to sort themselves into groups of similar speed and lengths; therefore, when they reach the shore, they have a fairly regular wavelength and velocity, figure 2.1b.



Figure 2.1: Ocean waves. Figures extracted from [1]

Waves can be roughly described by their wave height, H , period, T , and length, L , as shown in figure 2.2. H is the vertical distance from the trough to the wave's crest. L is the horizontal distance between consecutive crests. T is the time lapse for two successive crests passing a particular space point. The frequency, f , is also commonly used and is the inverse of the wave period, $1/T$. The wave celerity, C , is the speed at which waves propagate and is defined as L/T .

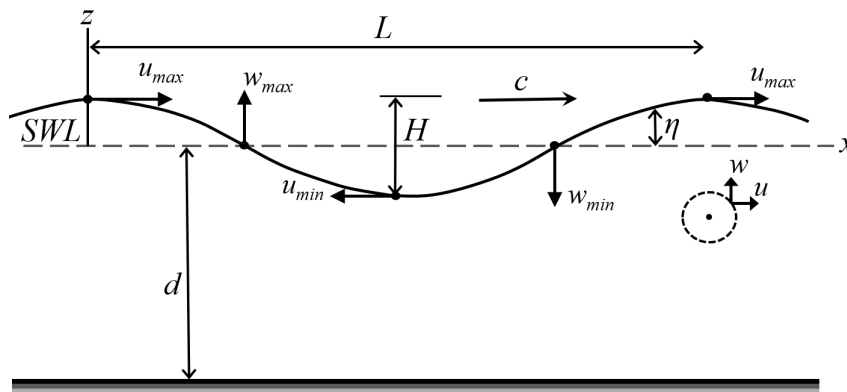


Figure 2.2: Linear Waves description.

Under the water surface, the particles move with an orbital trajectory, which decreases in amplitude with the water depth, as shown in figure 2.3. The particles

have a significant movement only in a range of $L/2$ depth; therefore, in deep water conditions, the waves are not affected by the morphology of the seabed. When the depth is smaller than $L/2$, the bottom affects the waves, and the particles change their circular orbit into a more elliptic one and flatter near the bottom. The waves slow down, decrease in length, and become steeper. As the water depth continues to decrease while the waves approach the shore, the particles near the bottom slow down faster than the particles near the surface. This imbalance and the increase in steepness make the waves collapse and break, transforming energy into turbulence.

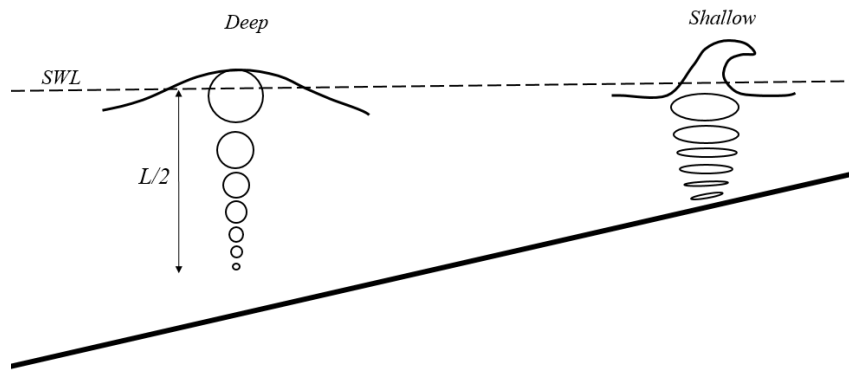


Figure 2.3: Water particles movement under the surface.

Different types of wave-breaking can occur depending on the wave conditions and the characteristics of the shore morphology figure 2.4. Studies have analysed this process due to its relevant role in coastal hydrodynamics [36, 37, 38]. The Iribarren Number or Surf Parameter (ξ) can be used to estimate the type of breaking to occur. ξ , equation 2.1, depends on the slope angle, α , and the wave steepness, $s = H/L$. In the spilling type, $\xi < 0.5$, a turbulent area is formed in the front of the wave, introducing air in the flow and dissipating energy. This type of breaking is common in gentle slopes and steep waves, and extended surf zones are present on the beach where this breaking is found. The presence of a curl wavefront is a characteristic of plunging breaking waves, $0.5 < \xi < 2.5$. This type of breaking is the most violent when the overturning jet plunges into the water ahead. An air pocket is created when the wavefront collapses, introducing significant air in the flow. $2.5 < \xi < 3.0$ generates a breaking condition where the curl of the wavefront is not as developed as the plunging type. The base of the wave collapses before

the overturning of the water jet. In the surging breaking type, $\xi > 3$, the wavefront does not collapse; however, an area of high turbulence is generated at the toe of the wavefront. The last two breaking types are characteristics of low-steepness waves and steep slopes.

$$\xi = \frac{\tan \alpha}{\sqrt{s}} \quad (2.1)$$

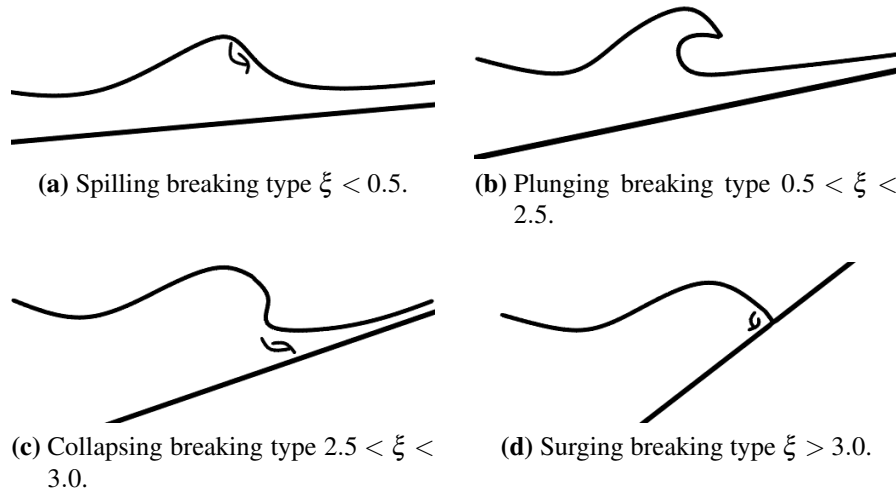


Figure 2.4: Wave breaking type and estimate ξ .

2.2 Wave Theory

2.2.1 Linear Waves

The Linear Wave theory, first presented by Airy in 1845, describes waves with small amplitude. It can be applicable to describe *swell* waves moving in deep water as regular waves or irregular waves as a sum of regular waves with different frequencies, as long as the amplitude is low. This mathematical formulation provides equations to describe the surface profile, the wave celerity, the pressure field and particle movement. For its deduction, the following assumptions are required:

- The water is homogeneous and incompressible, with negligible surface tension forces.

- Flow is irrotational. The velocity potential ϕ must satisfy the Laplace equation.

$$\frac{\partial^2 \phi}{\partial x^2} + \frac{\partial^2 \phi}{\partial z^2} = 0 \quad (2.2)$$

where x and z are the horizontal and vertical coordinates.

- The bottom is stationary, impermeable and horizontal. There is no adding or removing energy or generating reflections.
- The pressure in the air-water boundary is constant.
- The wave height is small compared to the wavelength and water depth. Thus, this theory applies to low steepness waves in deep-water conditions.

The profile of a linear wave travelling at a celerity (C) on a water depth (d) is presented in figure 2.2. The elevation reference, $z = 0$, is defined at the still water level (SWL). The wave surface profile is defined by η , as a function of the position x and time t .

Solving equation 2.1, according to the assumptions and boundary conditions [39], the free surface elevation can be calculated as follows:

$$\eta(x, t) = \frac{H}{2} \cos(kx - \omega t) \quad (2.3)$$

Where:

$$\begin{aligned} k &= 2\pi/L, \text{ wave number} \\ \omega &= 2\pi/T, \text{ wave angular frequency} \end{aligned} \quad (2.4)$$

The wave number k and the angular frequency ω , are related with the dispersion relation:

$$\omega^2 = gk \tanh(kd) \quad (2.5)$$

and

$$C = \sqrt{\frac{gL}{2\pi} \tanh\left(\frac{2\pi d}{L}\right)} \quad (2.6)$$

The relative water depth is defined as the water depth over the wavelength, d/L . When the relative depth is larger than 0.5, it is considered a deep-water condition, and the hyperbolic component in equation 2.6, is close to one; therefore, the wave's celerity can be estimated as:

$$C = \sqrt{\frac{gL}{2\pi}} \quad (2.7)$$

Inserting $C = L/T$ in equation 2.7, the following expressions can be obtained for deep-water conditions:

$$C = \frac{gT}{2\pi} \quad (2.8)$$

$$L = \frac{gT^2}{2\pi} \quad (2.9)$$

Equation 2.5, and the further deductions for deep water indicate that the celerity and length of the waves are independent of the wave height. This statement is valid for low-amplitude waves. As the wave steepness increases, a dependency between L , C , and H starts to grow, limiting the applicability of the Linear theory. Thus, higher-order solutions are needed to fully describe the characteristics of the wave .

In the Linear wave theory, the movement of the water particles is described by the following expressions:

$$u(x, z, t) = \frac{\pi H}{T} \left[\frac{\cosh(k(d+z))}{\sinh(kd)} \right] \cos(kx - \omega t) \quad (2.10)$$

$$w(x, z, t) = \frac{\pi H}{T} \left[\frac{\sinh(k(d+z))}{\sinh(kd)} \right] \sin(kx - \omega t) \quad (2.11)$$

where u is the horizontal velocity of the particle, and w is the vertical velocity. These two velocities are 90° out of phase, as shown in figure 2.2. The maximum

magnitude of u is reached at the crest and trough of the waves, with w being zero in those locations. On the other hand, the maximum magnitudes for w are reached at the surface when it is located at $z = 0$, with u equal to zero in those locations.

The wave energy is partly potential because of the wave shape and partly kinetic due to the velocity of the particles. Most energy is concentrated near the surface because their movement decreases with the water depth, figure 2.3.

According to the Linear Wave theory, surface waves have a sinusoidal profile; this is a reasonable assumption for low steepness and deep water conditions; however, for steeper waves in deep-water or transitional depths conditions, $d < L/2$, the wave's profile becomes more complex, figure 2.5. Vertical asymmetry appears, with the crest's fluctuation larger than the trough's. The troughs are longer and flatter, and the crests are steeper. Moreover, when waves get closer to shore, and the water depth is less than $L/2$, the particles' orbit becomes elliptical and flatter near the bottom. In this region, the Linear Theory loses its applicability. More complex theories, such as 2nd, 3rd and 5th order Stokes, Cnoidal and Singular waves, offer a better agreement when the assumptions of low amplitude and deep-water conditions are not satisfied. These theories follow similar assumptions to the one presented in the Linear theory; their deduction and formulations can be found in several sources in the literature.

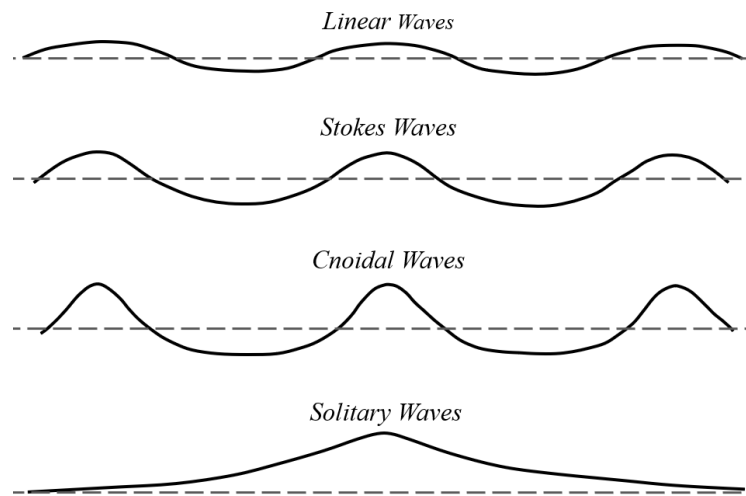


Figure 2.5: Representation of wave profiles for different theories based on [2].

Selection of the correct wave theory depends on the characteristics of the waves to reproduce, H and T , and the water depth. Figure 2.6 shows a plot based on Le Méhauté (1976), where the area of validity of different wave theories is proposed depending on the dimensionless depth and wave height. It is essential to highlight that this plot only delivers the first evaluation to define the theory to use; however, the final decision will depend on which theory is the most agreeable with the data available.

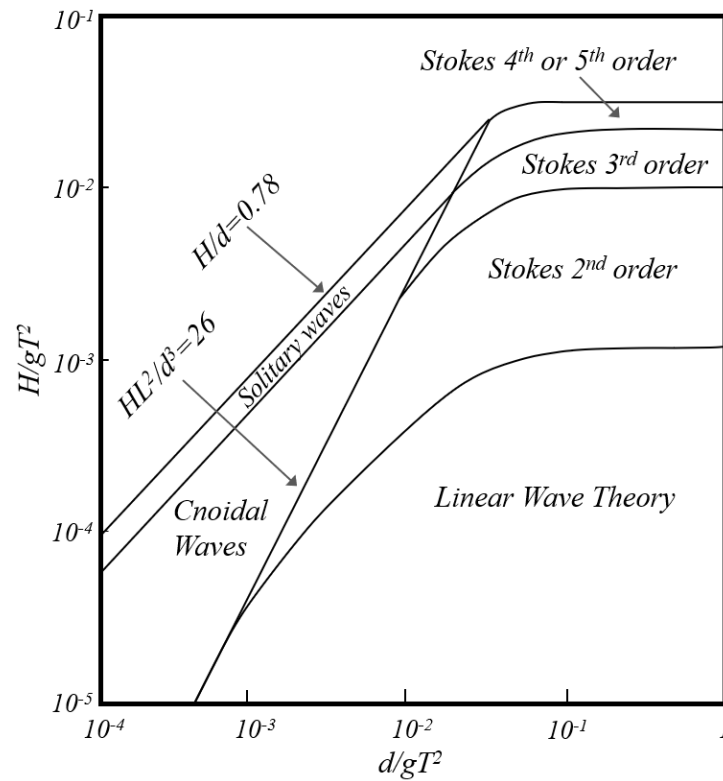


Figure 2.6: Wave theories depending on the dimensionless depth (X axis), and the dimensionless wave height (Y axis). Based on [3]

2.2.2 Stokes Waves

Stokes, [40], developed a theory that allows to describe wave with a steepness out of the applicability of the Linear Theory. This formulation can be used in deep and intermediate depths. This theory is formulated in terms of a power series in successively higher orders of the wave steepness.

$$\phi = \frac{c}{k} \sum_{n=0}^{\infty} [\phi_n \cosh(nk(d+z)) \sin(n(kx - \omega t))] \quad (2.12)$$

In this research, 2nd order Stokes Waves are used. The solution for the second order is obtained by truncating the solution to the second order. The water surface elevation and particle velocities for the Second order Stoke waves are presented in equations 2.13, 2.14 and 2.15.

$$\begin{aligned} \eta(x, t) = & \frac{H}{2} \cos(\omega t - kx) + \\ & \frac{H^2 k}{16} (3 \coth^3(kd) - \coth(kd)) \cos(2(\omega t - kx)) \end{aligned} \quad (2.13)$$

$$\begin{aligned} u(x, z, t) = & \frac{H}{2} \omega \left(\frac{\cosh(k(d+z))}{\sinh(kd)} \right) \cos(\omega t - kx) + \\ & \frac{3}{16} \omega (kH)^2 \left(\frac{\cosh(2k(d+z))}{\sinh^4(kd)} \right) \cos(2(\omega t - kx)) \end{aligned} \quad (2.14)$$

$$\begin{aligned} w(x, z, t) = & -\frac{H}{2} \omega \left(\frac{\sinh(k(d+z))}{\sinh(kd)} \right) \sin(\omega t - kx) - \\ & \frac{3}{16} \omega (kH)^2 \left(\frac{\sinh(2k(d+z))}{\sinh^4(kd)} \right) \sin(2(\omega t - kx)) \end{aligned} \quad (2.15)$$

where, H is the wave height, d the water depth at still water level, k the wave-number defined as $k = 2\pi/L$, with L the wave length.

The first term in equations 2.13, 2.14 and 2.15 is the Linear Wave theory solution. The second term is a function of the wave steepness which has a small value compared to the wave height, but increase in magnitude as the waves became steeper. The second component has twice the frequency of the first term generating that the two components reinforce each other at the wave crest and oppose each other at the wave trough. This effect create a a wave profile with a vertical asymmetry, which mean a stepper wave crest and flatter wave trough compared to Linear waves.

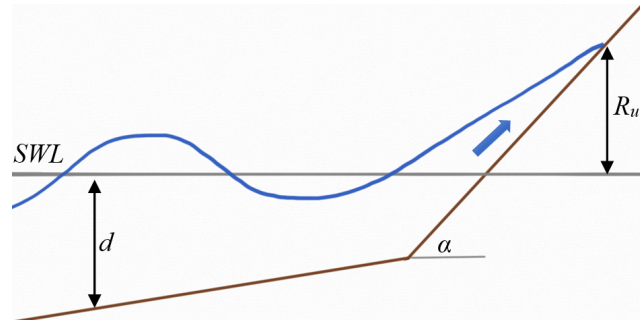
Higher order solutions can be found in the literature for example third order-order Stoke [41] and fifth-order in [42] and [43].

2.3 Wave Run-up and Overtopping

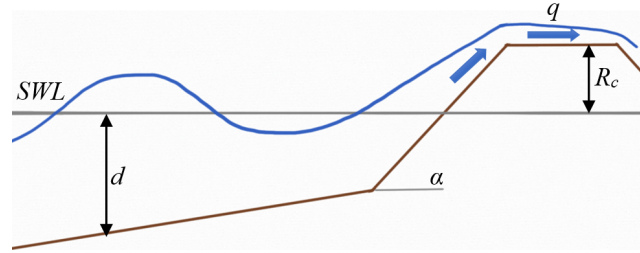
When waves crash against a sloped structure, an ascending flow, known as wave run-up, is generated on the structure's surface. The elevation that the front of the flow reaches is measured as R_u (m), figure 2.7a. After reaching the highest elevation, the water starts running down and back to the sea; this flow is known as run-down or backwash. When a run-up flow has enough energy to reach the top of the structure and pass over it, an overtopping discharge is produced, figure 2.7b. The overtopping is usually quantified as a mean discharge, q (m³/s), by metre width. These two parameters, R_u and q , are mostly used in coastal engineering to determine the dimensions of coastal defences, aiming to keep overtopping as low as possible but within the budget and to comply with operational and environmental restrictions. In a conservative design, no overtopping is allowed, forcing the design to increase the structure's freeboard, R_c , and maximise the energy dissipation during the wave breaking and run-up to prevent the flow from overtopping the breakwater.

Wave run-up and overtopping depend on the wave conditions (wave height, period and wave breaking), water depth, the structure's geometry (slope, freeboard R_c), the waves' angle of attack, the roughness of the slope, and obstacles presented on the structure.

Wave run-up and overtopping are highly turbulent flows, which makes it difficult to elaborate theoretical formulations that can accurately describe their process. In practice, the calculation of run-up and overtopping have been based on empirical formulations calibrated by laboratory and field studies [44, 45].



(a) Wave run-up over a sloped surface.



(b) Wave overtopping over a dike.

Figure 2.7: Wave run-up and overtopping.

2.3.1 Wave Run-up

One of the most used methodologies to estimate wave run-up for regular waves on a smooth and impermeable slope is through the surf parameter ξ , equation 2.1. The relationship between the run-up and the surf parameter was studied by Hunt in [46]. For breaking waves, $\xi < 2.5$, the run-up is proportional to ξ , equation 2.16. For non-breaking waves, $\xi > 2.5$, that proportion is lost, and the run-up is estimated to be limited to be 3 times the incident wave height: equation 2.17.

$$\frac{R_u}{H} = \xi \quad \text{for breaking waves} \quad (2.16)$$

$$\frac{R_u}{H} = 3 \quad \text{for breaking waves} \quad (2.17)$$

R_u/H is the maximum dimensionless run-up. No influence of the wave steepness and slope is proposed in [46] for non-breaking waves.

It has been detected that equation 2.17 works well in conditions of low ξ , less than 2, and gentle slopes [6, 7]. However, the equation loses effectiveness as ξ

grows into a non-breaker condition and steeper slope. Other formulations have been developed to account for this uncertainty. In [6], the effectiveness of equations 2.16 and 2.17 is studied, and a new formulation is proposed, equations 2.18 and 2.19.

$$\frac{R_u}{H} = \xi \quad \text{for } \xi \leq 2 \text{ and } \tan\alpha < 1/5 \quad (2.18)$$

$$\frac{R_u}{H} = 2 \left(\frac{\xi}{2} \right)^{\frac{0.04}{\tan^2\alpha}} \quad \text{for } \xi > 2, \text{ and } \alpha > 1/5, \text{ non-breaking condition} \quad (2.19)$$

Figure 2.8 compares equations 2.18 and 2.19 with data from previous laboratory studies [4, 5]. Equations 2.16 and 2.17, lines 1 and 2, respectively, are included, too. It can be seen that both formulations offer a good agreement for conditions with $\xi < 2$; however, for $\xi > 2$, a significant scatter is present in the data. The maximum value of 3 proposed by Hunt significantly overestimates the data, which shows an inflexion point at around $\xi = 2$. Equation 2.19 considers the structure's slope, resulting in different curves depending on the angle. It can be seen that the run-up prediction is reduced with the steepness of the slope. In [6], it is proposed that as the slope becomes steeper, the influence of the run-down flow increases due to the higher angle. This results in a more significant component of the fluid's weight acting opposite to the run-up flow of the subsequent wave, decreasing the run-up height. This influence may also be attributed to the intensity of the flow generated by different slope angles. It is expected that, with a more horizontal inclination, the run-down flow will be slower than in the case of a steeper slope, generating a less intense flow and therefore a weaker opposition to the advance of the incoming wave. This would reduce turbulence and energy dissipation, which would consequently lead to a higher run-up. This effect is investigated further in Chapter 5 of the present study.

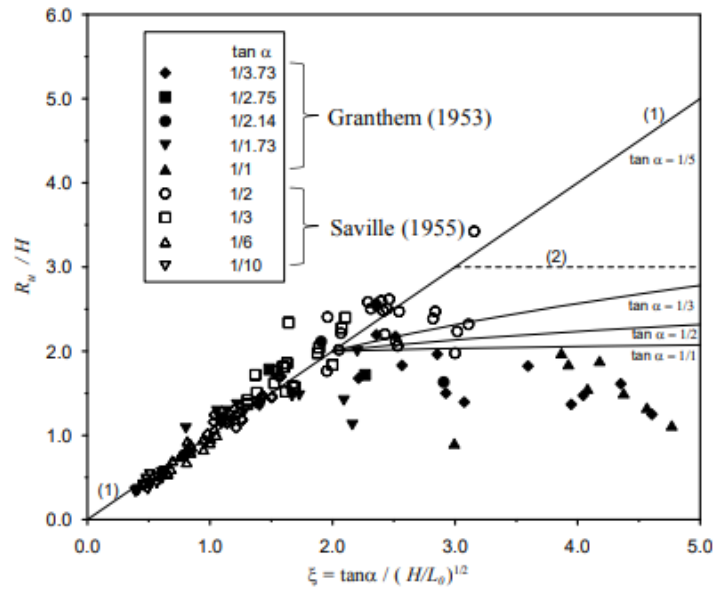


Figure 2.8: Run-up predictions compared with the laboratory results from [4, 5]. Figure extracted from [6].

A single curve was formulated in [47], proposing equation 2.20 for breaking and non-breaking conditions.

$$\frac{R_u}{H} = 2.25 \tanh\left(\frac{\xi}{2}\right) \quad (2.20)$$

In [7], a series of physical tests and numerical simulations were conducted to study the run-up on impermeable and permeable slopes. Figure 2.9 shows the results for impermeable slopes compared equations 2.16 and 2.17. In figure 2.9, the results are classified as breaking waves, $\xi < 3$ and black dots, and non-breaking waves, $\xi > 3$ and grey dots. It can be seen that some conditions, classified as breaking waves, behave more similarly to the non-breaking condition. The coloured dashed lines in figure 2.9 show the average run-up results by groups classified according to the relative depth, d/L_0 . In this case, it is easy to see clear groups and a downward trend when they reach a particular value of ξ . After further analysis of this behaviour, [7] detected that the value of ξ , which defined the transition between both trends, depended mainly on the structure's slope and the wave height. A new breaking criterion, equation 2.21, is proposed according to these findings.

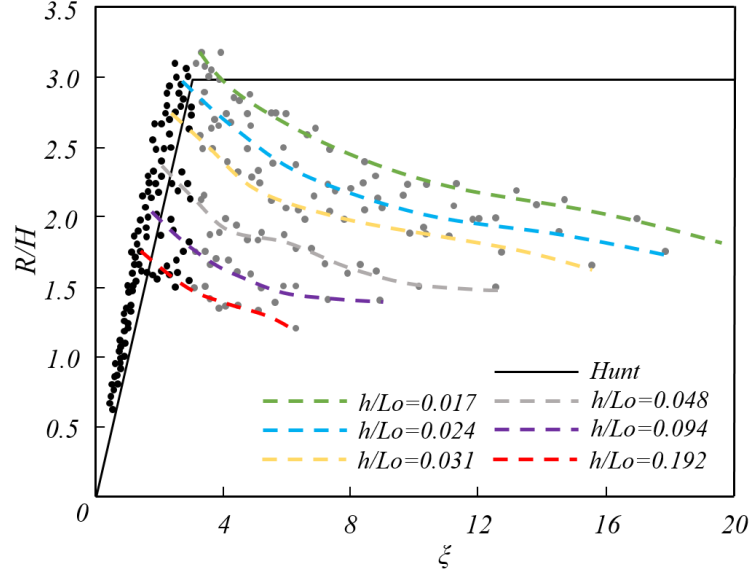


Figure 2.9: Dimensionless run-up results from [7] compared to Hunt's run-up formulation and visualisation of new breaker criteria. Black dots: $\xi < 3$, grey dots: $\xi > 3$. Coloured dashed lines indicate a trend according to the relative depth, d/L_0 . Data from [7].

$$\begin{aligned} \frac{\tan \alpha}{H/d} &< 1, \text{ breaking waves} \\ \frac{\tan \alpha}{H/d} &> 1, \text{ non-breaking waves} \end{aligned} \quad (2.21)$$

Equations 2.22 and 2.23 are proposed in [7] to estimate run-up after reformulating previous methodologies and considering the new breaking criteria. For breaking conditions, the formula proposed in [47], was adapted to the new data and breaker parameter. Regarding non-breaking conditions, a new dimensionless run-up formulation was elaborated, which depends on the slope, wave height, wavelength and water depth.

$$\frac{R_u}{H} = 3.74 \tanh(0.38\xi) \quad \text{for } \tan \alpha / (H/d) > 1 \quad (2.22)$$

$$\frac{R_u}{H} = 1.25 \left(\frac{d \tan(\alpha)}{\sqrt{HL}} \right)^{-0.32} \quad \text{for } \tan \alpha / (H/d) > 1 \quad (2.23)$$

The influence of permeable slopes on the wave run-up was also studied in

[7]. A series of physical tests using slopes conformed by perforated plates were conducted under the same conditions as the impermeable tests. It was found that the inclusion of a permeable slope decreases the wave run-up height compared to the impermeable cases; this reduction increases with the hydraulic conductivity of the slope. In the study, the plates were perforated in their whole length, including the breaking zone. Therefore, the filtration of water directly affects the breaking process, the run-up and run-down flows. In [7], a modification in the shape of the breaking waves is also reported, due to the permeability of the slope; however, the author establishes that the changes are not significant enough to modify the wave breaking types. In [48], the influence of different hydraulic conductivity and roughness of the slope was also studied. In this case, the results show variations of the breaking type when increasing the permeability, moving some cases from collapsing to surging and others from plunging to surging. In this case, it is not possible to analyse whether the breaker modifications are due to the variations in the permeability or the roughness of the slope. These studies indicate that breaking type and run-up can be modified by altering the slope characteristics; however, because of the experimental setups, it is not possible to isolate the effects that the variation of the run-down and breaking type have on the run-up height.

2.3.2 Wave Overtopping

Wave overtopping is generated when the run-up flow has sufficient energy to overpass the structure, generating a flow at the crest of the structure and a discharge of water at the rear of the defence. Coastal defences are designed with an overtopping tolerance to ensure their structure's reliability, control damage at the rear side of the coastal defence, and permit the operation of the protected installation (such as port and industrial activities).

The mean discharge, q , is the most common method to describe the overtopping. It is the total overtopping volume over time per structure width, with units of $\text{m}^3/\text{s}/\text{m}$. Like in the wave run-up, the traditional methods to estimate q are based on empirical formulas, adjusted with physical models and measurements conducted in actual coastal defences.

In [49] a methodology to estimate q for regular waves, based on the weir equation, is developed. Here, it is established that the overtopping over a coastal defence is related to the excess wave height over the structure, equation 2.24. This formulation requires the function $\eta_f(t)$, which describes the wave profile at the toe of the structure, and the calibration of the coefficients k and c , which relate the wave height in deep water to the wave height at the toe of the structure and the effect of different geometries.

$$q = c\sqrt{g}(kH)^{\frac{3}{2}} \left(\eta_f(t) - \frac{R_c}{kH} \right)^{\frac{3}{2}} \quad (2.24)$$

In equation 2.24, the kinetic energy and the effect of the flow running on the structure's surface are not considered directly but are absorbed by the calibration of the coefficients. The only parameter related to the structure is the freeboard height R_c . In [49], this formulation is compared to laboratory results, and a tendency to overestimate the overtopping volumes is found, especially for larger values of H/R_c .

In [50] an empirical formulation is presented to calculate the overtopping discharge, equation 2.25. This exponential equation relates the overtopping to the expected maximum run-up, R_u , if the slope is extended. Previous studies verified that overtopping and run-up are related. It is found that the maximum overtopping occurred at the same slope where the run-up is maximum. This relation can be explained by both processes depending heavily on the amount of energy dissipation during the wave breaking and the interaction of the run-up flow with the slope.

$$q = \sqrt{(gQ^*H^3)} e^{\left[\frac{-0.217}{S} \tanh^{-1}\left(\frac{R_c}{R_u}\right) \right]} \quad (2.25)$$

The coefficients Q^* and S in equation 2.25 were calibrated with data from several studies. Values of this coefficient are presented for different wave conditions and structure typology (wall or sea dike, height, slope and roughness). This formulation gives satisfactory results if an accurate estimation of the run-up is available. It was included in the *Shore Protection Manual* of the US Army Coastal Engineering

Centre [51].

One of the references most used by coastal engineering is the *Manual on Wave Overtopping of Sea Defences and Related Structures* (EurOtop) [44]. This manual is the result of several studies conducted since the 80s, such as [52, 53, 54, 47, 45]. It presents empirical formulations to calculate the mean wave overtopping discharge. Equations 2.26 and 2.27 are the main formulas to estimate the mean overtopping discharge over a sea dike for irregular waves. Like equation 2.25, the formulation presented in this manual is empirical and calibrated through experimental data, and it is also based on an exponential decrease of the overtopping with the increment of the crest freeboard, R_c . Like the run-up behaviour in the previous section, the EurOtop separate the calculation for breaking waves, equation 2.26, and non-breaking waves, 2.27. The overtopping increases with the surf parameter for breaking waves until the breaking type changes. Then, a maximum value of overtopping is estimated, which is independent of the surf parameter.

$$\frac{q}{\sqrt{(gH_{m0}^3)}} = \frac{0.023}{\sqrt{\tan\alpha}} \gamma_b \xi_{m-1,0} e^{-\left(2.7 \frac{R_c}{\xi_{m-1,0} H_{m0} \gamma_b \gamma_f \gamma_\beta \gamma_v}\right)^{1.3}} \quad (2.26)$$

With a maximum of:

$$\frac{q}{\sqrt{(gH_{m0}^3)}} = 0.09 e^{-\left(1.5 \frac{R_c}{H_{m0} \gamma_f \gamma_\beta \gamma^*}\right)^{1.3}} \quad (2.27)$$

The factors γ_b , γ_f , γ_β , γ_v , γ_b and γ^* represent the influence of a berm, the slope's roughness, oblique waves, a crest wall, and a storm wall, respectively. These factors take a value of one when the influence is not presented. If the influence is present, its factor takes a value smaller than one, decreasing the overtopping discharge.

The mean overtopping discharge q , is the most used parameter when designing with overtopping criteria. However, this parameter does not give complete information on the overtopping volume distribution in time. In an actual sea state, irregular waves reach the coastal defences. Not all waves generate an overtopping discharge,

and not all the overtopping volumes per wave have the same magnitude. Individual overtopping volume can differ significantly from one wave to another in irregular wave weather. Even in regular waves, a significant variation of overtopping volumes per wave occurred [49].

The turbulent characteristics of the breaking process and the run-up flow over the slope make the overtopping process a highly non-linear phenomenon, which varies between waves. This aspect explains why the empirical description of overtopping has been the primary methodology used by designers and researchers.

2.4 Wave Energy and Power

The total energy transmitted in the direction of the wave's propagation comprises kinetic energy KE , given by the particle movement, and potential energy PE related to particle elevation. Equations 2.28 and 2.29 show KE and PE calculated for one wave period and a unit width of wave crest. If PE under still water level conditions is subtracted from equation 2.29, the potential energy, only related to the wave's shape, is obtained: denominated dynamic potential energy, DPE , 2.30. The sum of KE and DPE gives the total mechanical energy TE transmitted by the wave.

$$KE = \int_0^T \int_0^{L_y} \int_{-d}^{\eta(t)} 0.5\rho(u^2 + v^2 + w^2) dz dy dt \quad (2.28)$$

$$PE = \int_0^T \int_0^{L_y} \int_{-d}^{\eta(t)} \rho g z dz dy dt \quad (2.29)$$

$$DPE = PE - \left[\int_0^T \int_0^{L_y} \int_{-d}^0 \rho g z dz dy dt \right]^{at\ SWL} \quad (2.30)$$

$$TE = KE + DPE \quad (2.31)$$

where u , v , w , are the velocities in the x , y and z directions, ρ is the fluid density

and g is the gravitational acceleration.

Assuming the Line Wave theory presented previously and deep water conditions, solving equations 2.28 and 2.29 yields:

$$KE = PE = \frac{\rho g L H^2}{16} \quad (2.32)$$

Then, the total energy, TE (J/m), for low amplitude waves and in deep water, in a full wavelength per unit width of wave crest, can be calculated by the following expression:

$$TE = \frac{\rho g L H^2}{8} \quad (2.33)$$

Another expression commonly used to describe wave energy transport is the wave energy density, \bar{E} . It represents the average energy per unit surface and can be calculated by dividing equation 2.33 by the wavelength L .

$$\bar{E} = \frac{\rho g H^2}{8} \quad (2.34)$$

The wave power, P_{wave} , is the energy per unit of time transmitted in the direction of the wave propagation and is commonly expressed in units of kW/m. It can be estimated by the dynamic pressure acting on a vertical plane normal to the direction of the waves and the particle velocity in the direction of the waves, equation 2.35.

$$P_{wave} = \frac{1}{T} \int_0^T \int_{-d}^{\eta(t)} (p + \rho qz) u dz dt \quad (2.35)$$

Assuming deep water conditions and the linear waves, equation 2.35 results as follows:

$$P = \frac{\rho g^2 T H^2}{32\pi} \approx 0.986 T H^2 \approx T H^2 \quad (2.36)$$

For deep water conditions and low amplitude regular waves, the wave power can be approximated as the product of the wave period and the square of its height. Another aspect to highlight is that longer waves transmit more energy when com-

pared with waves of equal height and depth. Longer waves are faster because the wave celerity C is proportional to the period, equation 2.7. On the other hand, near the surface, $d < L/2$, the velocities of the particles, equations 2.10 and 2.11, are inversely proportional to the period, so the particles move more slowly.

2.5 World Wave Energy

2.5.1 Worldwide Wave Energy

The wave energy available in the oceans has been estimated from 1 TW to 10 TW [55, 56]. With the improvement of numerical models and the advancement of equipment available for collecting natural wave information, such as satellites and buoys, better wave energy estimations have been generated.

Figure 2.10 presents the annual wave mean power density estimated in [8]. It can be seen that the wave power density is more concentrated in the north and south of the globe (especially the south). Additionally, the coastlines facing west are the most exposed to high-energy waves. Not all locations shown in the maps are feasible for wave energy harvest because of their remoteness and exposure to severe conditions. Moreover, depending on the wave energy converter chosen, the energy harvested could not follow the same pattern shown in figure 2.10, meaning that the places where the highest wave energy is estimated are not necessarily where more energy can be collected.

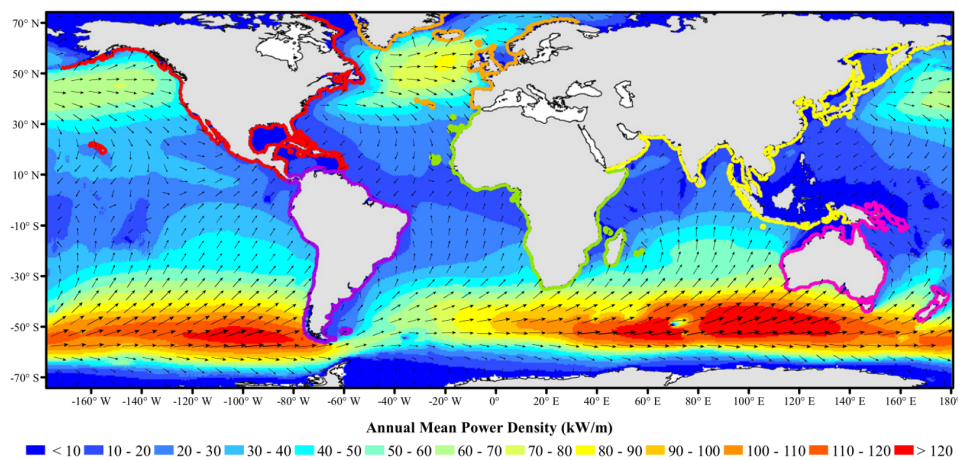


Figure 2.10: Annual mean wave power density and annual mean wave direction. Land buffer shows as a coloured band by continent. Extracted from [8].

Table 2.1 presents the wave energy power (P), the power yield (Ψ) by a virtual Pelamis P2 farm (more details of device in section 2.6.3), and the efficiency (η_{Ψ}) of that energy plant. The P is calculated only considering 30 nautical miles (nm) wide buffer zone from the coastline - coloured lines shown in figure 2.10. Australia, the United States and Chile - all with coasts facing west - have the most considerable wave energy resources. When considering output power, the top three countries are Australia, Canada, and Chile. The world wave power incident on the coast is estimated to be 2.11 ± 0.05 TW. The total wave power converted by the WEC selected is 96.6 ± 1.3 GW.

Figure 2.11 shows the energy resources by continent calculated in [8], the energy yield considering a deficiency of 4.6% and the electricity consumption by continent. It can be seen that, apart from Asia and North America, the wave power resources are more significant than the annual consumption; however, the energy yield is significantly lower than the energy consumption.

Table 2.1: Annual wave power resource P and output power yield ψ for selected countries, and considering a virtual Pelamis P2 wave farm, [8].

Country	P (GW)	Output Power Ψ (GW)	Efficiency (η_{Ψ})
Australia	280 ± 13	8.30 ± 0.20	3.0
United States	223 ± 12	3.59 ± 0.17	1.6
Chile	194 ± 11	4.62 ± 0.17	2.4
New Zeland	89 ± 16	3.51 ± 0.16	4.0
Canada	83 ± 7	5.13 ± 0.19	6.2
South Africa	69 ± 4	2.17 ± 0.08	3.1
UK	43 ± 4	2.44 ± 0.14	5.7
Ireland	29 ± 4	1.13 ± 0.09	3.8
Norway	29 ± 4	1.67 ± 0.12	5.7
Spain	20 ± 3	0.65 ± 0.05	3.3

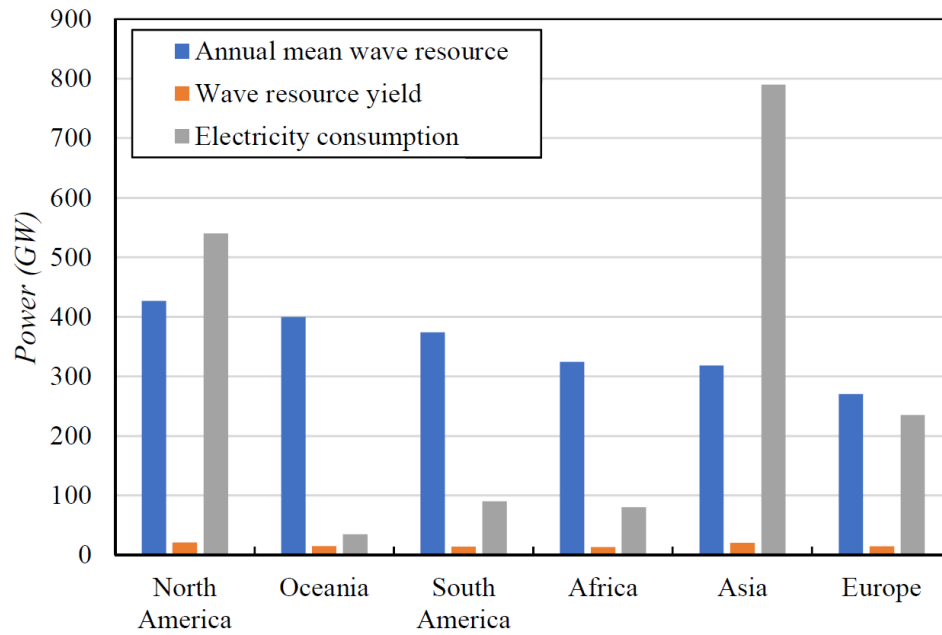


Figure 2.11: Wave power available and yield compared to electricity consumption in (GW). Data from [8]

2.5.2 Chilean Wave Energy

It can be seen in figure 2.10 and table 2.1 that the Chilean coast receives one of the most energetic wave climates in the world; reaching mean wave power values of 100 kW/m in the south. However, the progress in exploiting this energy source is low, with no concrete project to harvest marine energy in the short future. Nevertheless, several studies to better quantify the wave energy power have been supported by public institutions, like The National Institute of Hydraulics (INH) and Universities. International organisations and private companies, such as the Inter-American Development Bank and the British Embassy in Santiago, have also studied Chilean marine resources.

Studies have been conducted to estimate the wave energy resources on the Chilean Coast [9, 57, 58, 59, 10]. Figure 2.12 shows the mean wave power calculated by Monardez in [9] for 100 m and 50 m depth. It can be seen that the wave power increases with the latitude, with values from 23 kW/m in the north to 100 kW/m in the far south for the 100 m depth estimation and from 20 kW/m to 80 kW/m in the case of the 50 m depth calculations.

The variability of the energy resources is also important when evaluating the suitability of a location for energy production. A useful parameter to evaluate the variability of the energy resources are the parameters P_{10} , P_{50} , and P_{90} . These represent the wave power exceedance by 10%, 50%, and 90% of the time, respectively. P_{90} represents a start-up level to select a site to harvest wave energy; a P_{90} of 5 kW/m is usually considered a good indicator of a suitable location for wave energy harvest, [9, 10]. On the Chilean coast, the P_{90} very rarely descends below 10 kW/m, [9]. The interval between P_{90} and P_{10} indicates the wave power variation the chosen device will be exposed to. Its design should aim to operate efficiently within those levels, minimising losses and maximising the power output, but it will also have to endure extreme conditions.

Lucero, [10], calculated the wave power in central Chile using an exceedance approach; these results are presented as a wave energy map figure 2.13. For a condition of deep water, P_{50} and P_{90} don't change significantly along the Chilean coast. On the other hand, an increment of P_{10} with latitude is visible, which means that the extreme conditions get rougher in the south. In figure 2.13, it is possible to see the variation of the wave power as the waves approach the coast. In most places, the power level decreases; however, a wave energy concentration occurs in some areas. figure 2.14 shows hotspots near the shore. This phenomenon is more common near headlands, where wavefronts converge. These locations can be attractive places for nearshore wave energy farms.

In figure 2.13, it is observed how areas protected by islands and bays present a smaller variation between P_{90} and P_{10} , compared to open coasts. Less energetic waves reach these locations due to the protection offered by the geography. A narrow variability of the waves and reduced extreme conditions allow for better device optimisation, a benefit that can be translated into more energy yield than offshore devices.

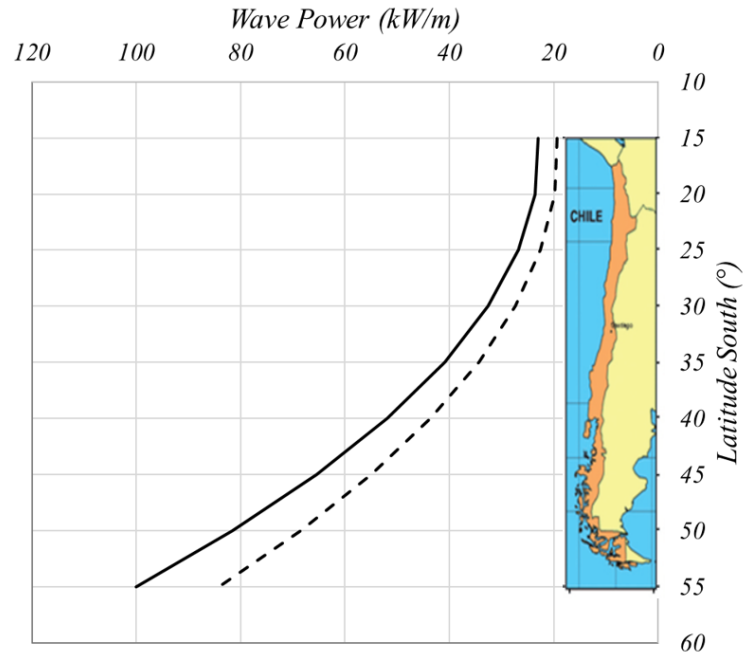


Figure 2.12: Wave power in front of the Chilean coast estimated in [9]. Solid Line: 100 m. depth, Dashed line: 50 m depth.

Directional variability is another key aspect of energy sources. This parameter gives the variation associated with the direction of the incoming waves. The wanted scenario is where waves only approach the WEC from one direction, so less adaptation of the devices is required, providing higher efficiency and more output power. In [60], the directional spectrum for the location of San Antonio Port in the centre of Chile is calculated, which shows that the 75% of the time waves approach that location from the southwest with a narrow band between 240° and 255° . This result shows a good directional variability for wave energy harvesting in San Antonio Port.

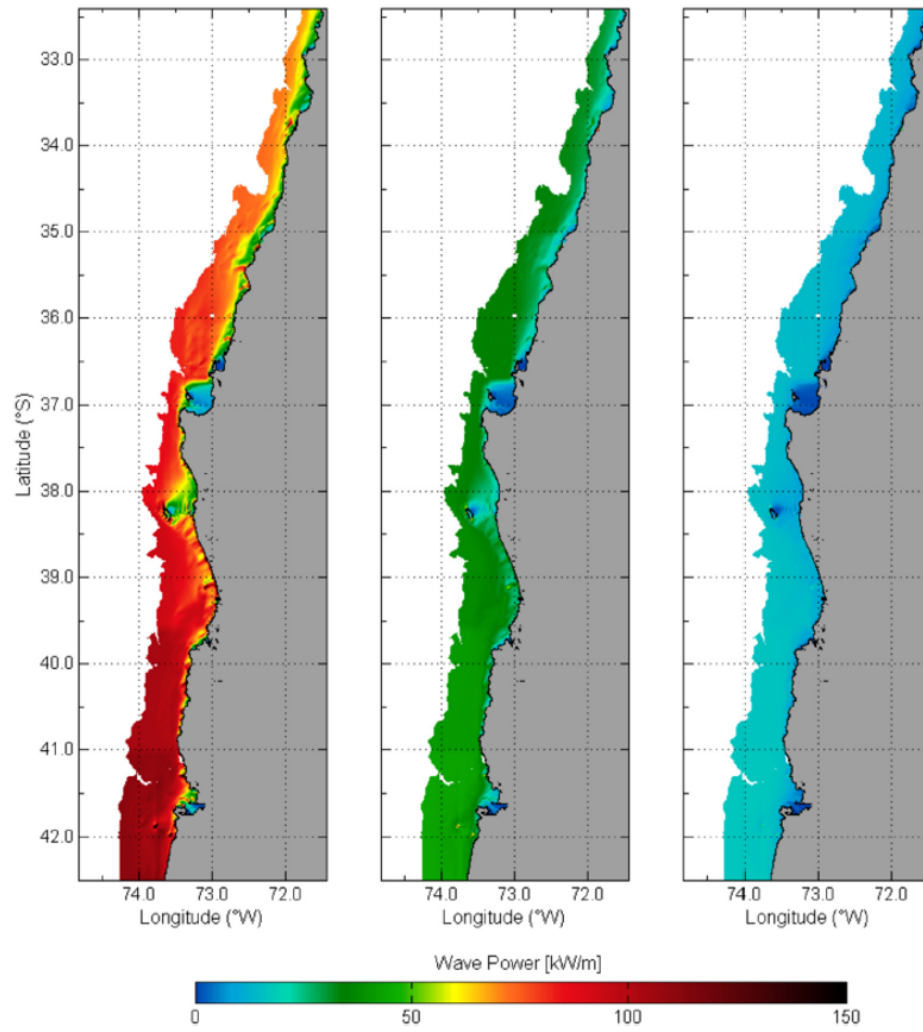


Figure 2.13: Central Chile wave power resources maps P_{10} , P_{50} and P_{90} presented in [10]. Extracted from [10].

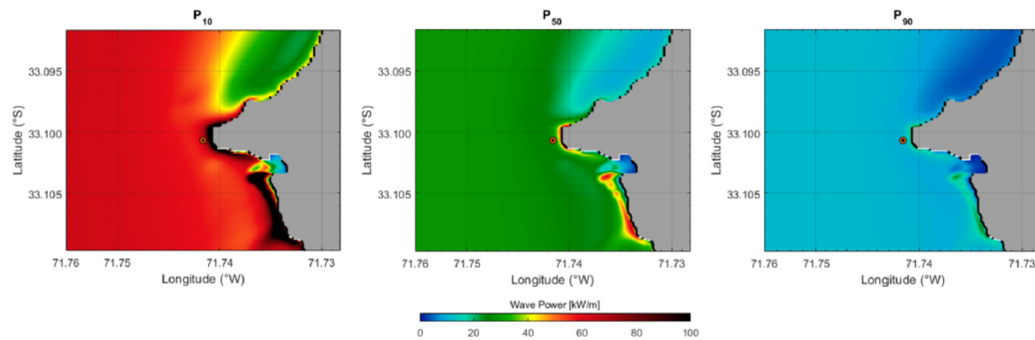


Figure 2.14: Concentration of wave power P_{10} , P_{50} and P_{90} near the shore presented in [10]. Extracted from [10].

2.6 Wave energy converters

The idea of collecting energy from waves is not new; the oldest pattern of a device for that purpose dates back to 1799 in France, where a floating device is described, however, it is unclear if it was ever built. One of the first records of a successful device to extract energy from waves was created in 1895 and installed in California, USA. This device took advantage of the water level oscillation to pump seawater, which was then used to moisten roads and reduce dust clouds. This device operated for 12 years [11].

This section reviews the main principles of harvesting wave energy and presents some of the most iconic WECs.

2.6.1 Wave Energy Converter Classification and Principles

Different criteria are used to classify WECs, according to their location from the shore, orientation, and working principle.

According to their distance to the shore, the devices are classified as Onshore, Nearshore and Offshore, figure 2.15. This classification is related to the water depth of the location where the device operates. On shore, devices are usually installed on the natural coast or coastal structure, such as breakwaters and piers. Nearshore energy converters are commonly fixed to the seabed at one end, leaving the other side free to move with the waves. Offshore devices located in deep water, more than 50 m depth, are floating devices moored to the seabed and use the oscillation of the water surface.

Regarding the orientation of the wave energy converters, figure 2.15, they are classified as “terminators” if their main dimension is parallel to the front of the waves and their length is comparable to the wavelength. If their main dimension is perpendicular to the wavefront, they are called “attenuators.” If the device dimensions are significantly smaller than the waves, they are called “point absorbers”.

Based on their working principle Falcao, [15], proposed three groups: OWC; OWEC; and oscillating bodies (OB). This last group has attracted more attention from developers; therefore, more devices that use that principle have been created. A review of each group is presented next.

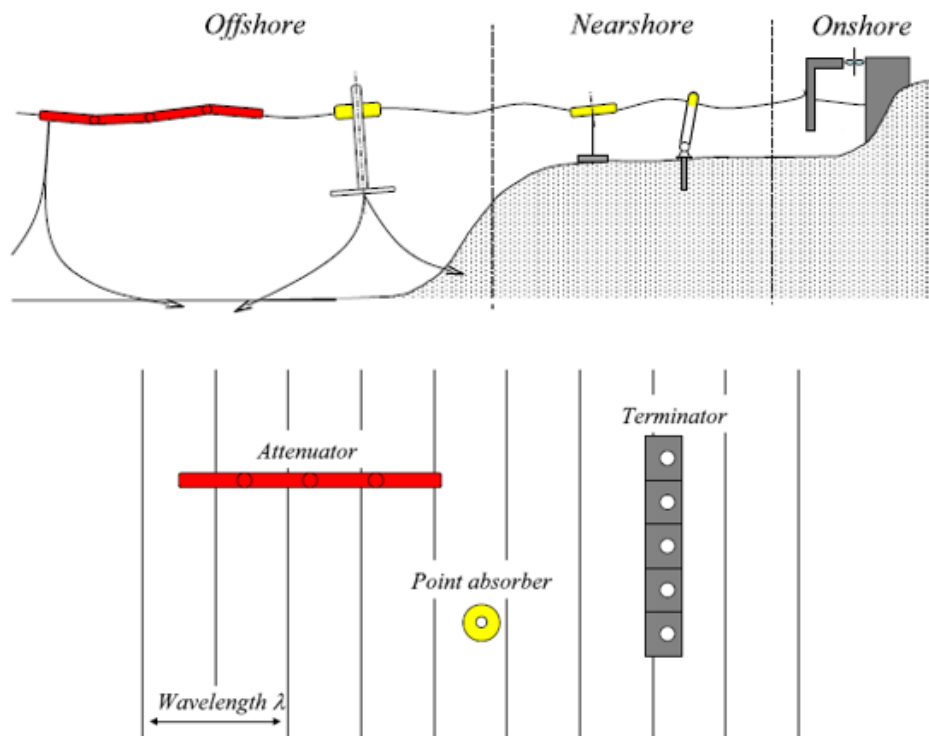


Figure 2.15: Wave energy converters classification according to: Above distance to the shore, bottom orientation to waves. Extracted from [11]

2.6.2 Oscillating Water Column (OWC)

OWCs use the water surface variation to generate an airflow in a partially submerged chamber, figure 2.16. The air moves out of the chamber through an orifice when the water level increases and goes back inside when the water level decreases. This airflow operates an Wells air turbine to produce electricity. This type of WEC can be projected on land, as a fixed structure, or as a floating device. One of the main advantages of this device is the lack of mobile parts, which makes this technology more robust and less sensitive to corrosion compared to oscillating WECs.

These kind of WECs was one of the first to be studied in full size, with projects conducted in several parts of the world: Norway 1985 (*Kvaerner column, Toftestallen*), Japan 1987 (*Saka Port*), India 1991 (*Vizhinjam Fisheries Harbor*), Portugal 1999 (*Pico, Azores Island*), UK 2000 (*Islay island*), Spain 2006 (*Mutriku breakwater*) and Italy 2013 (*ReWEC3 at Civitavecchia Harbor*). All these projects were constructed on the natural ground or in breakwaters. Other projects have been

built as independent structures, such as Osprey (*Scotland 1995*) and Oceanlinx (*Australia 2010 and 2014*); however, they could not be thoroughly tested because of damage caused during towing or severe weather conditions.

UK's LIMPET plant (Land installed marine power energy transmitter) installed on a rocky cliff on the island of Islay in Scotland in 2000 [12, 11], figure 2.17 was the first world WEC to be connected to a national electrical grid. Its rated power was 500 kW, and it input energy to the grid between 2000 and 2012 for more than 50,000 hours. The plant's operational efficiency was estimated at around 8%, much lower than the 48% initially estimated during the design [61].

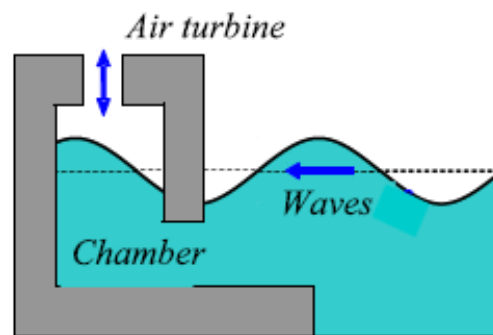
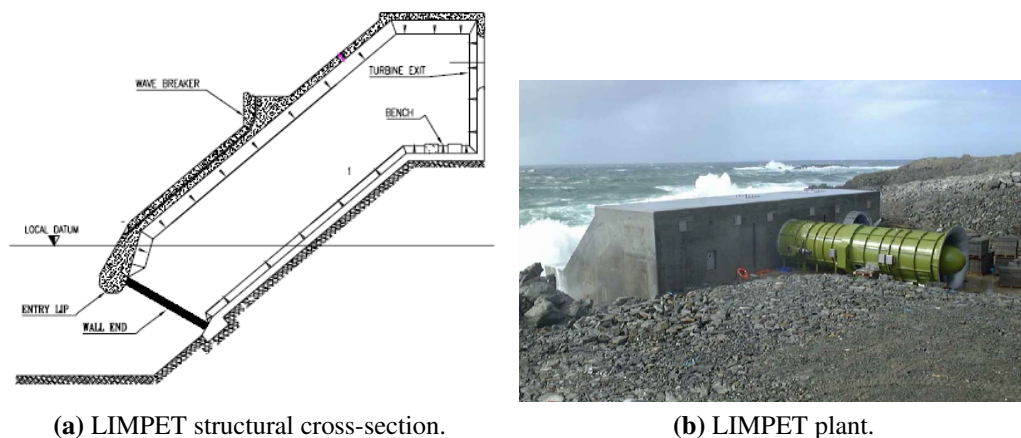


Figure 2.16: Oscillating water column (OWC). Extracted from. Extracted from [11]



(a) LIMPET structural cross-section.

(b) LIMPET plant.

Figure 2.17: LIMPET cross-section and general view. Extracted from [12]

A more recent OWC plant is the Mutriku in Spain, figure 2.18 commissioned by the Spanish Energy Agency of the Basque Government (EVE). The building started in 2006, and operations began in 2011. This initiative was included in the

breakwater design of the Mutriku village, adding new benefits to the project. The plant is 100 m long, has 16 chambers, and has a total power of 296 kW. Between 2014 and 2016, 246 kWh/year were supplied to the National Grid (reported by The Basque Energy Agency EVE). The plant's ability to generate energy has been proven but, its production has been lower than expected. However, its efficiency has improved during the years of operation, due to continuing research, which has increased from around 2.6% [61], to 26%, [62]. Mutriku regularly supplies electricity to the Spanish Grid.

The structure suffered significant damage from storms in its first years of operation; further analysis detected that internal pressures in the chamber were underestimated during its design [13]. Noise contamination due to the turbine operation and explosive air releases in rough wave conditions have also been a problem during the plant's operation [11].

One significant challenge to improving the operation of an OWC is the efficiency of the Wells turbine, estimated at around 70% for unidirectional flows, but it can be reduced to 45% due to the changes in airflow direction during the operation of an OWC [11]. The Mutriku wave energy plant has worked as a full-scale laboratory, allowing the researchers to improve their understanding of this kind of WEC and to refine the operation of the Wells turbines.

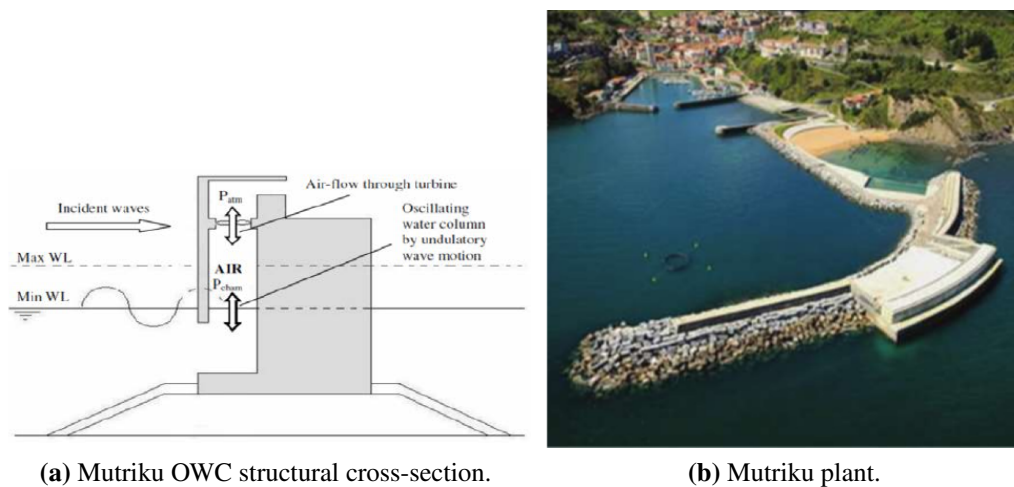


Figure 2.18: Mutriku plant, cross-section and general view. Extracted from [13].

2.6.3 Oscillating Bodies

Oscillating Bodies are based on the movement of their floating parts caused by their interaction with waves. They use the relative movement from the seabed or between their parts to generate electrical power. The implementation varies depending on the type of motion the floating part is free to do, whether it's fixed to the bottom or floating (mooring), as well as the number of moving elements that conform to the device.

The movement of any floating body is defined by six degrees of freedom: 3 in translation (surge, heave and sway) and 3 in rotation (pitch, roll and yaw).

Depending on their design, they can be installed in different water depth conditions. They are attractive options in deep water because they can be exposed to waves in their more energetic condition; therefore, the energy that they could yield is the largest compared to the other types of WECs, OWCs and OWECs [16]. However, these types of devices have the most complex mechanics and electrical conversion systems, increasing their cost and weaknesses. Moreover, the further the device is installed from the shore, the more the cost of installation and maintenance increases, along with the grid connection system.

A point absorber is a WEC that uses heaving and surge movements. Its size is small compared to the wavelength. Point absorbers can be floating or submerged, but their principle of operation is the same. They take advantage of the buoy's relative up-and-down movement relative to their fixed anchorage. This movement operates a pump that moves sea water through a turbine that produces electricity.

A CETO (cylindrical energy transfer oscillator) is an example of a submerged point absorber figure 2.19. In addition to producing electricity, some of the pressure water generated by the buoy's oscillation is used in inverse osmosis to produce desalinated water. This WEC is one of the most successful devices used in several initiatives worldwide (Norway, UK, Canada, Japan and Australia).

The Oyster system, figure 2.20, was developed in 2005 by Aquamarine Ltd and the Queen's University in Belfast [11]. This device is classified as a terminator-fixed WEC that exploits the water's horizontal movement below the surface. As it

was exposed before, in shallow water, the movement of the water's particles tends to be mainly horizontal due to the presence of the seabed. This type of WEC is intended to be installed in nearshore conditions (10 to 15 m depth). The movement of the pallet operates pistons that pump water to activate a hydroelectric turbine. There have been two versions of this device: Oyster 1, 12 m high and 18 m wide, with a rated power of 315 kW; and Oyster 800, 12 m high and 26 m wide, with a rated power of 800 kW. The increment in the size of the second version increased energy production by more than 50% per unit width [11]. The mooring system is critical because significant horizontal forces are generated during operation. The fluctuation in sea level due to the tidal range can considerably affect Oyster's energy production.

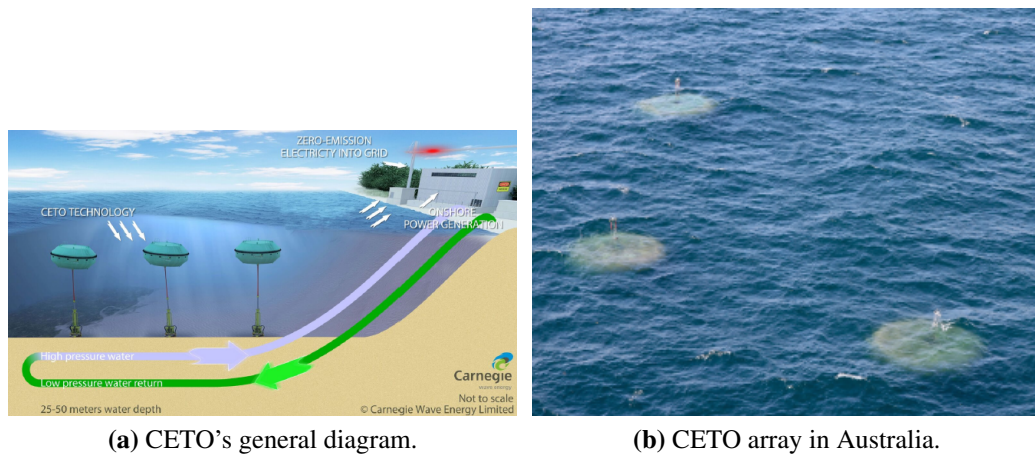


Figure 2.19: Point Absorber CETO. Pictures ©Carnie Clean Energy.

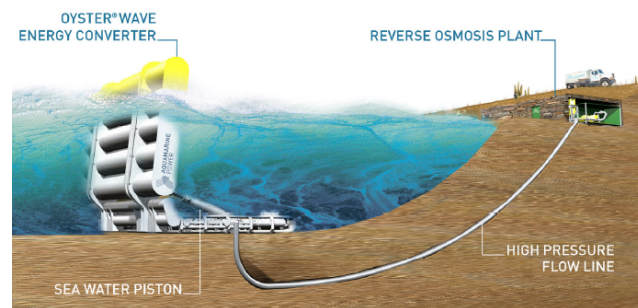


Figure 2.20: Oyster WEC diagram. Pictures ©Carnie Clean Energy.

A system that uses the pitching movement of a floating body is Pelamis, fig-

ure 2.21b, developed by Ocean Power Delivery. This device consists of an array of cylindrical bodies linked with articulated connections. The relative motions between the cylinders operate a hydraulic power take-off. The first prototype, P1, was tested from 2004 to 2007 near the Orkney Islands Scotland; it was 120 m long and 3.5 m in diameter and had 750 kW rated power [11]. In 2008, a 2.25 MW farm of 3 Pelamis P1 was installed in Portugal; it was the first worldwide wave energy farm connected to the National Grid, making an outstanding achievement for the marine energy industry. Unfortunately, technical problems related to the mooring rapidly appeared, and due to economic difficulties, the project was forced to stop with only a few months of operation. The implementation of this project made the creation of the energy conversion matrix for the devices installed possible, figure 2.21a. This chart gives the annual production in the function of the wave conditions [14]. A new version of Pelamis, P2, with an increased power of 820 kW, was installed and tested in the Orkney Islands in 2010. Sadly, the company went bankrupt in 2014, so the project was decommissioned the same year, and there have been no reports of significant improvements in this technology since then, to the author's knowledge.

		Power period (Ppow, s)																	
		5.0	5.5	6.0	6.5	7.0	7.5	8.0	8.5	9.0	9.5	10.0	10.5	11.0	11.5	12.0	12.5	13.0	
Significant wave height (Hsig, m)	0.5	empty	empty	empty	empty	empty	empty	empty	empty	empty	empty	empty	empty	empty	empty	empty	empty	empty	
	1.0	empty	22	29	34	37	38	38	37	35	32	29	26	23	21	empty	empty	empty	
	1.5	32	50	65	76	83	86	86	83	78	72	65	59	53	47	42	37	33	
	2.0	57	88	115	136	148	153	152	147	138	127	116	104	93	83	74	66	59	
	2.5	89	138	180	212	231	238	238	230	216	199	181	163	146	130	116	103	92	
	3.0	129	198	260	305	332	340	332	315	292	266	240	219	210	188	167	149	132	
	3.5	—	270	354	415	438	440	324	404	377	362	326	292	260	230	215	202	180	
	4.0	—	—	462	502	540	546	530	499	475	429	384	366	339	301	267	237	213	
	4.5	—	—	544	635	642	648	628	590	562	528	473	432	382	356	338	300	266	
	5.0	—	—	—	739	726	731	707	687	670	607	557	521	472	417	369	348	328	
	5.5	—	—	—	750	750	750	750	750	737	667	658	586	530	496	446	395	355	
	6.0	—	—	—	—	750	750	750	750	750	750	711	633	619	558	512	470	415	
	6.5	—	—	—	—	750	750	750	750	750	750	750	743	658	621	579	512	481	
	7.0	—	—	—	—	—	750	750	750	750	750	750	750	750	676	613	584	525	
	7.5	—	—	—	—	—	—	750	750	750	750	750	750	750	750	686	622	593	
	8.0	—	—	—	—	—	—	—	—	750	750	750	750	750	750	750	690	625	

(a) Energy conversion matrix for Pelamis P1.



(b) Pelamis P2 in Scotland 2012.

Figure 2.21: Pelamis WEC. Extracted from [14].

2.6.4 Overtopping Wave Energy Converters

An OWEC harvests wave energy by capturing the overtopping discharge generated when waves interact with their structure, figure 2.22. The water is held in a reservoir with an elevation higher than the mean sea water level. This height difference is transformed into electricity when the water captured is released into the sea through a turbine, converting the potential energy into electricity. The water level difference between the reservoir and the sea level is known as the hydraulic head, and it is the measure of the mechanical energy available to be collected.

One of the most attractive features of OWECs is their structural simplicity; they comprise a run-up ramp and a reservoir. They don't have moving parts for their operation, which is always a cause of concern in any mechanism. If the device is installed onshore, a significant reduction in construction, operation, and maintenance costs can be achieved compared to technologies that work in the sea. Moreover, they can be included in breakwater projects, new or existing, sharing their construction cost with the main structure and creating new benefits from the coastal defence.

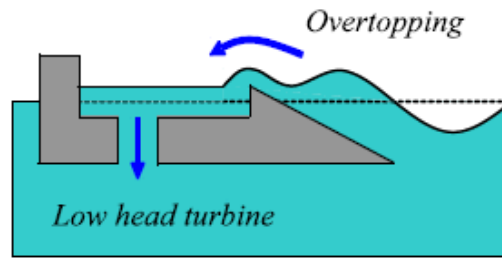


Figure 2.22: Overtopping wave energy converter (OWEC). Extracted from [11]

The downside of these devices is that in all of them the energy harvest is after the breaking of the waves; therefore, the wave energy available for collection is just a fraction of the wave energy in deep water. Their operation is highly sensitive to changes in wave heights. Small waves do not have the energy necessary to overtop the slope and reach the reservoir, generating periods without energy collection. The shape of the run-up ramp and the reservoir's capacity are essential to prevent significant fluctuations in energy production. Water level variations due to tides also affect their operation. A low level will increase the height difference between the mean water level and the reservoir, requiring more run-up to overtop the slope. However, a multi-level design could solve this problem, as proposed in the Seawave Slot-con Generator (SSG) [63].

The Tapered Channel Wave Power Device, commonly known as Tapchan, was a Norwegian initiative to produce energy using the wave run-up. It was built in 1985 in Toftestallen, Norway, figure 2.23. It was constructed on a natural rocky island on the Norway coast. It was composed of a cone-shaped channel that captured the waves, and then, with a gradual reduction of the width of the channel, a wave height increase was achieved. The water volume was then captured in a reservoir of approximately $8,500 \text{ m}^2$. The output flow passes through a low-head turbine back to the sea. Its rated power was 350 kW, and it operated for around six years before being decommissioned due to severe storm damage [11].

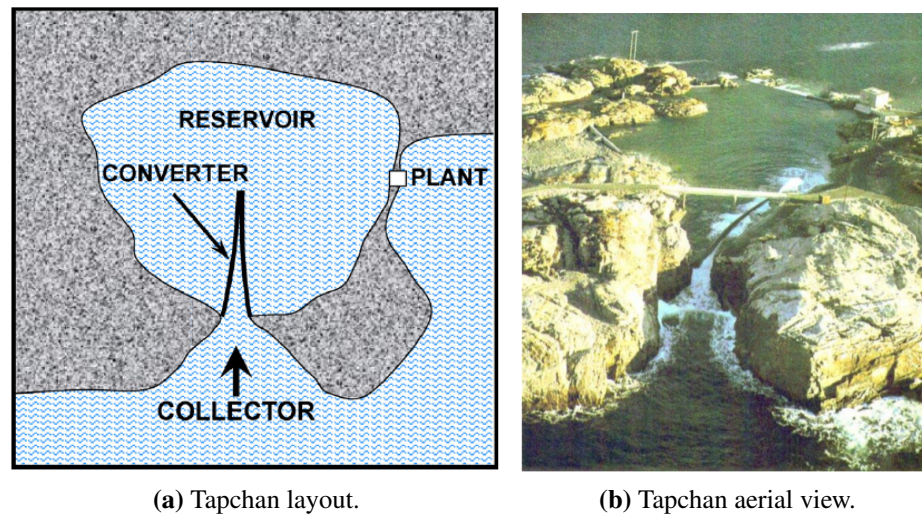


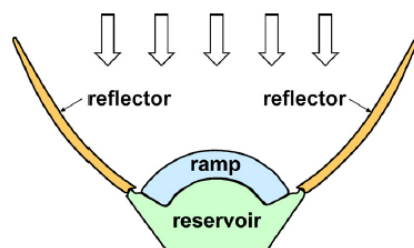
Figure 2.23: Tapchan. Extracted from [15].

A wave overtopping energy converter can also be installed as a floating device, allowing to be exposed to more energetic conditions. This is the case with the Wave Dragon device, developed in Denmark in the early 2000s, figure 2.24. In 2003, a 1/4.5 prototype, 57 m wide and 237 tonnes, was installed in Nissum Bredning and was tested until 2007 [11]. It was a moored floating structure composed of a reservoir with a metallic curve ramp that acted as a beach. One of the key features of this device is the curved arms that are intended to focus the waves to the run-up ramp in the centre of the structure.

Integrating an OWEC with breakwaters is one characteristic that makes them highly attractive. A modern example is the overtopping breakwater for wave energy conversion, OBREC, developed at the University of Campania Luigi Vanvitelli in Italy, figure 2.25 [64, 65]. This device can be integrated into a traditional rubble-mound breakwater. It comprises of a run-up ramp, a reservoir, and the machine room where a low-head turbine is located: 1, 2 and 3, respectively in figure 2.25a. This design derives from the Sea Slope-cone Generator, SSG, figure 2.28. OBREC was designed to be a simpler structure with low maintenance and it was adapted to operate in a low-mild nearshore shore wave climate (<10 kW/m). A series of physical models, with a scale of 1/30, were conducted between 2012 and 2015 to compare the hydraulics performance of traditional rubble mound breakwaters against

OBREC to optimise the device's geometry and assess the energy performance.

In 2015 a full-scale OBREC prototype was built in the San Vincenzo break-water in Naples harbour in Italy, [64], figure 2.25b, where a mean wave power nearshore between 1.6 and 2.5 kW/m was estimated. Two sections with different crest heights were constructed to study the device's performance with different free-boards, 1.78 m and 0.79 m from the highest tide level. Three low-head turbines with a total power of 2.5 kW/m were installed. Reports of the first two years of operation have been published [32], showing the ability of the system to produce energy, which was used to power the acquisition system installed on-site. The necessity of creating specially designed turbines for this type of application has been detected. At the moment of the device's construction, all the turbines available were intended for fresh water under quasi-static water conditions. OBREC is an ongoing research project; more information related to energy collection and generation is expected to be published in the near future.



(a) Wave Dragon layout. Extracted from [15].



(b) Wave Dragon prototype in operation. Extracted from [11].

Figure 2.24: Wave Dragon.

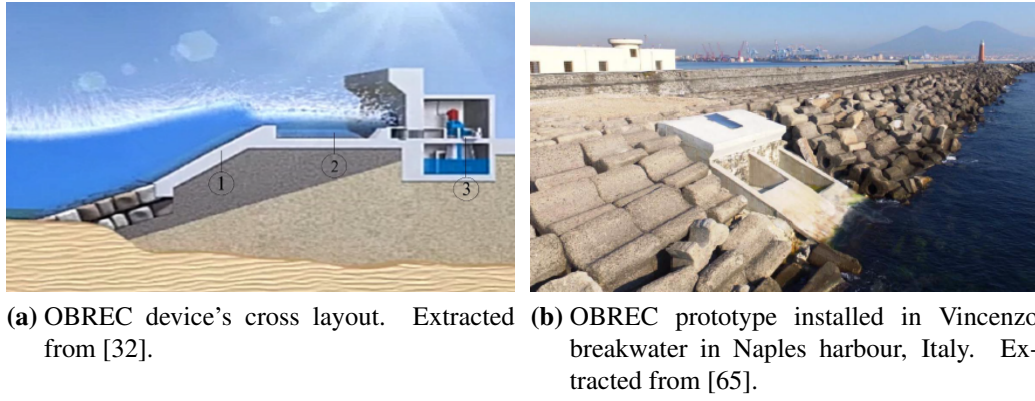


Figure 2.25: OBREC device, cross-section layout and prototype.

2.6.5 Wave Energy Converters Comparison

The performance of a WEC to capture the wave energy can be evaluated with hydraulic efficiency (η_{hyd}), which is the ratio of the output power generated by the device to the wave power available in the location: equation 2.37. Figure 2.26 shows the estimated η_{hyd} for different WECs, [66, 60, 65, 62, 33, 16]. As most of the devices have not passed to full-scale studies, the η_{hyd} presented in figure 2.26 are based on laboratory and numerical simulations, except for one of Mutriku plants, which is based on the actual performance of the wave farm [62]. Wavebob (point absorber) and Oyster have an estimated η_{hyd} of 40%. Mutriku, Wavedragon, SSG and Aquaboy (point absorber) have η_{hyd} in the range of 20% to 26%. Pelamis and OBREC η_{hyd} are estimated to be in the range of 15%. There is a significant variation in the η_{hyd} within WECs; even devices with the same operating principle can have significantly different values of η_{hyd} . For example, Aquaboy and Wavebob, which are both point absorbers, but the latter has double the efficiency of the former.

$$\eta_{hyd} = \frac{P_{out}}{P_{wave}} \quad (2.37)$$

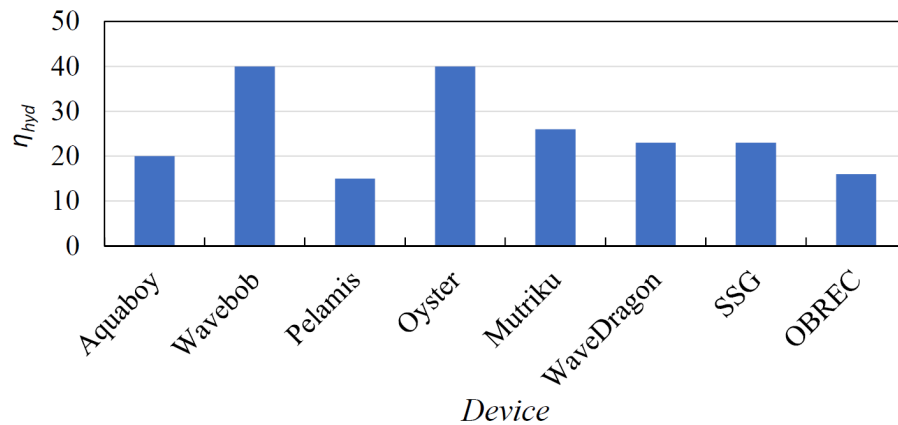


Figure 2.26: Hydraulic efficiency (η_{hyd}) for various WECs.

The η_{hyd} is not the only criterion for deciding which WEC is the best option for a project. Aspects such as the reliability of the device, cost of installation, operation and maintenance and environmental impact are among the key elements to consider. In [16] an analytic hierarchy process (AHP) is applied to evaluate the overall performance of a WEC. Five perspectives are considered in the analysis: energy capture (η_{hyd}), technology cost, device reliability, environmental friendliness, and adaptability. A factor is given for each criterion, and a performance factor is calculated for each technology, figure 2.27. A higher factor means a more attractive WEC. It is important to note that, to evaluate the performance of the devices, results from large-scale projects carried out in the sea are prioritised; however, given the lack of sea trial prototypes of some devices, theoretical and experimental results are used to close the gap. This consideration affects the results of the study, as it is common for theoretical and experimental models to exhibit higher performance levels than full-scale prototypes tested in real sea conditions. It is observed that the Oyster device and Point absorber are the technologies that perform better. OWCs and OWECs have similar factors, albeit slightly higher for the OWCs. The Pelamis device, attenuator, has the lowest factor. The low performance of this WEC is explained by its limited efficiency, 15% reported from a full-scale prototype and used in [16], which negatively impacts the economic and energy capture factor. In addition, its complex mechanical design and large scale, 150m, reduce its reliability and environmental factors, respectively. With respect to OWECs, the factor calcu-

lated does not consider integrating the device into a breakwater. This integration would considerably increase the factors related to the technology cost and environmental friendliness, increasing the comprehensive performance factor of an OWEC, making this technology more competitive.

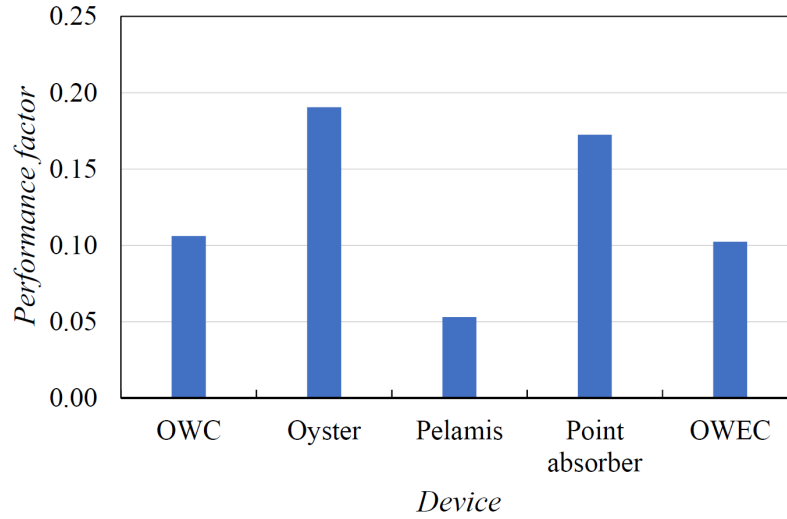


Figure 2.27: Performance factor for various WECs technologies, [16].

2.7 Overtopping Wave Energy Converter Studies

This section presents more detailed information related to the development of OWECs, including their main parameters of design, geometry optimisation studies, conceptual prototypes and performance results.

OWECs are designed to capture the water that overtops the run-up ramp into a reservoir. The captured water is then returned to the sea through a turbine, which transforms the potential energy held in the reservoir into electricity.

The output power generated by an OWEC can be calculated with the equation 2.38. Here, the general form of the equation is presented, which needs to be adapted for each specific application, such as natural sea states or a multi-level OWEC, where a summation of all reservoirs needs to be done.

$$P_{out} = \sum P_{crest} \eta_{res} \eta_{tur} \eta_{gen} \quad (2.38)$$

P_{out} is the total power yield by the system. P_{crest} is the power at the crest of

the ramp before entering the reservoir. η_{res} is the reservoir efficiency, η_{tur} is the turbine's hydraulic efficiency and η_{gen} is the generator efficiency.

The equation 2.39 estimates the mean power at the structure's crest. It is a function of the mean overtopping discharge, q , and the crest freeboard, R_c .

$$P_{crest} = \rho g q R_c \quad (2.39)$$

The ratio between P_{crest} and the available wave power, P_w , yields the hydraulic efficiency at the crest of the device, $\eta_{hyd-crest}$. As stated previously, this parameter is widely used to indicate the device's performance.

$$\eta_{hyd-crest} = \frac{P_{crest}}{P_{wave}} \quad (2.40)$$

If P_{wave} is calculated in deep water, $\eta_{hyd-crest}$ will be affected by all the energy losses during the shoaling process and the interaction with the structure. If the wave power is calculated at the toe of the structure, $\eta_{hyd-crest}$ will consider only the energy losses due to the wave-structure interaction.

The range of values of $\eta_{hyd-crest}$ found in the literature for an OWEC is broad: from 1% to 50% [34, 67, 18, 65]. The hydraulics efficiency is sensitive to the wave condition and the structure's geometry, which are the main aspects that define the breaking condition. The lower efficiency values are explained because not all of the studies optimised the devices; however, they focused on analysing the wave structure interaction. When model geometry has been optimised, $\eta_{hyd-crest}$ fluctuates between 20% and 30%. If a multilevel OWEC is used, the hydraulic efficiency can reach approximately 50%. These values have been calculated from laboratory and numerical simulations.

The efficiency of the reservoir, η_{res} , is related to the elevation loss when the flow falls in the reservoir. Also, this can be related to the fluctuation of the energy head between overtopping events. It is typically estimated to be 75%; however, its value will depend on the specific design of the device.

The turbine efficiency, η_{tur} , is another critical aspect of the operation of an

OWEC. They must work in conditions of low head and significant variation over time. The water level in the reservoir will increase with an overtopping event and decrease between waves. Moments of zero flow can also occur, generating start-up and shutdown losses. The marine environment's aggressive characteristics must be added, too, which demand high endurance to corrosion to any mechanical device. In the literature, the turbine efficiency of low-head turbines is usually set in a range between 80% to 90% [17].

The generator efficiency, η_{gen} , relates to the losses due to the equipment, generator and electronics, and it usually takes values of 95%.

2.7.1 Overtopping Wave Energy Converters Development

The Sea Slope-cone Generator (SSG), figure 2.28, is one of the most studied prototypes for overtopping wave energy conversion and has inspired newer devices, such as the OBREC. Its structure consists of multiple reservoirs with different elevations, aiming to maximise the overtopping collection. One of the earliest studies related to this device can be found in [34], where a series of physical models were conducted to find the geometry with the best hydraulic efficiency and how much could be improved by using a multilevel reservoir. The tests were conducted in a 0.5m wide flume built inside a 3D wave flume at the Hydraulics & Coastal Engineering Laboratory, Aalborg University, Denmark. The models were scaled using a geometrical scale of 1:50, and irregular waves based on the JONSWAP spectrum were used.

The mean power, P_{crest} , and hydraulic efficiency, $\eta_{hyd-crest}$, were used as a parameter to evaluate each model's performance. Their results estimated that a single level OWEC could obtain a hydraulic efficiency of 20% to 25%. This efficiency could be increased to 35% if a convex ramp or guiding walls were used. No tests, including curve ramps and guiding walls simultaneously, were conducted. It was found that implementing a 4-level OWEC could increase the hydraulics efficiency to 49% if the device was optimised to the local wave conditions.

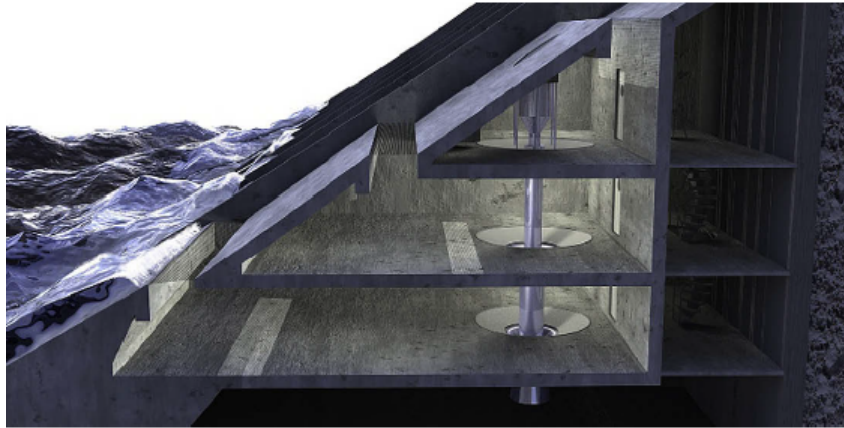


Figure 2.28: Cross section of SSG presented in [17] Extracted from [17].

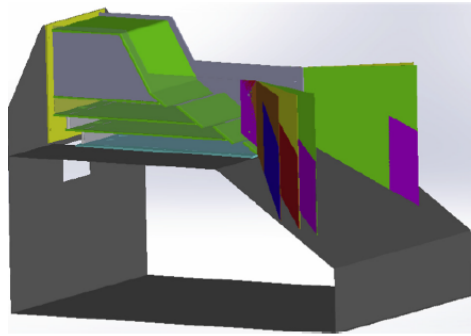
Curve slopes were also studied by [34]. First, the slope angle of a linear slope was studied. It was found that an angle of 30° maximises the overtopping collection, generating a hydraulic efficiency, $\eta_{hyd-crest}$, of 20% to 25%. This finding agrees with previous research [4]. When analysing curved ramp profiles, it was found that a convex shape, based on an elliptical curve, increased the overtopping discharges by an overall 18%. On the other hand, a concave shape reduced the overtopping by more than 11%. Guiding walls were also studied by [34]. It was found that walls with an opening ratio of 20° give the best performance, increasing the overtopping discharge by an overall 15%. It was detected that opening ratios below 15° incremented the reflections, decreasing the overtopping. No conclusive differences between linear and curved walls were found. The author estimated that the hydraulics efficiency of an OWEC could be increased to 35% with the results of the modified slopes and guiding walls.

In [17], the design and performance of a three-level full-scale SSG is presented. 2D physical models yield an overall efficiency of 46%; however, a 30% efficiency in natural operating conditions (effect of directionality and spreading of waves) was estimated and verified from 3D physical models. An SSG pilot plant was proposed to be built on the Norwegian coast, with a power production of 320 MWh/year. However, the project was never carried out.

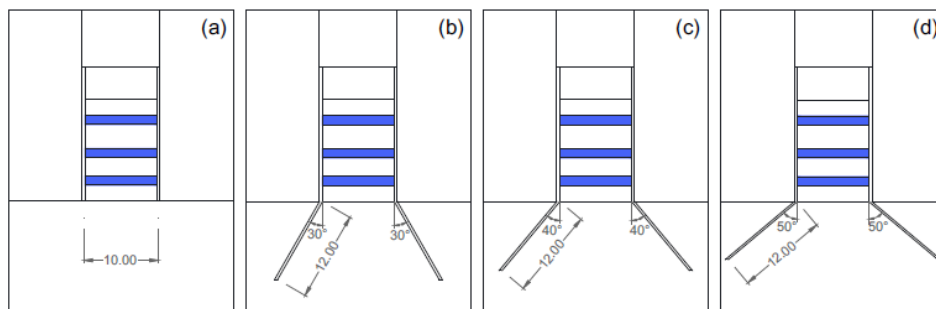
The effects of guiding walls on the performance of an SSG were studied [18]. Physical models with a 1/40 geometrical scale were conducted in a wave flume

constructed inside a 3D wave basin at the laboratory of the Hydraulics, Water Resources and Environment Division (SHRHA) of the Faculty of Engineering of the University of Porto (FEUP), Portugal. The model consists of a 3-level OWEC, as shown in figure 2.29. Four structure configurations were tested: one with no guiding walls and three others with different opening angles. Wave conditions representative of the west Portuguese coast were used. Regular waves were also used, but only the results of irregular waves are presented in the paper. The mean power at the device's entrance was calculated with equation 2.39. The guiding walls improved the mean power in all geometries and wave conditions by 46% up to 1,020%. The results indicate that guiding walls are more effective in moderate wave conditions, which explains the high-performance gain. Waves that couldn't produce overtopping with the traditional geometry could reach the lower reservoir when the converging walls were included. The authors detected a slight advantage for the configuration with an angle of 40° . This study found a lower level of efficiency than the one reported by [34]. For the sea states with smaller significant wave height, η_{hyd} was less than 1%, and varied between 4% and 20% for the higher significant wave height. The authors highlighted that the model was not optimised for the wave conditions, which explains the low hydraulics efficiency obtained in some tests. These results confirm that this device is sensitive to the local sea state and that optimal configuration must be found.

In [19], a two-level SSG was tested with physical models in the laboratories of the Ocean University of China. This project aimed to explore the influence of the upper slope angle and the opening width of the lower reservoir. The experiments were conducted in a 0.6 m wide and 30 m long wave flume. The authors decided to use regular waves because this condition allowed them to explore the run-up and overtopping flows in more detail. The model scale ratio used was 1:16, due to the facility's capability. The tests were limited to 15 incident waves to reduce reflecting effects. The parameter used to evaluate the performance of each test was the mean overtopping discharge in its dimensionless form, Q , equation 2.41.



(a) 3D view of SSG physical model tested in [18]. Extracted from [18].



(b) Layout of guiding walls tested in [18]. Extracted from [18].

Figure 2.29: Schematic of physical model tested in [18]

$$Q = \frac{q}{H_w \sqrt{gH_w}} \quad (2.41)$$

Figure 2.30a shows snapshots of one overtopping event recorded in [19] and reported in [20]. At $T/4$, the wave hunches upstream, and a turbulence zone at the toe of the wave is observed as a result of interacting with the slope's surface and the run-down flow of the previous wave. Significant energy losses can occur in this instance. In the next image, the run-up flow reached the crest. Heavily aerated water is presented at the front of the flow. In $3T/4$, the overtopping spills into the reservoir. The authors indicate that the flow separates in sub-fingers after passing the slope's crest. At T , the run-down flow is almost finished; it is possible to appreciate that this process is less turbulent than the run-up.

In [20] a 2D numerical wave tank (NWT) was used to simulate and expand the research presented by [19]. This numerical code is developed on the CFD

software ANSYS-Fluent, based on the Reynolds-Average Navier-Stokes method, and the water surface was tracked with the Two-phase Volume of Fluid methodology (VOF). Data from the laboratory, when only overtopping volumes reached the lower reservoir, were used to validate the simulation. Figure 2.30b compared the dimensionless mean overtopping discharge, Q , resulting from the simulation and the laboratory for three wavelengths (the wave height was kept constant). It can be seen that shorter waves produce more overtopping than the longer ones. An overall error of 3.8% is calculated. Also, it is demonstrated that the NWT adequately reproduce the water-surface variation during the breaking, run-up and overtopping process. Once validated, the NWT is used to expand the research conducted in [19], analysing different slope angles and their impact on the device's performance. It is found that a slope angle of 30° generates the best performance in capturing overtopping flows, a result that agrees with previous research [34]. Due to the characteristic of the numerical flow used, RANS, no detailed study of the hydrodynamics of the overtopping flow is conducted.

In [21], two concepts for OWEC were presented. In the first alternative, a lower seawall is placed in front of a coastal defence, creating a reservoir for energy conversion figure 2.31. This front sea wall would allow overtopping, maintaining an inflow into the pool. A small head difference would be expected, but this could be compensated with the dimension of the reservoir, which could have the same length as the coastal defence. Two programmes of scale tests were conducted at the University of Southampton in the UK. The performance of this idea was tested with regular waves in two wave flumes; one 7 m long, 0.2 m wide, and 0.2 m high, allowing a model with a scale of 1:50, and the second 12 m long, 0.5 m wide and 0.45 m high; 1:23 models were run here. Overtopping discharge and forces against the rear wall were measured during the test.

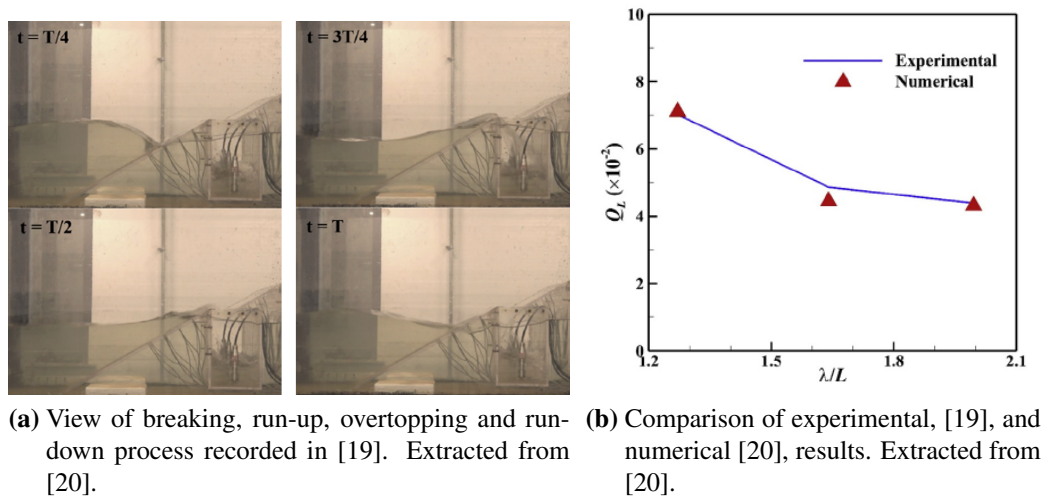


Figure 2.30: View of test run in [19] and numerical results from [20]

The alternative presented in [21] was a single reservoir OWEC that can be installed in a breakwater. This publication marks the start of the development of the OBREC device. Several projects have studied this device [68, 22, 65, 32]. The following bullet points present the main conclusion of the hydraulic device's performance derived from these studies.

- The reflections generated by the structure are in the same range or lower than a traditional rubble mound breakwater. A reduction of 20% was detected when a low-crested freeboard was used.
- Including the device with a crown wall and nose can reduce overtopping at the breakwater's rear side, improving the structure's operation as a coastal defence. This overtopping also proved to be sensitive to the width of the reservoir.
- Standard formulas to calculate overtopping are not applicable to estimate the inflow in the reservoir and at the back of the structure.
- Flat ramps performed better than curved ramps in capturing overtopping flows. This finding disagrees with other studies presented previously ([4] and [34]), which detected that a convex ramp increases the overtopping discharge.

- It has been demonstrated that OBREC can dissipate wave energy similar to a traditional rubble breakwater. Therefore, its implementation doesn't affect the functionality of a coastal defence.
- The device geometry must be optimised to the location's wave and depth conditions.

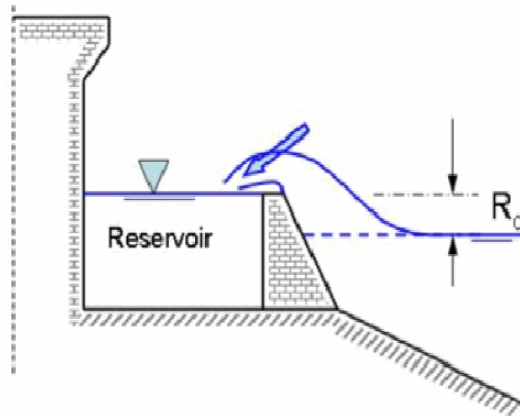


Figure 2.31: Sketch of OWEC presented in [21]. Extracted from [21]

Within the OBREC project, the hydraulic performance of curve and flat ramps was studied in [22], figure 2.32b. The experiments were carried out on a scale of 1/30 (Froud scaling) in a 25m long and 1.5m wide wave flume at the Hydraulic and Coastal Engineering Laboratory of Aalborg University in Denmark. The wave flume was divided lengthwise into two by guiding walls, allowing the two models to be located simultaneously. The structures were tested under irregular wave conditions. They detected two zones of operation of an OWEC, figure 2.32a. In the first one, the overtopping discharge increased when the crest freeboard decreased. The second zone is described as a saturated condition, which occurs when the reservoir is insufficient to accumulate the overtopping flows, generating an overtopping at the rear of the structure and overflows. In this last condition, the reservoir discharge, which generates energy, decreased when the crest freeboard decreased. An optimal design aimed to operate in the first zone, optimising the use of the overtopping discharge and avoiding overflows. Comparing the performance of the curve and flat ramps, it was found that the convex geometry collected approximately 22% less

overtopping than the flat ramp, a result that differs from that found by [34] where a convex ramp performed the best. The reflection coefficient generated by both structures was also investigated. A consistency difference was found only for low values of the crest freeboard, where the flat geometry generated higher levels of reflections.

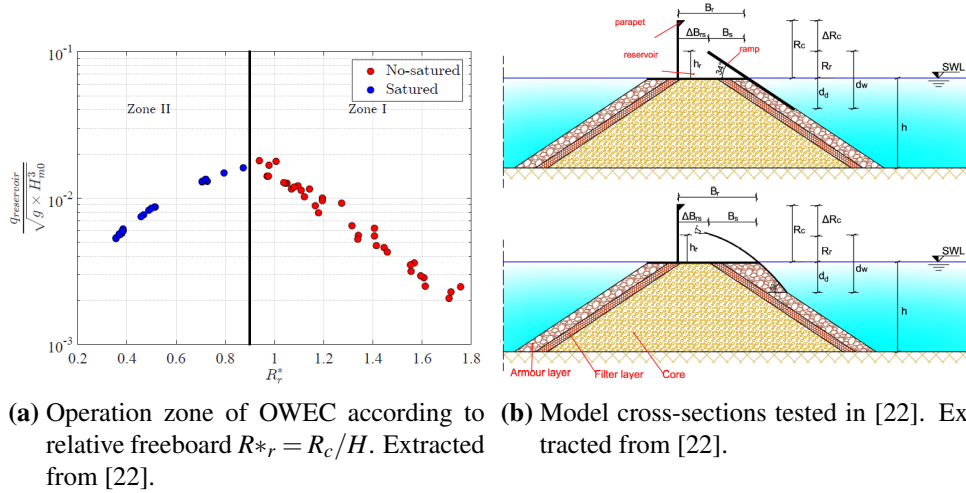


Figure 2.32: Results and models from [22].

CFD has been an important tool in developing the OBREC project. In [23, 69] a numerical code that solves the RANS equations was used to expand and complement the results from physical models. These studies aimed to optimise the device's geometry to improve the mean overtopping discharge and analyse pressures against the structure. The simulations reproduced the wave conditions and reflections measured in both laboratories well. In [69], the forces against the structure were studied, and it was found that the simulation underestimated them, between 10% and 20%; errors are considered acceptable by the authors. Differences between the physical and the numerical models were expected since the numerical method used was insufficient to simulate complex hydrodynamics processes during the wave structure interaction, such as air entrainment, run-up over the slope and energy dissipation due to turbulence. These differences indicate that the numerical simulation did not achieve a comprehensive representation of the hydrodynamics involved in the wave-structure interaction.

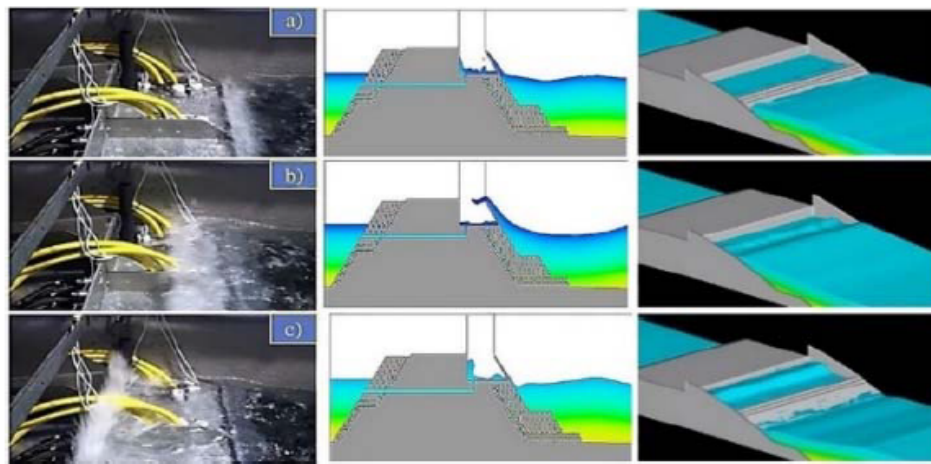


Figure 2.33: Comparison of waves' overtopping between laboratory and numerical simulations in [23]. Extracted from [23]

The performance of curve ramps was extended in [24]. A series of 1:15 scale experiments at the National Hydraulic Research Institute Malaysia (NAHRIN) were conducted. Irregular wave conditions representing different wave weather on the Malaysian coast were used to test the models. Figure 2.34 shows the geometries and overtopping discharge over time of one wave condition. It can be seen that the ramps with cubic (-ve) and convex shapes were the ones that performed the best, generating an increment in the mean discharge of around 30%. The quantic, cubic and concave shapes produced less overtopping than the linear ramp. These results agree with the one presented in [34], where the overtopping was also maximised with a convex shape, however, they disagree with the findings of [22], where a convex shape reduced the overtopping discharge. This difference could be related to the wave conditions and geometry differences. For example, in [22], the models were steeper than those tested in [34, 24]. The performance differences of the geometries in [24] were explained to be related to flow resistance, generation of reflection, and the platform size available to develop run-up flows. In [24], geometries with a crest angle towards the reservoir presented better behaviour in capturing the overtopping flows.

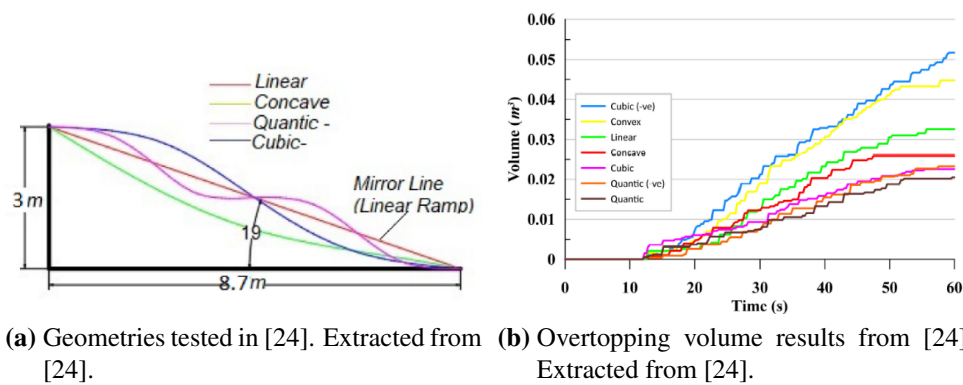


Figure 2.34: Cross section geometries of run-up ramp tested in [24] and overtopping results for each geometry.

2.7.2 Advantages of Overtopping Wave Energy Converters

The structural simplicity of OWECs compared to other WECs that comprise complex mechanics, such as Pelamis and Oyster, makes these types of devices less susceptible to structural failures, and they demand less maintenance. Besides the turbine, it does not have more movable parts. It is well known that the marine environment is one of the most hostile for structures. The corrosive environment, sediment transportation, wildlife, and extreme loads can easily affect the function of any mobile mechanism, affecting its performance and damaging it and increasing the necessity for regular maintenance.

One of the more attractive advantages of OWECs is that they can be integrated into coastal structures, such as breakwaters and vertical walls. They can be considered from the design of a new coastal defence or installed in existing ones. This option brings several benefits:

- The coastal defence and the energy converter share the cost. One of the main drawbacks of WECs is their high cost. OWEC can use the same foundation of the breakwater and part of the superstructure, representing a considerable reduction in the total budget for the OWEC.
- The device is easily accessible, decreasing the cost of construction, maintenance and operation compared to offshore and nearshore devices.

- More benefits generated by the coastal defence. A modified breakwater offers protection from the sea and acts as an energy generator. More efficient resource use can be achieved through a multi-functional coastal defence. This final aspect aligns with friendlier environmental coastal engineering, which is crucial to achieving sustainable development of coastal areas.
- Reduction of environmental impacts. Sharing the foundations with a coastal defence eliminates the need to generate a special structure to receive the WEC. This is especially attractive when considering the integration of an OWEC into an existing breakwater. The coastal defence structure is already placed on the shore; therefore, there is no need to create a new intervention in the natural morphology.

Research has detected that including an OWEC can improve the operation of a breakwater. A comparison between a traditional rubble mound breakwater and one with an OWEC integrated was conducted in [68]. The innovative breakwater showed a similar average reflection coefficient to a traditional rubble breakwater. However, the reflection could be reduced by approximately 20% when a low free-board was used for the reservoir. The overtopping at the rear of the coastal defence can be significantly reduced if a crown wall with a “nose” is used to redirect the uprushing wave back to the reservoir. A reduction of overtopping volume of up to 89% was measured during an extreme wave condition.

Implementing an OWEC at the seaside of a vertical seawall was analysed in [70]. It was estimated that including such a device could reduce the reflection by up to 40% compared to a traditional vertical breakwater under extreme wave conditions. This finding agrees with [68], where likewise, a more significant reflection reduction in extreme wave conditions than in mild sea conditions was detected. In extreme weather, more waves are expected to overtop the reservoir compared to milder conditions, explaining why the reflection levels decreased with the growth of the waves. The effects on the structural stability due to adding an OWEC in a caisson breakwater were analysed, too. It was found that the overall stability can be improved by integrating an OWEC at the front of the vertical wall. The device’s ge-

ometry helps to uncouple the maximum vertical and horizontal forces and increase the downward force component, contributing to the stability of the structure.

2.8 Conclusions

The design of OWECs has been of great interest in recent years, with more alternatives proposed and several physical models being conducted. Nevertheless, it is still quite behind in its development compared to other green energy sources and WECs, leaving significant gaps to be explored. Their operation is based on their capacity to capture the overtopping flows as high as possible. However, the amount of water captured and the reservoir's height are inversely proportional. Therefore, the most efficient geometry needs to be found.

The operation of an OWEC depends on the ramp geometry, the reservoir design, and the efficiency of the turbine and electronics. The ramp is a key element in an OWEC because it is where the greatest energy losses occur, which directly affects the amount of overtopping captured by the device. Its performance can be assessed by the hydraulic efficiency at the crest of the device's ramp, $\eta_{hyd-crest}$, which evaluates the power capture over the total wave power available. It's been estimated from laboratories that $\eta_{hyd-crest}$ of an optimised device fluctuates between 20% and 30%. However, experiences with other WECs show that experimental efficiency can overestimate the real performance of full-scale devices in real sea conditions. As OWECs are just starting to be tested at full scale, there is no complete information about their actual performance in natural sea conditions.

The ability to optimise the overtopping discharges into the reservoir is a central performance aspect of any OWEC. In coastal engineering, the methodologies to estimate overtopping are empirical formulations based on detailed observations of the run-up and overtopping behaviour, calibrated with results from scaled physical models and actual measurements in real coastal defences. Due to the nature of these methodologies, their application is limited to specific types of structures and geometries. They deliver mean and statistical results, which are helpful for the design process. However, they don't provide information related to the instantaneous

parameters of the flow, such as velocities, turbulence, and energy dissipation. When non-conventional geometries are considered, these formulations lose their applicability.

The overtopping discharge is related to the breaking condition. Two behaviours can be identified in a plot q versus ξ . For breaking waves, approximately $\xi < 2.5$ (spilling and plunging waves), the mean discharge grows with ξ . For non-breaking waves, approximately $\xi > 2.5$ (collapsing and surging), the relation between mean discharge and ξ is reduced or lost. Similar behaviour is found in the wave run-up, R_u . This indicates a strong relationship between the energy losses during the breaking process and the overtopping discharge and run-up.

The design of the run-up ramp is a crucial factor in increasing the total efficiency of an OWEC, considering that this is where the most significant energy losses occur. Over the ramp, the energy transmitted by the waves is transformed into kinetic energy in the run-up flow. As the flow climbs up the slope, that kinetic energy is gradually transformed into potential energy. It is demonstrated that the ramp's geometry can affect the overtopping discharge. A slope of 30° to 35° has been found to maximise the overtopping. Also, a curved ramp can modify the amount of overtopping. Discrepancies in results are found in the literature, but there are more indications that a convex shape could increase the mean discharge. Converging walls with an appropriate opening angle can also increase the energy captured, especially in low-wave conditions.

OWECs are sensitive to fluctuations of the sea level, which directly modify the crest freeboard, R_c . Multi-level OWEC treats this condition by including reservoirs at different levels. Studies have detected that a significant improvement in the energy harvested by the device can be achieved with this solution. However, the structure increases its complexity and cost. In addition, enclosed reservoirs are susceptible to being damaged by internal pressures generated by air displacement by the incoming wave. From experience in the Mutriku OWC plant, internal pressure can severely damage the structure.

Run-up and overtopping are among the most studied processes in coastal en-

gineering, yet their hydrodynamics are highly uncertain. Most studies in this area are related to the design of coastal defences, focusing on evaluating parameters that better describe the mean and extreme behaviour. These parameters are used to dimension the crest freeboard and slopes within safety factors and operational levels. The study of the instantaneous parameters has not witnessed the same development.

The variation of overtopping volume between waves varies significantly. This behaviour can be observed even in regular waves, where a uniform overtopping would be expected. This irregularity is related to the non-linearity of processes that occur during the wave structure interaction, such as:

- Wave breaking
- Water splash and jets
- Turbulence
- Air entrainment
- Effect of the run-down acting against the incoming wave.

All of these processes affect the overtopping discharge. They have a short life but are responsible for energy losses before reaching the device reservoir.

Research has confirmed that an OWEC's geometry needs to be optimised to achieve and improve its performance. In the literature, geometries have been found to improve the performance of an OWEC. However, no detailed analyses of the hydrodynamics of the run-up and overtopping flow on slope impermeable coastal structures have been found. There are clear indications that the run-up ramp is one of the key aspects to be optimised, considering that this is where significant energy losses occur.

OWECs operate in the swash zone where rapid energy losses occur in the flow. These energy losses need to be reduced to improve the device's efficiency.

Chapter 3

Numerical framework

3.1 Introduction.

This research aims to study the hydrodynamics when waves interact with a sloped structure, like the run-up ramp of an OWEC. This wave-structure interaction includes processes such as wave breaking, run-up, and run-down flows. The flow parameters to analyse include instantaneous velocity field, turbulence structures, energy dissipation (kinetic, potential, and total), run-up, and overtopping discharges. A numerical tool capable of simulating the flow's instantaneous parameters and structures (unsteady eddies) is needed to represent the processes of interest.

In this chapter, the characteristics of the three main classifications of computational fluid dynamics (CFD) methodologies are presented, introducing the concepts of Direct Numerical Simulations (DNS), Reynolds-average Navier Stokes (RANS) and Large Eddy Simulations (LES). The second part contains a detailed presentation of the numerical framework of the LES-base code Hydro3D-NWT used in the present research. Finally, the main conclusions of the content of this chapter are given.

3.2 Large Eddy Simulations

In CFD, the flow is described by numerically solving the continuity and 3d-Navier Stokes equations, equations 3.1 and 3.2. The methodologies for solving this problem can be divided into three main categories: DNS, RANS and LES. In DNS, the flow equations are solved without any model being introduced. In this method,

all eddies are solved in the mesh; therefore, the grid size must be smaller than the smallest eddy present in the flow; this makes DNS a highly computationally demanding method. On the other hand, in RANS simulations, the flow quantities are separated into mean and turbulent fluctuations. The mean values are solved in the mesh, and a RANS turbulent model models the fluctuating quantities representing the turbulence structure. Before solving the mean quantities, the turbulent model has to be described to introduce the effect of turbulence on the mean quantities. Due to the fact that in RANS, only the mean values are solved, and the turbulence is just modelled, the computational cost of this type of simulation is much smaller than for DNS. Large Eddy simulations emerge between DNS and RANS. In an LES, the larger-scale motions are completely resolved in the mesh, and the structures smaller than the grid size are modelled using a Sub-Grid-Scale model (SGS). This technique allows for a complete description of the larger eddies responsible for most of the energy dissipation, with a smaller computational demand than DNS.

$$\frac{\partial u_i}{\partial x_i} = 0 \quad (3.1)$$

$$\frac{\partial u_i}{\partial t} + \frac{\partial u_i u_j}{\partial x_j} = -\frac{1}{\rho} \frac{\partial p}{\partial x_i} + \frac{\partial}{\partial x_j} \left(\nu \frac{\partial u_i}{\partial x_j} \right) - g_i \quad (3.2)$$

where u_i is the velocity in x_i direction, p is the pressure field whereas ρ and ν are the fluid density and kinematic viscosity, respectively and g_i is the gravitational acceleration.

Almost all natural flows contain different scales of turbulence structures, manifesting as vorticities in all directions and eddies of different sizes interacting with each other. These structures influence all aspects of the fluid motion, such as energy dissipation, momentum, mass and heat transfer, and sediment transport. Turbulence is a highly complex phenomenon with unsteady and irregular and 3D structures. Figure 3.1 presents the life cycle of an eddy. It starts with a large eddy, which takes energy from the mean flow. Then, this large eddy breaks into smaller eddies, transferring energy from larger structures to smaller ones. This phenomenon occurs

until the viscous forces participate, dissipating the energy in the smallest eddies. This process is known as the energy flux in turbulent flows and is the basis of the Energy Cascade concept shown in figure 3.1. This figure presents the turbulent spectrum, which indicates the variation of the kinetic energy density, KE , with the turbulence's wave number, k . The wave number is proportional to the frequency and inverse of the eddy size. It can be seen that eddies with small k contain most of the kinetic energy. As k increases, the energy decreases until the viscous forces fully dissipate it. Three sections can be identified in the turbulent spectrum. First is the production range, where the eddies extract energy from the mean flow. According to Kolmogorov's law, the second section is the Inertial Range, where the energy decays by a $k^{-3/5}$. In these two first stages, the viscous effects can be neglected. The last stage is the dissipate range, where the viscous effects dominate, and the KE is dissipated into heat. Integrating $KE(k)$ gives the total turbulent kinetic energy in the location. The mesh solves all the turbulent kinetic energy in a DNS. By contrast, in a RANS simulation, it is modelled. In LES, a $k_{cut-off}$ is defined to separate the eddies that are solved and the ones that are modelled. This cut-off value needs to be located in the inertial range, and as a general rule, it is desired that at least 80% of the total turbulent kinetic energy is resolved in the mesh.

A simulation based on DNS would be able to simulate the instantaneous aspects of the flow. However, their high demand for computer resources narrows their applicability to specific applications that can be sufficiently described with small domains and short simulations. In this research, several waves must be simulated to obtain statistically relevant information from the flow. The domain dimension must be long enough to control wave reflections from the inlet boundary, which can affect the results. In addition, the domain width will have to permit the reproduction of 3D effects and limit the reflection from the side boundaries against the structure. These requirements make a DNS-based simulation unfeasible due to the high computer resources demanded to run the simulations.

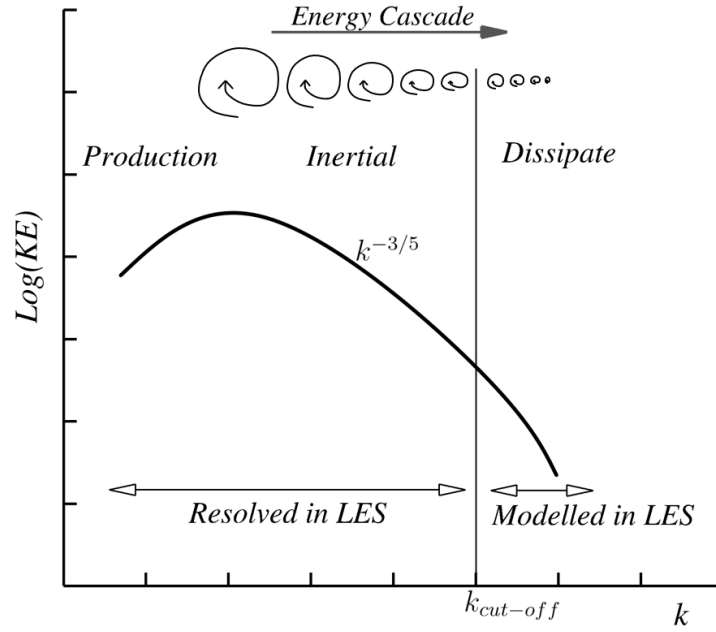


Figure 3.1: Turbulent Spectrum and energy cascade.

Previous studies have used RANS-based numerical codes to evaluate the wave overtopping discharge and run-up without analysing the hydrodynamics of the flows in detail [23, 69, 20]. This research has studied the effects of various geometries on the mean parameters of the flow, such as mean overtopping discharge and forces on the structure. In [69], the authors conclude that more advanced software is needed to recreate the complex wave-structure interaction. RANS simulations' reliability is limited when complicated flow phenomena are included in the fluid, such as turbulence and complex wave-structure interactions, such as in the case of breaking waves.

LES offer a balance in terms of the capability and demand of computer resources. In an LES, the eddies that account for most energy dissipation are solved in the mesh, and the SGS model takes account of the smaller turbulence structures. This methodology can reproduce unsteady fluid problems where the turbulence structures must be modelled to obtain an accurate simulation. This is the case with breaking waves and run-up and overtopping flows, where large-scale turbulence structures influence all aspects of the flow, such as energy dissipation and momentum transfer. The ability of LES to simulate complex 3D features also makes

this tool an appropriate methodology for the present research. It is planned to simulate cases that will include 3D turbulence structures in the flows, and their correct simulation will be critical to assessing the performance of each scenario. In summary, LES capabilities allow for studying the kinematics and dynamics of interest in this research.

LES are extending their application in engineering problems, and the hardware limitations are decreasing with increased computer power. Studies have used LES applicability to recreate wave structure interaction and breaking waves [71, 72, 73, 74, 75]. However, the information about wave run-up and overtopping on steep slope structures is scarce, with an Iribarren number of over 2.5. Most studies focus on gentle slopes, which are more representative of natural bathymetries than coastal defences.

In the present project, the code Hydro3d-NWT (Numerical Wave Tank) is used to study the hydrodynamics of breaking waves, wave run-up and overtopping flows. Hydro3d-NWT is a LES-based Numerical Wave Tank developed over several years in-house. Several studies have confirmed its suitability for fluid mechanics applications, including wave-structure interaction [76, 77, 78, 79, 35, 80]. However, few studies [80] have included breaking waves and wave run-up and overtopping flows, which are the focus in the present research. Here, the performance of Hydro3d-NWT to simulate these hydrodynamics processes is assessed and validated. In the following section, the main aspects of the structure of the code are presented.

3.3 Hydro3D-NWT.

This study employs the LES-based open-sourced code Hydro3D-NWT to simulate the interaction of periodic waves with various structures. Several studies have confirmed the suitability of this code for fluid mechanic applications [76, 81, 77, 82], including complex wave-structure interactions [79, 35]. In the present section, the numerical background of the code is described.

Hydro3D-NWT utilises the LES method to solve the unsteady, incompressible, viscous spatially-filtered Navier-Stokes equations:

$$\frac{\partial \bar{u}_i}{\partial x_i} = 0 \quad (3.3)$$

$$\frac{\partial \bar{u}_i}{\partial t} + \frac{\partial \bar{u}_i \bar{u}_j}{\partial x_j} = -\frac{1}{\rho} \frac{\partial \bar{p}}{\partial x_i} + \frac{\partial}{\partial x_j} \left(\nu \frac{\partial \bar{u}_i}{\partial x_j} \right) - \frac{\partial \tau_{ij}^{SGS}}{\partial x_j} + f_i + g_i + F_i^{sf} \quad (3.4)$$

where u_i is the instantaneous filter velocity in x_i direction, \bar{p} is the pressure field, whereas ρ and ν are the fluid density and kinematic viscosity, respectively. τ_{ij}^{SGS} is the sub-grid scale stress tensor, treated with the method of LES and eddy viscosity model and f_i is the forcing term introduced by the Immersed Boundary method (IBM) to enforce a no-slip boundary condition on solid structures. Finally, g_i is the gravitational acceleration and F_i^{sf} represents the water surface tension.

The filtering process required to separate the solved eddies and unresolved, figure 3.1, is directly related to the grid size of the mesh selected. Only the motions larger than the grid size are resolved, and the smaller ones are computed by the SGS model.

3.3.1 Domain Discretisation.

A staggered uniform Cartesian grid is employed to discretise the domain. Here, the scalar quantities, ρ , ν , p and ϕ (defined in section 3.3.4), are computed in the centre of the cell, and the vector, velocities and their derivatives, in the centre of the cell's face, as shown in figure 3.2. In this figure, i and k represent the cell indices in x and z directions, respectively.

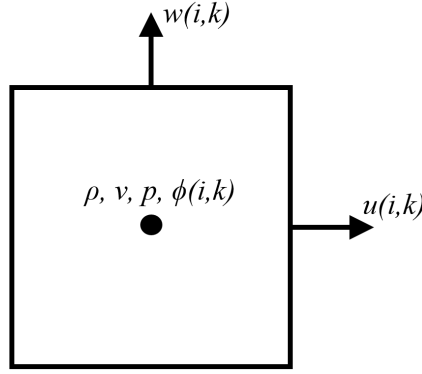


Figure 3.2: Uniform Staggered Cartesian grid and locations of computation of quantities.

The spatial derivatives of the convective component of the momentum equation, 3.4, are calculated by using a 4th order central differencing (4CDS), whereas for the diffusive terms, a 2th order central differencing (2CDS) is used.

$$\text{Convective terms : } \frac{\partial \bar{u}_i \bar{u}_j}{\partial x_j} \quad (3.5)$$

$$\text{Diffusive terms : } \frac{\partial}{\partial x_j} \left(\nu \frac{\partial}{\partial \bar{u}_i x_j} \right) \quad (3.6)$$

3.3.2 Time Fractional-step.

Time advance is archived using the fractional-step method proposed in [83], via an explicit 3rd-order Runge-Kutta (RK) scheme presented in equation 3.7.

$$\frac{\tilde{u}_i - u_i^{l-1}}{\Delta t} = \alpha_l \frac{\partial}{\partial x_j} \left(\nu \frac{\partial u_i^{l-1}}{\partial x_j} \right) - \alpha_l \frac{1}{\rho} \frac{\partial p^{l-1}}{\partial x_i} - \alpha_l \left(\frac{\partial u_i u_j}{\partial x_j} \right)^{l-1} - \beta_l \left(\frac{\partial u_i u_j}{\partial x_j} \right)^{l-2} + \alpha_l g_i \quad (3.7)$$

Where Δt is the current time-step and α_l and β_l are the Runge-Kutta coefficients at each sub-step. Three sub-steps are conducted in each time-step ($l = 1, l = 2$ and $l = 3$). In the first sub-step, $\alpha_1 = \beta_1 = 1/3$, a non-divergence free velocity \tilde{u} is calculated using the velocity and pressure field solved at the previous time-step. A new non-divergence free velocity \tilde{u} is calculated considering $\alpha_2 = \beta_2 = 1/2$ in the intermediate sub-step. In the last sub-step the velocities are updated again considering $\alpha_3 = \beta_3 = 1$.

In the case of including the external force, f_i , due to the IBM, an additional step is conducted to enforce a non-slip condition at the location of the Lagrangian marker, equation 3.8.

$$\tilde{u}_i^* = \tilde{u}_i + f_i \Delta t \quad (3.8)$$

\tilde{u} denotes velocities calculated at intermediate steps of the RK method, and the tilde * indicates velocity corrected after enforcing the IBM condition.

The Poisson equation, 3.9, is applied to determine a scalar function \tilde{p} . This is solved using an iterative multi-grid algorithm, which divides the sub-domain into smaller sub-domains. In the case of the simulations conducted in this research, a three-times division is applied. Equation 3.9 is iterated until it satisfies the continuity condition, equation 3.1. A tolerance residual, ϵ , of 10^{-7} is adopted in this case.

$$\frac{\partial}{\partial x_i} \left(\frac{1}{\rho} \frac{\partial \tilde{p}}{\partial x_i} \right) = \frac{1}{\alpha_l \Delta t} \frac{\partial \tilde{u}_i^*}{\partial x_i} \quad (3.9)$$

After the new \tilde{u}_i^* is determined, the velocity and pressure of the current time-step are updated by equations 3.10 and 3.11.

$$u_i^t = \tilde{u}_i^* - \alpha_l \Delta t \frac{1}{\rho} \frac{\partial \tilde{p}}{\partial x_i} \quad (3.10)$$

$$p^t = p^{t-1} + \tilde{p} - \frac{\nu \alpha_l \Delta t}{2} \frac{\partial}{\partial x_i} \left(\frac{\partial \tilde{p}}{\partial x_i} \right) \quad (3.11)$$

Two options are available in Hydro3D-NWT to determine the time-step of each iteration, Δt . The first one is a fix-time step, which is directly established by the user in the code's control panel. The second option is a variable time step. In this case, the code calculates the time step at the beginning of each iteration by applying the Courant Friedrichs Lewy (CFL) criterion and the viscous limit (VSL):

$$\Delta t_{CFL} = \min \left(\frac{dx}{u_{max}}, \frac{dy}{v_{max}}, \frac{dz}{w_{max}} \right) \quad (3.12)$$

$$\Delta t_{VSL} = \left(\left| \frac{u_c}{dx} \right| + \left| \frac{v_c}{dy} \right| + \left| \frac{w_c}{dz} \right| + 2\nu \left(\frac{1}{dx^2} + \frac{1}{dy^2} + \frac{1}{dz^2} \right) \right)^{-1} \quad (3.13)$$

then Δt is calculated as $\min(\Delta t_{CFL}, \Delta t_{VSL}) \cdot SF$, with SF a safety factor usually set between 0.1 and 0.2. In the present research, a value of 0,1 is used, as it found during the work that larger values tend to introduce a lag in the waves propagation.

3.3.3 Sub-Grid-Scale Model.

In LES, the large flow structures are directly resolved in the mesh, whereas eddies smaller than the grid cell can't be simulated, and therefore, their effect on the flow needs to be modelled. The SGS role is to remove turbulent kinetic energy from the system.

In Hydro3D-NWT, the Wall-Adapting Local Eddy Viscosity (WALE) SGS model is employed, [84]. This method improves the efficiency of the widely used Smagorinsky model within the viscous sublayer, laminar-turbulent transitions and highly three-dimensional flows and additionally does not require a wall-damping function to reproduce turbulent behaviour near solid surfaces.

A sub-grid scale stress tensor, τ_{ij}^{SGS} , is introduced in the momentum equation to account for the unresolved velocity fluctuations according to the following equation:

$$\tau_{ij}^{SGS} = \tau_{ij} + \frac{1}{3} \tau_{kk}^{SGS} \delta_{ij} \quad (3.14)$$

where δ_{ij} is the Kronecker delta and τ_{kk}^{SGS} is twice the kinetic energy k^{SGS} of the sub-grid scale fluctuation. The term τ_{ij} is defined as follows:

$$\tau_{ij} = -2\nu_t \bar{S}_{ij} \quad (3.15)$$

here ν_t is a virtual viscosity added in the equations to account for the effects of the eddies not simulated and \bar{S}_{ij} is the deformation tensor of the resolved field,

3.16.

$$\bar{S}_{ij} = \frac{1}{2} \left(\frac{\partial \bar{u}_i}{\partial x_j} + \frac{\partial \bar{u}_j}{\partial x_i} \right) \quad (3.16)$$

In WALE, the resolved velocity tensor information is used to calculate the eddy viscosity:

$$\nu_t = (C_w \Delta)^2 \frac{(S_{ij}^d S_{ij}^d)^{3/2}}{(\bar{S}_{ij} \bar{S}_{ij})^{5/2} + (S_{ij}^d S_{ij}^d)^{5/4}} \quad (3.17)$$

C_w is an empirical constant set to 0.46, and Δ is the filter width calculate as $(dxdydz)^{1/3}$ and S_{ij}^d the traceless symmetric part of the velocity tensor.

$$S_{ij}^d = \frac{1}{2}(\bar{g}_{ij}^2 + \bar{g}_{ji}^2) - \frac{1}{3}\delta_{ij}\bar{g}_{kk}^2 \quad (3.18)$$

with

$$\bar{g}_{ij} = \frac{\partial u_i}{\partial x_j} \quad (3.19)$$

3.3.4 Free-surface Capturing.

The water surface is captured with the level-set method (LSM) presented in [85]. In this method, the domain is occupied by a continuous fluid with a transition zone between gas and liquid, which is evaluated in each iteration. Here, a signed distance function ϕ from the cell to the water surface, free-surface, is defined as follows:

$$\phi(x, t) \begin{cases} < 0, & \text{if } x \in \Omega_{gas} \\ = 0, & \text{if } x \in \Gamma \\ > 0, & \text{if } x \in \Omega_{liquid} \end{cases} \quad (3.20)$$

ϕ takes positive values in the liquid, negative in the gas and zero in the water surface. It is calculated from the pure advection equation:

$$\frac{\partial \phi}{\partial t} + u_i \frac{\partial \phi}{\partial x_i} = 0 \quad (3.21)$$

The spatial derivation of ϕ is calculated using a 5th order weighted essential non-oscillatory (WENO) scheme [86]. The time advancement is achieved by a 3th order Runge-Kutta scheme.

$$\phi^t = \phi^{t-1} - \Delta t \left(u \frac{\partial \phi^{t-1}}{\partial x} + v \frac{\partial \phi^{t-1}}{\partial y} + w \frac{\partial \phi^{t-1}}{\partial z} \right) \quad (3.22)$$

where ϕ^t is the current step calculation and ϕ^{t-1} are the values of the intermediate sub-steps in the RK scheme.

$$s(\phi_0) = \frac{\phi_0}{\sqrt{\phi_0^2 + (|\nabla \phi| \varepsilon_r)^2}} \quad (3.23)$$

To smooth the transition between air and water in the interface, a Heaviside function $H(\phi)$ is implemented in a zone of width 2ε .

$$H(\phi) \begin{cases} = 0, & \text{if } \phi < -\varepsilon \\ = \frac{1}{2} \left(1 + \frac{\phi}{\varepsilon} + \frac{1}{\pi} \sin \frac{\pi \phi}{\varepsilon} \right), & \text{if } |\phi| \leq \varepsilon \\ = 1, & \text{if } \phi > \varepsilon \end{cases} \quad (3.24)$$

The present study uses a $\varepsilon = 2\max(dx, dy, dz)$. Then the density and viscosity of the fluid are calculated as follows inside the transition zone:

$$\begin{aligned} \rho(\phi) &= \rho_g + (\rho_l - \rho_g)H(\phi) \\ \mu(\phi) &= \mu_g + (\mu_l - \mu_g)H(\phi) \end{aligned} \quad (3.25)$$

A re-initialisation technique proposed in [87] is employed in Hydro3D-NWT to ensure that $|\nabla \phi| = 1$ inside the transition zone as:

$$\frac{\partial \phi}{\partial t_a} + s(\phi_0)(|\nabla \phi| - 1) = 0 \quad (3.26)$$

where t_a is an artificial time defined as the grid size times, a factor less than one, ε_r represents one grid size, $\phi_0(x, 0) = \phi(x, t)$ and $s(\phi_0)$ is the smoothed signed function defined as:

The LSM employs the scalar function, ϕ , to capture the water surface, enabling

it to generate smooth interfaces for complex shapes that undergo large deformations and exhibit high curvatures [80] [88]. One of the key advantages of LSM is its ability to naturally handle topological changes such as splitting and merging, without the need for additional algorithms. Given that this research involves phenomena like wave breaking, run-up, run-down, and overtopping flows, a method capable of accurately capturing the detailed behaviour of the water surface is essential. Furthermore, LSM has demonstrated numerical stability in simulations involving complex hydrodynamic conditions.

The inherent tendency of the Level Set Method (LSM) to smooth the water surface—along with its representation of the interface between grid points—can lead to issues with mass conservation, particularly when tracking small fluid volumes [89] [90] [91]. In the context of the present research, this limitation may result in the dissipation or loss of thin water layers or small droplets generated during wave breaking, potentially compromising the physical accuracy of the results.

An alternative method commonly used for tracking the water surface is the Volume of Fluid (VOF) technique, which is inherently mass-conserving [92] [93]. VOF maintains mass balance by accurately computing the flux of fluid through cell faces. As a result, it significantly reduces mass conservation issues by preserving a consistent volume of fluid within each computational cell. However, VOF often struggles to produce smooth and continuous interfaces, especially in scenarios involving complex or highly deformed free surfaces [94].

To address the mass conservation issue associated with LSM in this research, an appropriate grid resolution has been selected. This ensures the accurate representation of complex water surface geometries while minimizing excessive smoothing. Moreover, given that the simulations conducted here do not involve scenarios such as long free-falls or extensive thin fluid layers, the limitations of LSM regarding mass conservation have a negligible impact on the results.

3.3.5 Immersed Boundary Method

Solid structures are introduced in the domain using the IBM according to [95]. In this method, the geometry of the solid is represented by Lagrangian markers, in which an external force is introduced to enforce a non-slip condition. This method allows it to be implemented in structured meshes, as in Hydro3-NWT.

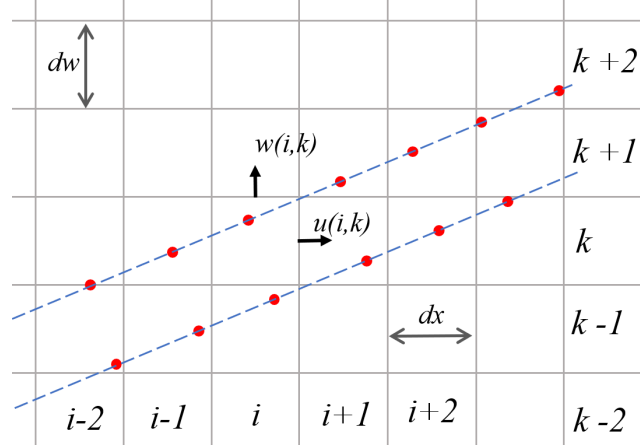


Figure 3.3: Grid and Lagrangian markers. Red dots Lagrangian markers, dashed blue line surface simulated.

First, a non-divergence velocity, U_{iL} , equation 3.27, is calculated in the Lagrangian marker by interpolating \tilde{u}_{ijk} , obtained in the 2^{nd} RK sub-step, equation 3.7, from the nearest Eulerian fluid cells. Note that capital letters indicate properties calculated at the L Lagrangian marker, and N_L is the total number of nodes used.

$$U_{iL} = \sum_{ijk=1}^{ne} \tilde{u}_{ijk} \delta(x_{ijk} - X_{iL}) \Delta x_{ijk} \quad (3.27)$$

Where n_e is the total number of Eulerian cells to be considered in the interpolation process, x_{ijk} and X_{iL} are the coordinated of the Eulerian cell and Lagrangian marker, respectively and Δx_{ijk} is the volume of the Eulerian cell ($dx \times dy \times dz$). A discrete delta function δ is used to conduct the interpolation and defined as:

$$\delta(x_{ijk} - X_{iL}) = \frac{1}{\Delta x_{ijk}} \phi\left(\frac{x_{ijk} - X_L}{dx}\right) \phi\left(\frac{y_{ijk} - Y_L}{dy}\right) \phi\left(\frac{z_{ijk} - Z_L}{dz}\right) \quad (3.28)$$

where ϕ is a Kernel function defined according to [96] and [97].

In the next step, the calculation of the force, F_{i_L} , necessary to impose the non-slip condition in the Lagrangian market, is conducted in equation 3.29.

$$F_{i_L} = \frac{U_i^* - U_{i_L}}{\Delta t} \quad (3.29)$$

The parameter U_i^* is a target velocity, in the case of this research, and because only fixed structures are analysed $U_i^* = 0$.

In the last step F_{i_L} is interpolated back to the fluid cell to evaluate f_i :

$$f_i = \sum_{ijk=1}^{ne} F_{i_L} \delta(x_{ijk} - X_{i_L}) \Delta V_L \quad (3.30)$$

with ΔV_L is the volume of the current Lagrangian market, which is of the order of the grid cell's volume.

In the last sub-step of the RK method, f_i is included to update the final velocities to account for the action of the structure upon fluid: equation 3.8.

3.3.6 Surface Tension

To better simulate the water surface fluctuation, especially in breaking wave conditions, a Continuum Surface Force (CSF), [98], is implemented in Hydro3D-NWT. The surface tension force F_i^{sf} is defined as follows:

$$F_i^{sf} = \sigma k \delta(\phi) n_i \quad (3.31)$$

Where σ is the surface tension coefficient, k is the curvature of the interface, and $\delta(\phi)$ is a function to smooth the surface force in a transition zone over the water surface. These parameters depend on the function ϕ defined in the LSM and according to the next formulation:

$$k = -\nabla n_i, \quad n_i = \frac{\nabla \phi}{|\phi|} \quad (3.32)$$

and

$$\delta(\phi) \begin{cases} = \frac{1}{2}(1 + \cos(\frac{\pi\phi}{\varepsilon})), & \text{if } |\phi| < \varepsilon \\ = 0, & \text{if } \text{else.} \end{cases} \quad (3.33)$$

ε represents the extension of the transition zone in each phase, and it is defined with the same width as the transition zone used in the LSM. A modified delta function $\delta^{scaling}$ is employed in Hydro3D-NWT. This method shifts δ towards the higher-density fluid and improves the stability of the model.

$$F_i^{sf} = \sigma k \delta^{scaling}(\phi) n_i, \quad \delta^{scaling} = 2H(\phi)\delta(\phi) \quad (3.34)$$

ϕ is interpolated to the cell face, where using a 2^{nd} order central difference k , n_i are calculated, 3.32. $\delta(\phi)$ is also defined to apply the surface tension only near the water surface. Then, the values at the faces of the cell are calculated using simple interpolation.

3.3.7 Waves Input and Relaxation

Waves are input at the west boundary of the domain using an analytical solution to specify the water surface elevation and particle velocities. In this research, 2^{nd} order Stokes Waves are specified by equations 3.35, 3.36 and 3.37.

$$n(x, t) = \frac{H_w}{2} \cos\left(\omega t - \frac{\pi}{2} - kx\right) + \frac{H^2 k}{16} (3 \coth^3(kd) - \coth(kd)) \cos\left(2\left(\omega t - \frac{\pi}{2} - kx\right)\right) + d \quad (3.35)$$

$$u(x, z, t) = \frac{H}{2} \omega \left(\frac{\cosh(kz)}{\sinh(kd)} \right) \cos\left(\omega t - \frac{\pi}{2} - kx\right) + \frac{3}{16} \omega (kH)^2 \left(\frac{\cosh(2kz)}{\sinh^4(kd)} \right) \cos\left(2\left(\omega t - \frac{\pi}{2} - kx\right)\right) \quad (3.36)$$

$$w(x, z, t) = -\frac{H}{2}\omega \left(\frac{\sinh(kz)}{\sinh(kd)} \right) \sin\left(\omega t - \frac{\pi}{2} - kx\right) - \frac{3}{16}\omega(kH)^2 \left(\frac{\sinh(2kz)}{\sinh^4(kd)} \right) \sin\left(2\left(\omega t - \frac{\pi}{2} - kx\right)\right) \quad (3.37)$$

where, H_w is the wave height, d the water depth at still water level, k the wave-number defined as $k = 2\pi/L_w$, with L_w the wave length. The dispersion relation defines the angular frequency ω :

$$\omega^2 = gk \tanh(kd) \quad (3.38)$$

In the case of the simulations presented in Chapter 4 waves are input at $x = 0m$. To avoid perturbation in the result due to wave reflections from the west boundary, the structure is placed as far as possible from the inlet boundary, allowing the collection of enough data for analysis before the reflections reach the structure.

In Chapter 5, the waves are generated in a zone of one wavelength; additionally, this section implements an absorption zone to dissipate the reflection from the structure, preventing them from bouncing back towards the area of interest. This implementation allows a reduction in the size of the domain.

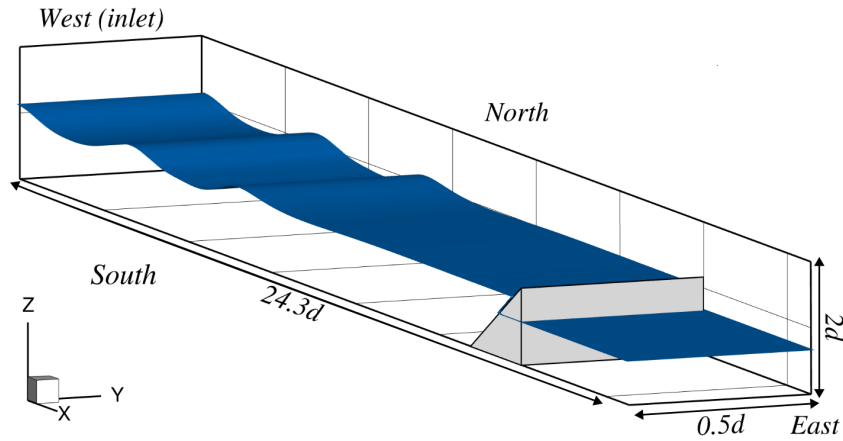


Figure 3.4: 3D sketch of Hydro3D Domain including a sloped structure.

The absorption zone is based on the Relaxation Method (RM) described in [99]. A relaxation function $\Gamma(x_r)$ is defined to modify the water surface elevation

and particle's velocities towards the analytical solution. Γ is a function of a secondary coordinate, x_r ; $x_r = 0$ at the end of the relaxation zone, $x = x_{er} = L_w$, and $x_r = 1$ at $x = 0$ m.

$$\Gamma(x_r) = 1 - \frac{e^{x_r^R} - 1}{e - 1} \quad (3.39)$$

$$x_r = \frac{x_{er} - x_i}{x_{er}} \quad (3.40)$$

The coefficient R prescribe the relaxation rate in the relaxation zone. A value of $R = 3.5$ is used in the present study. After Hydro3D-NWT computes the location of the free surface, this is updated by 3.41, shifting the solution towards the analytical solution. The same process is conducted for the velocities in every sub-step of the Range-Kutta scheme, 3.42.

$$\phi = \Gamma(x_r)\phi_{computed} + (1 - \Gamma(x_r))\phi_{analytical} \quad (3.41)$$

$$u_i = \Gamma(x_r)u_{icomputed} + (1 - \Gamma(x_r))u_{ianalytical} \quad (3.42)$$

A relaxation zone is also employed at the end of the domain's east boundary. In it, the water surface is shifted towards the still water level (d), and the velocities are reduced to zero over the length of the relaxation zone. This prevents waves from reflecting back from the east boundary in Chapter 4 and relaxes the water condition downstream of the structure in Chapter 5.

3.3.8 Code Parallelisation and Work Sequence

As explained previously, LES requires a sufficiently fine grid to resolve at least 80% of the turbulent kinetic energy. This requirement is translated into a significant computational effort. To improve computational performance, Hydro3D-NWT is parallelised by dividing the domain into sub-domains, which can be solved in parallel using multiple processing units. A message-passing interface (MPI) between

subdomains/processors conducts the information exchange between processors. This implementation improves the calculation speed.

In figure 3.5, the work sequence followed by Hydro3-NWT is presented. First, the code generates the domain with its subdivision, allocates the variables and assigns each CPU processor to its respective subdomain. After this, the flow is initiated, passing to the flow solver loop. The time step is calculated at the beginning of each iteration if a variable time step is selected. Then, the location of the water surface is determined, followed by the calculations of the SGS stress tensor, using information from the initial condition or the previous time step. The boundary conditions are updated in the next step (wave in-put). Then N-S equations are solved, and the time advance is achieved with a 3rd RK. If a body is included, the IBM is applied in the last sub-step of the RK, and the velocities are updated to u^* . The final section calculates the pressure field, and the continuity condition is verified. With the continuity condition satisfied, the velocity u^t and pressure field p^t of the current time step are found. This loop continues until the last time step is reached and the final output files are saved. If non-converged conditions occur or the CFL restriction can't be satisfied when calculating the time step, Hydro3D-NWT stops, and a notice is printed for the user.

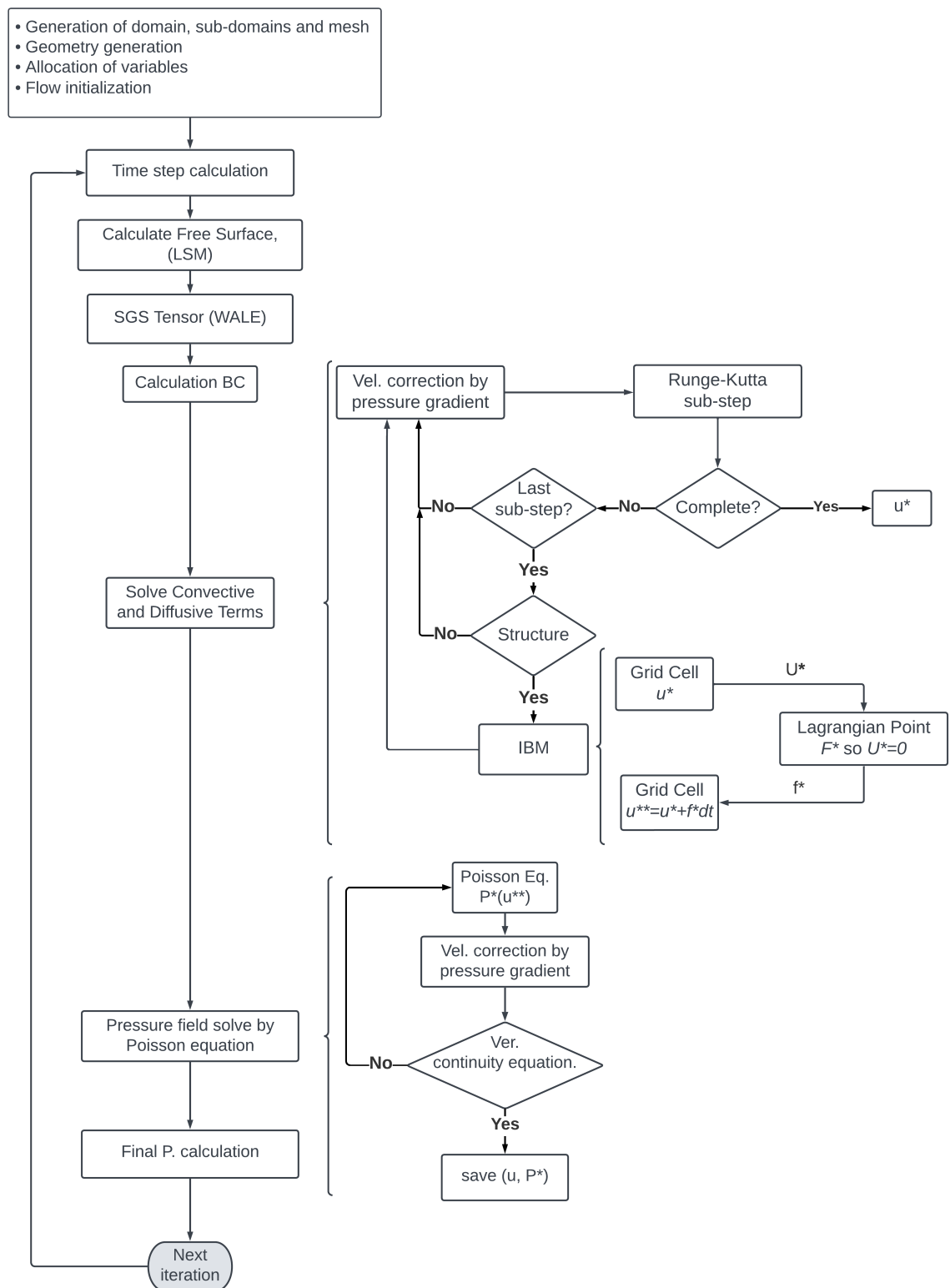


Figure 3.5: Hydro3D-NWT flow chart.

3.3.9 Conclusion.

LES offer the opportunity to study in detail the flow structures that contribute to energy dissipation due to turbulence but with a lower computational cost than DNS. The LES method solves all the flow motions larger than the mesh and models, with an SGS, the smaller structures. This capability allows to study the structures containing most of the energy flow. A correct LES should simulate at least the 80% of the flow energy.

HYdro3D-NWT is a LES-based code that couples advanced numerical techniques to solve the N-S equations. It uses the WALE SGS model to include the effect of non-resolved eddies. The water surface is captured by an LSM, and structures can be included in the domain by IBM. This component offers the capability to simulate complex wave-restructure interaction.

In the following chapters, Hydro3D-NWT is validated by experimental results collected from the literature, well-known theories, and empirical equations. Then, the code is employed to expand and analyse the hydrodynamics of wave structure interaction.

Chapter 4

Study of Waves and Submerged Trapezoidal Structure

4.1 Introduction

Research on wave-structure interaction has been fundamental in developing durable and cost-effective coastal defences. In the past, effective coastal engineering design was based on experiences from full-scale projects or laboratory physical models. With the advent of computers and their steady increase in capacity, numerical tools have become essential in designing coastal structures. Given the high diversity related to coastal projects (e.g., wave conditions, shoreline morphology, and type of structure), scale models in laboratories complemented by numerical simulations are a powerful prediction tool for investigating complex and non-standard coastal engineering problems.

Coastal defences can have multiple objectives, such as protecting areas of interest (like residential, ports, and railways), generating calm sea conditions in harbours and docking areas, and controlling coastal erosion. This variety of functions has led to various structure typologies. Standard emergent options are permeable breakwaters built with rubble and/or concrete blocks and sloped or vertical impermeable walls. An alternative is submerged breakwaters, which feature their crest below the mean water level [100]. This alternative generates great interest among coastal developers because it has a low impact on the shoreline's aesthetic and allows water

exchange [101]. Early studies analysed the performance of this type of coastal defence, such as: [102, 103, 104, 105], proving that submerged breakwaters affect the wave transformation when approaching the shore, contributing to wave energy dissipation. They have been used in several projects, such as in Italy, the USA, Japan and Australia, as reviewed by [106]. Submerged breakwaters dissipate wave energy by forcing the shoaling process before the waves reach the shoreline, promoting wave breaking and turbulence at the structure-water interface and causing wave reflection [107, 108, 109]. Their performance as a coastal defence depends heavily on the level difference between the water surface and the crest of the structure, their distance to the shoreline, their geometry and the permeability of the structure. From their implementation in full-scale projects, it has been observed that they may have little effect on the shoreline when not correctly designed [106, 110].

Experimental and numerical models have been employed to expand and better understand the hydrodynamics of wave-structure interaction of submerged breakwaters. Wave height can be reduced by up to 40% of the incident wave height after passing over the structure [103, 111, 100, 108]. It has been detected that Bragg reflection can generate wave dissipation [108], but more than one line of breakwater is needed to create that effect. The results from research and experience on-site are compiled in guidelines to design breakwaters in coastal engineering manuals like "The Coastal Engineering Manual" (CEM) of the U. S. Army Corps of Engineers, but their application is restrictive to specific structure geometries and wave conditions. Planning non-standard breakwaters usually requires experimental and numerical models. In the case of submerged breakwaters, most of the data found in the literature corresponds to trapezoidal, triangular and square structures [102, 103, 104, 25, 107, 108, 109], which are the most common geometry used in coastal defences. Numerical simulations offer the opportunity to expand physical experiments and explore different geometries without laboratory installations. In addition, CFD allows for studying the hydrodynamics of wave-structure interaction in a way that is impossible in a laboratory, providing great details of the water surface, particle movement, and forces on the structure.

Several 2D numerical models have been applied to study breakwaters, e.g. [25, 112, 108], analysing transmission and reflection coefficients. However, these models don't allow for exploring the turbulence structures near the water-structure interface, which is most prominent in the case of porous structures. In [107], a 3D LES method is used to explore the effect of the permeability and length of the crest of trapezoidal submerged breakwaters in its performance. It is found that the turbulent kinetic energy near the surface of the structure plays an essential role in wave dissipation. LES is a method that resolves large-scale turbulence and only models the effect of small-scale turbulence [113] and hence directly simulates the vast majority of energy dissipation in wave-structure interaction problems.

In the present chapter, Hydro3D-NWT is used to study the propagation of monochromatic waves over submerged berm breakwaters of various geometry. The study's main objective is to clarify the effect of the front slope shape on the wave profile evolution over the structure and acting hydrodynamic forces on the structure. Hydro3D-NWT is first validated, after which the physical model presented in [25] is expanded by exploring different geometries of the front slope: concave, cubic and convex shapes are investigated.

In addition, the execution of this study allows to verify the ability of Hydro3D-NWT to simulate wave structure interaction with less complex processes compared to the next step of the research, Chapter 5. This makes it possible to identify key routines or aspects of the code that need to be treated or improved to achieve correct simulations.

4.2 Simulations of a submerged trapezoidal structure

Submerged trapezoidal structures are widely used as benchmark cases to analyse the performance of numerical codes. This case is a good application for validating the wave transformation during the shoaling and de-shoaling processes. In the present study, the laboratory study presented in [25] is simulated using Hydro3D-NWT and its accuracy in capturing the water surface is analysed. Figure 4.1a sketches the

numerical wave tank and the trapezoidal submerged structure. The still water level is set to $d=0.4\text{ m}$, the structure is fixed at $16.25d$ (6.5 m) from the wave-maker, it has an extension of $16.25d$ (6.5 m), $0.75d$ (0.3 m) height and it extends throughout the total width of the tank. For analysis purposes, the structure is divided into three sections: front slope ($x = 6.5\text{ m}$ to $x = 8.0\text{ m}$), berm ($x = 8.0\text{ m}$ to $x = 10.0\text{ m}$), and rear slope ($x = 10.0\text{ m}$ to $x = 13.0\text{ m}$). The transition edge from the front slope to the berm is denominated nose.

The incident waves are generated at the west boundary (inlet) using the kinematics from 2^{nd} order Stokes theory with wave height $H_w = 0.02\text{ m}$ ($0.05d$), wave period $T = 1.3\text{ s}$ and wave steepness of $H_w/L = 0.00923$. Figure 4.1b shows the wave gauge locations inside the tank to record the water surface fluctuations - the exact locations used in the experiments. The numerical domain is discretised by a uniform grid resolution of $dx/d = dy/d = 0.025$ and $dz/d = 0.0125$. A fixed time-step of $\Delta t = 0.001\text{ s}$ is adopted, allowing a CFL number below 0.1 in all simulations, calculated with the maximum velocity in each direction. A Dirichlet boundary condition is applied for velocities and the water surface at the west boundary. The east boundary and bottom of the tank are treated as no-slip boundary conditions, whereas the sidewalls and top wall as free-slip boundaries. The waves are absorbed inside a relaxation zone (A. Z.) over the domain's last 2.0 m ($0.92L_w$).

Figure 4.2 presents the water surface elevation time series obtained from both Hydro3D-NWT simulations and experimental measurements, aligned according to their respective wave periods. The incident wave profiles recorded by $WG - 1$ and $WG - 2$ are accurately reproduced by the numerical model. However, at $WG - 2$, a slight overestimation of the wave trough elevation is observed as the local water depth decreases to $0.4d$. At $WG - 3$, located on the berm of the structure where the depth is further reduced to $0.25d$, the wave profiles become steeper and display both horizontal and vertical asymmetries. These transformations are well captured by Hydro3D-NWT, although the model slightly overestimates the crest elevation by an average of 4.4%. From $WG - 4$ onward, the separation of higher harmonic components becomes evident. A secondary peak begins to form at the

wave crest, and wave decay is noticeable due to the de-shoaling process as the waves transition from shallower to deeper water. The simulated surface elevation remains consistent with laboratory observations. Further downstream, $WG - 5$ and $WG - 6$ capture continued wave decay and the amplification of the secondary crest, resulting in a distinct double-crested wave pattern. This change suggests a redistribution of wave energy relative to the initial conditions observed at $WG - 1$. In these downstream locations, discrepancies between the numerical and experimental results become more pronounced at the wave crests than at the troughs. Notably, at $WG - 6$, Hydro3D-NWT slightly underestimates the amplitude of the secondary peak. Overall, Hydro3D-NWT demonstrates strong predictive capability in simulating the wave transformation across the structure, accurately capturing key phenomena such as wave steepening, wave decay and the emergence of higher harmonics.

Figure 4.3a, figure 4.3b and figure 4.3c show the wave spectrum for the locations of $WG - 1$, $WG - 3$ and $WG - 6$, calculated for the experimental data [25] and Hydro3D-NWT in red and black lines, respectively. The amplitude is normalised by the fundamental amplitude of $WG1$. In figure 4.3a, the spectrum of $WG - 1$ is plotted, two peaks are observed in Hydro3D-NWT's results, the most energetic at $f_0 = 0.77 \text{ s}^{-1}$, and a minor peak at $f_1 = 1.54 \text{ s}^{-1}$, which corresponds to both components of the 2^{nd} order Stokes waves used. It is observed that the experimental spectrum shows higher harmonics, with no specific peak at f_1 , this is related to the scatter of the available laboratory data, which does not allow a small peak to be identified. In the other wave gauges, the higher harmonics peaks are clearly visible in both datasets. At $WG - 3$, higher harmonics appear in the spectrum, being the most important at $f_2 = 2.30 \text{ s}^{-1}$ and $f_3 = 3.07 \text{ s}^{-1}$. A significant increment of the second component is appreciated in this location. This is explained by the reduction in the water depth, which generated an energy concentration in a smaller water column. The higher frequency components in the spectrum are more affected by this energy concentration. Figure 4.3c records the spectrum downstream the structure

at $WG - 6$. A decay in the spectrum is observed, and the higher frequencies shown in figure 4.3b are almost undetectable. The results indicate that the presence of the structure significantly influences water surface fluctuations by modifying the wave profile and inducing the generation of higher-order harmonics. A comparative analysis of the numerical and experimental data reveals that the numerical simulation captures the same wave transformation processes observed in the laboratory. In particular, higher harmonic components emerge at corresponding frequencies in both datasets, although minor discrepancies in amplitude are present.

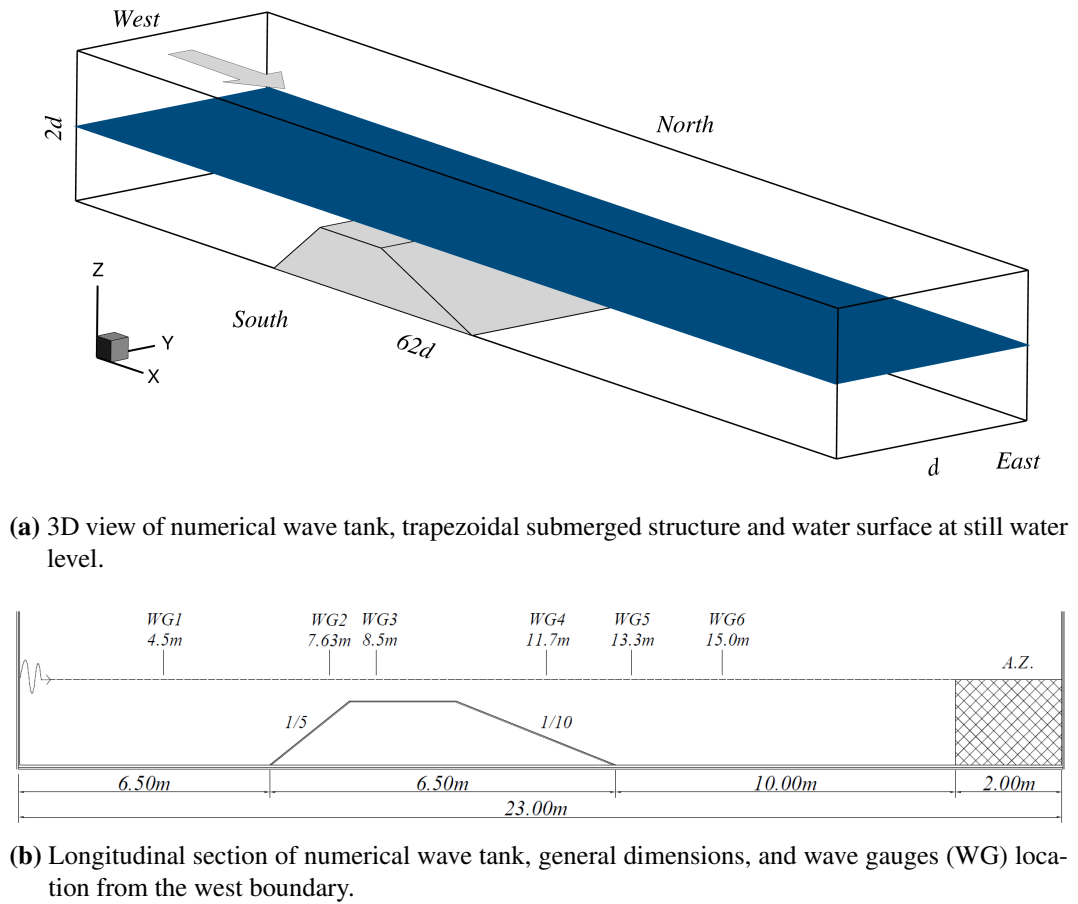


Figure 4.1: 3D view of the domain and longitudinal section.

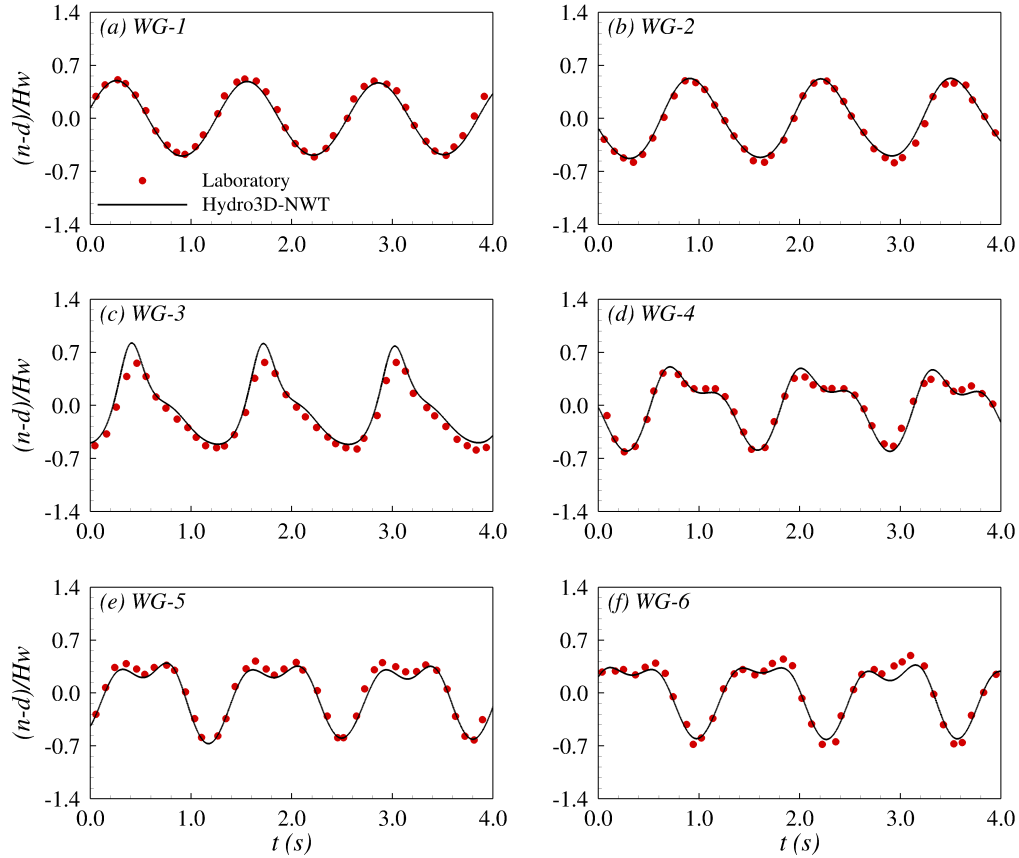


Figure 4.2: Water surface fluctuations at each wave gauge (WG). Solid line Hydro3D-NWT, dots laboratory data.

Figure 4.3d presents with black lines the wave envelope at the centre of the wave tank generated with Hydro3D-NWT's results. Two water surface instances over the structure are plotted with red and green lines. The structure (not in scale) is included as a reference to visualise its location. The upper line of the wave envelope shows the highest wave crest elevation reached in each location, and the lower line indicates the lowest level reached by the wave trough. Therefore, the wave envelope gives the area where the water surface fluctuates. It can be seen that for $x < 4$ m, the wave envelope does not show areas of wave amplification. From $x > 4$ m., locations where amplification occurs are visible, which are related to reflections generated due to the wave structure interaction. Over the berm, the wave envelope presents an increasing trend, meaning that the wave crest and trough get higher as the waves travel through it. This phenomenon is explained by the reduced water depth, provoking the shoaling of the waves. The maximum wave height reaches the

rear edge of the berm. No indication of wave breaking is observed in the simulation and the experimental results. Over the rear slope, the waves rapidly decrease in height, and higher frequency waves are visible, generating locations where the wave height is significantly amplified and others where it is reduced. As the waves move downstream, these locations slowly disappear, and the wave envelope resembles the input side. At $x = 23$ m, the effect of the absorption zone is visible, gradually taking the water level to the still water level condition.

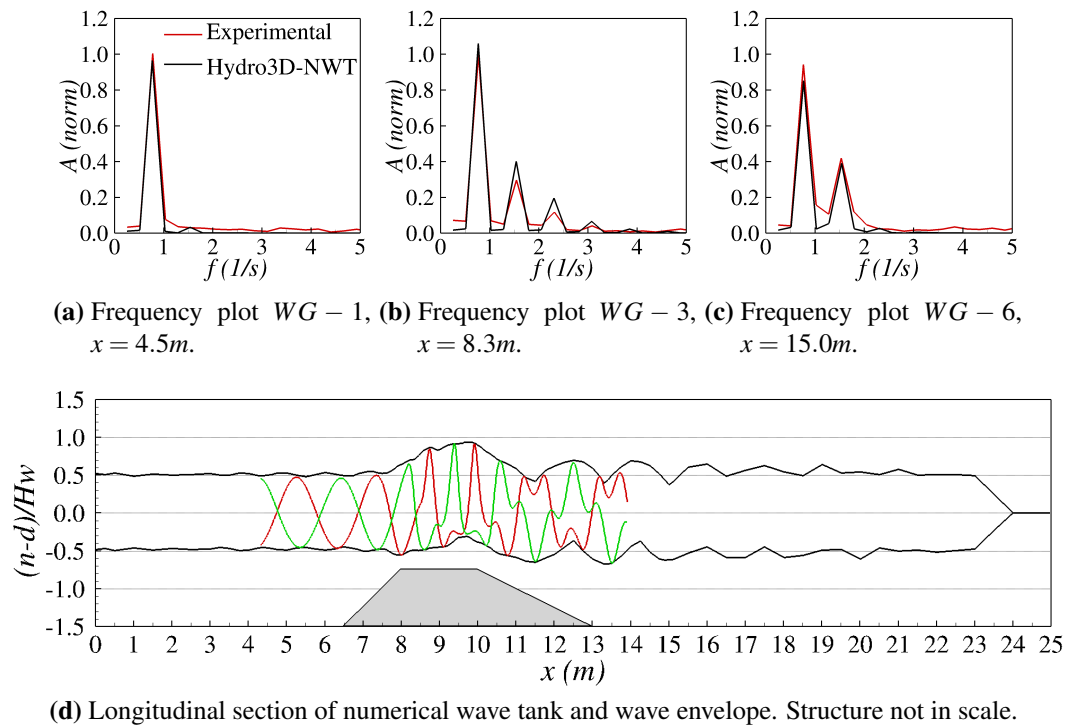


Figure 4.3: Figures a), b) and c) frequency spectrum for WG1, WG3 and WG6 respectively, experimental data [25] (red) and Hydro3D-NWT results (black). Figure d) Hydro3D-NWT wave envelope and two instantaneous water surface.

Overall, the ability of Hydro3D-NWT to capture the wave progression over a trapezoidal structure is validated, reinforcing its applicability for simulating wave-structure interactions.

4.3 Numerical study of front slope geometry





In this section, the geometry of the front slope of the structure used in [25] is modified to investigate if changes in its shape can affect the wave evolution over the

berm and the forces on the structure. These two aspects are of great concern in the design of any coastal structure.

The simulation parameters, domain size, grid, boundary conditions, water depth, and wave parameters used in this analysis are the same as those used in the validation.

In addition to the original 1/5 linear slope tested in [25], three different front slope shapes are investigated. Each case's corresponding curve function and cross-section are shown in Table 4.1. All slopes start at $x=6.5$ m and $z=0.0$ m, and have a total length of 1.5 m and a maximum height of 0.3 m. In the case of the cubic and convex shapes, the gradient of the slope is set to zero ($dz(x)/dx = 0$) at $x = 8.0$ m (nose) to obtain a smooth transition into the horizontal berm. In the concave shape, the slope gradient at the nose is 0.7. The geometries presented in Table 4.1 are adapted from those utilized in [24].

Table 4.1: Study cases, front slope functions and a sketch of geometries.

Case	$z(x) =$	Geometry
Linear	$\frac{1}{5}x + \frac{-6.5}{5}$	
Concave	$\frac{28}{135}x^3 + \frac{-13}{3}x^2 + \frac{2,719}{90}x + \frac{-18,967}{270}$	
Cubic	$\frac{-8}{45}x^3 + \frac{58}{15}x^2 + \frac{-416}{15}x + \frac{1,183}{18}$	
Convex	$\frac{-2}{15}x^2 + \frac{32}{15}x + \frac{-247}{30}$	

4.3.1 Water surface results

Figure 4.4 plots the time-averaged wave envelopes over the structure for each geometry tested. For the construction of the wave envelope, 10 waves are considered starting from $7T$, neglecting the first 6 waves that reach the toe of the structure. In each location where the water surface is probed, the maximum (crest) and mini-

num water level (trough) are recorded for each wave period and then averaged for 10 waves. The top solid lines show the progression of the average wave crest elevations, and the solid lower lines show the progression of the average wave trough. Dashed lines represent the differences in the crest level between the new geometries and the linear case. It is observed that the convex structure imposes a faster increase in wave height as the waves run over the front slope, followed by the cubic and linear cases, whereas the concave structure generates a slower increase in wave height. The faster increment of the wave crest in the convex and cubic cases causes the wave height to peak earlier over the berm compared to the other geometries, at 9.305 m and 9.355 m, respectively (Table 4.2). After these locations, the wave height experienced a gentle decay, which can be related to energy dissipation; no breaking waves were detected in the simulations. On the other hand, in the linear and concave cases, the wave height grows until the end of the berm. From there, wave height reduction occurs for all cases due to the de-shoaling process generated by the downward slope.

Different wave behaviours upstream of the structure are visible in Figure 4.4. The concave case exhibits higher levels of reflection, forming a partial standing wave pattern that is translated into locations where the wave height is amplified and others where it is reduced. In the remaining cases, this phenomenon is less pronounced.

Figure 4.5 presents the amplitude wave spectrum for all cases at three locations $WG-1$, $WG-3$ and $WG-5$, according to figure 4.1b. The amplitude is normalised by the fundamental amplitude of $WG1$. In figure 4.5a the input waves are visible with the two frequencies, $f_0 = 0.77 \text{ s}^{-1}$ and $f_1 = 2 \times f_0 = 1.54 \text{ s}^{-1}$, peaks related to the 2^{nd} order Stokes waves used. All cases present a similar spectrum, with minor variations in the higher frequency component for the concave case, which can explain the different behaviour of the waves before the structure. At $WG-3$, figure 4.5b, located just downstream of the nose of the structure, new higher frequency waves appear in all cases at, $f_2 = 3 \times f_0 = 2.31 \text{ s}^{-1}$, $f_3 = 4 \times f_0 = 3.08 \text{ s}^{-1}$ and $f_4 = 5 \times f_0 = 3.85 \text{ s}^{-1}$. A significant growth of the second harmonic is

detected. No significant changes are appreciated in the fundamental harmonic. The differences between the spectra are more predominant in f_1 , where the convex has the largest amplitude, followed by the cubic, linear and concave geometries. This difference aligns with the wave height variations presented in the wave envelope, indicating a more efficient energy distribution from deep to shallow water with the convex and cubic geometries. Figure 4.5c shows the spectrum downstream of the structure. In this case, the higher frequency components present in $WG - 3$ are dissipated, and the amplitudes of f_1 and f_2 are significantly reduced. The lowest frequency wave's amplitude also reduces its amplitude in all cases. The main difference between the cases is concentrated in f_1 , but the magnitudes are inverted compared to the $WG - 3$. During the evolution of waves over the structure, higher-frequency waves are generated, which affect the wave profile. The results showed that the higher-frequency waves in the cases studied are more sensitive to the structure. When there is a reduction in water depth, the waves pass over the front slope and berm, generating a concentration of wave energy that leads to the generation of higher-frequency waves and an increase in their amplitude as the waves move over the berm.

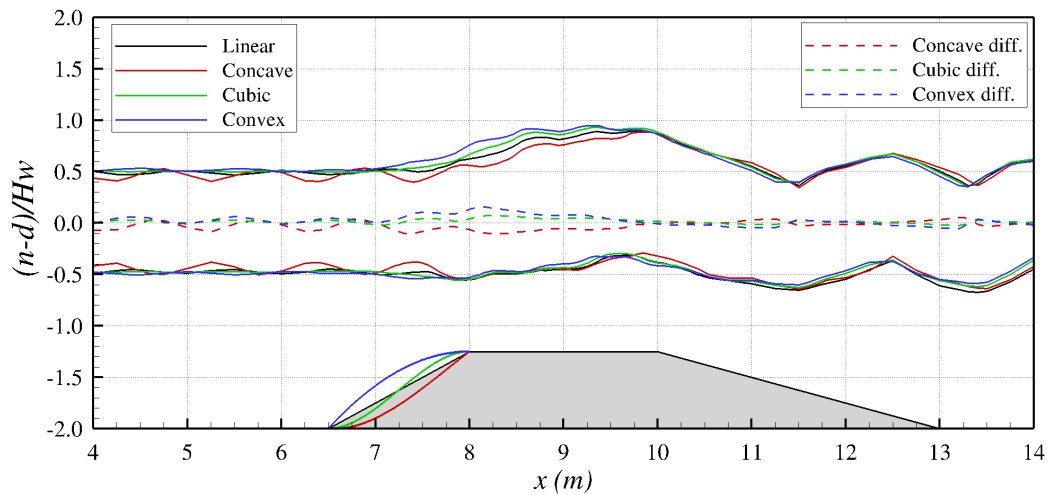


Figure 4.4: Wave envelopes (solid lines) and crest level difference (dashed line) compared to linear geometry. Structure not in scale, to indicate the location of the front slope, berm, and rear slope.

Table 4.2: Location where waves peak x_p , wave height (H_p) at x_p , shoaling coefficient ($K_{sp} = H_p/H_w$) at x_p , ratio compared to linear case ($r_p = H_p/H_{pL}$) at x_p .

	x_p (m)	H_p (m)	K_{sp}	r_p
Linear	9.855	0.0244	1.219	1.00
Concave	9.855	0.0236	1.180	0.967
Cubic	9.355	0.0256	1.278	1.049
Convex	9.305	0.0255	1.274	1.045

Figure 4.6 plots the distribution of the shoaling coefficient $K_s = H/H_w$, against the water depth $d(x)$. H is calculated from figure 4.4 as the difference between the crest and trough envelope, and $d(x)$ is the distance from the structure to the water surface in still water level condition. Figure 4.6 shows the evolution of K_s from the toe of the structure, $x = 6.5$ m and $d = 0.4$ m, to the location where the maximum wave height is reached over the berm, which corresponds to x_p in table 4.2 and $d = 0.1$ m. The X axis in figure 4.6 is inverted to facilitate the comparison with Figure 4.4. At $d = 0.1$ m, symbols indicate the maximum K_s reached in each case. Similar results between the convex and cubic cases are shown. Initially, no change in K_s is observed in the case of convex geometry, followed by an increase at $d = 0.26$ m until it stabilises at $d = 0.13$ m after which it rapidly increases to reach a maximum value of $K_s = 1.37$. In the cubic case, the shoaling coefficient decreases slightly at the beginning of the slope but then increases steadily until $d = 0.12$ where K_s further increases to achieve a maximum value of $K_s = 1.34$. The linear and concave cases present fluctuations of K_s as d decreases. The linear case starts with a smooth increase of K_s until $d = 0.35$ m, after which it then experiences a fluctuating growth to a maximum K_s of nearly 1.3. The concave case is the geometry which generates a more irregular evolution of the K_s over the structure. First, rapid growth of K_s is observed, then sharply decays to values $K_s = 0.78$ at a water depth close to 0.36 m. It follows a gradual increment of K_s until it levels at $K_s = 1, 1$. On the berm, K_s reaches its maximum of about 1.25. As shown in Figure 4.4, the convex and cubic cases allow for the biggest increment of the wave height over the structure, followed by the linear and concave cases. The high fluctuations in the linear and concave geometries are related to the appearance of high-frequency

waves generated by the interaction with the structure. These two geometries have the steepest shapes near the nose, therefore, a sharper transition from the slope to the horizontal berm. Considering that the particle's velocities are larger closer to the water surface, it explains that the generation of reflections is more significant in these geometries than in the convex and cubic slopes, which have a smother change from the front slope to the berm and their steepest section of the slope are deeper and interacts with slower particles.

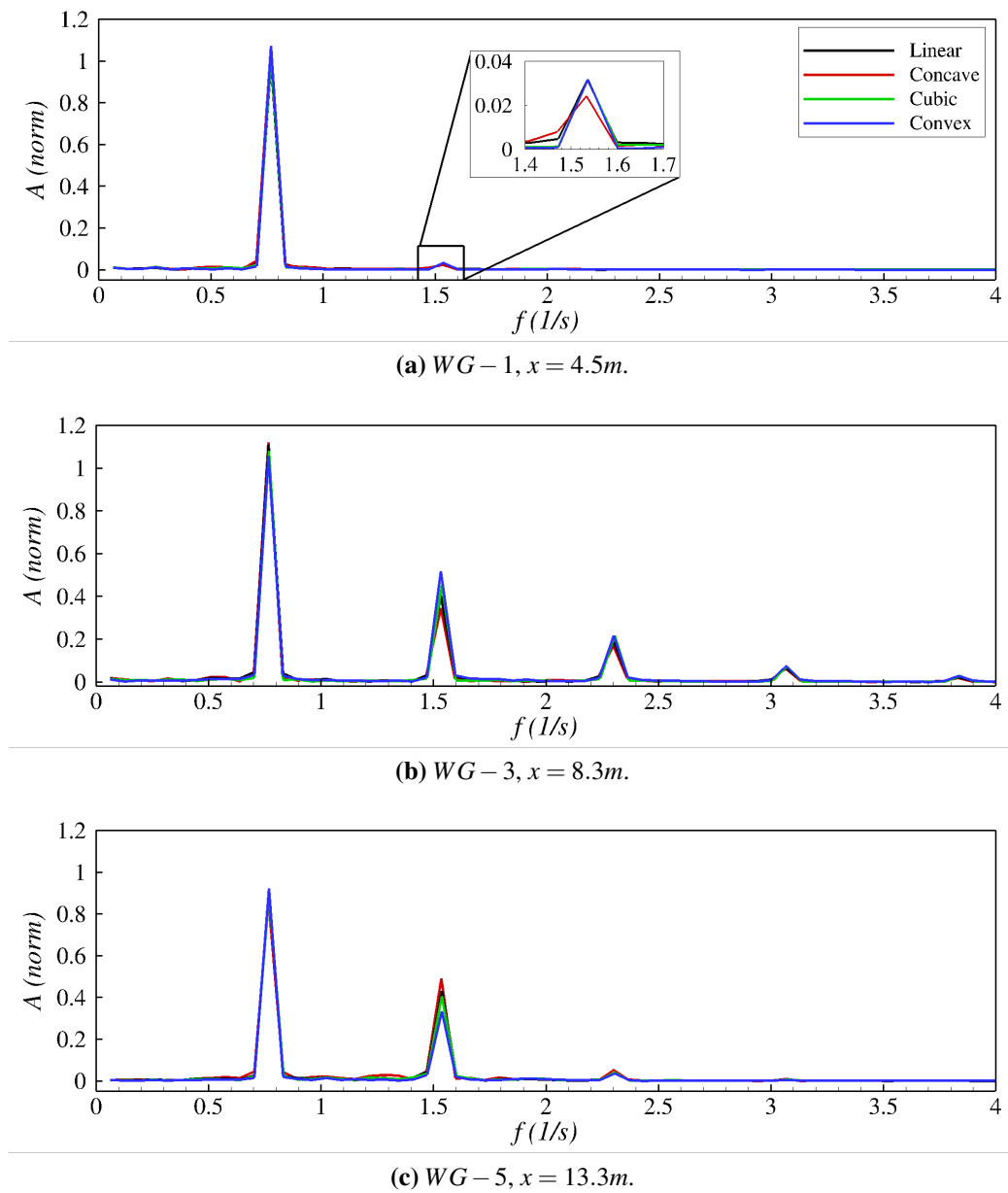


Figure 4.5: Amplitude spectrum for all cases.

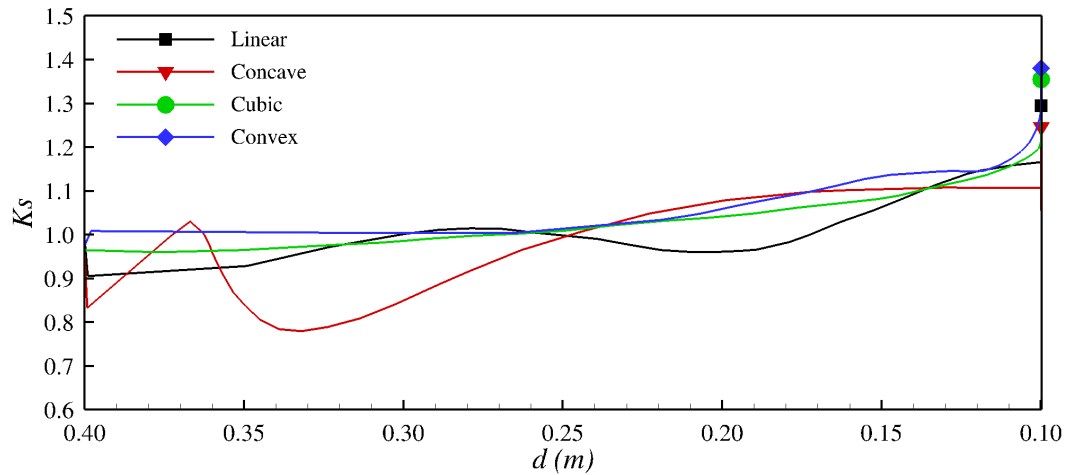
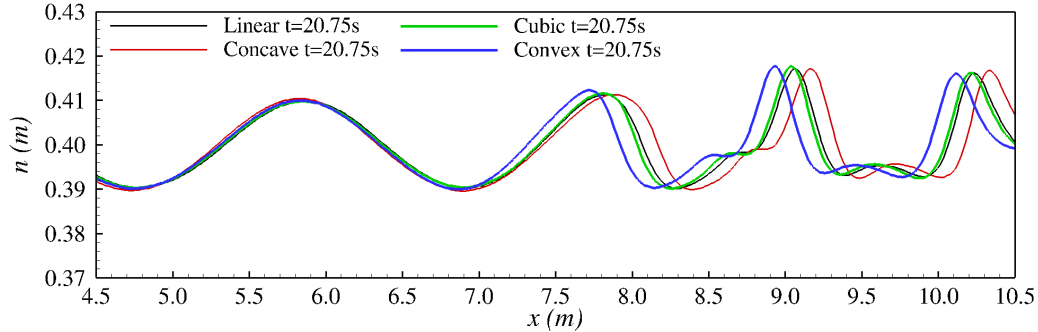


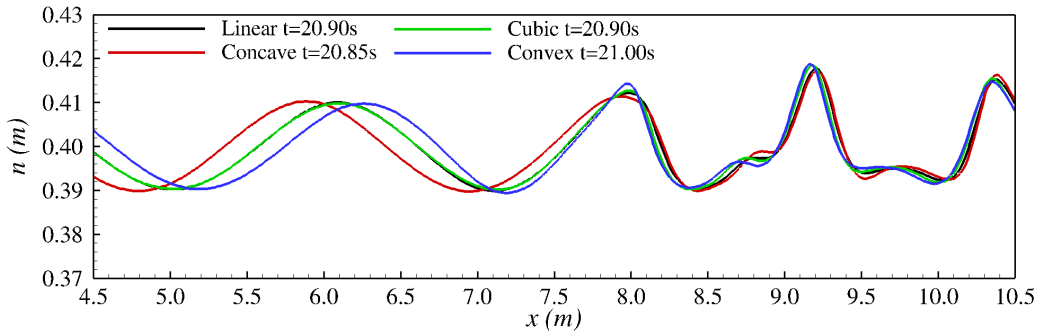
Figure 4.6: Shoaling coefficient, $K_s = H/H_w$, variation over the front slope and berm.

Figures 4.7a and 4.7b shows the instant water surface at $t = 20.75$ s and aligned at $x = 8.0$ m respectively, for each geometry analysed. Table 4.3 presents the average wave height (H) calculate from the wave envelope, figure 4.4, at the toe of the slope, $x_1 = 6.0$ m, and on the nose, $x_2 = 8.0$ m. The average wave celerity on the slope, c_{av12} , is calculated between x_1 and x_2 for each one of the ten waves considered in the analysis and then averaged. From Figure 4.7a no significant delay or time shift is detected in the waves before the structure, $x < 6.5$ m, after which the different geometries of the front slope affect the wave celerity and wave height. Overall, the linear and cubic cases present similar results, with an average celerity variation of less than 1% as calculated from $x = 6.0$ m to $x = 8.0$ m (Table 4.3). The concave and convex cases generate different results. In the former, the waves travel faster over the front slope, increasing their celerity by 1.05 compared to the linear case. On the other hand, the convex geometry reduces the average wave celerity by a factor of 0.92 compared to the linear case. Figure 4.7b shows the wave profile when the wave crests are located over the nose, $x = 8.0$ m. The linear and cubic geometries result in similar wave profiles. In the concave case, the wave height is reduced by approximately 5%, and a longer wave profile is also observed. The waves generated over the convex slope experience a 10.7% increment in their wave height, formed by a leaner and shorter wave profile. The variations in wave celerity and water surface are a result of the different rates of the water depth's reduction

in each geometry, which affects the shoaling process and how the waves reach the horizontal berm. Over the berm, the disalignments of the waves are maintained with almost no change.



(a) Water surface at $t = 20.75s$.



(b) Waves aligned at $x = 8.00m$.

Figure 4.7: Comparisons of the water surface elevations at different times of the simulations.

Table 4.3: Average wave height (H) at $x_1 = 6.0$ m and $x_2 = 8.0$ m, average wave celerity (c_{av12}) between x_1 and x_2 and wave height ratio compare to linear case at x_2 .

	H_{x1} (m)	H_{x2} (m)	c_{av12} (m/s)	$H_{x2}/H_{L,x2}$
Linear	0.0198	1.381	1.448	1.000
Concave	0.0192	1.311	1.526	0.948
Cubic	0.0197	1.389	1.440	1.043
Convex	0.0195	1.494	1.339	1.107

Figure 4.8 plots instantaneous water surface in terms of the iso-surfaces at $\phi = 0$, for the case of a concave front slope at (a) $t = 20.41$ s (figure 4.8a) and (b) $t = 20.06$ s (figure 4.8b). In these figures, the increment of the wave height due to the shoaling process over the front slope is observed. It is appreciated that no wave breaking occurs in any location of the domain. Therefore, the decay of the

wave height over the berm can be related to friction on the structure's surface or turbulence. The reduction of the wave height and the appearance of high-frequency waves over the rear slope, discussed in the previous paragraphs, are also observed in Figure 4.8.

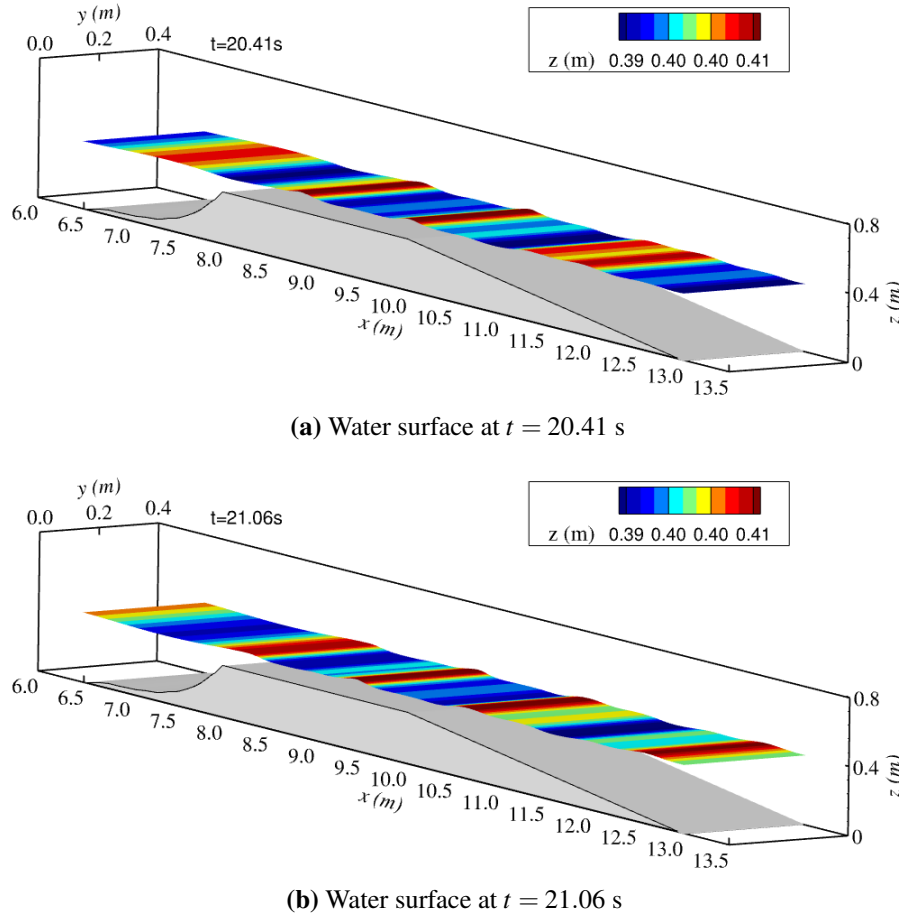


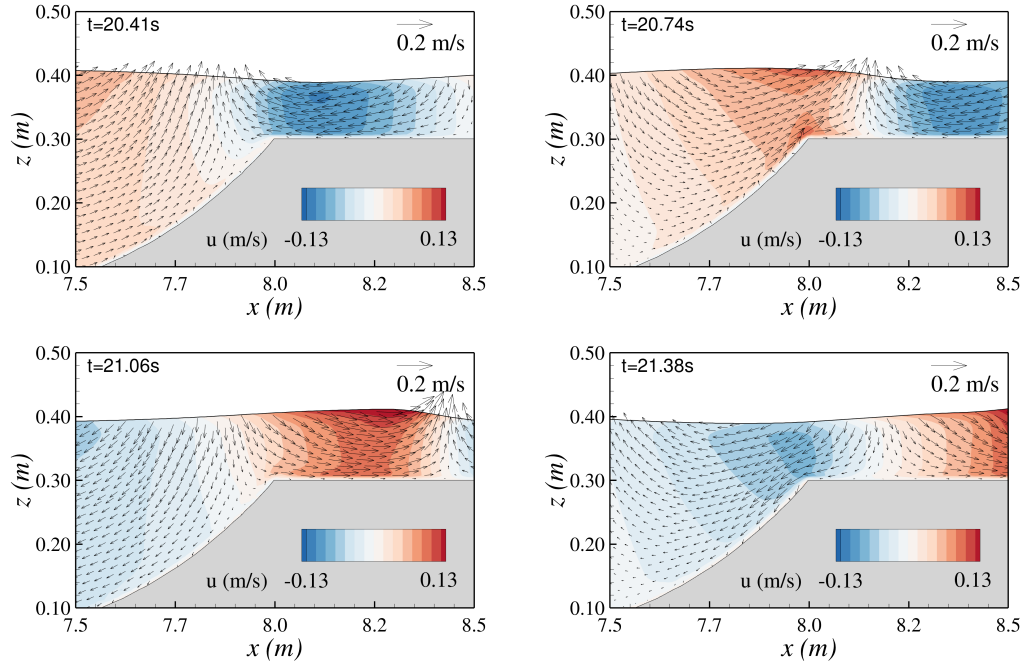
Figure 4.8: Water surface over structure, Concave case ($x/y=1$, $x/z=1$).

Figure 4.9 shows one wave passing over the nose of the structure for the concave and convex cases. The vectors represent the velocity field, and the contour indicates the horizontal velocity u . In figure 4.9a, it is possible to observe an increment of the velocity magnitude as the water depth decreased; this is shown by the increment of the vector's size and the contour's colour intensity. This velocity variation is more significant in the convex geometry than in the concave case. In the vicinity of the nose of the structure, a more perturbed velocity field is observed in the concave case compared to the convex geometry, especially at $t = 20.74$; this

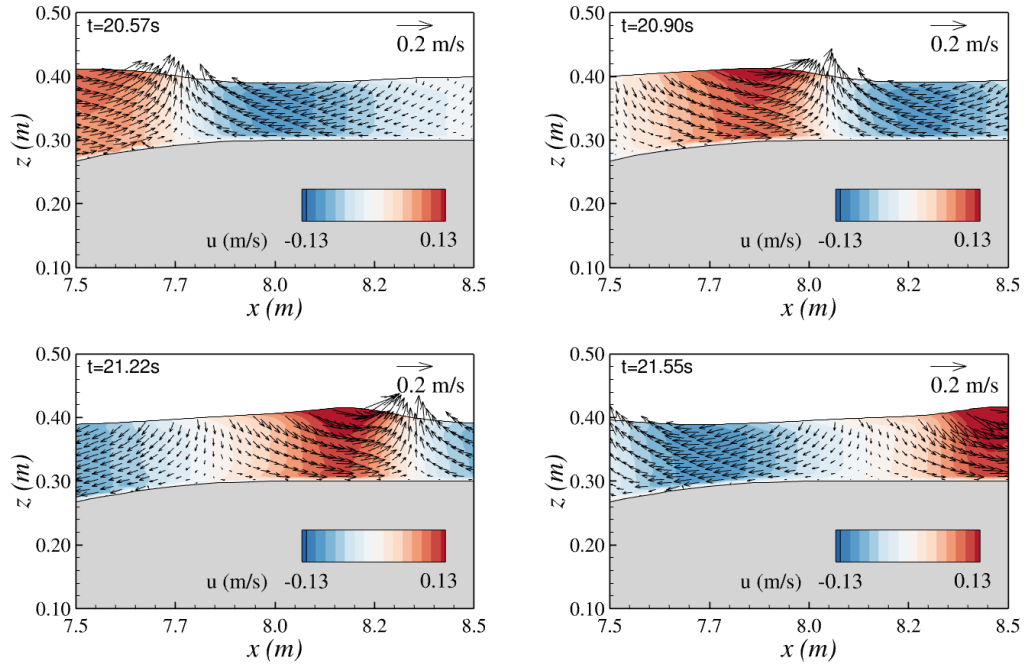
is expected due to a sharper edge between the front slope and berm in the concave case. However, no clear indication of eddies is shown in the figures. Unlike other studies that include breaking waves on sloped structures [38, 114], no undertow current is visualised over the front slope. This current that flows seaward is characteristic of the surf zone and occurs beneath breaking waves, focusing near the seabed. Because in the present research, the slope is not extended over the water surface and no wave breaking conditions are present, an undertow current is not generated.

The Q -criterion is implemented to visualise the formation of eddies over the structure [115] [116]. This method utilises a scalar quantity derived from the velocity gradient tensor to distinguish between rotational motion and shear, helping to identify vortices in a fluid flow. Figure 4.10 to figure 4.13 present 2D slices of the centre of the wave tank coloured by the Q -criterion, of the instance when higher values of Q are reached. These results have cyclical behaviour wave by wave. In addition, 3D views where an Iso-surface of Q -criterion at $Q = 7$ coloured by the Y -vorticity are presented. In Figure 4.10, eddies generated over the nose of the structure are visualised, figure 4.10a and figure 4.10b present the instance under the trough of the waves, at this moment a negative (anticlockwise) rotation is detected. In figure 4.10c and figure 4.10d, an instance when the wave crest is passing over the structure is presented; in this case, a similar eddy is observed but with a positive (clockwise) rotation. In both conditions, the eddy generated is extended in the total width of the domain. Areas of positive Q are also appreciated upstream the nose in both instances, see figure 4.10d, but not strong enough to be detected with an Iso-surface of $Q = 7$. Similar turbulent behaviour is appreciated in the concave case, figure 4.11, where a main eddy appears over the nose of the structure, with a negative and positive rotation according to the trough and crest of the wave. However, the eddies are larger for the same Q -criterion, $Q = 7$, figure 4.11b and figure 4.11d, compared to the linear case. In figure 4.11d, a slim eddy is generated upstream of the structure's nose. The results for the cubic case are presented in figure 4.12; in this geometry, less energetic eddies are visualised, especially under the trough

where no eddies are detected with $Q = 7$, figure 4.12b. Four spots of positive Q are visualised instead of one main hot spot detected in the linear and concave cases. Under the crest, two eddies are observed with a $Q = 7$; however, both are significantly smaller than the ones visualised in the linear and concave cases. The convex case, figure 4.13, yield similar results to the cubic case; however, in this case, more eddies are generated over the surface of the curved slope, and in both instances, under trough and crest, the Iso-surface $Q = 7$ can detect vortices. A clear main eddy is visualised in figure 4.13c and figure 4.13d. In all simulations, eddies are generated only under the trough and crest of the waves. The two cases that generated the larger eddies, linear and concave cases, are the ones that present the slower and smaller increment of the wave height according to figure 4.4 and table 4.2. In the cubic and convex cases, more than one eddy is detected, but they are smaller and less energetic, which can explain the better energy conservation and distribution detected from the analysis of figures figure 4.4 and figure 4.5.



(a) Velocity field on front-slope/berm transition, concave case. Contour horizontal velocity, u .



(b) Velocity field on front-slope/berm transition, convex case. Contour horizontal velocity, u .

Figure 4.9: Velocity fields on front-slope/berm transition for concave and convex case. ($x/z = 1/1.6$).

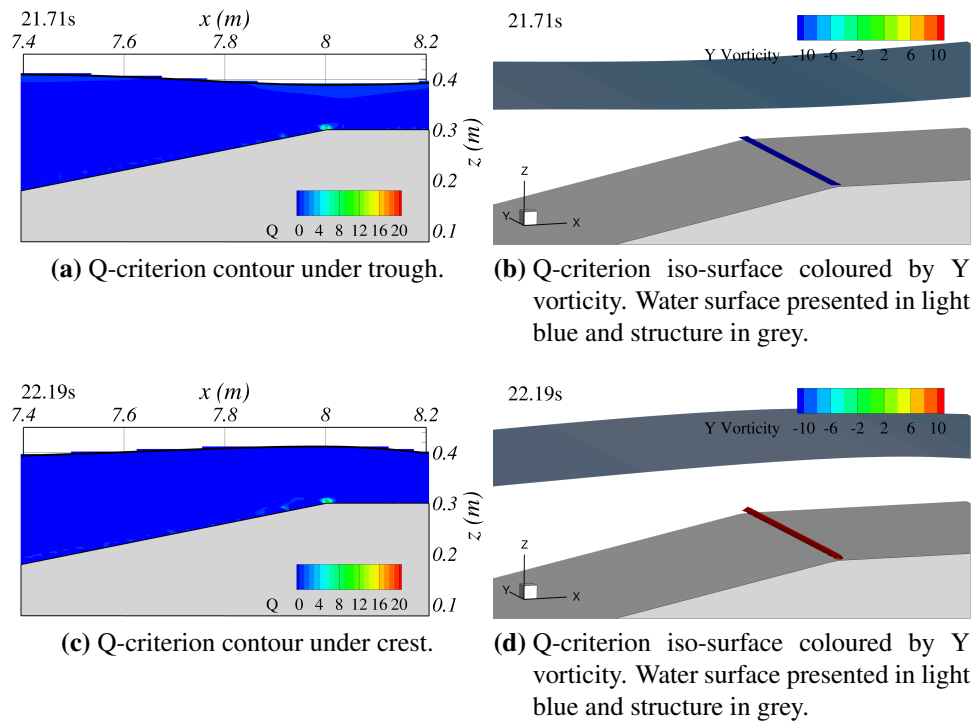


Figure 4.10: Q-criterion and Y-Vorticity for the linear case.

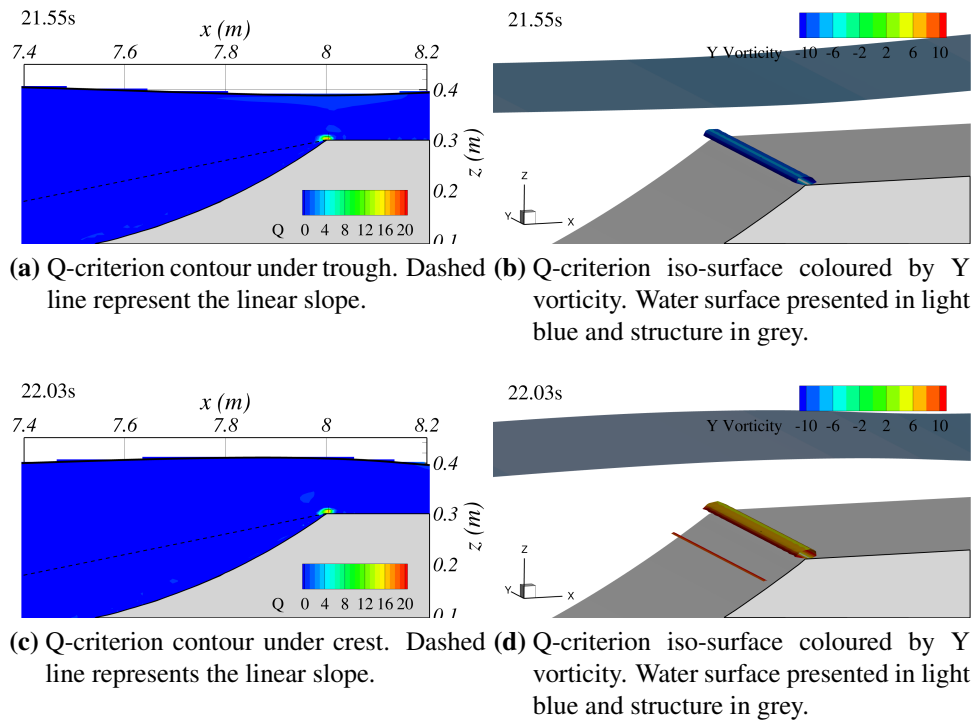


Figure 4.11: Q-criterion and Y-Vorticity for concave case.

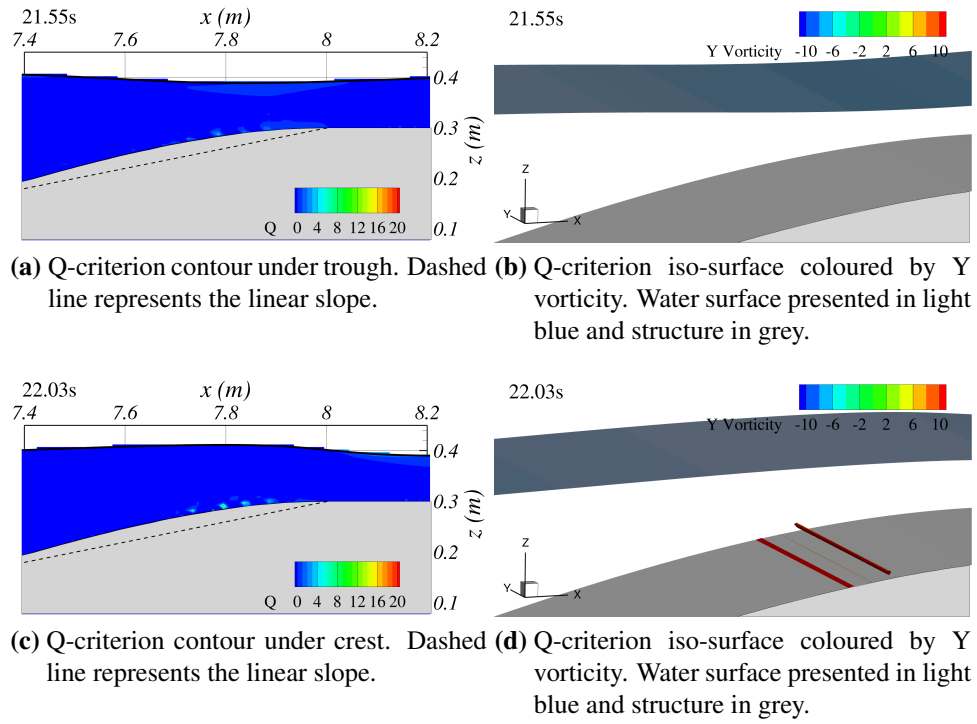


Figure 4.12: Q-criterion and Y-Vorticity for cubic case.

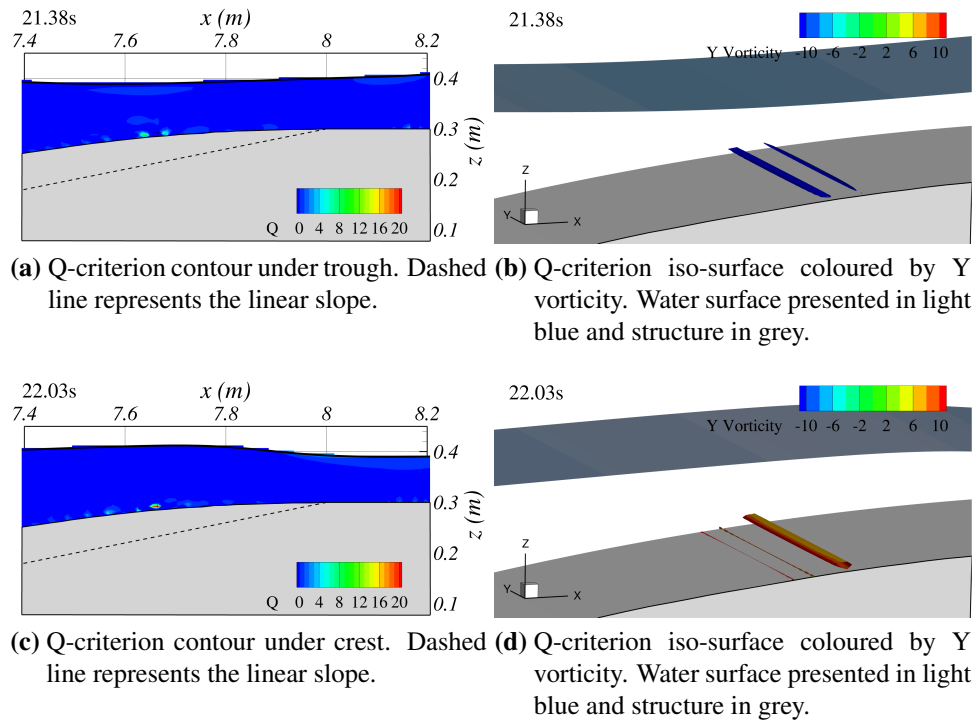


Figure 4.13: Q-criterion and Y-Vorticity for convex case.

4.3.2 Forces results

This section analyses the forces, f , acting against the structure for each geometry studied. The instantaneous force normal to the structure's surface is represented by f , and is calculated using the hydrodynamic pressure simulated by hydro3D-NWT (P) near the water-structure interface over the width of the solid body, equation 4.1. To identify if the geometry variation of the front slope affects the structure's stability, the total forces, F , are calculated for the whole structure and for each section of the body, front slope, berm, and rear slope. The total forces are decomposed in the horizontal F_x and vertical F_z components by integrating $f(x, z)$ over the surface of the solid, equations 4.2 and 4.3. To better appreciate the pure effect of the water surface fluctuation, a dynamic force, f_D is calculated by deducting the still water level hydrostatic force from f , equation 4.4.

$$f(x, z) = \int_0^W P(x, y, z) \hat{n}(x, z) dy \quad (4.1)$$

$$F_x = \int_{x_1}^{x_2} \int_{z_1}^{z_2} f(x, z) \hat{n}_x(x, z) dz dx \quad (4.2)$$

$$F_z = \int_{x_1}^{x_2} \int_{z_1}^{z_2} f(x, z) \hat{n}_z(x, z) dz dx \quad (4.3)$$

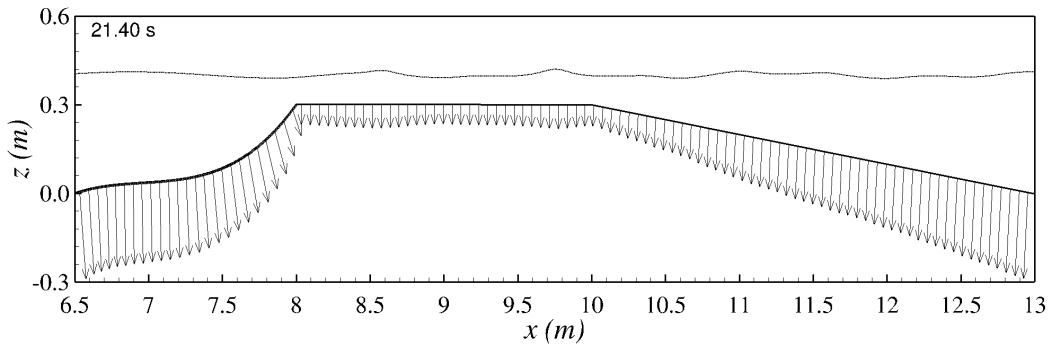
$$f_D(x, z) = f(x, z) - \int_0^W P_h(x, y, z) \hat{n}(x, z) dy \quad (4.4)$$

$$P_h(x, y, z) = \rho g d(x) \quad (4.5)$$

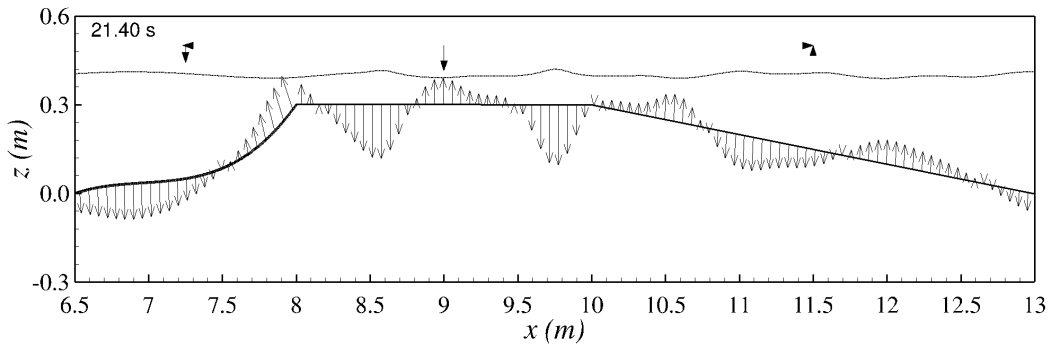
$P(x, y, z)$ is the total pressure simulated by Hydro3D at the surface of the structure, $\hat{n}(x, z)$ unitary normal vector at the surface of the structure, P_h hydro-static pressure at the surface of the structure and calculated in water still level condition, W the domain width, and $d(x)$ still water depth calculated as $d - z(x)$. F_x and F_z are the resultant forces in x and z directions respectively, calculated in the section of interest (front slope, nose, berm or rear slope), $\hat{n}_x(x, z)$ and $\hat{n}_z(x, z)$ are the components

in x and z directions respectively of $\hat{n}(x, z)$.

Figure 4.14a shows the normal forces, $f(x, z)$, acting on the structure in the concave case at $t=21.4$ s. It shows that the forces increase under the wave's crest and decrease under the wave's trough. No upward forces are recorded in all simulations. In Figure 4.14b, the spanwise dynamic forces, $f_D(x, z)$, are presented. The resultant dynamic forces, calculated according to equations 4.2 and 4.3 but integrating f_D over the surface instead of f , for the front slope, berm, and rear slope are shown in filled arrows above each section. The dynamic forces only account for the variation related to the water surface fluctuation in relation to the still water level and the particle velocities. As noticed before, the forces increase under the wave's crest, and an upward force variation is generated under the trough.



(a) Water surface and total forces acting on the structure at $t=20.4$ s, concave case.



(b) Water surface and dynamic forces acting on the structure at $t=20.4$ s, concave case.

Figure 4.14: Water surface and total and dynamic forces acting on the concave case, at $t=20.40$ s. Scale $x/z = 1/2$.

Figure 4.15 plots the fluctuations of the resultant horizontal (left panel) and vertical forces (right panel) (F_x and F_z) over two wave periods acting on the com-

plete structure. Table 4.4 presents the resultant maximum average forces and the amplitudes and ratios of the force fluctuations, considering the complete structure and specific sections. As expected, the horizontal and vertical forces follow the wave's behaviour in a periodic motion defined by the wave period. A time shift is observed only in the horizontal forces, causing the maximum and minimum forces to occur at different moments. This means that the peak horizontal forces in each case occur when the waves are over different parts of the structure. In the convex shape, the maximum horizontal forces occur when the wave crest is passing over the steepest section of the front slope, in this case, located in the first half of the slope, whereas in the concave case, it is in the second half of the slope. From figure 4.15 and table 4.4, it is observed that the maximum horizontal forces increase in all cases compared to the linear slope. The concave shape generates the smallest increment in the maximum horizontal force with a factor $R_{F_x} = 1.05$, while significant increments with factors of $R_{F_x} = 1.48$ and $R_{F_x} = 1.55$ are generated by the convex and cubic geometries, respectively. The vertical forces do not experience a significant change between the linear and cubic cases. However, an increase in magnitude by an average factor of $R_{F_z} = 1.08$, is generated with the concave geometry (table 4.4). A reduction of $R_{F_x} = 0.94$ is calculated for the convex case. These differences are mainly related to the volume of water over the structure, which is larger in the concave shape and smaller in the convex case.

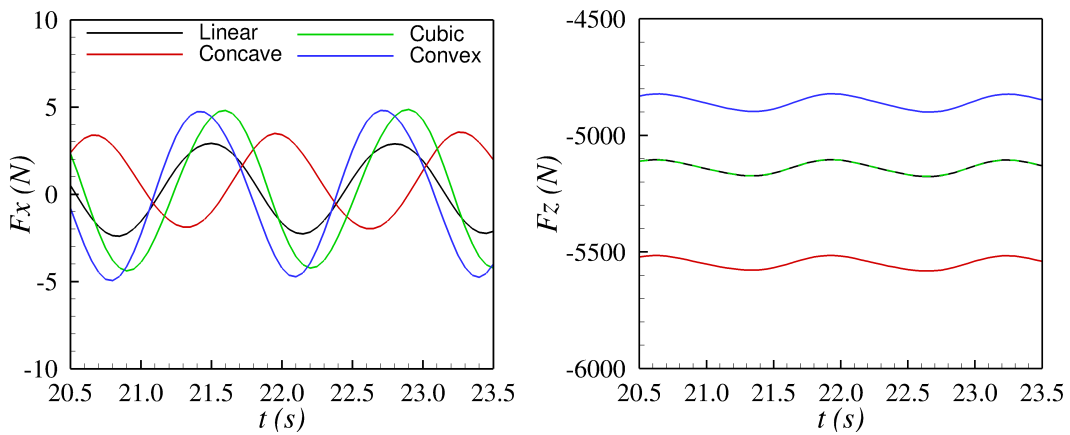


Figure 4.15: Resultant force variations for the complete structure over two wave periods. Left: resultant horizontal force F_x , Right: resultant vertical force F_z .

Table 4.4: Resultant maximum average forces (F_{xmax} and F_{zmax}), amplitude of force fluctuations (Fa_x and Fa_z) and ratios compared to linear case ($R_{Fx} = F_{xmax}/Fl_{xmax}$, $R_{Fz} = F_{zmax}/Fl_{zmax}$, $R_{ax} = Fa_x/Fal_x$ and $R_{az} = Fa_z/Fal_z$) for the complete structure, front slope, nose, and each case.

Case	F_{xmax} (N)	F_{zmax} (N)	R_{Fx}	Fa_x	R_{ax}	R_{Fz}	Fa_z	R_{az}
<i>Full structure</i>								
Linear	3.75	-5102.85	1.00	6.20	1.00	1.00	74.83	1.00
Concave	3.93	-5513.22	1.05	6.31	1.02	1.08	70.95	0.95
Cubic	5.80	-5102.12	1.55	10.28	1.66	1.00	75.42	1.01
Convex	5.56	-4820.10	1.48	10.52	1.69	0.94	80.36	1.07
<i>Front Slope</i>								
Linear	294.91	-1447.36	1.00	5.44	1.00	1.00	27.18	1.00
Concave	295.19	-1852.60	1.00	6.52	1.20	1.28	33.33	1.23
Cubic	296.60	-1448.18	1.01	8.93	1.64	1.00	25.21	0.93
Convex	297.45	-1167.07	1.01	11.00	2.02	0.81	26.06	0.96
<i>Nose</i>								
Linear	35.87	-287.33	1.00	3.87	1.00	1.00	33.29	1.00
Concave	124.69	-368.66	3.48	8.74	2.26	1.28	29.06	0.87
Cubic	18.13	-261.15	0.51	2.25	0.58	0.91	33.41	1.00
Convex	6.40	-248.24	0.18	0.99	0.26	0.86	37.05	1.11

From figure 4.15, it can be seen that together with the increment of the magnitude of the maximum horizontal force Fx , the amplitude of the force fluctuation is likewise affected. Figure 4.16 presents the ratio in the amplitude of the force's fluctuation (R_{ax} and R_{az} in table 4.4) for each case. The amplitudes are calculated as the maximum force minus the minimum force for each wave period, and then average in the 10 waves considered in the analysis. When the complete structure is considered, the fluctuation of the horizontal force has almost no change in the concave case, whereas in the cubic and convex cases, the horizontal force increases by a factor of 1.66 and 1.69, respectively. The amplitude of the fluctuations on the vertical forces experiences minor changes compared to the horizontal forces. The fluctuations decrease by 0.95 in the concave shape, a slight increment of 1.01 in the cubic geometry, and grow by 1.07 in the convex case. In the right panel of figure 4.16, the resultant forces acting only on the front slope are presented. In all cases, the horizontal fluctuations increase in amplitude, almost double that of the

linear fluctuations in the convex geometry. The vertical forces experience minor changes, with an increase by a factor of 1.23 in the concave case and reductions by a factor 0.93 and 0.96 for the cubic and convex cases, respectively. These results indicate that changes in the front slope geometry impact the load cycle of the structure, particularly in the front section.

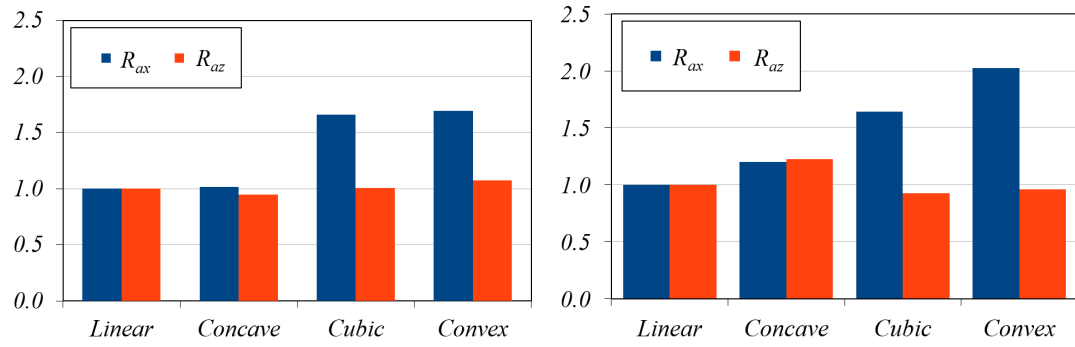


Figure 4.16: Ratio of the force variation's amplitude concerning the linear case (Blue R_{ax} , red R_{az}). Left: complete structure, Right: front slope.

To analyse the changes generated on the nose of the structure, the forces applied on a section of 0.68 m long, centred at $x = 8.0$ m is considered, as shown in figure 4.17. This section is selected because it allows to capture the maximum and minimum vertical forces as shown in the right plot at figure 4.17.

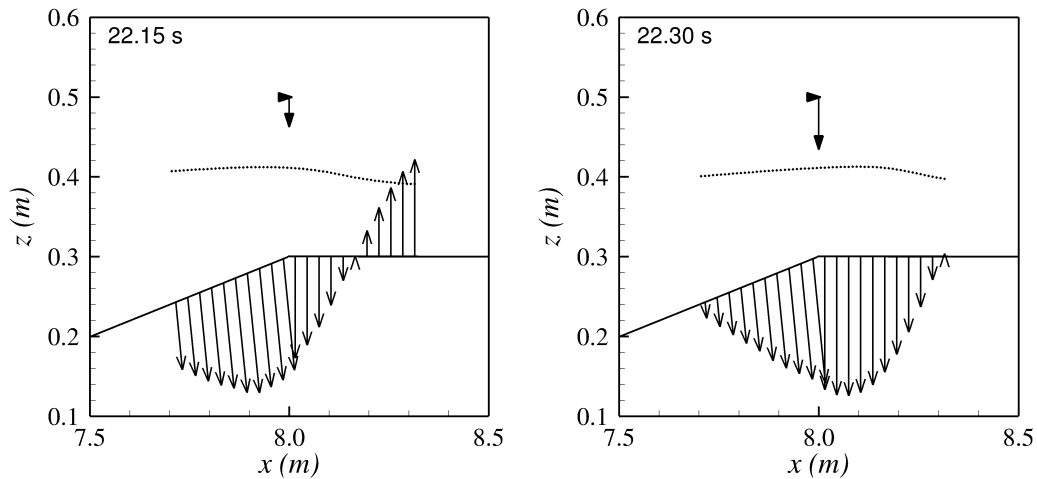


Figure 4.17: Instance of maximum horizontal force at the nose (left) and maximum vertical force at the nose (right) for the linear case.

Figure 4.18 shows the ratio of the variation of the resultant horizontal (left

panel) and vertical (right panel) forces applied in the vicinity of the nose, as shown in figure 4.17. The vertical force increases by 1.28 in the concave geometry, compared to the linear case, and decreases in the cubic and convex cases by a factor of 0.91 and 0.86, respectively, see table 4.4. The changes in the horizontal forces are more significant, in which the concave shape generates an increment by a factor of 3.48 compared to the horizontal forces in the linear case. On the other hand, the cubic and convex reduce the magnitude of the horizontal forces by a factor of 0.51 and 0.18, respectively. The variation in the geometry significantly alters the fluctuation of the horizontal forces. It can be seen in table 4.4 and figure 4.18 that the horizontal fluctuations in the concave case are more than double the results for the linear slope, and as in the forces, the cubic and convex reduce the fluctuations by factors of 0.58 and 0.26, respectively. All these variations are generated mainly due to the steepness of the slope near the berm. A steeper slope allows the generation of greater horizontal forces, which is the case in the concave case (gradient of 0.7). The cubic and convex shape geometries were set to have a zero gradient when reaching the berm; therefore, almost all the pressure over the structure is transformed into vertical forces.

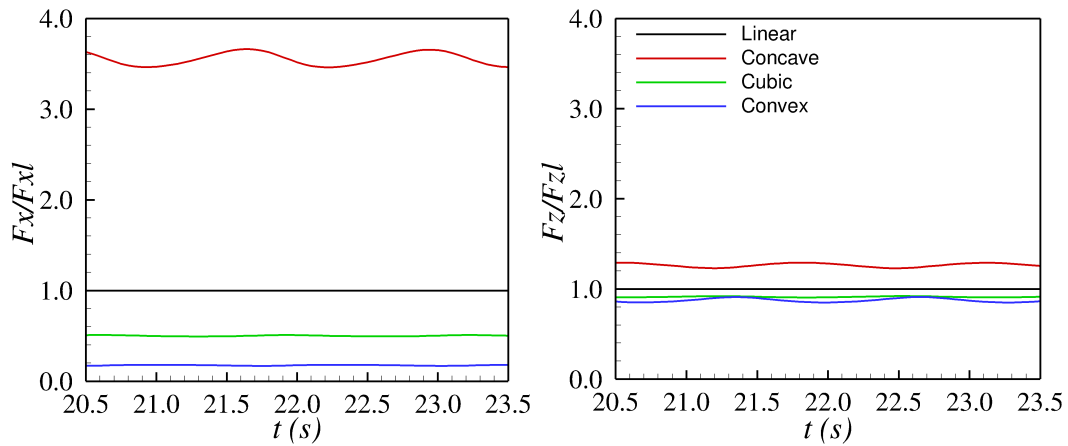


Figure 4.18: Variation of resultant forces at the nose of the structure normalized by the the linear case for two wave periods. Left: horizontal forces F_x , Right: vertical forces F_z .

Figure 4.19c presents the moment in the y axis (M_y), calculated for the front slope and considering the pivot point O , as shown in figure 4.19a. Figure 4.19a and

figure 4.19b present the location of the water surface and force diagram acting on the front slope for the convex case at the instance of maximum and minimum M_y , indicated by vertical lines in figure 4.19c. The averaged values of the maximum and minimum moment ($M_{y\max}$, $M_{y\min}$), the average range of fluctuation and ratio compared to the linear case are given in table 4.5. It is appreciated that M_y fluctuates with the wave period and no significant time shift occurred between cases. The cubic case presents little variation compared to the linear case; less than a 3% reduction is calculated in table 4.5 in all the parameter studies. The concave geometry increases the maximum M_y by a 1.12 factor. On the other hand, the convex case experiences a reduction of the $M_{y\max}$ by a factor of 0.90. In all cases, the maximum positive M_y occurred when the wave crest passed over the last section of the front slope, near the structure's nose, figure 4.19a. The negative M_y peaks are generated when the wave crest passes over the front slope's first half, as shown in figure 4.19b.

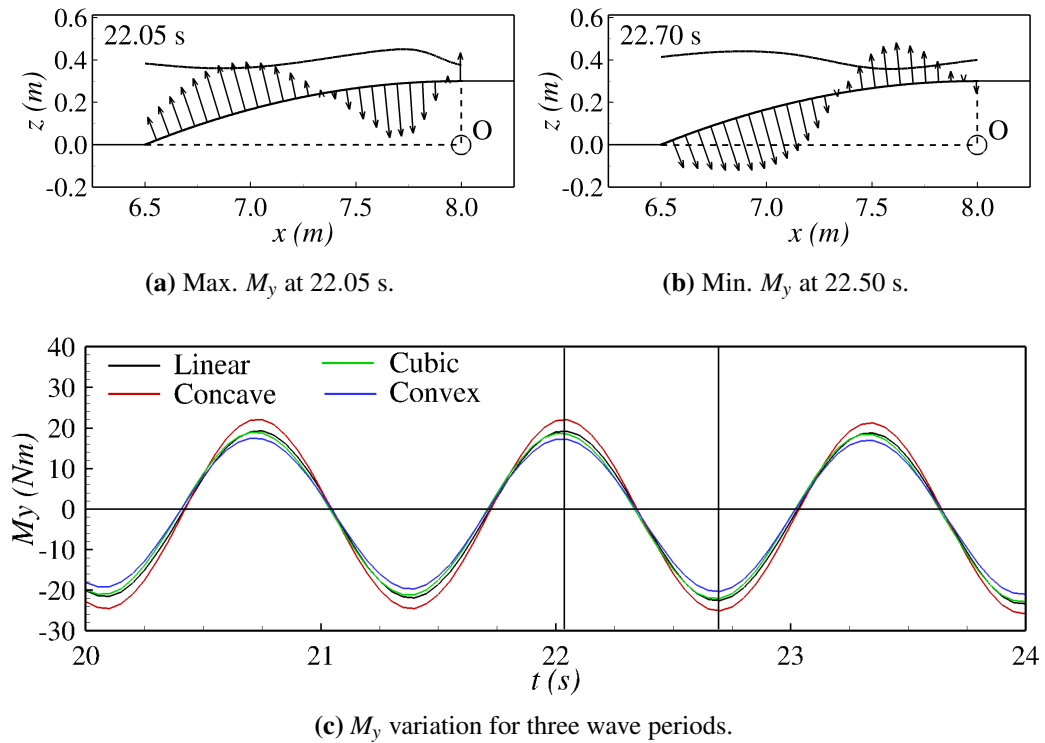


Figure 4.19: Water surface and forces diagram for concave case, and M_y for three wave periods.

Figure 4.20 present M_y (same that in Figure 4.19c), and the horizontal force,

F_x , for the concave and convex cases, and only for the front slope. The linear and cubic geometries present behaviours similar to those of the convex case. Therefore, they are not included in the figure to avoid overloading the plot. In the convex geometry, M_y and F_x present a time shift, occurring the maximum F_x , when the minimum (negative) M_y occurs. This time shift explains the reduction of the M_y in the convex case. A positive value of F_x generates a positive moment around "O", which reduces the negative peaks of M_y . On the other hand, a negative value of F_x generates a negative moment, which produces a reduction of the maximum M_y . In the concave case, the moment generated by the horizontal forces agrees in direction with M_y , producing an increment of the M_y 's peaks. The present analysis indicates that the convex geometry contributes to a greater M_y stability than the rest of the cases; conversely, the concave case is the least stable.

Table 4.5: Average maximum y moment M_{ymax} in Nm, average minimum y moment M_{ymin} in Nm, Average M_y range Ra_{My} in Nm, ratios respect to Linear case R_{Mymax} , R_{Mymin} and R_{RaMy} .

Case	M_{ymax}	R_{Mymax}	M_{ymin}	R_{Mymin}	Ra_{My}	R_{RaMy}
Linear	18.88	1.00	-23.20	1.00	42.08	1.000
Concave	21.60	1.14	-25.60	1.10	47.20	1.12
Cubic	18.39	0.97	-22.62	0.98	41.01	0.97
Convex	16.90	0.89	-20.96	0.90	37.86	0.90

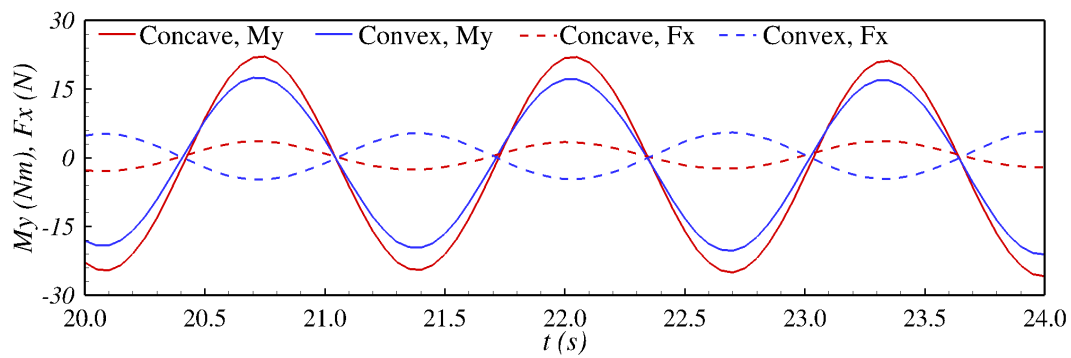


Figure 4.20: M_y and F_x applied in front slope for three wave periods and concave and convex cases.

In the present study, three different geometries of the front slope, concave, cubic, and convex, have been added to the linear reference case used in [25], and

their effects on the evolution of the waves over the bar and forces on the structure have been analysed.

The four cases studied generate different wave envelopes and different peaks of wave height, with the convex and the cubic shapes as the ones that generate the greatest waves over the berm of the structure. On the contrary, the concave shape decreases the wave height compared to the linear case. The forces acting on the structure have also been studied. Significant variations of the horizontal forces have been found, especially in specific sections of the structure, like the nose. Moreover, the range of the force fluctuation is affected by the different geometries, increasing the loading and unloading cycle of the structures. The moment stability was also studied, detecting that the most stable geometry studied is the convex, followed by the cubic, linear, and concave shape.

In the next chapter, Hydro3D-NWT is used to simulate the interaction of waves and slope structures that pierce the surface of the water, allowing to study what happened over the run-up ramp of an OWEC. These cases include complex hydrodynamic processes such as wave breaking, wave run-up, and wave overtopping, which contribute to the energy dissipation in the operation of an OWEC.

4.4 Conclusions

The LES numerical code, Hydro3D-NWT, has been used to simulate the interaction between regular waves and a submerged trapezoidal structure. Hydro3D-NWT have proven to: (i) accurately generate waves according to the 2nd order Stokes Waves; (ii) reproduce accurate water surface fluctuations due to the wave-structure interaction similar to the previously conducted experimental study presented in [25].

The experiments from [25] are expanded by modifying the front slope's geometry to concave, cubic, and convex shapes. It is found, for the wave condition studied, that these changes affect the water surface fluctuations over the structure, the maximum wave height reached over the berm, and the location where that maximum wave height occurs. The cubic and convex geometries generated the highest waves at the end of the front slope and over the horizontal berm. The results show

that the concave produced the smallest waves.

The generation of eddies over the structure is also analysed. It is found that eddies occurred over the structure's front slope and under the wave's crest and trough. Under the crest, eddies rotate clockwise; in contrast, under the trough, they rotate anticlockwise. In the linear and concave cases, a main eddy is formed at the nose of the structure. A larger eddy is appreciated in the concave case. In the cubic and convex geometries, small eddies are formed over the top section of the front slope. However, these are less strong than the ones detected in the linear and concave cases. The differences detected in the turbulence near the structure further help to explain the different wave heights reached over the structure. More significant energy dissipation is expected to occur in the linear and concave cases compared to the cubic and convex due to the size of visualised vortices.

In the present study, a single wave period is used to analyse the effects of different front slope geometries on wave transformation and the forces applied on the structure. It is expected that waves with different periods will respond differently to changes in the structure. The findings indicate that higher harmonics undergo more significant changes as waves travel over the structure. As water depth decreases, the amplitude of higher harmonics increases noticeably, while the lower frequency components experience only minor changes. This suggests that higher harmonics are more sensitive to depth variations than lower frequency components. Consequently, shorter waves are expected to be more sensitive than longer waves to changes in front slope geometry.

Different geometries can affect the shoaling process and produce different wave heights at the same water depth. This phenomenon can be used depending on the structure's purpose. For instance, in the case of coastal defence, a higher level of wave dissipation will be wanted, so a slope with a concave shape would give better results. On the other hand, if a lower level of wave dissipation is required, a cubic or convex shape is a better option. This could be the case with coastal defence and wave energy converters integration.

It is found that the geometry of the front slope affects the resultant forces acting

over the structure. The forces in specific locations of the structure can be significantly affected by changes in the geometry. For instance, in the structure's nose, the horizontal forces increased by 3.48 with the concave shape and decreased by 0.18 with the convex slope. The forces fluctuate with the same period of the waves, and the amplitude of that variation is also affected by the front slope's geometry. The Y moment applied on the front slope is affected by the different geometries, modifying the peak values of M_y . In the convex case, time misalignment between M_y and F_x leads to a reduction of the extreme values of M_y by a factor of 0.9. On the other hand, M_y is amplified by F_x in the concave case by a 1.12 factor. These changes affect the stability of the submerged structure and reduce or increase the risk of damage from the action of waves; therefore, selecting the appropriate geometry can extend the life of a structure.

The validation and analysis conducted in the present chapter reinforce the use of LES as an accurate tool for simulating wave-structure interactions. Such numerical methods expand existing physical studies, allowing researchers to investigate new conditions and measure parameters in detail that would be much difficult to do in physical flumes.

Chapter 5

Study of Waves and Sloped Structure

5.1 Introduction

Wave energy (WE), with worldwide wave power resources estimated at 2 TW [8], is a promising renewable energy source. Studies and projects [15], [16], have confirmed that it is possible to harvest energy from waves and can contribute electricity to national grids, thereby diversifying the energy mix. However, the WE industry has not grown at the speed expected from a source with such potential. The challenges involved in adapting new technology to the harsh and corrosive environment, its exposure to extreme conditions, and the remoteness of the operation make any enterprise in this field a high-risk investment.

Wave energy converters can be classified as off-shore, nearshore and on-shore devices. Like the Pelamis Wave Power device [16], off-shore WE converters are exposed to the highest wave energy density; however, they must endure extreme conditions in remote areas, making their study and deployment a high-risk project. On-shore devices like OWC and OWECs [16], are technologies that can be installed in existing breakwaters, a factor that favours their construction and maintenance and reduces their cost and risk. However, the harnessable wave energy near the shore is significantly less than at off-shore locations, but high-efficiency devices can overcome the lower energy resource. OWCs have demonstrated their potential with the WE plant in operation in the port of Mutriku since 2011 [31]. This plant has contributed more than 2,8 GWh to the Spanish electricity Grid since its

commissioning, according to The Basque Energy Agency EVE. OWECs are some steps behind OWC in their development. In 2015, a full-scale OWEC prototype, OBREC (overtopping breakwater wave energy converter), was built in the port of Naples' breakwater [32] to study the real potential of this type of WEC. One of the most significant advantages of an OWEC is its structural simplicity; it comprises a ramp, a reservoir, a fully submerged turbine, and power electronics, and no moving parts (besides the turbine) are included. The performance of an OWEC depends on its ability to capture wave overtopping, thereby generating enough level difference to produce energy through the turbine when the water is returned to the sea. The efficiency of an OWEC device is related to transforming the total wave energy into pure potential energy. A large scatter of the estimated hydraulic efficiency of OWECs is found in the literature, with values ranging from 3% to nearly 30% [33], [16]. However, most of these estimates are derived from small-scale models, of which very few have been turned into full-scale prototypes.

Four main stages can be identified when waves interact with the structure of an OWEC: (i) wave breaking as it approaches the overtopping structure, (ii) wave run-up, (iii) overtopping discharge, and (iv) run-down of water that does not reach the crest during stage (ii). Except for the overtopping, all processes occur on the ramp of the structure. The run-down interacts with the incoming wave during the breaking stage. The energy losses during the breaking process are among the most important, and they depend on the wave conditions and geometry of the run-up ramp. Several studies have focused on optimising the OWEC's run-up ramp design. [34] and [24] studied the ramp geometry and found that a convex shape can maximise the overtopping discharge, whilst [34] reported that an elliptical geometry maximises the water volume captured. [18] studied the implementation of converging lateral walls and reported that an appropriate opening angle could improve the overtopping water volume in moderate wave conditions. No information was found in the literature about the direct energy losses related to the interaction between the incoming wave and the run-down flow.

The main objective of the present research is to explore the role of the run-

down flow and to quantify the energy dissipation that occurs on the ramp of an OWEC. The findings of this chapter aim to detect alternatives to improve the efficiency of OWEC and promote the development of the WEC industry.

5.2 Validation

Two processes are validated to demonstrate that Hydro3D-NWT reproduces wave interaction with a sloping structure correctly: wave overtopping and run-up. For the first one, experimental data from [19] are used, and to validate the run-up empirical formulations [47, 6, 7] are used.

5.2.1 Wave overtopping validation

Experimental results from [19] are used in this research to validate the ability of Hydro3D- NWT to simulate wave overtopping discharge. In [19], a two-level OWEC scale model was studied. The experiments were conducted in a wave flume, 30 *m* long and 0.6 *m* wide, at the Ocean University of China. Two openings of the structures at different levels were implemented to simulate a two-level OWEC. The overtopping discharge in each reservoir was measured by pressure gauges installed at the bottom of each reservoir. The effects of the slope's angles and opening of the lower reservoir on the overtopping discharge were quantified. Regular waves were selected to conduct the study, and three still water levels were used to simulate tidal variations. As the present research is focused on one level OWEC, only the cases where no or negligible overtopping discharge was recorded in the upper reservoir are used. The cases with a 30° slope angle are selected for the present study because it is a frequent inclination used in coastal structures [117].

Table 5.1: Cases used to validate overtopping discharge, wave height H_w , wave period (T), wavelength L_w , water depth in still water level d , structure freeboard R_c and slope angle α

Case	H_w (m)	T (s)	L_w (m)	d (m)	R_c (m)	α °
$ Ov_1$	0.050	1.0	1.373	0.3	0.05	30
$ Ov_2$	0.075	0.8	0.960	0.3	0.05	30
$ Ov_3$	0.075	1.0	1.373	0.3	0.05	30
$ Ov_4$	0.075	1.2	1.770	0.3	0.05	30
$ Ov_5$	0.075	1.4	2.154	0.3	0.05	30

Figure 5.1 presents a 3D sketch and longitudinal view of the simulation set-up of Hydro3D-NWT. As this research aims to simulate the capture of the lower reservoir used in [19], only the lower slope is included in the simulation. The waves are prescribed at the inlet boundary using 2nd order Stokes Waves theory. A no-slip condition is employed at the far end and bottom of the numerical wave tank. The lateral boundaries are treated with a periodic boundary condition, and a slip boundary is used at the top of the domain. The distance from the inlet to the structure is $2L_w$, considering the longest wave condition used, case OV_5 . The first wavelength in the domain is used to input the wave parameters and to absorb the reflection generated by the structure. A 1.0 m. long relaxation zone is implemented in the east boundary to reduce the flow complexity after overtopping. To determine the spatial resolution required for accurate simulation results, three uniform grids are tested; these are detailed in table 5.2.

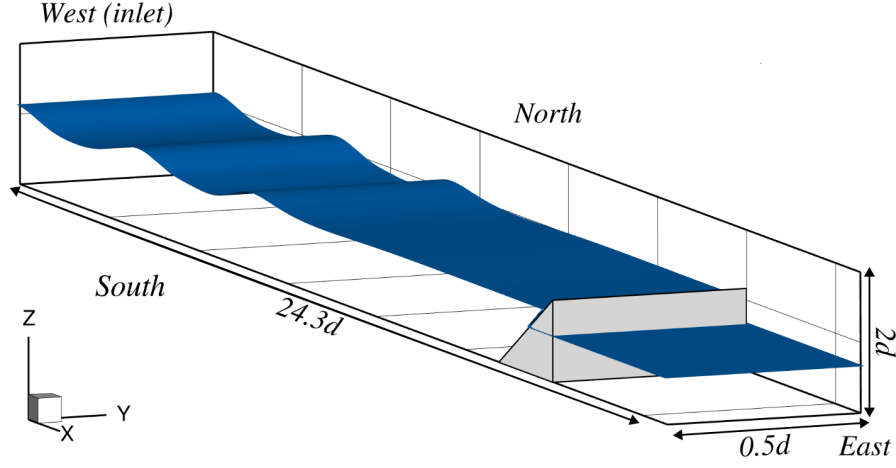
The instantaneous overtopping discharge, f_{ov} , is measured on the crest of the structure, according to equation (5.1) and figure 5.2 and is calculated by a one-metre width of the structure; its unit is m³/s/m.

$$f_{ov} = \frac{\sum u_i A_{cell}}{L_y} \quad (5.1)$$

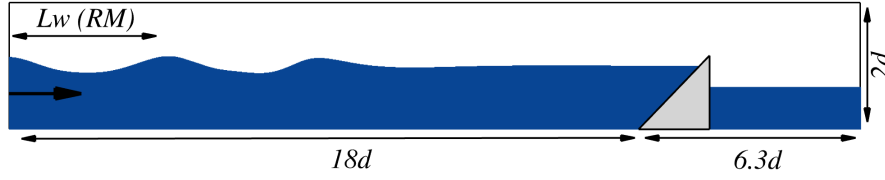
with u_i the instantaneous horizontal velocities simulated by Hydro3D-NWT in the centre of each cell, A_{cell} is the cell's cross-section perpendicular to the flow and L_y the width of the domain.

Table 5.2: Grids resolution.

Name	dx (m)	dy (m)	dz (m)
<i>Grid1</i>	0.008750	0.010	0.005000
<i>Grid2</i>	0.004375	0.010	0.003125
<i>Grid3</i>	0.035000	0.005	0.002500



(a) 3D view domain for Overtopping validations.



(b) Lateral view of domain for Overtopping validations.

Figure 5.1: 3D and lateral view of domain

In [19], a dimensionless overtopping discharge Q is used to evaluate the wave overtopping discharge. Q is calculated as the total volume, V_{ov} that overtops the structure, considering the first 15 overtopping events, over the total time t_{ov} , normalized by $H_w \sqrt{gH_w}$.

$$Q = \frac{V_{ov}}{t_{ov}} \frac{1}{H_w \sqrt{gH_w}} \quad (5.2)$$

with

$$V_{ov} = \int_0^{t_{ov}} f_{ov} dt \quad (5.3)$$

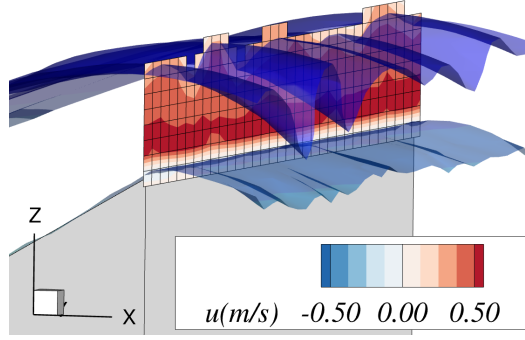


Figure 5.2: Section where the overtopping flow is calculated and coloured by the horizontal velocity u_i . The blue iso-surfaces represent the upper and lower boundaries of the water surface in the overtopping flow.

Case OV_3 is selected to evaluate the influence of the grid resolution on the simulation results. This case is selected because it represents an intermediate wave condition within the range of scenarios considered in this study. table 5.3 and figure 5.3 present Q for each grid resolution evaluated and the experimental result from [19]. The numerical error E is calculated according to ???. The results indicate a significant improvement with increasing the grid resolution. The error decreases from $-30,9\%$ for *Grid1*, to -23.6% for *Grid2* and to -3.2% for *Grid3*. The numerical simulation underestimates the overtopping discharge, however, a satisfactory result is obtained with *Grid*.

Table 5.3: Dimensionless overtopping discharge Q results and error E compared to experimental data.

	Q (m)	E (m)
<i>Experimental</i>	0.0629	—
<i>Grid1</i>	0.0434	-30.9%
<i>Grid2</i>	0.0480	-23.6%
<i>Grid3</i>	0.0609	-3.2%

$$E = \frac{(Q_{Grid} - Q_{Exp})}{Q_{Exp}} 100 \quad (5.4)$$

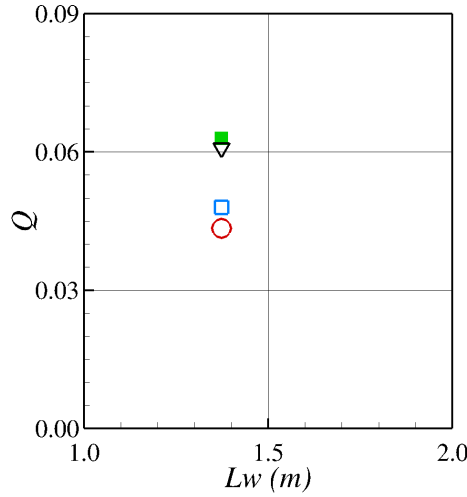


Figure 5.3: Overtopping dimensionless discharge Q for case OV_3 . Green squares experimental data from [19], Hydro3D-NWT results: red circle *Grid1*, blue square *Grid2* and black triangles *Grid1*.

Figure 5.4 shows 3d views of the run-up phase for each grid evaluated, the water surfaces are coloured by the elevation z . In these images, two main regions of the water surface can be identified. The first is the upper water surface, which includes the top layer of the flow and the wave front. The second is the lower water surface, which is the interface that is in direct contact with the slope, and in this case, interacts directly with the Lagrangian points used in the IBM to create the structure. It is possible to observe that *Grid1* and *Grid2* produce "toothed" type alike wave fronts with sharp features following the grid resolution. Meanwhile, with *Grid3*, that type of feature is not generated, and the front of the flow looks more realistic with softer curvatures and a thinner flow. In addition, in the case of the two coarser grids, the interface between the water surface and the slope is not well captured. This results in detachment of the lower water surface from the slope, which adversely affects the accuracy of the flow representation during wave run-up and rundown. With the *Grid3*, the lower water surface is maintained flat against the slope's surface. This problem arises because the density of the Lagrangian points, used in the IBM, is unable to accurately represent the impermeable surface of the slope with the coarser grids. As a result, an ascending airflow is generated from the region below the slope. This problem is solved by increasing the grid resolution,

which is done with *Grid3*. Another option to solve this issue would be to fill the entire volume of the structure with Lagrangian markers, but this solution will have a significant computational cost. These results indicate that *Grid1* and *Grid2* are not fine enough to represent the water surface's morphology in a realistic manner, and to generate an impermeable structure affecting the characterisation of the particle hydrodynamics near the surface.

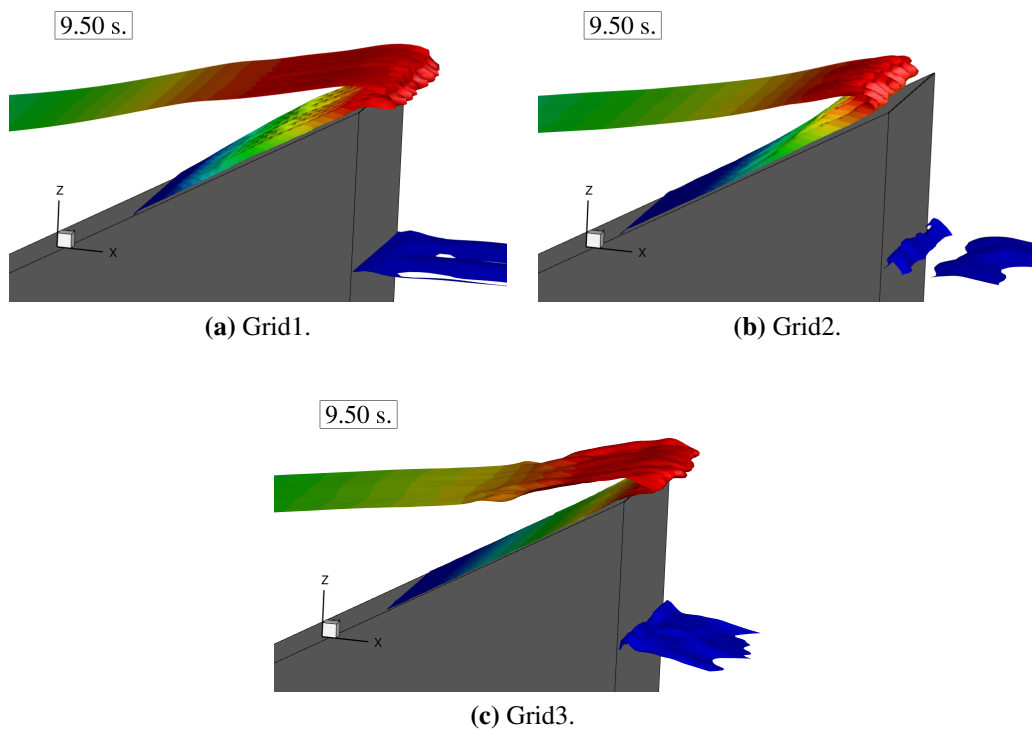


Figure 5.4: Water surface during run-up flow for 3 Grid resolution. Water surface coloured by elevation. Dark grey represents the structure.

From the grid sensitivity analysis, it is concluded that *Grid3* is able to capture the curvature of the water surface, producing realistic results. Additionally, *Grid3* yields satisfactory agreement of the overtopping discharge compared to the experimental results. Therefore, *Grid3* is selected to conduct the rest of this study. A coarser grid compromises the no-slip condition of the structure, and a finer grid considerably increases the computational costs for each simulation.

Figure 5.5 presents four snapshots that exemplify the process when waves break and overtop the structure, here for the case $H_w = 0.05$ m and $T = 1.0$ s. Hydro3D-NWT's results are presented in solid blue, and the water surface extracted from the laboratory results from [19] and presented as snapshots in [20] as black dashed lines. These snapshots capture the entire structure, enabling accurate scaling of the water surface for a proper representation of the wave profile and comparison with the Hydro3D-NWT results. Four stages are presented in the figures: first ($T/4$) the wave approaching and collapsing upstream of the structure, second ($T/2$) the run-up flow, third ($3T/4$) the overtopping and finally T the run-down flow. At ($T/4$), the front of the wave has a convex shape due to the lower water particles being slowed down by interacting with the surface. In Hydro3D-NWT, part of the run-down flow generated by the previous wave is still present, whereas no water is visible on the slope's surface in the laboratory snapshots. This inaccuracy is perhaps due to the immersed boundary treatment creating a non-smooth surface. In the next instance, ($T/2$), the breaking of the wave is complete, and a full run-up flow is observed. Good agreement between the laboratory and Hydro3D-NWT is found, but a slightly faster flow is observed in the experimental results (rougher surface in the LES). At $3T/4$, the run-up spills over the crest and drops into the rear side of the structure (see insert). This water jet gets separated into sub-fingers, as [20] mentioned. The last snapshot shows the run-down flow, which is found to be faster in the experimental results compared to the simulation results; a difference that explains the water layer in front of the wave at $T/4$. This analysis shows that Hydro3D-NWT reproduces the sequence of approach, breaking and overtopping reasonably well. It agrees with the type of breaking observed in the laboratory and generates an overtopping discharge into the rear of the structure. However, as mentioned, the flow over the slope moves more slowly than in the laboratory, a difference that can be explained by using the IMB to define the structure geometry. A finer grid resolution can reduce these differences at a significant computational cost.

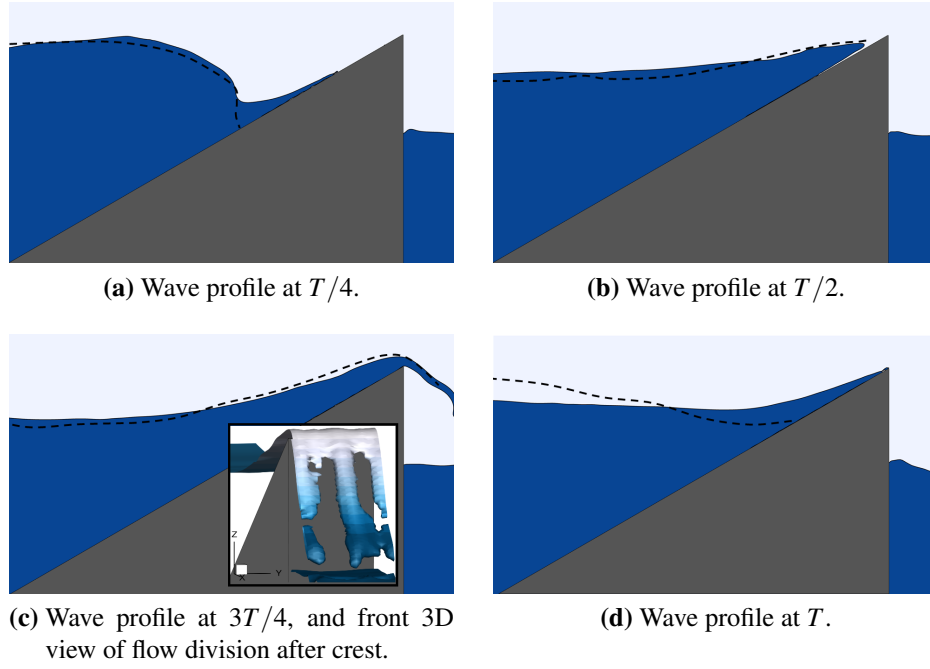


Figure 5.5: Sequence of wave-structure interaction case Ov_1 . Black dashed line from experimental results from [20]. Blue are hydro3D-NWT results, and grey structure.

Figure 5.6 presents the dimensionless overtopping discharge Q for wave height $H_w = 0.075$ m and the four wavelengths tested (cases Ov_2 to Ov_5). The solid green squares are the experimental data from [19], and the results generated by Hydro3D-NWT are presented in black triangles. Hydro3D-NWT reproduces the increasing trend of Q with the wavelength. There is very good agreement of the predicted results with the measurements for the two shorter waves $L_w = 0.96$ m and $L_w = 1.37$ m, with an underestimation of 8.0% and 3.2%, respectively. Hydro3D NWT overestimates the overtopping discharge for the two longer waves. For $L_w = 1.77$ m, Hydro3D-NWT overestimates the experimental results by 17.9%; an error that can be considered acceptable due to the high variability that wave overtopping creates. For the longest wave, $L_w = 2.154$ m Hydro3D-NWT overpredicts the laboratory data by 29%. This overestimation could be related to the occurrence of small turbulent structures in the experimental flow that Hydro3d-NWT is not representing, therefore underestimating the energy dissipation, and consequently overestimating the overtopping at the crest of the slope. This energy underestimation could not

be as important in the other cases, which, with a lower ξ , are more controlled by bigger turbulent structures produced by the plunging behaviour of the wave front.

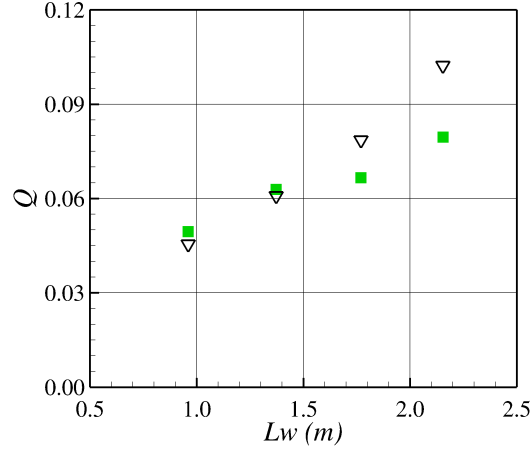


Figure 5.6: Overtopping dimensionless discharge Q . Green squares: experimental data from [19], black triangles Hydro3D-NWT results

5.2.2 Wave run-up validation

Another process of great interest to coastal engineers is the wave run-up, R_u . When the structure's freeboard is high enough to prevent overtopping, the maximum height reached by the run-up flow over the slope is known as R_u , see figure 5.7. R_u is a critical parameter that defines the height of the freeboard of coastal defences.

R_u is affected by the energy dissipation during wave breaking, the wave's velocity and the slope's geometry, roughness and permeability. It has been found that R_u can be estimated with the Iribarren number (or surf similarity parameter) ξ . This parameter is a function of the wave steepness and the slope angle as presented in equation (2.1).

It has been found that R_u increases with an increase of ξ in the range of spilling and plunging breaking types, $\xi < 2.5$, which are commonly referred to as breaking conditions, but when it transitions to collapsing and surging breaking type, $\xi > 2.5$, referred to as non-breaking conditions, R_u reaches a maximum and no longer increases with ξ . This relationship is identified by Hunt in [46] and equations (5.5) and (5.6) are proposed. More recent research has determined that Hunt's formulation tends to overestimate R_u for $\xi > 2.0$, and new equations have been proposed,

such as [47, 6, 7], equations (5.7) to (5.10). An equation that works for breaking and non-breaking conditions is proposed in [47]. In [6] the transition from breaking to non breaking condition is set at $\xi = 2$ and depending on the slope angle, α . A new parameter to define the breaking condition is defined in [7]. The above-introduced equations read:

Hunt, [46]:

$$\frac{R_u}{H_w} = \xi \quad \text{for } \xi < 2.5, \text{ breaking condition} \quad (5.5)$$

$$\frac{R_u}{H_w} = 3 \quad \text{for } \xi > 2.5, \text{ non-breaking condition} \quad (5.6)$$

Schüttrump, [47]:

$$\frac{R_u}{H_w} = 2.25 \tanh\left(\frac{\xi}{2}\right) \quad (5.7)$$

T. W. Hsu, [6]:

$$\frac{R_u}{H_w} = \xi \quad \text{for } \xi \leq 2, \text{ and } \alpha \leq 1/5, \text{ breaking condition} \quad (5.8)$$

$$\frac{R_u}{H_w} = 2 \left(\frac{\xi}{2}\right)^{\frac{0.04}{\tan^2 \alpha}} \quad \text{for } \xi > 2, \text{ and } \alpha > 1/5, \text{ non-breaking condition} \quad (5.9)$$

Arana, [7]:

$$\frac{R_u}{H_w} = 1.25 \left(\frac{d \tan(\alpha)}{\sqrt{H_w L_w}}\right)^{-0.32} \quad \text{for } \tan \alpha / (H_w/d) > 1, \text{ non-breaking condition} \quad (5.10)$$

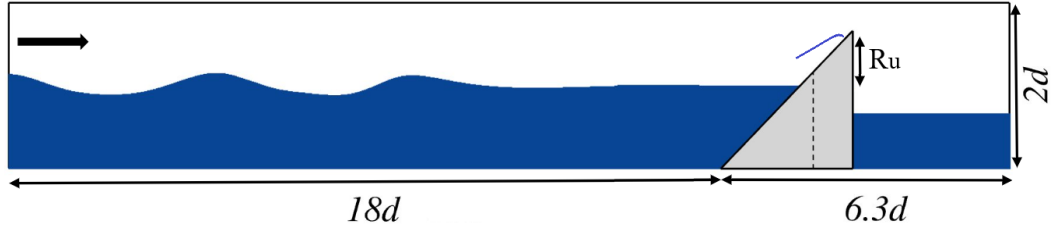


Figure 5.7: Longitudinal view run-up simulations. In dashed line limit of structure used in overtopping simulations $R_c = 0.05$ m.

In the following analysis, Hydro3d-NWT's run-up predictions are compared against the latter three equations to review if the results generated by the code are in accordance with these parameterisations. Four scenarios are selected table 5.4. The scenarios Ru_2 , Ru_3 and Ru_4 correspond to the wave condition with the best results in the overtopping study introduced in the previous section, and a shorter wave condition with $T = 0.7$ s ($L_w = 0.755$ m) is added to analyse a steeper wave condition. The numerical parameters and domain dimensions are the same as in section section 5.2.1. The structure's location and slope are also unchanged. However, the structure's freeboard is increased to prevent wave overtopping, see figure 5.7. The run-up height, R_u is measured in the centre of the numerical wave tank, and a total of 20 waves are considered for the analysis in each case. R_u is the maximum elevation above the still water level that the front of the water reaches on the slope.

Table 5.4: Cases used to validate wave run-up, H_w , wave period (T), wavelength L_w , ξ , and slope angle

Case	H_w (m)	T (s)	L_w (m)	ξ	α °
Ru_1	0.075	0.7	0.755	1.83	30
Ru_2	0.075	0.8	0.960	2.07	30
Ru_3	0.075	1.0	1.373	2.47	30
Ru_4	0.075	1.2	1.770	2.80	30

Figure 5.8 presents the wave breaking type for the simulations analysed. The water surface is presented with the blue iso-surface. It is observed that the shape of the wavefront aligns with the type of breaking expected for each scenario. Cases Ru_1 and Ru_2 clearly show a curled front characteristic of a plunging breaking type. In cases Ru_3 and Ru_4 , the breaking process changes; a less curled wavefront is

observed, and a highly perturbed water surface is present at the toe of the wave. Evidently, Hydro3D-NWT is able to reproduce the correct wave-breaking type in dependence of ξ .

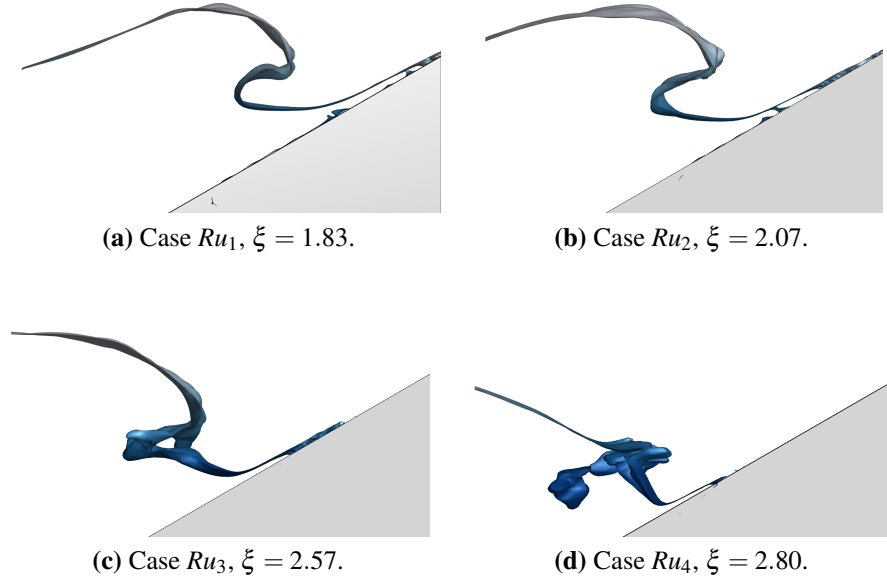


Figure 5.8: Lateral view of wave breaking conditions cases Ru_1 , Ru_2 , Ru_3 and Ru_4 , blue iso-surface represents the water surface, and light grey the structure

Figure 5.9 compares the R_u calculated from Hydro3D-NWT results, black triangles, with predictions made by three empirical methodologies to estimate R_u for regular waves [47, 6, 7]. In addition, the range for each breaking type is indicated with vertical lines. It is observed that Hydro3D-NWT underestimates R_u/H_w compared with the R_u/H_w using [47] and [6] equations but overestimates R_u/H_w when compared to the estimation using [7]'s equation. Previous studies have shown high variability in the run-up results. Hydro3D-NWT reproduces the transition of R_u/H_w with the change of the breaking condition. The results demonstrate that Hydro3D-NWT satisfactorily predicts the wave run-up for the conditions studied.

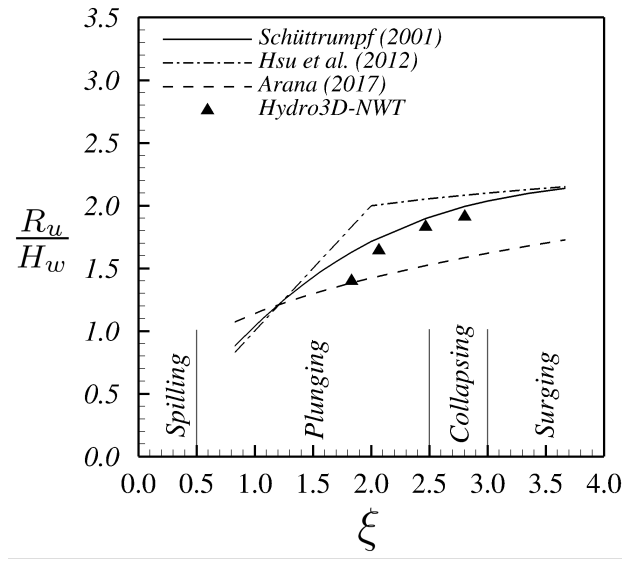


Figure 5.9: Comparison of Hydro3D-NWT's run-up results against empirical formulations.

5.2.3 Validation conclusion

The results related to wave overtopping show that Hydro3D-NWT can reproduce the wave overtopping discharge with a satisfactory agreement for three of the four wave conditions studied. The longer wave shows some overestimation of the results. The wave breaking type and transition according to the value of ξ are well reproduced by Hydro3D-NWT. The run-up, R_u , computed by Hydro3D-NWT agrees well with predictions by well-established empirical equations.

In the next section, the effect of the run-down flow in the energy dissipation during wave breaking and run-up is analysed in depth for three wave conditions with the best agreement in the overtopping study, $T = 0.8$ s, $T = 1.0$ s and $T = 1.2$ s, plus the shorter wave, $T = 0.7$ s.

5.3 Methodology

The present study assesses whether the run-down flow affects energy dissipation when waves interact with a sloped structure. This analysis is conducted by varying the run-down flow without changing the incoming waves. Different levels of run-down flows are achieved by allowing wave overtopping by lowering the structure's crest, which reduces the flow that runs back down the structure. For each

wave condition, four structures are tested as shown in figure 5.10. In the first, no overtopping is allowed; therefore, full run-up and run-down occur. The freeboard is subsequently reduced, generating three modifications to the run-down. The lowest freeboard is higher than the location of the wave breaking, so as not to affect the breaking process.

Four wave conditions are studied, all with a wave height of $H_w = 0.075$ m, whereas the wave period (T) ranges from 0.7 s to 1.2 s (table 5.5).

A vertical cross-section, S , is introduced, at which the energy distribution is assessed post wave breaking, see figure 5.10. This section is positioned downstream of the breaking zone, considering the case with no overtopping. A vertical cross-section S is employed instead of one oriented normal to the slope, because it aligns with the Cartesian grid, thereby facilitating more efficient and accurate data acquisition. However, this generates an overestimation of the energy that runs up and down the slope, but because the study aims to compare cases, this overestimation does not affect the study's conclusion.

The distribution of energy flux through section S varies depending on its location on the slope. As the elevation of the control section increases, the kinetic energy decreases while the potential energy increases. A reduction in total energy is also expected with increasing elevation of section S , due to energy dissipation during the run-up flow.

A cross-section located within the breaking zone would not allow for a proper evaluation of the energy associated with the run-up flow, which is the energy that could be collected by an OWEC. On the other hand, positioning the section too high on the slope would lead to interference from overtopping flow, compromising the assessment of energy variations caused by different run-down flow conditions.

In this study, the specific location of section S was determined through careful inspection of the simulation results, enabling the identification of a location for all conditions tested that allows the evaluation of the energy flow after the breaking zone and at the beginning of the run-up flow .

The instantaneous kinetic energy (KE), dynamic potential energy (DPE) and

total energy are calculated according to equations (5.11), (5.12) and (5.13), respectively. (DPE) is the potential energy generated only due to the action of the waves, calculated as the total potential energy of the flow minus the potential energy during SWL condition. KE , DPE and TE are calculated in the section S to obtain the energy during the run-up and run-down stages of the wave-structure interaction and in the inlet of the domain for one wave period to obtain the wave energy input into the system.

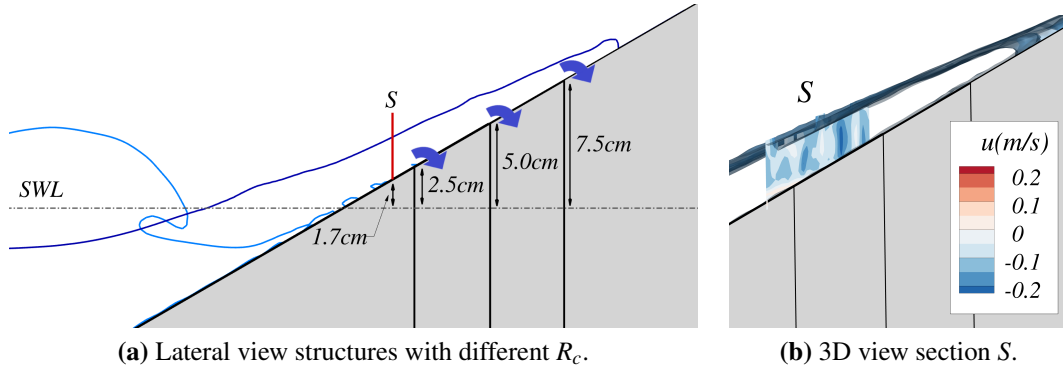


Figure 5.10: Lateral view of structure with different freeboards (R_c), and 3D view of cross-section S where the flow's energy is quantified.

Table 5.5: Study cases, wave height H_w , wave period (T), wave length L_w , freeboard R_c , Iribarren number ξ .

Case	H_w (m)	T (s)	L_w (m)	R_c (m)	ξ
Case1 $_{Ru}$	0.075	0.7	0.755	R_u	1.83
Case1 $_{75}$	0.075	0.7	0.755	0.075	1.83
Case1 $_{50}$	0.075	0.7	0.755	0.050	1.83
Case1 $_{25}$	0.075	0.7	0.755	0.025	1.83
Case2 $_{Ru}$	0.075	0.8	0.960	R_u	2.07
Case2 $_{75}$	0.075	0.8	0.960	0.075	2.07
Case2 $_{50}$	0.075	0.8	0.960	0.050	2.07
Case2 $_{25}$	0.075	0.8	0.960	0.025	2.07
Case3 $_{Ru}$	0.075	1.0	1.373	R_u	2.47
Case3 $_{75}$	0.075	1.0	1.373	0.075	2.47
Case3 $_{50}$	0.075	1.0	1.373	0.050	2.47
Case3 $_{25}$	0.075	1.0	1.373	0.025	2.47
Case4 $_{Ru}$	0.075	1.2	1.77	R_u	2.80
Case4 $_{75}$	0.075	1.2	1.77	0.075	2.80
Case4 $_{50}$	0.075	1.2	1.77	0.050	2.80
Case4 $_{25}$	0.075	1.2	1.77	0.025	2.80

$$KE = \int_0^T \int_0^{L_y} \int_{-d}^{\eta(t)} 0.5\rho(u^2 + v^2 + w^2) dz dy dt \quad (5.11)$$

$$DPE = \int_0^T \int_0^{L_y} \int_{-d}^{\eta(t)} \rho g z dz dy dt - \left[\int_0^T \int_0^{L_y} \int_{-d}^{\eta(t)} \rho g z dz dy dt \right]_{\text{at SWL}} \quad (5.12)$$

$$TE = KE + DPE \quad (5.13)$$

The overtopping discharge is measured at the crest of each structure using the same methodology as explained in section 5.2.1. The first three overtopping events are neglected to consider only fully developed flows. Five overtopping events are considered in the present research. Two quantities of the overtopping are used: an individual overtopping volume per wave, Vo , which is the total volume that spills to the rear of the structure divided by the number of waves considered (5); and the mean overtopping discharge q , which is the total overtopping volume divided by time.

To estimate the mean power at the crest of the structure, equation (5.14) is used. This equation is used in the design of OWEC, to estimate the power that can be collected at the crest of the ramp before the water spills into the reservoir [18]. It depends on water density (ρ), the gravitational acceleration (g), the mean overtopping discharge (q) and the crest's freeboard R_c .

$$P_{crest} = \rho g q R_c \quad (5.14)$$

5.4 Results and discussion

Figure 5.11 presents the water surface and contours of the horizontal velocity, u , during the breaking process for cases *case1_{Ru}* and *case1₂₅*. These cases highlight the difference in the run-down flows when comparing their respective hydrodynamics. Figure 5.11a and figure 5.11b show the incoming wave before breaking. In

case1_{Ru}, a more vertical wavefront is observed compared to *case1₂₅*. In addition, a downward (negative) flow, indicated by the blue velocity contours, is observed in *case1_{Ru}*, whilst in *case1₂₅* negative horizontal velocities are detected only near the water surface. This indicates that the run-down flow is more pronounced in *case1_{Ru}* compared to *case1₂₅*. This is expected due to the occurrence of overtopping in *case1₂₅*, which reduces the run-down flow. The presence of this downward flow contributes to the wave to curl over in *case1_{Ru}*, forming an overturning jet, figure 5.11c; a phenomenon that is less marked in *case1₂₅*, figure 5.11d. In this case, the front of the wave is less curled and an almost vertical wave toe is appreciated. In addition, due to a reduced run-down flow, which acts in the opposite direction to the wave's advance, the wavefront in *case1₂₅* has climbed higher in the same amount of time compared with *case1_{Ru}*. In $t = 10.89$ s figure 5.11e, the wave in *case1_{Ru}* plunges into the sloped surface and air gets trapped inside the curl, after which the wave runs up the slope. At the same instance, a significantly different condition is presented in figure 5.11f where a fully developed run-up flow reaches the crest of the structure. At $t = 11.02$ s, all the air trapped during the breaking of the wave in *case1_{Ru}* is dissipated; however, a more disturbed water surface is observed, compared to *case1₂₅* shown in figure 5.11f and figure 5.11h. The findings presented in figure 5.11 indicate that the reduction in the run-down modulates the breaking type of the wave, shifting from a plunging type in *case1_{Ru}* to a collapsing type of breaking in *case1₂₅*. This has a significant effect on energy conservation because the collapsing and surging of the wave, *case1₂₅*, are expected to result in reduced energy dissipation due to a less turbulent and violent nature of the breaking in comparison to the plunging wave of *case1_{Ru}*.

Figure 5.12 shows a sequence of the breaking process of *Case1_{Ru}* and *Case1₂₅*. The Q-criterion is employed to visualise turbulence structures. In figure 5.12 iso-surfaces of $Q = 1,000$ coloured with the vorticity magnitude are presented. As previously mentioned, these cases are presented because they undergo more significant hydrodynamics alterations due to the decrease of the run-down flow. Figure 5.12a

and figure 5.12b are instances when the waves curl in *Case1_{Ru}* and *Case1₂₅*, respectively. Larger turbulence structures are observed in *Case1_{Ru}* than in *Case1₂₅* and the vorticity magnitude is also greater in *Case1_{Ru}*. In addition, *Case1_{Ru}* shows that the eddies originate from the run-down flow and are then lifted up by the wavefront. In both cases, these roller-type longitudinal structures align with the $x - axis$, which agrees well with observations and records of the wave-breaking process [118]. In the next instance, $t = 10.89$ s, the overturning jet crashes against the slope in figure 5.12c. The vortices are stretched, i.e. increasing in length and reducing in diameter. Smaller vortices are also observed in the wave tongue. *Case1₂₅* present a different scenario for the same instance, figure 5.12d, because the curling phase of the breaking is significantly shorter than in *Case1_{Ru}*, hence the front of the wave moves faster up the slope, and no vortices are observed. At the last instance, figure 5.12e, a fully developed run-up flow is observed; however, vortices are still present in the flow but have reduced in dimension, number, and vorticity magnitude. Figure 5.12f shows, as in the previous instance, no turbulence structures in the run-up flow. Furthermore, *Case1_{Ru}* features a more disturbed water surface than *Case1₂₅* as seen in figure 5.11g and figure 5.11h. Different turbulence structures are generated during the breaking process due to a reduction in the run-down flow in *Case1_{Ru}*, leading to a more disturbed and less energetic run-up.

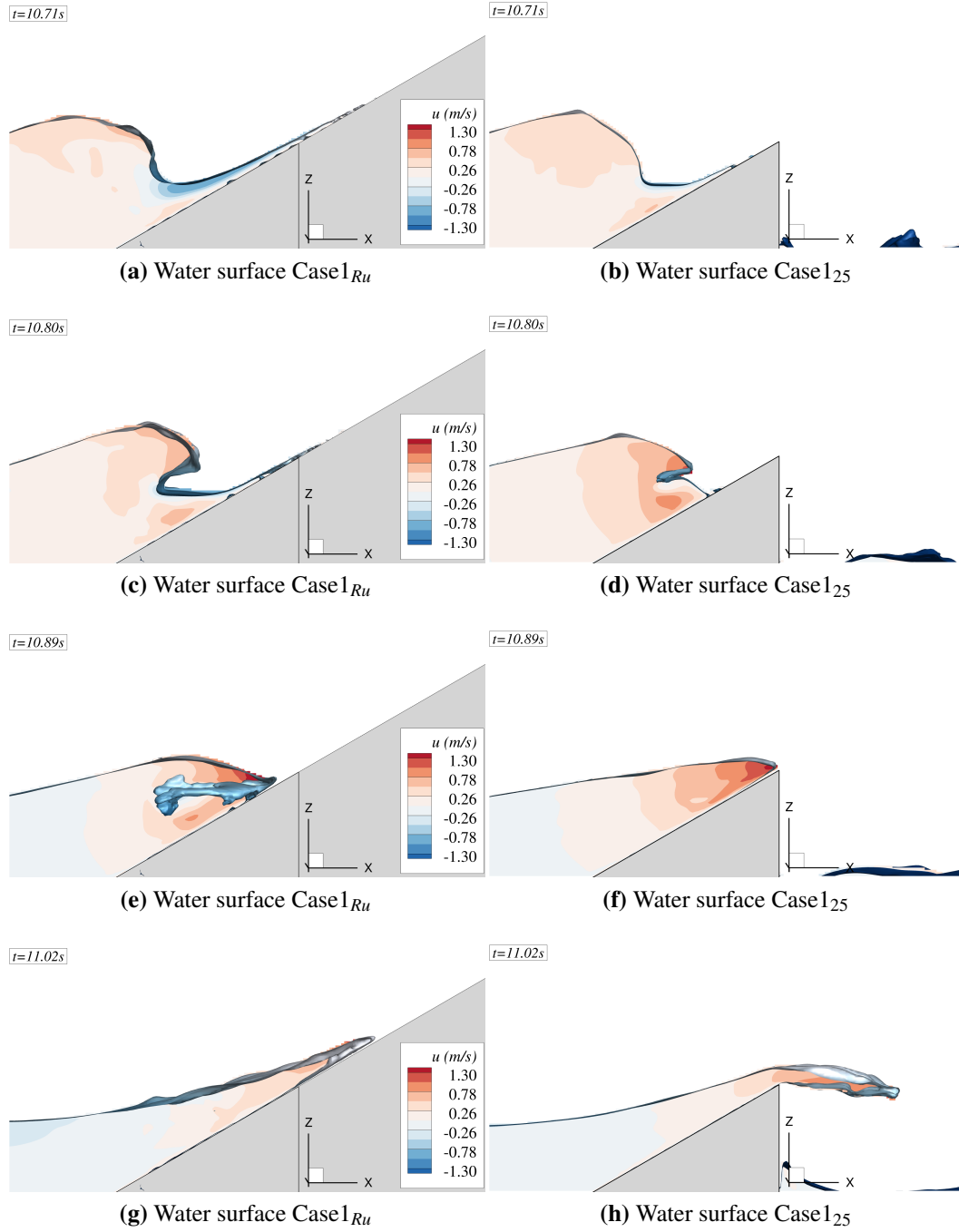


Figure 5.11: Wave breaking of cases *case1_{Ru}* and *case1₂₅* at selected instants in time. Blue iso-surface shows water surface and contoured horizontal velocities u .

For *case4*, the longer waves, a sequence of the breaking process is presented in figure 5.13. These cases are presented because they exhibit less pronounced hydrodynamic modification compared to *case1*, therefore providing contrast in how the flow varies depending on the breaking type. Similar to the findings for *case1*,

higher turbulence levels are present in $Case4_{Ru}$ in comparison to the overtopping counterpart, $Case4_{25}$. However, no change in the breaking type is observed for longer waves. The wavefront in both cases has a similar shape and behaviour, albeit a more compact wavefront is observed in $Case4_{25}$. Both conditions present a collapsing type of breaking without a significant overturning jet. Therefore, the stage when the wavefront crashes against the slope, as shown in figure 5.12c, does not occur for this wave condition. Again, roller-type vortices are appreciated in both cases, especially in figure 5.13a and figure 5.13c. Higher levels of vorticity are also observed for $Case4_{Ru}$. At $t = 8.89$ s no turbulent structures are detected in $Case4_{25}$, figure 5.13f, whilst in $Case4_{Ru}$ some vortices are still present in the flow. As there is no change in the breaking condition, the differences in the turbulence structures between $Case4_{Ru}$ and $Case4_{25}$ are not as significant as for $case1$, figure 5.12, where a clear plunging type of breaking is generated in $case1_{25}$.

Figure 5.14 presents the distribution of energy through section S , as defined in section 5.3, for $case2_{Ru}$ (solid lines) and $case2_{50}$ (dashed lines) over one wave period; the left graph plots the kinetic energy KE , the dynamic potential energy DPE is plotted in the centre, and the right graph contains the total energy TE , calculated from equations (5.11), (5.12) or (5.13), respectively. Only this case is presented because it clearly illustrates the characteristic behaviour of the energy distribution through S across all cases. The kinetic energy plot allows visualisation of the run-up and run-down of the flow through section S , which are separated by the vertical dashed line. In the run-up, the kinetic energy in both cases peaks sharply and then decreases to almost zero; this instance marks when the flow reaches a near stop before running down the slope. Then, the kinetic energy increases again, but not as fast and to a lower level before decreasing to zero when no more water passes through the section. The graph of the dynamic potential energy is different: during the run-up, the dynamic potential energy also increases rapidly, but then gently decreases until the end of the flow. The dynamic potential energy is related to the water depth of the flow in the control section, which reaches a maximum

during the run-up. The total energy is the sum of the kinetic and dynamic potential energy, and it is observed that the peak is reached in the run-up and then decreases during the run-down. Comparing *case2_{Ru}* and *case2₅₀*, it is observed that in the run-up, *case2₅₀* reaches a higher energy peak in all plots, and then because of the reduced run-down, the energy during the run-down stage is lower than for *case2_{Ru}*. These findings align with what is deducted from figure 5.12. The reduction of the run-down flow decreases the turbulence during the breaking process, allowing more water to run up the slope and generating growth in the kinetic and dynamic potential energy in the run-up stage. The energy that could be harvested for a WEC at the crest of the slope is related to the energy flow during the run-up; therefore, for the rest of the plots, only the cumulative energy during the run-up is considered.

Figure 5.15 presents the energy that passes through section S per run-up event (E_{sru}) normalised by the wave energy (E_w) calculated from 2nd Order Stokes Waves theory. The Kinetic, Dynamic Potential and Total energy are presented in red, blue and black, respectively. The set-up with no overtopping is shown with solid lines, and $R_c = 7.5$ cm, $R_c = 5.0$ cm and $R_c = 2.5$ cm with dashed, dotted and dash-dotted lines, respectively. Table 5.6 quantifies the KE , DPE and TE data plotted in figure 5.15 and figure 5.16. It is observed that the energy that passes through section S increases with the wave period (T). For *case1_{Ru}* only around 50 % of the total wave energy passes through S during each run-up, whereas for *case4_{Ru}* that value increases to approximately 110 % (it should be noted that a value above 100 % is a result of the cross-section being vertical instead of perpendicular to the surface, see section 5.3. As the freeboard decreases, the value of E_{sru}/E_w increases, suggesting that scenarios with high freeboard (as well as the pure run-up) suffer from increasing energy dissipation during the breaking process. In addition, the amount of energy dissipation also depends on wavelength due to the type of breaking, which varies according to the Iribarren number ξ . In all cases, the kinetic energy is less than the dynamic potential energy, representing about 1/3 of the Total energy. As quantified in table 5.6, *case1*, figure 5.15a, the shortest wave

experiences the greatest energy difference at the section S compared to the run-up case. For $case1_{25}$, 26 % more energy is available at the reference section than for the same wave at the same location for the pure run-up case. On the other hand, for the longest waves, i.e. $case4$, only around 3.6 % more TE per wave is available in $case4_{25}$ as compared to the pure run-up. These values align with what was observed in figure 5.13, no significant change in the wave breaking process when the run-down is reduced, and, clearly, OWECs are more suitable for long wave conditions.

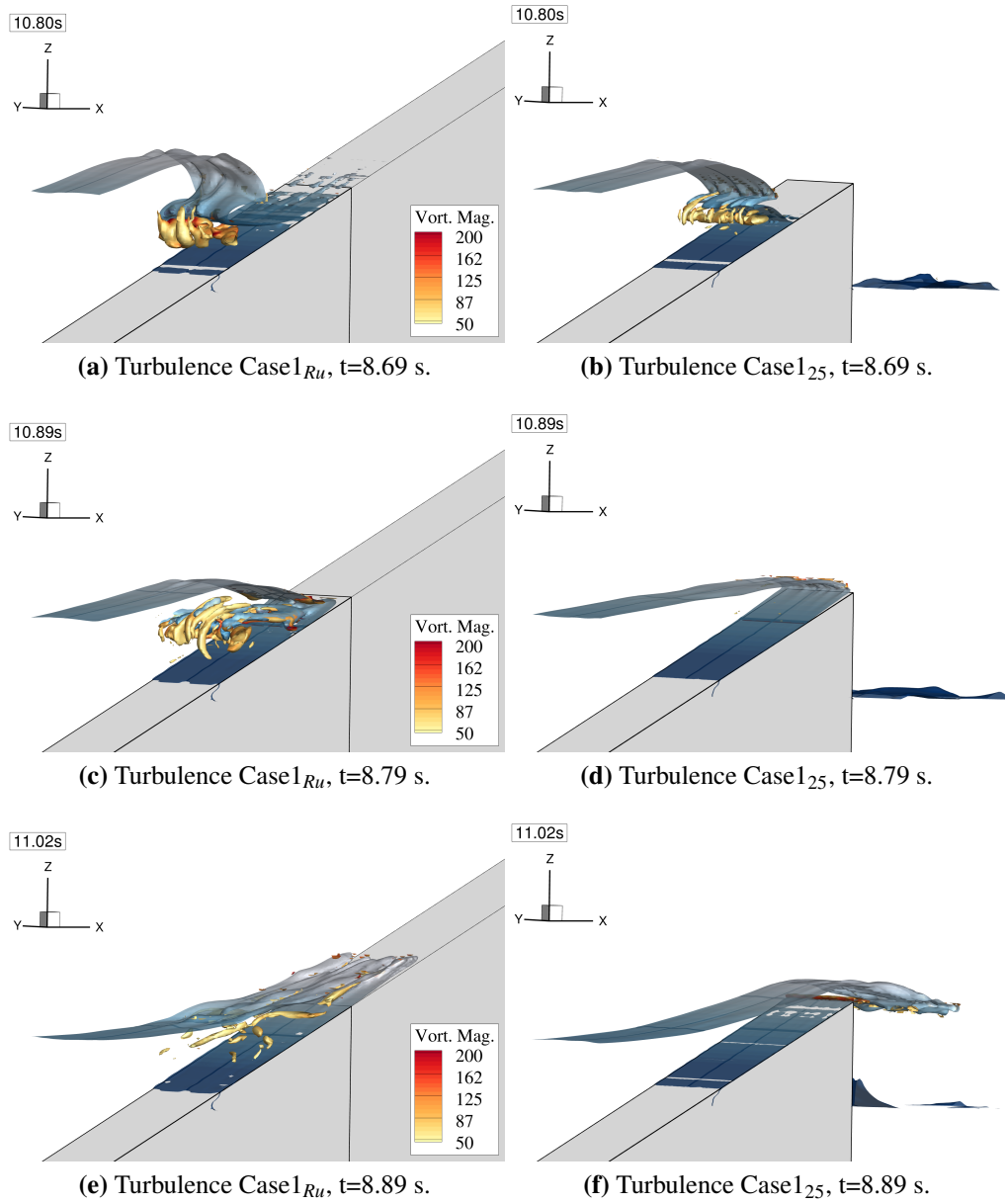


Figure 5.12: 3D view of wave breaking for cases *case1_{Ru}* and *case1₂₅* at selected instants in time. Blue iso-surface: water surface; and iso-surface according to Q criterion contoured by vorticity magnitude.

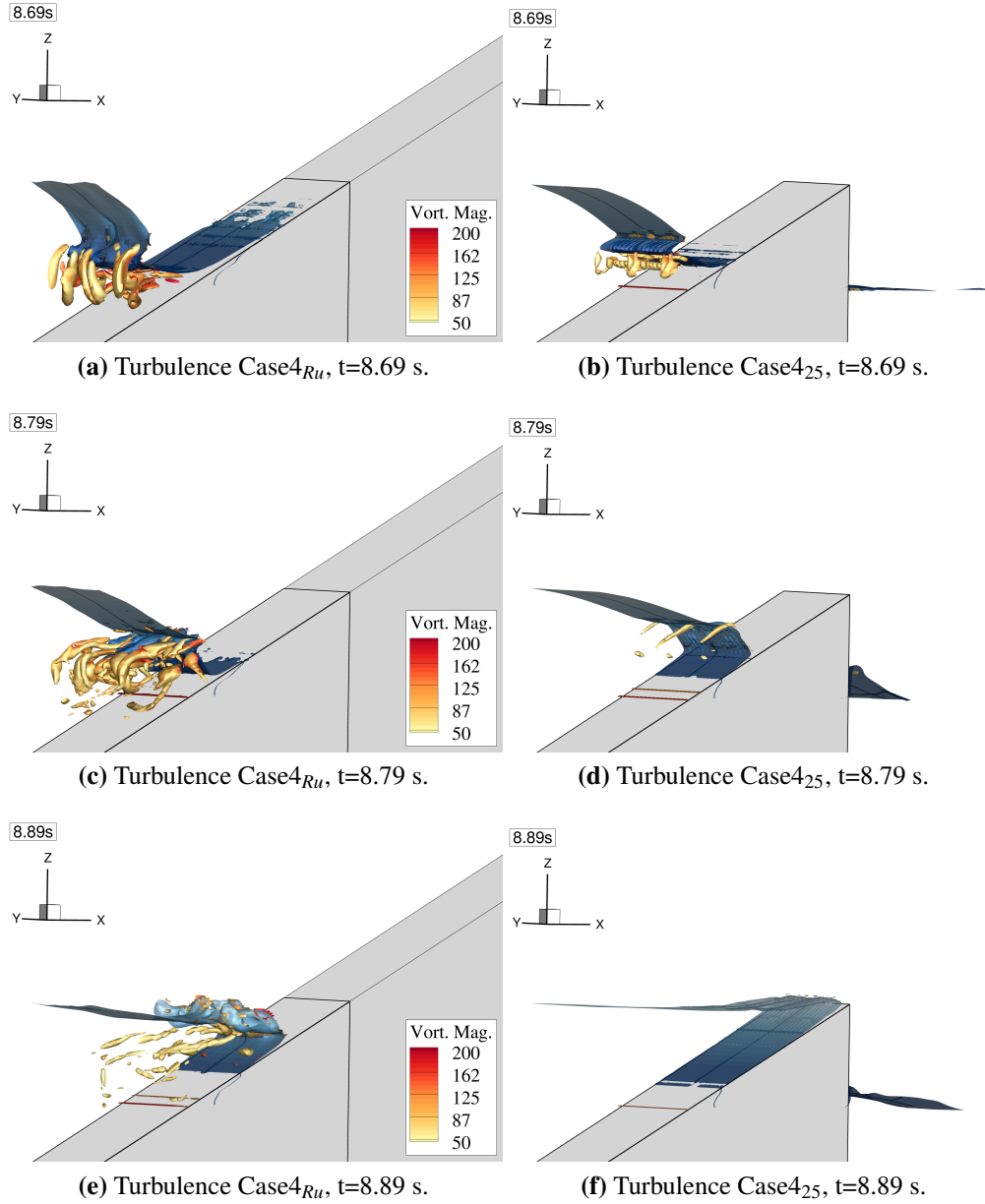


Figure 5.13: 3D view of wave breaking for cases *case4_{Ru}* and *case4₂₅* at selected instants in time. Blue iso-surface: water surface; and iso-surfaces of the Q criterion contoured by vorticity magnitude.

Figure 5.16 shows the cumulative energy per run-up event (E_{sru}) that passes through section S , normalised by the wave energy (E_w), calculated from figure 5.15 for each case. The type of lines and colours are the same as in figure 5.15. A linear growth of the energy that passes through section S with the number of waves is observed; this rate increases with the wave period T . From figure 5.16, it is also possible to observe the amplitude of the change generated by reducing the run-

down flow. *cases1* and *case2*, have more significant variation, follow by *case3*, and a small amplitude is observed in *case4*. The cumulative variations of TE for the five waves analysed are presented in table 5.6, $VarTE_{ac}$. *Case1* and *case2* have a variation over the 20 %, 25.7 % and 22.1 % respectively, *case3* a variation of 12.7 %, and in *case4* the increment of the cumulative TE dropped to 3.5 %. Specifically in *case1*, figure 5.16a, it is possible to appreciate that the more significant energy variation is achieved between cases *case1*₇₅ and *case1*₅₀, which is when the transition from plunging to collapsing breaking type occurred.

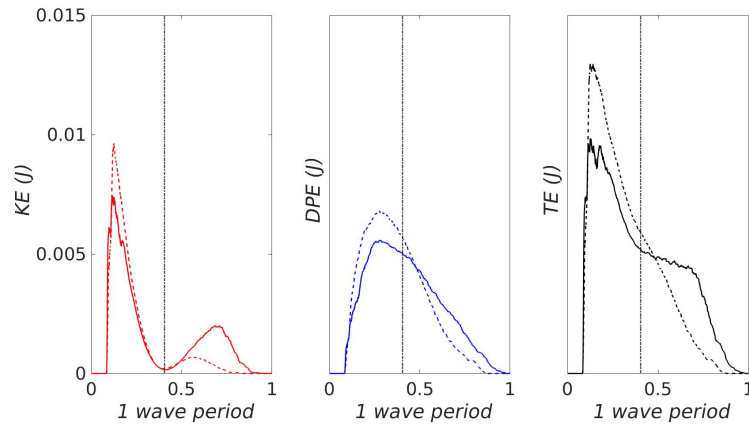


Figure 5.14: Energy distribution through section S over one wave period. KE: Kinetic energy, DPE:dynamic potential energy and TE: total energy. Solid lined: *case2* _{R_u} , dashed lines: *case2*₅₀.

Figure 5.17 presents the average normalised total energy that passes through section S per run-up event as a function of the average dimensionless overtopping volume per wave for various ξ . Each data point represents a freeboard height, from the highest (left), R_u , to the lowest (right) $R_c = 2.5$ cm. The normalised overtopping volume V_{ow} can be related to the reduction in the run-down flow. It is observed that the gradient of TE_{Ru} as a function of V_{ow} is smaller with increasing ξ , suggesting that conditions with lower ξ are more sensitive to the run-down. As already mentioned previously, the run-down flow affects the breaking type in the shorter waves, here, from a plunging breaking type to a collapsing type of breaking; the latter being more advantageous for the run-up, because there is less energy dissipation. The conditions with higher ξ do not experience such a significant change in their

breaking condition - the breaking type remains a collapsing type for all cases; only a more compact wavefront is observed with the reduction of the run-down flow. The turbulent structures and vorticity magnitude in the flow are reduced in all cases with the decrease of the run-down flow.

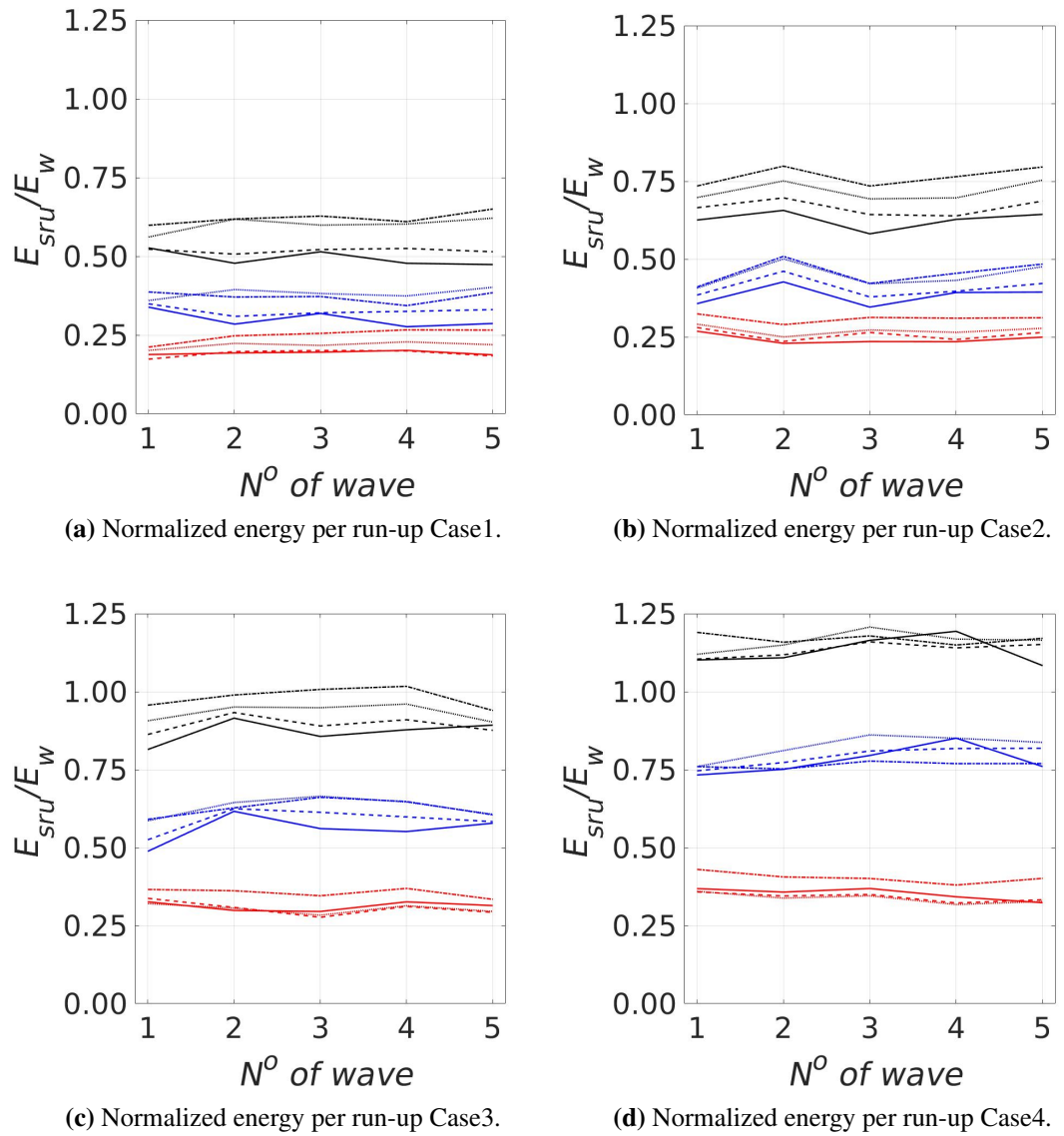
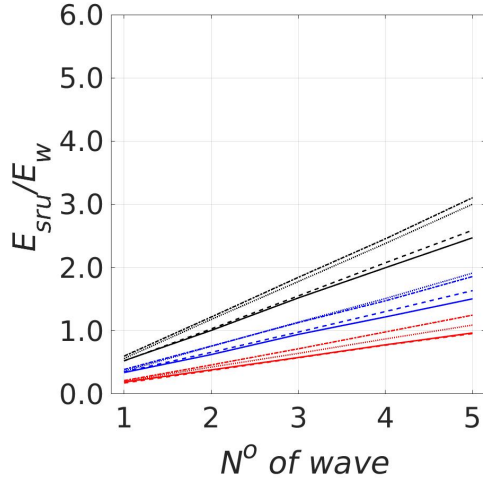
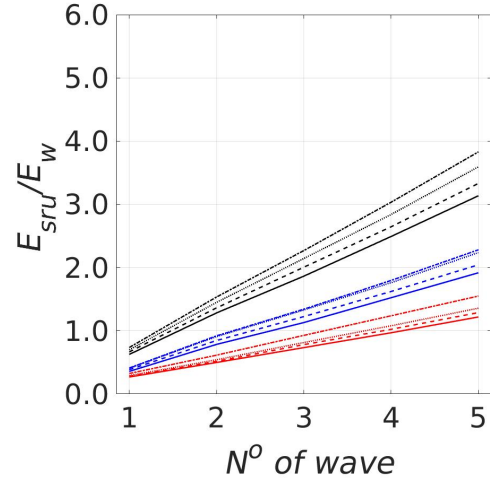


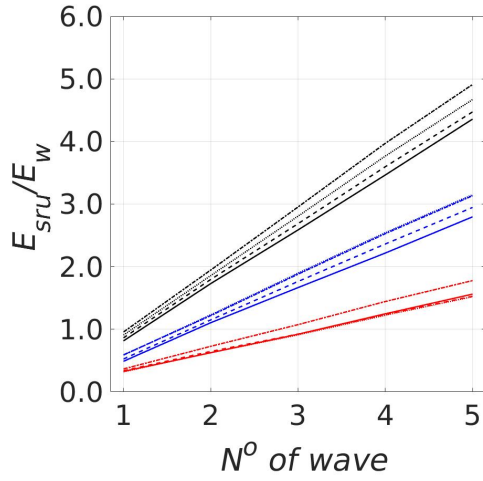
Figure 5.15: Normalised energy per run-up flow (E_{sru}/E_w). Black:TE, Blue:DPE, Red:KE, Solid Line: R_u , Dashed: $R_c = 0.075$ m, Dotted: $R_c = 0.05$ m and Dash-Dot: $R_c = 0.025$ m.



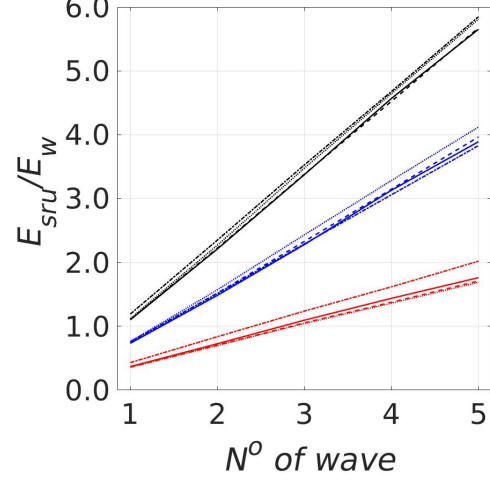
(a) Normalised cumulative energy per run-up Case1.



(b) Normalised cumulative energy per run-up Case2.



(c) Normalised cumulative energy per run-up Case3.



(d) Normalised cumulative energy per run-up Case4.

Figure 5.16: Normalised cumulative energy per run-up flow (E_{sru}/E_w). Black:TE, Blue:DPE, Red:KE, Solid Line:Ru, Dashed: $R_c = 0.075$ m, Dotted: $R_c = 0.05$ m and Dash-Dot: $R_c = 0.025$ m.

Figure 5.18 presents the power at the crest of the structure estimated with (5.14) as a function of the average normalised total energy per run-up event, TE , in section 5. Each colour represents a case with the same freeboard. The ratio between the increase of TE and P_{crest} is approximately 0.6. This plot indicates that an increment of P_{crest} is related to an increment of TE_{sru} . This result is used in figure 5.19.

Table 5.6: Averaged normalised energy per run-up event though section S. KE_{av} : Average normalised kinetic energy; DPE_{av} : Average normalised dynamic potential energy; TE_{av} : Average normalised total energy; $VarTE_{wave}$: % variation of TE_{av} relative to run-up case; $VarTE_{ac}$: % variation of cumulative total energy relative to run-up case.

Case	KE_{av}	DPE_{av}	TE_{av}	$VarTE_{wave}$ (%)	$VarTE_{ac}$ (%)
Case1 _{Ru}	0.193	0.301	0.494	-	-
Case1 ₇₅	0.191	0.327	0.518	5.0	4.8
Case1 ₅₀	0.218	0.382	0.600	21.9	21.5
Case1 ₂₅	0.249	0.372	0.621	26.0	25.7
Case2 _{Ru}	0.244	0.383	0.627	-	-
Case2 ₇₅	0.258	0.409	0.666	6.3	6.2
Case2 ₅₀	0.271	0.447	0.719	14.7	14.6
Case2 ₂₅	0.310	0.456	0.766	22.2	22.1
Case3 _{Ru}	0.312	0.559	0.871	-	-
Case3 ₇₅	0.305	0.589	0.894	2.7	2.6
Case3 ₅₀	0.304	0.630	0.934	7.3	7.2
Case3 ₂₅	0.355	0.627	0.982	12.9	12.7
Case4 _{Ru}	0.352	0.778	1.130	-	-
Case4 ₇₅	0.342	0.793	1.135	0.5	0.4
Case4 ₅₀	0.338	0.824	1.162	2.9	2.8
Case4 ₂₅	0.404	0.766	1.170	3.6	3.5

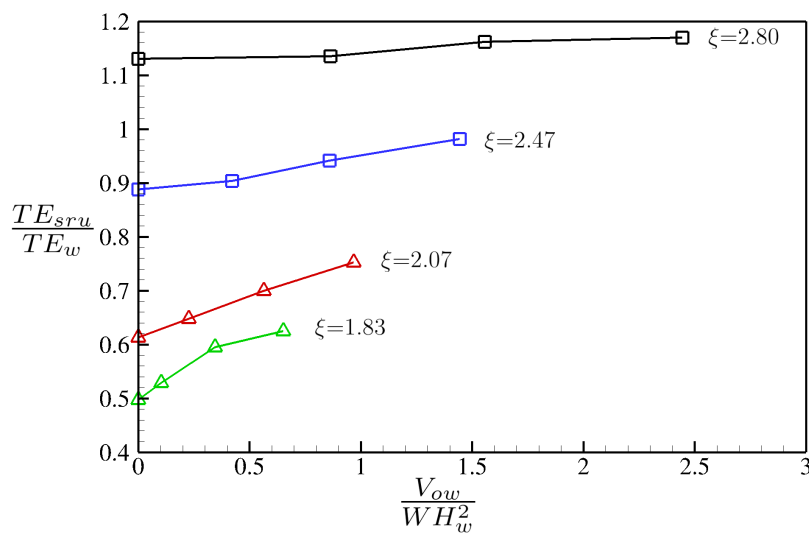


Figure 5.17: Energy variation versus variation in overtopping, separate by ξ .

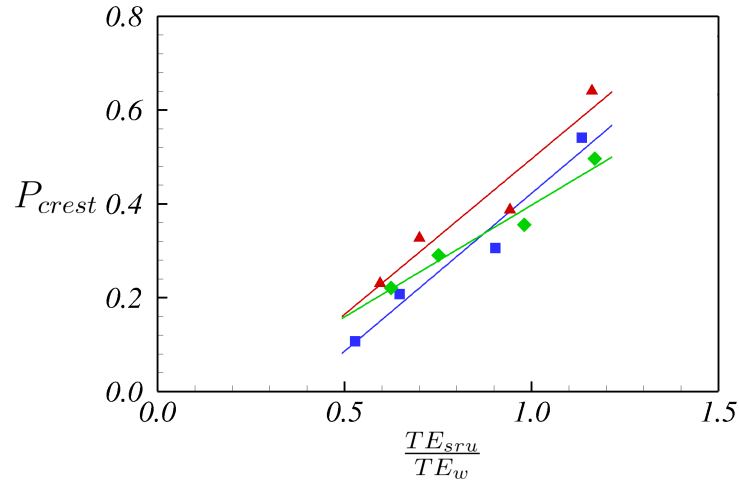


Figure 5.18: Power at the crest of the structure (P_{crest}) as a function of average normalised Total energy per run-up event (TE_{sru}/TE_w). Blue squares: $R_c = 0.075$ m, Red triangles: $R_c = 0.050$ m and Green Diamonds: $R_c = 0.025$ m. Lines present the best fit for each R_c according to the symbols' colours.

Figure 5.19 presents a graph, based on figure 5.17, that relates the overtopping volume, V_o , to the power at the crest of the ramp, P_{crest} , for an OWEC, for instance at the crest of a sloped breakwater, similar to an OBREC device. In this plot the X – axis shows the normalised overtopping volume, V_o/WH_w^2 , and the Y – axis the wave power at the crest of the structure calculated with 5.14 and normalised by the total wave power, P_{crest}/P_w . Using the overtopping volume calculated by design, V_{cal} , and the corresponding ξ curve representative of the wave condition, it is possible to estimate the power at the crest, P_{cal} , for that overtopping. In addition, this plot can be used to calculate an improved power, P_{imp} , at the crest of the structure as a result of reducing the run-down flow. In this case, V_{def} is the volume of run-down flow deflected, which, added to V_{cal} , results in a virtual overtopping volume, V_{vi} . This V_{vi} can be used to determine P_{imp} , giving the new improved power at the crest of the structure.

In the X – axis in figure 5.19 represents the overtopping volume per wave, a parameter which is complex to determine in natural conditions; this is why the mean overtopping discharge, q , is most used in coastal design manuals. A relation between V_o and q will be explored.

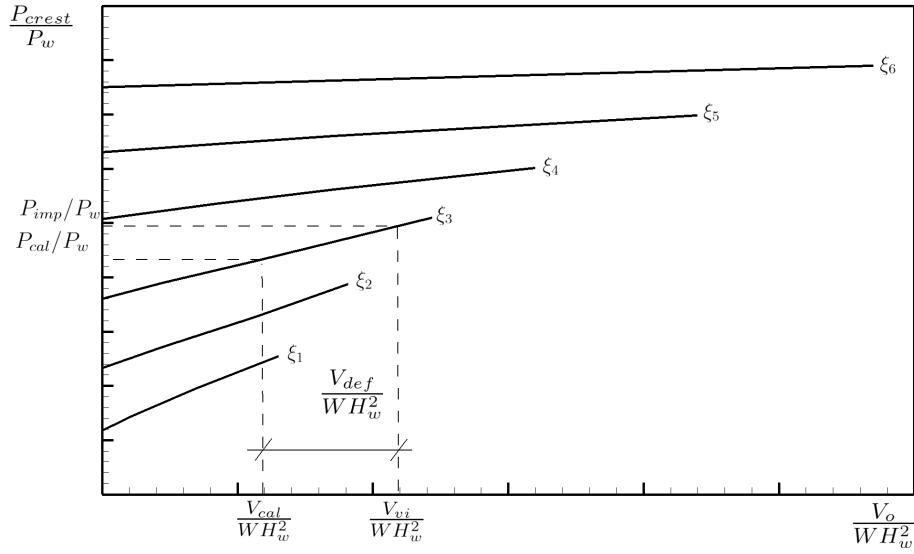


Figure 5.19: Energy variation versus variation in overtopping.

5.5 Conclusions

Large eddy simulations of waves and sloped structures interaction have been performed. These simulations include a pure run-up scenario and by lowering the freeboard of the structures analysed, three different wave overtopping discharge have been accomplished.

When waves interact with a slope, four main processes occur: (i) wave breaking as it approaches the overtopping structure, (ii) wave run-up, (iii) overtopping discharge, and (iv) run-down flow. Wave overtopping occurs depending on the wave conditions and height of the structure. This study has focused on the effect of the run-down flow on the energy dissipation during the breaking process of the waves. It has been found that the run-down flow affects the breaking type of the waves and also impacts the turbulence that occurs during the breaking and run-up stages.

In this section, the LES code Hydro3d-NWT, implemented with LSM to track the water surface, is used for the first time to simulate breaking waves, run-up, and overtopping flows. The results show the extraordinary capability of the code to simulate complex water surface morphology. The code is able to generate the correct type of wave breaking for the conditions studied, and expected processes

such as roller-type eddies, air entrapment and overturning water jets are visualised in the results.

Hydro3D-NWT's ability to simulate wave overtopping discharge and run-up has been validated. It has been shown that Hydro3D-NWT is capable of predicting wave overtopping discharge with satisfactory accuracy for three of the four wave conditions analysed. Hydro3D-NWT considerably overestimated the discharge for the longer wave condition compared to the laboratory experiment. In a second validation case, pure run-up has been simulated, and Hydro3D-NWT's predictions have agreed well with estimates calculated by well-known empirical equations. Moreover, the simulated wave breaking matches well the type of wave breaking expected according to the respective Iribarren number.

The wave conditions with the best performance in the validation study have been used to investigate the effect of run-down on energy dissipation in wave-structure interaction. Four wave conditions have been chosen to generate four different wave steepnesses and Iribarren numbers, ξ . For each wave condition, four structures have been employed. Each structure has featured a different crest elevation, one high enough to not allow overtopping and the others with a lower crest to generate different overtopping discharges, thus modifying the run-down flow.

The energy flow through a selected cross-section downstream of wave breaking has been quantified for each case. The kinetic energy has allowed for the identification of the run-up and run-down stages. It has been found that the energy flow reaches its maximum in the early stages of the run-up and then decays until the end of the run-down. The energy in the run-up stage increases as the run-down flow decreases. It is found that shorter waves are more sensitive to the run-down changes.

It is observed that the interaction of the run-down with the incoming wave affects the overturning of the front of that wave, which may result in the formation of a plunging breaking type (in particular for shorter waves). It has been found that a reduction in the run-flow can reduce the curl of the wave's front, and if the reduction is significant (e.g. due to overtopping), the breaking type can change from

plunging to collapsing. This change in the breaking condition results in a substantial reduction in turbulence levels during the breaking process and in the run-up. A significant part of the energy losses during a plunging breaking type is due to the overturning jet collapsing against the slope. This process is avoided when changing the breaking condition from plunging to collapsing. Another significant change due to the minor curled wavefront is the air entrapment; a more compact breaking wraps less air inside the flow, generating a less perturbed flow. No change in the breaking type has been detected for long wave conditions, for which a collapsing type of breaking occurs in all cases.

The results indicate that variations in run-down flow have a greater impact on smaller ξ than on larger ξ , leading to a more significant increase in energy flux through the control section. In this study, the shorter waves correspond to plunging-type breakers. Further investigation is required to determine whether this trend also applies to spilling-type breakers. However, it is expected that spilling waves would be less sensitive to run-down flow, as their breaking behaviour is primarily governed by wave steepness and occurs on gently sloping bathymetries.

Additionally, larger ξ —associated with collapsing-type breakers— also appear to be less influenced by run-down flow, as supported by the findings. The behaviour of bigger ξ is of particular interest in this research, as they are more relevant to breakwater applications. In contrast, spilling-type breakers are more characteristic of natural coastal environments and are thus of lesser relevance in the context of this study.

These findings suggest that the wave power captured by an OWEC can be improved by reducing the run-down flow. This improvement is anticipated to be more significant for conditions with Irribaren numbers less than 2.5 when plunging conditions are expected. Based on the results of this research, a prototype graph to estimate the improvement of the power harvested by an OWEC is proposed.

In the next chapter, the findings of this research are used to proposed novel run-up ramp's geometries that can improve the wave power capture by an OWEC.

Chapter 6

Conceptual structures.

This chapter explores different run-up ramp geometries to reduce the run-down flow. The results obtained from the previous chapter show that the run-down flow plays an important role in the energy dissipation during the breaking process. Reducing the run-down can improve the energy in the run-up flow, which leads to an increment in the power available to collect at the crest of the structure. This increment can be especially significant, more than 20%, when a change of the breaking type from plunging to collapsing is accomplished.

Simulations conducted in Hydro3D-NWT are presented in the first section of this chapter. These simulations have two objectives. First, to evaluate the inclusion of a gap in the slope that can allow the deflection of the run-down flow and how that change affects the overtopping discharge. The second is to evaluate the performance of Hydro3D-NWT to conduct these more complex simulations and to detect components in the code that need to be modified or revised to improve the simulations.

In the second section of this chapter, and based on the previous results, four conceptual designs are presented to improve the operation of an OWEC. These designs aim to deflect the run-down flow. Thus, less water runs against the incoming wave, reducing the energy dissipation.

6.1 Simulation new geometries

Figure 6.1a presents a 3D view of two new geometries simulate in Hydro3D-NWT, *Geo1* and *Geo2*. Figure 6.1b shows the cross-section of the structure's crests, dark grey represents *Geo1* and light grey *Geo2*. These geometries aim to allow part of the run-down flow to be evacuated through the gap included in the slope. Due to the impulsive nature of the first stage of the run-up flow, the run-up is expected to be less affected by the presence of the gap on the slope than the run-down. This change could increase the overtopping flow and, therefore, the power available to collect at the crest of the structure. *Geo1* consider a flat slope with a gap of $4dx$ width at $z = R_c/2$ (half of the slope freeboard), the ramp presents a constant slope of 30° like the structures presented in table 5.1. *Geo2* include a step-down at $z = R_c/1.78$ that generate a vertical gap of $4dz$. A stepper upper section is generated with an inclination of 47° . The crests of both geometries are located at the same coordinates and have the same freeboard, $R_c = 0.05$ m.

The numerical parameters and domain dimensions are the same as in section section 5.2.1. The wave conditions used are the same as in *case250* indicated in table 5.5 ($H_w = 0.075$ m and $T = 0.8$ s). This case is used as a reference scenario to evaluate the effect of the new geometries on the overtopping discharge.

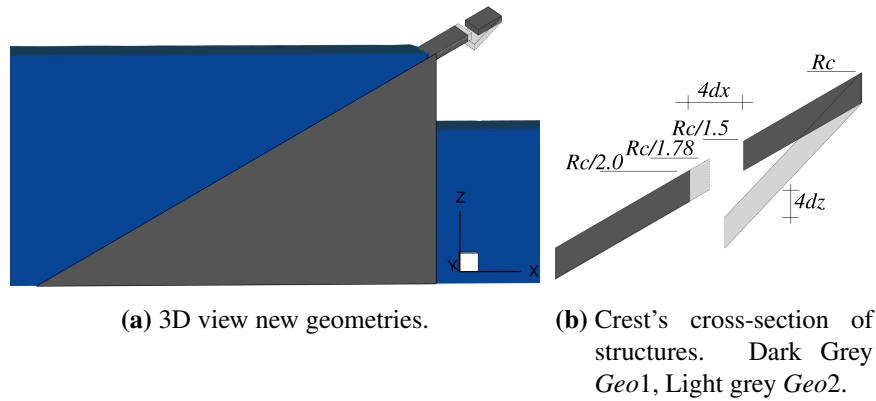
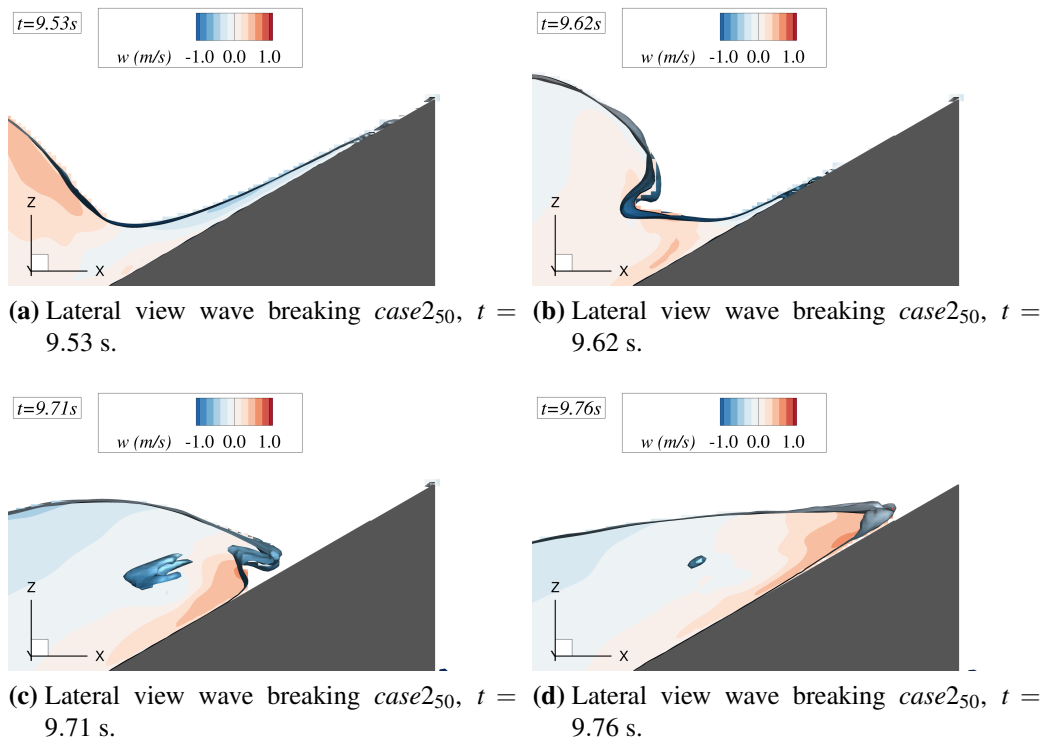
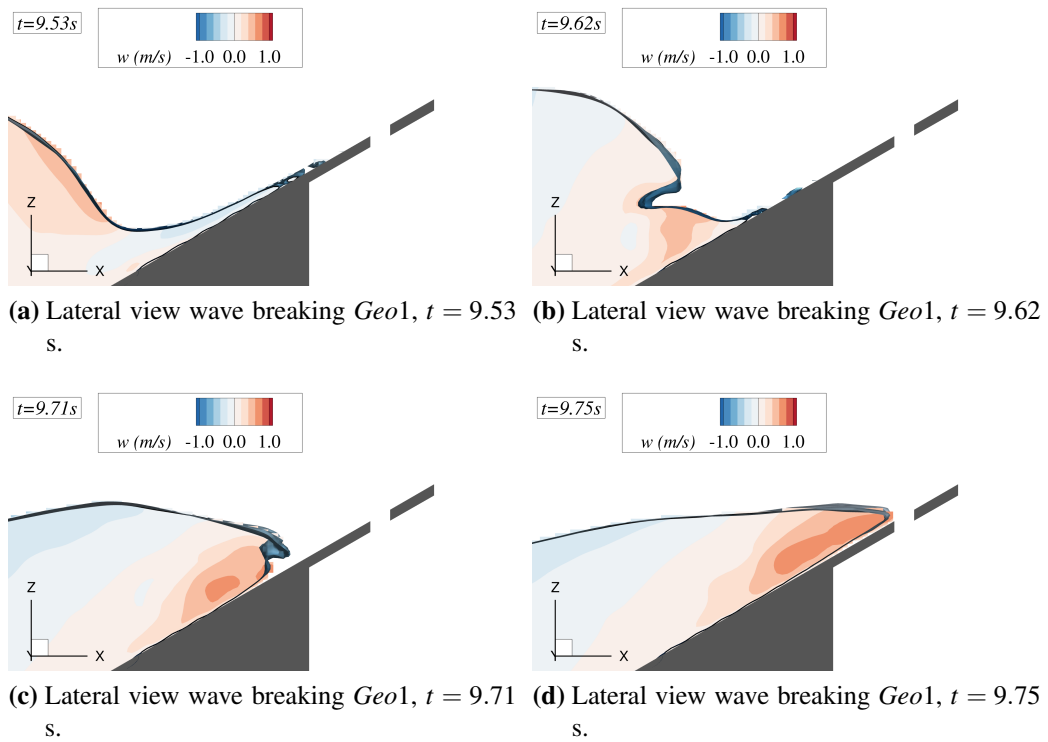


Figure 6.1: 3D and cross-section view of geometries *Geo1* and *Geo2*.

6.1.1 Results of new geometries

Figure 6.2 to figure 6.4 present sequences of the wave breaking process for *case250*, *Geo1* and *Geo2* respectively. The contours indicate the vertical velocity w , and the

water surface is presented in blue. It can be seen that in all cases, the wavefront curves due to the presence of the slope. A run-down flow is still present over the slope, indicated by the blue contours, in the three structures. The wavefront curls in the next instance; however, the curl in the 3 cases is not as important as the one generated in *case2_{Ru}*, see figure 5.8b, indicating a transition from a plunging-type breaking to a collapsing-type type. A more compact wavefront is observed in figure 6.3b, compared to *case2₅₀* and *Geo2*, especially compared to the latter. This more compact curl explains why no air entrapment is observed in figure 6.3c; in contrast, in *case2₅₀* and *Geo2*, air gets trapped in the flow after the wave plunges into the water head. In the last instance, a full run-up flow is achieved, and smoother water surface and higher vertical velocities are observed in figure 6.3d for *Geo1*. In figure 6.4 a significant volume of water is visualised in the step-down's vicinity. This volume of water doesn't flow through the gap smoothly; instead, it is trapped between the Lagrangian points, which are used in the IBM to generate the structure. This indicates that the Lagrangian points' density is insufficient to generate a non-slip condition in *Geo2*. This volume of water alters the run-up trajectory when the flow reaches its location, see figure 6.3d. In contrast, the water spills smoothly, and no volume is trapped between the Lagrangian points in *Geo1*.

**Figure 6.2:** Lateral view wave breaking *case2*₅₀.**Figure 6.3:** Lateral view wave breaking *Geo1*.

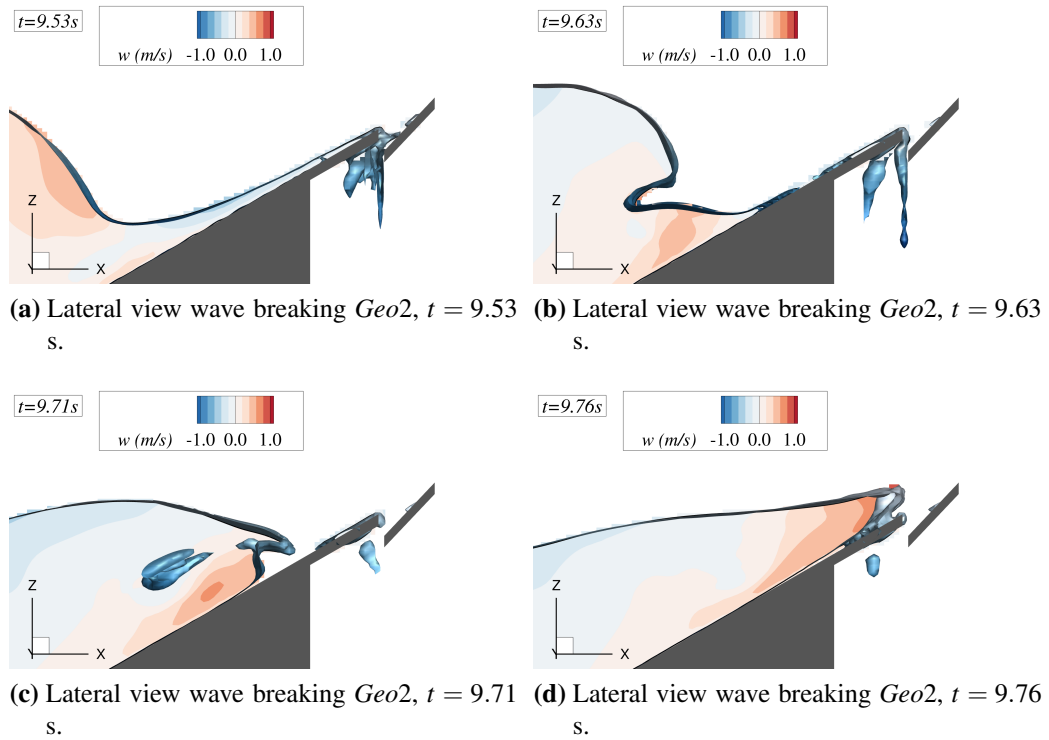


Figure 6.4: Lateral view wave breaking *Geo2*.

Figure 6.5 and figure 6.6 show the run-up and run-down flow passing over the gap and step-down in *Geo1* and *Geo2*, respectively. The contours indicate the vertical velocity w . In Figure 6.5a, the front of the flow leaps the gap without being disturbed. A slight deformation of the water surface and disturbance in the vertical velocities are visible behind the front of the flow. At $t = 9.82$ s, a clear downflow through the gap is observed, while overtopping is generated over the crest of the structure. At $t = 9.97$ s, a depression in the water surface over the gap is observed, and the flow is divided by the spill occurring through the gap. The contours still show positive velocities, but the gap divides the flow; in this instance, the upward flow below the gap contributes only to the spill through the gap, not the overtopping. In the last instance, the overtopping is finished, and the run-down flow is divided into two parts: one portion runs down to the front side of the structure, and the other runs through the gap to the rear of the structure. Figure 6.6 shows the results of *Geo2*. First, the run-up flow leaps over the step-down; however, the flow is affected by the water present on the crest of the lower section of the ramp; as explained

in the previous paragraph and shown in figure 6.4, a volume of water gets trapped between the Lagrangian points. Figure 6.6b shows the run-up flow interacting with the upper section of the flow. There, it is observed that the flow is divided into two parts; one part generates the overtopping, and the other part runs towards the gap. At $t = 9.97$ s, part of the run-up flow spills through the gap. However, the flow does not run smoothly as in *Geo1*. In the last snapshot, the overtopping is finished, and water is still observed in the upper section of the structure.

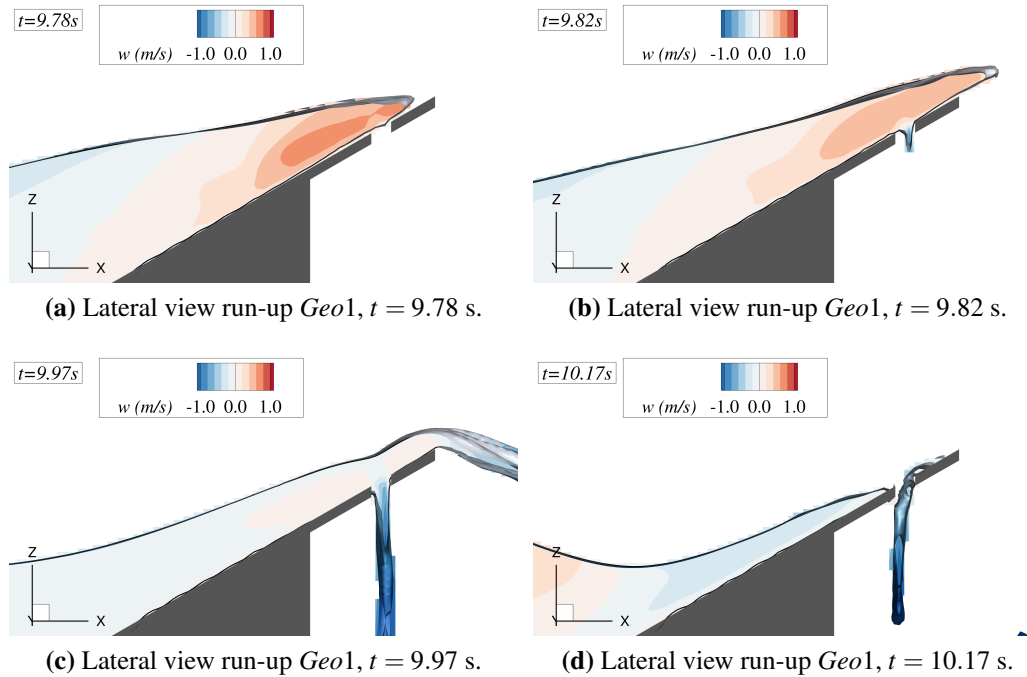


Figure 6.5: Lateral view run-up *Geo1*.

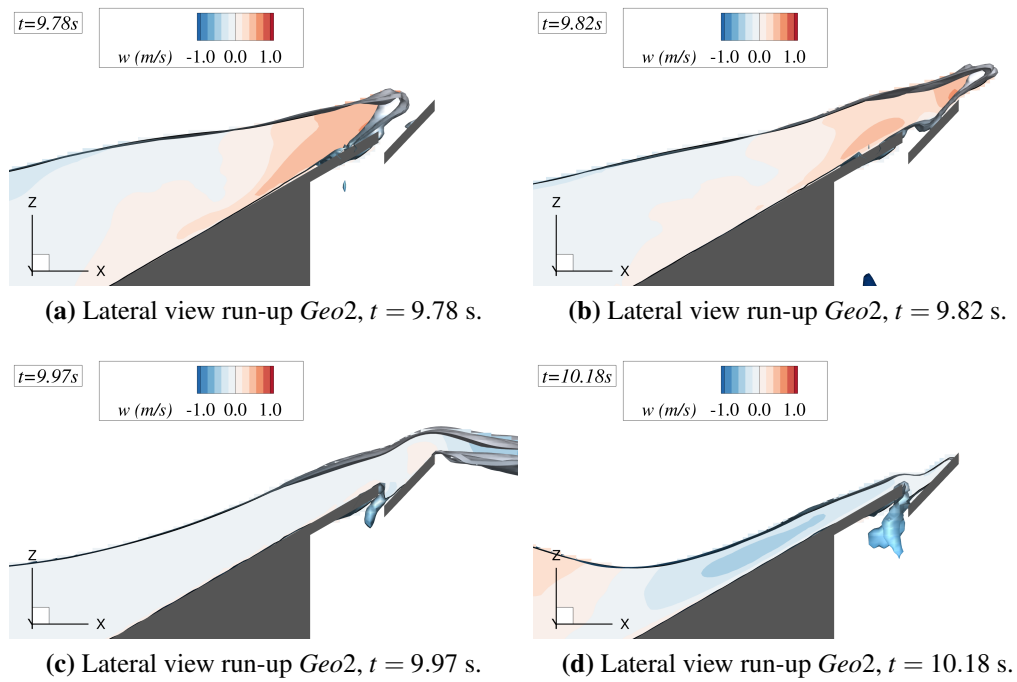


Figure 6.6: Lateral view run-up *Geo2*.

Figure 6.7 presents the phase average overtopping flow, f_{ov} (equation (5.1)), at the crest of the structures, as in figure 5.2, normalised by the peak overtopping flow, f_{max} , of *case250*. Results from *case250*, *Geo1* and *Geo2* are presented in black, red and blue, respectively. In all cases, it can be seen that the peak of the overtopping flow occurred near the first 20% of the wave period. During the first instances of the overtopping, the flow increases at similar rates in the three structures; however, a higher peak is reached in *case250*, followed by *Geo1*, with a reduction of 4% approximately, and *Geo2* with a 10% reduction approximately. After reaching the peak, the overtopping flow decreases at a similar rate to that of the increase stage. It is observed that the reduction of the overtopping flow for *Geo1* is sharper than for *Geo2*. A long tail is appreciated in *case250*; this behaviour is not observed in *Geo1* and *Geo2*. This means that including a gap in *Geo1* and *Geo2* geometries speeds up the end of the overtopping flow by decreasing the flow's peak and the duration of the overtopping flow. Table 6.1 presents the overtopping discharge, q , calculated for 12 waves at the crest of the structure and normalised by *case250* overtopping discharge. Both structures, *Geo1* and *Geo2*, generate a reduction of q by similar

factors. The overtopping flow in *Geo1* reaches a higher peak but decreases faster than *Geo2*; this behaviour results in similar values of q . It is important to note that the results of *Geo2* are affected by the unrealistic behaviour of the water near the step-down detected in figure 6.4 and figure 6.6, which doesn't allow a smooth flow through the gap. Considering the steeper angle of the upper section of the slope in *Geo2*, more water is expected to spill through the gap, accelerating the reduction of the overtopping flow.

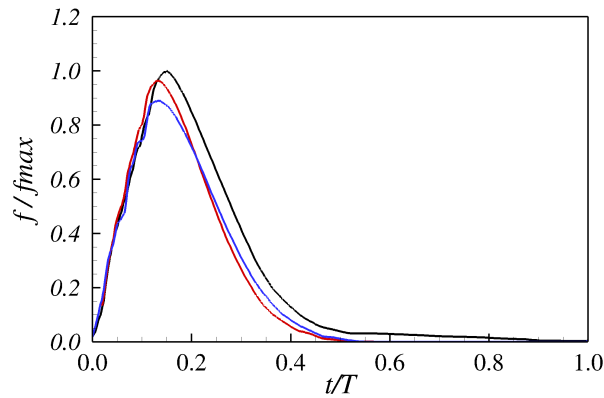


Figure 6.7: Phase average overtopping flow over the crest of the structure, normalised by the maximum flow in *case250*. Black line: *case250*, Red line: *Geo1*, Blue line: *Geo2*.

Table 6.1: Cases and overtopping discharge q normalised by *case250*

Case	$q/q_{case150}$
<i>Case250</i>	1.00
<i>Geo1</i>	0.859
<i>Geo2</i>	0.863

6.1.2 Conclusions of new geometries

Two novel structures have been simulated to evaluate the performance of Hydro3D-NWT and to analyse their effect on the overtopping discharge. As a base case *case250*, presented in 5.3, is used. The first structure, *Geo1*, includes a gap in the slope before the crest. In the second structure, *Geo2*, the slope is divided by a step-down, generating a vertical gap and a steeper upper section.

Hydro3D can realistically reproduce the breaking condition in the three structures. Concerning *Geo1*, the numerical code can simulate the water running through

the gap and overtopping to the rear side of the structure. In the case of *Geo2*, it is observed that a non-slip condition on the crest of the lower slope is not well generated, which causes part of the flow to get trapped between the Lagrangian points used to create the structure. This volume of water trapped around the lower slope's crest blocks the water's free flow through the gap. This problem could be solved by increasing the density of the Lagrangian points, thereby enhancing the impermeability of the structure interface, as it is detected in figure 5.4. To achieve this, it is necessary to increase the grid resolution. It is expected that a finer grid would help to reduce the problem, but it would also be at a significant computational cost. The current simulations require 24 hours running on UCL's supercomputer (Kathleen) to generate an 18-second simulation, allowing 13 fully developed overtopping events. A higher grid resolution, for example, a reduction by a quarter of the current grid size, applied across the entire domain, will reduce the duration of the simulation, yielding fewer overtopping events, and not enough information to evaluate the performance of the geometry. To address this limitation, it is imperative to implement a Local Mesh Refinement (LMR) compatible with LSM in the code. Several attempts were made to run LMR with LSM for this case, but were unsuccessful.

It is observed that *Geo1* generated a more compact wave breaking compared to *case2₅₀*. A reduction of the run-down generates this change because part of the volume that runs up the ramp is deflected through the gap. In *Geo2*, a significant change in the breaking process is not visible; this could be related to the problem detected on the crest of the lower slope. The overtopping discharge decreases in both structures compared to *case2₅₀* with a factor of 0.86 approximately, which would produce a reduction of the power available at the crest of the structure. Therefore, both structures fail to increase the power at the crest of the structure.

6.2 Conceptual designs

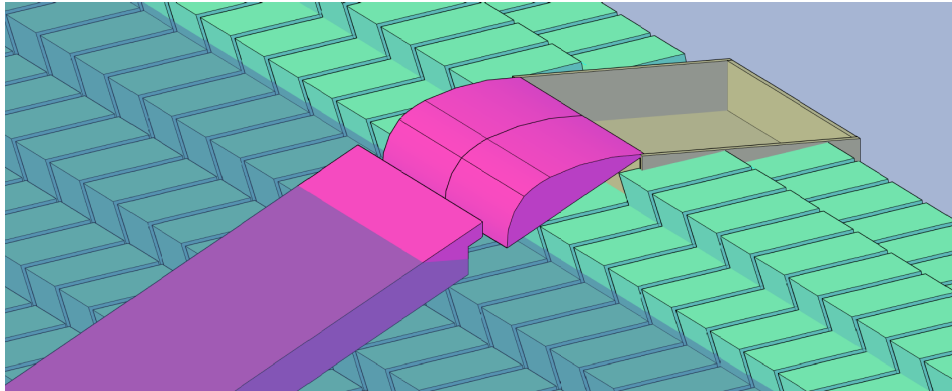
6.2.1 Concept 1

Figure 6.8 shows 3D views of the conceptual design 1 installed over a breakwater. In this design, the run-up ramp is divided into two sections. The lower part is a linear surface, and the upper is a curved surface. These two sections are separated by a gap that deflects the run-down flow into the permeable breakwater. A crucial aspect of the design of this structure is the dimension of the gap between the two sections, as detected in the previous simulations, figure 6.5 and figure 6.6. This distance must be sufficient to allow all the water over the upper section that didn't overtop the ramp to be discharged before the arrival of the next run-up event. On the other hand, this gap shouldn't affect the run-up flow, which limits the gap separation. The location of the gap is a crucial aspect to be designed; this should be located where the run-up flow has primarily an upward direction and high speed, so the waterfront would leap the gap, causing no water loss under the ramp. The gap needs to be higher on the slope from the breaking zone; what is shown in the simulations is that the plunging jet has a downward direction, which would lead to a significant loss of run-up flow. To evacuate all the run-down flow capture, the permeability of the breakwater needs to allow the water to filter before the occurrence of the next run-down event. This condition will be easily met as the outer layer of a breakwater is composed of large elements (rocks or concrete armoured) to generate a high wave dissipation. The scour under the run-up ramp will need to be controlled.

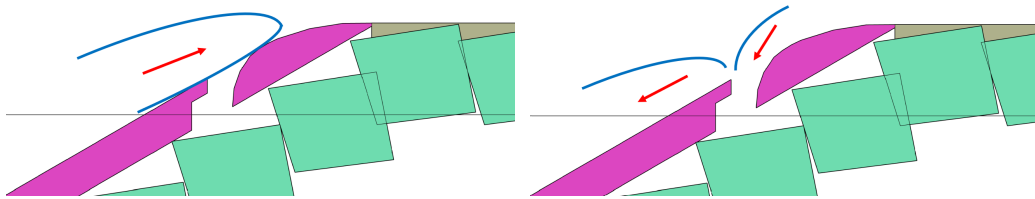
6.2.2 Concept 2

Figure 6.9 presents the conceptual design 2. In this case, the slope is equipped with blade-type sections that permit a smooth run-up flow and allow the deflecting of the run-down flow into the breakwater. The geometry of the blades (in this case, a curved surface is proposed) should be designed to affect the run-up flow as little as possible. The separation between the blades is a key aspect to be defined. In comparison to design 1, in this case, the gap between the blades is smaller, allowing

the inclusion of more gaps on the slope, which could permit more water absorption. Moreover, the distance between the blades could be variable on the slope, being smaller in the locations closer to the breaking zone and bigger where the fastest run-up flow occurs.



(a) 3D-view conceptual design 1.



(b) Lateral view conceptual design 1, run-up.

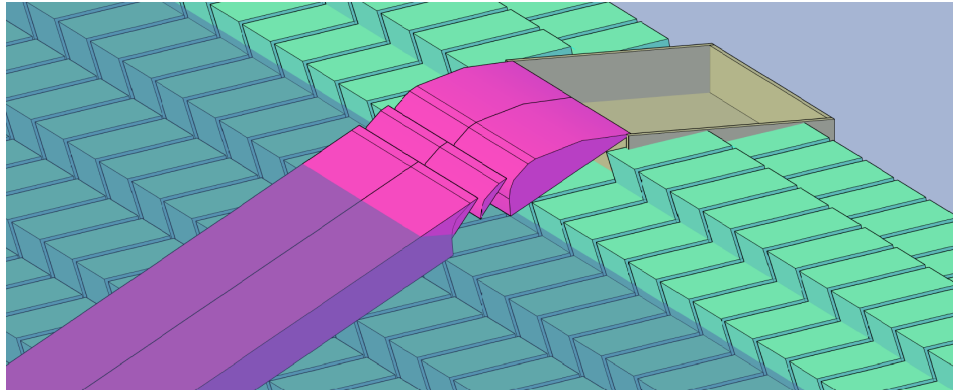
(c) Lateral view conceptual design 1, run-down.

Figure 6.8: 3D and lateral views conceptual design 1.

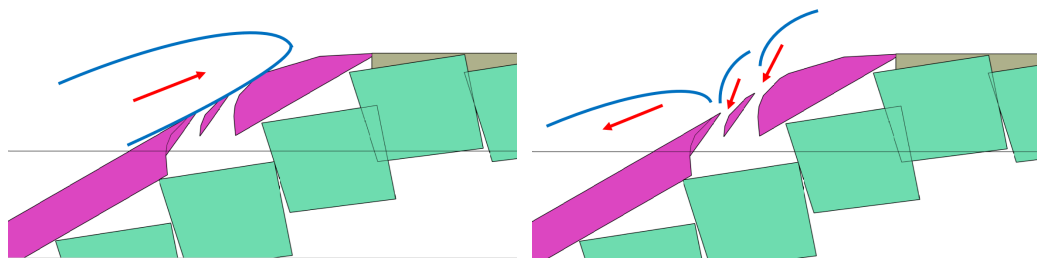
6.2.3 Concept 3

Figure 6.10 shows the conceptual design 3. In this case, the upper section is composed of a perforated plate. The results presented in section 6.1 show that a gap in the ramp can also affect the run-up flow, which involves a reduction of the overtopping discharge. This alternative includes holes in the upper ramps' surface to avoid elements that can significantly disturb the flow. Covering the perforations is included to prevent the reduction of the run-up. These protections have a smooth surface on the run-up side and are open on their upper side to maximise the run-down flow capture. In this case, the diameter and the density of the holes in the plate are critical for the run-down flow capture. The design of the geometry of

the protection is also crucial to reduce the effect on the run-up flow. Compared to designs 1 and 2, this alternative offers a less invasive solution to the run-up flow. However, the run-down capture capacity would be smaller than the previous alternatives. This solution could also be affected by marine life and sediments that can block the holes in the ramp, reducing its efficiency. More frequent maintenance would be required in this solution compared to alternatives 1 and 2.



(a) 3D-view conceptual design 2.



(b) Lateral view conceptual design 2, run-up.

(c) Lateral view conceptual design 2, run-down.

Figure 6.9: 3D and lateral views conceptual design 2.

6.2.4 Concept 4

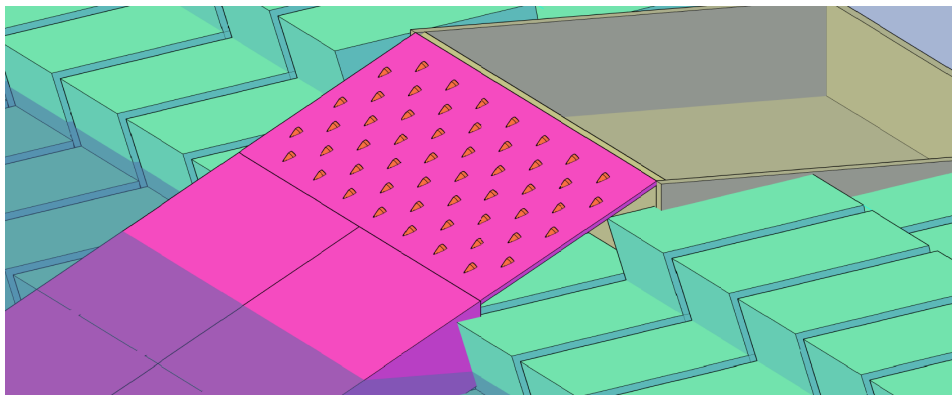
Figure 6.11 and figure 6.12 present the conceptual design 4. This proposal is a mechanism that includes opening gates to deflect the run-down flow. During the run-up event, the gates are closed, generating a flat surface so the run ramp operates like a regular ramp. When the run-up reaches the condition with no velocities, indicating the start of the run-down event, the gates open to evacuate the water over them and to allow the deflection of the run-down flow from the crest of the structure. As the gates are only open during the run-down, they can be placed lower in the

ramp, compared to alternatives 1 and 2, allowing for a more significant reduction of the run-down flow and, thus, decreasing the energy dissipation due to the interaction of the run-down flow and the incoming wave. More benefits can be obtained with this design; however, it is more complex than designs 1, 2 and 3, making it more prone to failure. The timing and mechanism of the opening and closing of the gates is the more challenging part of this device; it needs to operate in coordination with the run-up and run-down events, which are not periodic in natural sea conditions. In addition, the movement of the gates can be obstructed by sediments or marine life, affecting the operation of the device. Two ideas on how these gates can operate are presented; both work with the water flow and don't require an external power source.

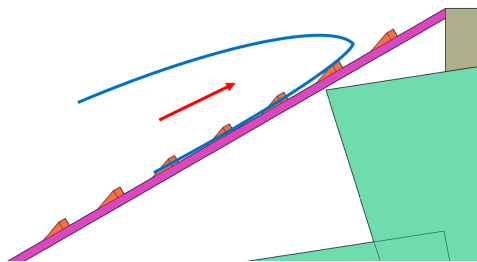
In alternative 1, figure 6.11, the gates are elaborated by flexible stripes. During the run-up event, these stripes overlap like a fish scale, allowing the flow to run up the ramp smoothly. During the run-down flow, the particle movement would flex the stripes up, exposing the gap to evacuate the run-down flow. When the run-down flow is finished, the stripes return to the original position, closing the gaps. The second alternative is a series of plates that can rotate around a pin, see figure 6.12. The rotation pin is shifted from the centre, allowing the plates to rest open. When the wave strikes with enough energy to reach the crest of the ramp, the momentum of the run-up flow will push the plates and close the gaps, permitting the flow to run up the ramp. When the flow loses momentum, the gates will open by their natural eccentricity and the weight of the water, allowing the evacuation of the run-down flow. The operation of this alternative will depend on the correct design of the plates and the location of the rotational axis, which allows a fast evacuation of the run-down flow but disturbs the less possible run-up flow. This alternative could also be affected by sediment and marine life, disrupting the smoothness of the plate rotations or obstructing the optimal closing of the gaps.

This alternative could significantly reduce the run-down flow but increase the system's complexity by including moving parts, which is always a cause for con-

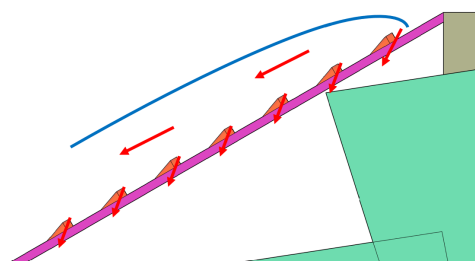
cern in any system working in the marine environment. One of the advantages of the OWEC is simplicity; therefore, this alternative reduces that advantage. However, a significant increase in the device's performance could justify an increase in the system's complexity.



(a) 3D-view conceptual design 3.



(b) Lateral view conceptual design 3, run-up.



(c) Lateral view conceptual design 3, run-down.

Figure 6.10: 3D and lateral views conceptual design 3.

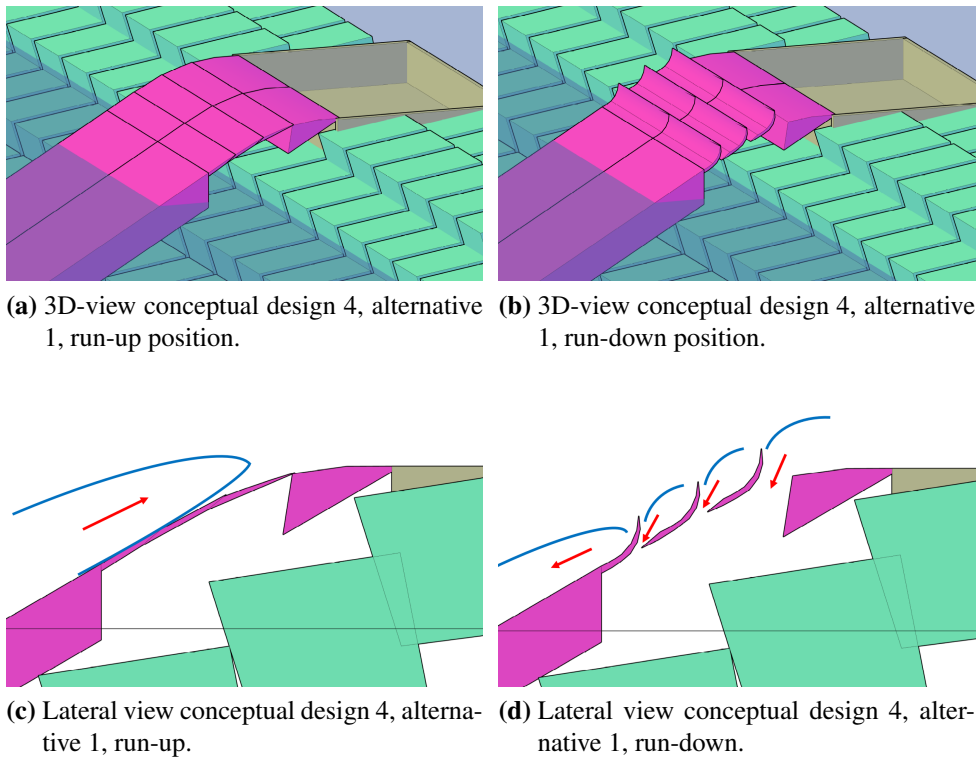


Figure 6.11: 3D and lateral views conceptual design 4, alternative 1.

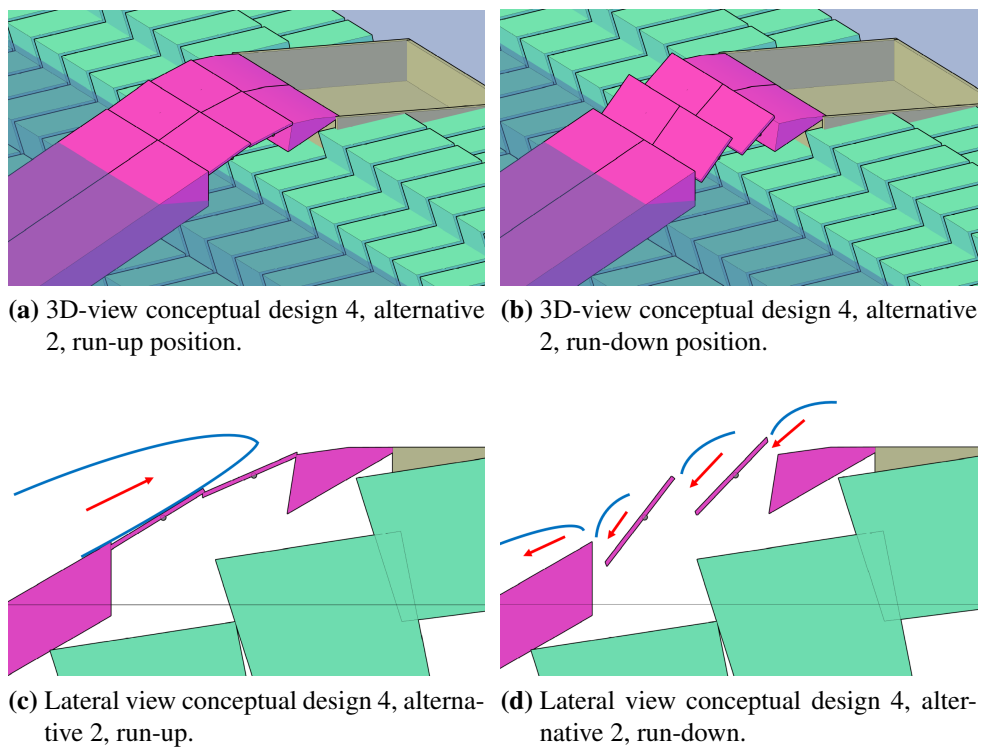


Figure 6.12: 3D and lateral views conceptual design 4, alternative 2.

6.3 Conclusions

In this chapter, two new geometries, *Geo1* and *Geo2*, have been simulated, and their performance in increasing the overtopping discharge has been evaluated. These new geometries include a gap in the slope that allows the flow over the ramp to be deflected below the structure, reducing the run-down flow. It has been found that the geometries tested can deflect the run-down flow, but they also significantly affect the run-up process. Therefore, the reduction of the run-down does not come with an increment of the overtopping discharge. It is important to note that no optimisation has been conducted to improve the structure's performance. They are intended to be a first iteration that allows the identification of critical aspects to be considered in the design.

The simulations conducted with the new geometries have allowed for the verification of the capability of Hydro3D-NWT to simulate complex wave/structure interaction, which in these cases includes wave breaking, run-up, overtopping, run-down and the flow through the gap included in the new geometries. Hydro3D-NWT has been able to simulate these complex scenarios, but critical aspects must be improved to allow the simulations of more complicated structures. The most important aspects are identified below:

- Fine grid resolution is needed for sharp edges to achieve a non-slip condition.
- Local Mesh Refinement (LMR) is a tool that allows for the refinement of the grid in the areas of the domain where it is needed and leaves a coarser grid where it is not required. This implementation allows for optimising the number of cells and the computational demand. In this research, a finer grid is required near and in the structure's location. In Hydro3D-NWT, an LMR is implemented; however, it is not entirely compatible with the LSM, demanding that all the subdomains where the water surface fluctuates must be in the finer grid. Therefore, it does not generate the desired benefits.

Four conceptual ramps have been proposed to improve the efficiency of an

OWEC. These new geometries aim to deflect the run-down flow, reducing the energy dissipation during the breaking process. The first structure includes a gap in the run-up ramp that seeks to deflect the run-down flow. The second structure includes blade-shaped elements in the slope, creating gaps on the ramp to absorb the rundown flow. The blades' inclination, separation, location and shape must be designed to allow the run-up to flow smoothly without introducing new turbulence that would lead to more energy dissipation. The following structure consists of a ramp equipped with perforations. The perforations are covered at an angle to prevent leaking water during the run-up event. The last concept that has been proposed includes moving blades, which are closed during the run-up flow and open for the run-down, deflecting the flow into the breakwater. From this alternative, a bigger rundown flow reduction can be achieved; however, it increases the complexity of the ramp, and its performance is susceptible to sediment and marine life.

Chapter 7

Conclusions and Further Works

7.1 Conclusions

This research has focused on investigating the hydrodynamics during wave-structure interaction. Two types of structure have been studied in detail: a submerged trapezoidal structure, representing a submerged breakwater, and a sloped structure with a positive freeboard, mimicking the run-up ramp of an OWEC. The water surface morphology, particle kinematics, turbulent structures, energy dissipation and forces acting on the structure have been evaluated with different geometries and wave conditions. An open-source LES-based numerical code, Hydro3D-NWT, has been employed to conduct the study. The chosen tool has allowed a detailed study of the wave structure interaction, including complex hydrodynamic processes such as wave shoaling, breaking, run-up, overtopping and run-down. Hydro3D-NWT's performance has been first validated with experimental data and well-established empirical formulations for each case of interest.

From the study of the submerged trapezoidal structure, and for the wave condition studied, the following conclusions can be made:

- Different geometries of the front slope can affect the shoaling process, increasing or decreasing the wave height reached over the structure. The present study found that cubic and convex front slope shapes can generate the highest waves over the berm of the submerged structure. On the other hand, a concave

geometry of the front slope produces smaller waves.

- Different turbulent structures near the surface of the solid were detected. These structures are located near the transition from the front slope to the horizontal berm. The formation of one main eddy was detected over the structure's nose in the linear and concave geometries. On the other hand, a group of smaller eddies is formed over the cubic and convex slopes. The generation of eddies occurs under the crest and trough of the waves. Under the crest, a clockwise rotation was detected, and anticlockwise under the trough.
- The stability of the structure is affected by the geometry of the front slope. The forces near the nose of the structure have been specially analysed; it was found that the horizontal forces are increased by more than 3.0 times with the concave geometry compared to the linear case. The convex slope produces a reduction factor of 0.18 concerning the linear case.
- Different geometries of the front slope can produce a time shift of the peaks of the horizontal and vertical forces; this variation affects the moment stability of the structure. In the convex geometry, a reduction of the Y moment is detected, and an amplification of the Y moment is produced with the concave shape.

This finding indicates that the geometry of the front slope is a relevant element in the performance of the submerged breakwater. It speeds or slows the shoaling process, generates different turbulent fields near the structure's surface, and alters its stability. Therefore, it affects the structure's response to the waves' actions. Correctly selecting the structure's geometry can extend the structure's life and improve its efficiency as a breakwater.

From the study related to the interaction of waves with a sloped surface, presented in chapter 5, and for the wave conditions studied, the following findings can be highlighted:

- The run-down flow generated during the wave structure interaction and after the run-up flow plays a significant role in the energy dissipation during the breaking process. The run-down flow interaction with the incoming wave contributes to the generation of turbulence at the base of the incoming wave.
- Additionally, the run-down flow foments the formation of plunging breaking type. The flow running down the slope slows down the base of the incoming wave, generating the wave's crest to plunge over the front. The collapse of the water jet is related to significant perturbations in the flow, which produce high turbulence, air entrapment and an abrupt change in the direction of the front of the water tongue. In addition, the presence of a large curl contributes to trapping air inside the water when the front of the wave collapses, increasing the flow turbulence. All these phenomena that occur during the breaking of a wave contribute to increased energy dissipation. Decreasing the run-down flow can reduce or prevent the curl of the wave crest, creating a more compact breaking. This change reduces the energy losses and promotes a stronger run-up flow, increasing the overtopping discharge.
- The run-down flow is important in defining the breaking type. Strong run-down flows promote the generation of a plunging kind of breaking. On the contrary, weak, run-down flows allow for a more compact and less violent wave-breaking.

These findings indicate that reducing the run-down flow can decrease the energy losses during the breaking and early stages of the run-up flow, leading to more water overtopping the structure, increasing the power available at the crest of the ramp, and improving the performance of an OWEC. The results show that the improvement can be more significant in conditions with an Irribarren number less than 2.5.

The results indicate that reducing the run-down flow would benefit the operation of an OWEC. A series of novel run-up ramp geometries have been elaborated.

These geometries aim to deflect the run-down flow to reduce energy losses. Two geometries have been simulated using Hydro3D-NWT, and their performance in increasing the overtopping discharge has been evaluated. Both geometries could deflect the run-down, but one generated a more significant change in the breaking condition compared to the reference case, reducing the curl of the wavefront and the air entrapment. However, no increment in the overtopping discharge was achieved. A redesign of the geometries is needed. Four conceptual designs of run-up ramps have been elaborated and presented as 3D sketches.

Throughout this research, the capability of the LES open code Hydro3D-NWT has been tested in complex wave structure interaction, and the following remarks on its performance can be highlighted:

- Hydro3D-NWT accurately reproduce regular waves according to the 2nd order Stokes Waves.
- In the present research Hydro3D-NWT was used for the first time to simulate wave breaking, run-up, run-down and overtopping. The results show a remarkable capability of the code to simulate complex hydrodynamics processes.
- The inclusion of structures with the IBM increases the numerical complexity of the simulations. This increment is especially significant when the structure pierces the water surface. In this case, the LSM and the IBM interact in the same zone, which can create errors or unrealistic results. The grid resolution and the width of the transition zone in the LSM are key parameters that need to be adjusted to obtain good-quality results.
- The grid resolution affects the capacity of the IBM to simulate a non-slip condition in the interface water structure. Complex simulations and intricate structure geometries require fine grids, increasing the computational time to run the simulations. A balance between accuracy and computational demand needs to be found in each case study.

- During the multiple iterations conducted with Hydro3D-NWT to define a better set-up of the simulations, a problem was identified in the LSM when more than two interfaces interact. An unrealistic shape of the wavefront was detected when the waves curl over the slope, and two or more interfaces (water/air) interact when the curl closes. This issue was solved by reducing the width of the interface used in the LSM, testing different interpolation functions used in the IBM, and reducing the water depth downstream of the slope's surface.
- During the spilling of the water to the rear of the structure, a tendency to dissipate water volume was detected. This means water drops reduce their volume and mass as they fly through the air before falling into the main water volume.

Interest in OWEC has increased in the last few years, with new studies and a full-size project currently underway. The low efficiency of these devices is a key aspect that needs to be improved to make this technology more attractive for researchers and investors. The present study has investigated the role of the run-down flow in the energy dissipation that occurs on the run-up ramp of an OWEC. Results obtained with periodic waves show that the efficiency of an OWEC can be improved by decreasing the run-down flow. Conceptual ideas to accomplish this reduction of the run-down flow have been elaborated and presented in the present thesis. These solutions, plus other alternatives such as curve slopes and converging walls, which have been studied in previous research found in the literature, can improve the efficiency of an OWEC, making them a more attractive WEC to be considered in future studies and projects.

A diverse energy matrix is needed to accomplish the energy plans established by several countries, including the EU. Wave energy can potentially be an important contributor to the energy matrix. However, the wave energy industry has not grown at the speed that other renewable energy industries have. The high risk and costs of this project explain the slower pace. Continuing research to improve the operation

of WECs, especially those that can operate in easily accessible locations, as presented in this thesis, can instigate the development of the WE industry, helping to achieve energy goals.

7.2 Further Works

The results obtained from this study can have significant applications in coastal engineering, especially in the design of OWECs. However, more research is needed to validate the results completely. The following list highlights the main works needed to continue this research:

- Conduct physical models to generate experimental data to validate Hydro3D-NWT results near the structure's surface in more detail, including wave breaking, overtopping, run-up and run-down flows.
- Expand the wave conditions studied to a broader range of the Irrabaren number, focusing on values higher than 0,5, which are more characteristic of coastal structures. In addition, including irregular waves is needed to evaluate a more realistic improvement in the efficiency of OWECs.
- Expand the structure geometries studied, including gentler slopes representing OWEC run-up ramp. Curve geometries are also interesting because previous studies have detected their positive effect in increasing the overtopping discharge.
- Implement a Local Mesh Refinement compatible with the LSM in Hydro3D-NWT. This tool will allow for the optimisation of the grid, permitting it to refine the grid only in the needed locations. This improvement is of great importance for studying more complex geometries.
- Conduct a physical model to study and prove the conceptual designs. At first instance, a similar experimental set-up as the one presented in [?] can be conducted, but in case of the permeable slope, only perforate the upper

sections of the slope so as not to alter the breaking zone and the early stages of the run-up flow.

- Numerical optimisation of the new geometries presented in chapter 6. To conduct this study, implementing an LMR is imperative; this will allow for the evaluation of different gap dimensions and locations in the slope, to soften the sharp edges of the structure.
- Explore the relation between V_o (overtopping volume per wave) and the overtopping mean discharge q to reformulate plot 5.19.
- To improve the study of overtopping flows, the LSM mass conservation limitation must be addressed. In the present project, this issue was not a relevant problem, but it was detected in the spillage process at the rear of the structure. If the study of the overtopping is to be expanded to the characterisation of post-overtopping flows, for example, spilling into a reservoir of an OWEC, the mass conservation needs to be verified.

Bibliography

- [1] Beyá J., Álvarez M., Gallardo A., Hidalgo H., Aguirre C., Valdivia J., Parra C., Méndez L., Contreras F., Winckler P., and Molina M. Atlas de oleaje de Chile. primera edición. *Valparaíso, Chile, Escuela de Ingeniería Civil Oceánica - Universidad de Valparaíso*, 2016.
- [2] US Army Corps of Engineers. Water wave mechanics em 1110-2-11000 (part 2), 2008.
- [3] Judith Bosboom and Marcel J. F. Stive. *Coastal Dynamics*. TU Delft Open, 2021.
- [4] K. N. Granthem. A model study of wave run-up on sloping structures, technical report. Series 3, Issue 348, Institute of Eng., Univ. of California. California, 1953.
- [5] T. Saville Jr. Laboratory data on wave run-up and overtopping on shore structure. technical memorandum. *Washington, DC, USA: Beach Erosion Board, US army Corps of Engineering*, 1955.
- [6] T. W. Hsu, S. J. Liang, B. D. Young, and S. H. Ou. Nonlinear run-ups of regular waves on sloping structures. *Natural Hazards and Earth System Science*, 12:3811–3820, 2012.
- [7] Alejandro Hammeken Arana. Wave run-up on beaches and coastal structures. 2017.
- [8] Kester Gunn and Clym Stock-Williams. Quantifying the global wave power resource. *Renewable Energy*, 44:296–304, 8 2012.

- [9] Patricio Monárdez, Hugo Acuña, and Doug Scott. Evaluation of the potential of wave energy in chile. volume 6, pages 801–809, 2008.
- [10] Felipe Lucero, Patricio A. Catalán, Álvaro Ossandón, José Beyá, Andrés Puelma, and Luis Zamorano. Wave energy assessment in the central-south coast of chile. *Renewable Energy*, 114:120–131, 2017.
- [11] Aurélien Babarit. *Ocean Wave Energy Conversion Resource, Technologies and Performance*. ISTE Press Ltd. and Elsevier Ltd., 2017.
- [12] The Queen’s University of Belfast. Islay limpet wave power plant. Technical report, 2002.
- [13] E. Medina-López, W. Allsop, A. Dimakopoulos, and T. Bruce. Damage to the mutriku owc breakwater – some lessons from further analysis. pages 957–967, 1 2018.
- [14] Bernard Multon Aurélien Babarit Alain Clément Judicael Aubry, Hamid Ben Ahmed. Wave energy converters. *Bernard Multon. Marine renewable energy handbook*, 2011.
- [15] António F.de O. Falcão. Wave energy utilization: A review of the technologies. *Renewable and Sustainable Energy Reviews*, 14:899–918, 4 2010.
- [16] Yongxing Zhang, Yongjie Zhao, Wei Sun, and Jiaxuan Li. Ocean wave energy converters: Technical principle, device realization, and performance evaluation. *Renewable and Sustainable Energy Reviews*, 141, 5 2021.
- [17] L. Margheritini, D. Vicinanza, and P. Frigaard. Ssg wave energy converter: Design, reliability and hydraulic performance of an innovative overtopping device. *Renewable Energy*, 34:1371–1380, 5 2009.
- [18] P. Oliveira, F. Taveira-Pinto, T. Morais, and P. Rosa-Santos. Experimental evaluation of the effect of wave focusing walls on the performance of the sea-wave slot-cone generator. *Energy Conversion and Management*, 110:165–175, 2 2016.

- [19] Zhen Liu, Zhi Han, Hongda Shi, and Wanchang Yang. Experimental study on multi-level overtopping wave energy convertor under regular wave conditions. *International Journal of Naval Architecture and Ocean Engineering*, 10:651–659, 9 2018.
- [20] Zhi Han, Zhen Liu, and Hongda Shi. Numerical study on overtopping performance of a multi-level breakwater for wave energy conversion. *Ocean Engineering*, 150:94–101, 2 2018.
- [21] D Vicinanza, D Stagonas, G Müller, J H Nørgaard, and T L Andersen. Innovative breakwaters design for wave energy conversion. *Coastal Engineering*, 2012.
- [22] Claudio Iuppa, Pasquale Contestabile, Luca Cavallaro, Enrico Foti, and Diego Vicinanza. Hydraulic performance of an innovative breakwater for overtopping wave energy conversion. *Sustainability (Switzerland)*, 8, 2016.
- [23] M. Azlan Musa, A. Yazid Maliki, M. Fadhli Ahmad, W. Nik Sani, Omar Yaakob, and K. B. Samo. Numerical simulation of wave flow over the overtopping breakwater for energy conversion (obrec) device. *10th International Conference on Marine Technology, MARTEC 2016*, 194:166–173, 2017.
- [24] M. A. Musa, M. F. Roslan, M. F. Ahmad, A. M. Muzathik, M. A. Mustapa, A. Fitriadhy, M. H. Mohd, and M. A.A. Rahman. The influence of ramp shape parameters on performance of overtopping breakwater for energy conversion. *Journal of Marine Science and Engineering*, 8:1–18, 11 2020.
- [25] Z. L. Zou, H. Jin, L. Zhang, M. Z. Xie, J. C. Lv, and Y. Zhang. Horizontal 2d fully dispersive nonlinear mild slope equations. *Ocean Engineering*, 129:581–604, 2017.
- [26] Christoph Kost, Paul Muller, Jael Sepulveda Schweiger, Verena Fluri, and Jessica Thomsen. Study: Levelized cost of electricity- renewable energy technologies. *Fraunhofer Institute for Solar Energy System ISE*, 2024.

- [27] Lazard and Roland Berger. Lcoe levelized cost of energy version 17.0, 2024.
- [28] S. Astariz, A. Vazquez, and G. Iglesias. Evaluation and comparison of the levelized cost of tidal, wave, and offshore wind energy. *Journal of Renewable and Sustainable Energy*, 7, 9 2015.
- [29] Chenglong Guo, Wanan Sheng, Dakshina G. De Silva, and George Aggidis. A review of the levelized cost of wave energy based on a techno-economic model, 3 2023.
- [30] Christian Santana, Mark Falvey, Marcelo Ibarra, and Monserrat Garcia. Energías renovables en chile. potencial eolico, solar e hidroelectrico de arica a chiloe. *Ministerio de Energia Chile*, 2014.
- [31] Y Torre-Enciso, I Ortubia, L I López De Aguilera, and J Marqués. Mutriku wave power plant: from the thinking out to the reality.
- [32] Pasquale Contestabile, Gaetano Crispino, Enrico Di Lauro, Vincenzo Ferrante, Corrado Gisonni, and Diego Vicinanza. Overtopping breakwater for wave energy conversion: Review of state of art, recent advancements and what lies ahead. *Renewable Energy*, 147:705–718, 3 2020.
- [33] Tunde Aderinto and Hua Li. Review on power performance and efficiency of wave energy converters, 11 2019.
- [34] Jens Peter Kofoed. Wave overtopping of marine structures utilization of wave energy. *Hydraulics Coastal Engineering Laboratory, Department of Civil Engineering, Aalborg University*, 2002.
- [35] Aristos Christou, Thorsten Stoesser, and Zhihua Xie. A large-eddy-simulation-based numerical wave tank for three-dimensional wave-structure interaction. *Computers and Fluids*, 231, 12 2021.
- [36] David R Basco and M Asce. A qualitative description of wave breaking. *J. Waterway, Port, Coastal Eng.*, pages 171–188, 1985.

- [37] P C M Jansen. Laboratory observations of the kinematics in the aerated region of breaking waves. 1986.
- [38] Francis C K Ting and James T Kirby. Coastal engineering observation of undertow and turbulence in a laboratory surf zone. 1994.
- [39] Robert M. Sorensen. *Basic Coastal Engineering*. Springer, 2006.
- [40] Stokes George. On the theory of oscillatory waves. pages 197–229, 1847.
- [41] Zhi Yao Song, Hong Jun Zhao, Ling Li, and Guo Nian Lü. On the universal third order stokes wave solution. *Science China Earth Sciences*, 56:102–114, 1 2013.
- [42] John D Fenton'. A fifth-order stokes theory for steady waves. *Journal of Waterway, Port, Coastal and Ocean Engineering*, Vol. 111, pages 216–234, 1985.
- [43] J D Fenton. Nonlinear wave theories. *Ocean Engineering Science, The Sea*, Vol9, 1990.
- [44] *EurOtop Manual on wave overtopping of sea defences and related structures*. 2018, www.overtopping-manual.com.
- [45] M.R.A. Van Gent, B. Pozueta, H.F.P. Van den Boogaard, and J.R. Medina. *Prediction method Neural network modelling of wave overtopping at coastal structures, Project: Clash*. Deltares (WL), <http://resolver.tudelft.nl/uuid:8213517a-30d0-491e-9aa8-d3725e664add>, 2005.
- [46] Ira A. Hunt. Design of seawalls and breakwaters. *U S Lake Survey and U S Army*, 1958.
- [47] Holger Friedrich Rolf Schüttrumpf. Wellenüberlaufströmung bei seedeichen-experimentelle und theoretische untersuchungen. 2001.

- [48] Javier L. Lara, Inigo J. Losada, and Philip L.F. Liu. Breaking waves over a mild gravel slope: Experimental and numerical analysis. *Journal of Geophysical Research: Oceans*, 111, 11 2006.
- [49] Hiroyoshi Shi-Igai and Hsu Rong-Chung. An analytical and computer study on wave overtopping. *Coastal Engineering*, 1:221, 1977.
- [50] J Richard Weggel. Wave overtopping equation. *15th Int. Conf. on Coastal Engineering*, (pp. 2737-2755). Honolulu, 1976.
- [51] US Army Coastal Engineering Centre. Shore protection manual. 1984.
- [52] Design of seawalls for wave overtopping. Technical report, Hydraulics Research Station Wallingford, 1980.
- [53] J P De Waal and J W Van Der Meer. Wave runup and overtopping on coastal structures. *Coastal Engineering*, 1992.
- [54] M. R. A. van Gent. *Wave Interaction with Permeable Coastal Structures*. PhD thesis, Delft University of Technology, 1995.
- [55] T W Thorpe. A brief review of wave energy a report produced for the uk department of trade and industry. *ETSU*, 1999.
- [56] Steve Barstow, Jan Petter Mathisen, Stephen Barstow, Gunnar Mørk, and Lasse Lønseth. Worldwaves wave energy resource assessments from the deep ocean to the coast. *8th European wave and tidal energy conference, Uppsala, Sweden*, pages 149–159, 2011.
- [57] Garrad Hassan and Partners Limited. Preliminary site selection-chilean marine energy resources. Technical report, Inter-American Development Bank, 2009.
- [58] H. Acuña, P. Monárdez, and D. Zimmer. Wave energy map in intermediate and shallow water depth in chile based on a 30 year long validated 2d spectral

- hindcast of the pacific ocean. In *4th International Conference on Ocean Energy, 17 October, Dublin, 2012*.
- [59] D. G. Mediavilla and D. Figueroa. Assessment, sources and predictability of the swell wave power arriving to chile. *Renewable Energy*, 114:108–119, 2017.
- [60] E. Di Lauro, P. Contestabile, and D. Vicinanza. Wave energy in chile: A case study of the overtopping breakwater for energy conversion (obrec). *Proceedings of the 12th European Wave and Tidal Energy Conference 27th Aug -1st Sept 2017, Cork, Ireland*.
- [61] Diego Vicinanza, Enrico Di Lauro, Pasquale Contestabile, Corrado Gissoni, Javier L. Lara, and Inigo J. Losada. Review of innovative harbor breakwaters for wave-energy conversion. *Journal of Waterway, Port, Coastal, and Ocean Engineering*, 145, 7 2019.
- [62] Gabriel Ibarra-Berastegi, Jon Sáenz, Alain Ulazia, Paula Serras, Ganix Esnaola, and Carlos Garcia-Soto. Electricity production, capacity factor, and plant efficiency index at the mutriku wave farm (2014–2016). *Ocean Engineering*, 147:20–29, 1 2018.
- [63] Jens Peter Kofoed, Diego Vicinanza, and Espen Osaland. Estimation of design wave loads on the ssg wec pilot plant based on 3-d model tests. *The proceedings of the Sixteenth (2006) International Offshore and Polar Engineering Conference: ISOPE : San Francisco, [California] USA, 2006*.
- [64] Diego Vicinanza, D Vicinanza, P Contestabile, and E Di Lauro. Overtopping breakwater for wave energy conversion: Status and perspective cfd modeling of wave loadings on wave energy converters view project prince view project overtopping breakwater for wave energy conversion: Status and perspective. 2017.

- [65] Pasquale Contestabile, Ferrante Vincenzo, Enrico Di Lauro, and Diego Vicinanza. Full-scale prototype of an overtopping breakwater for wave energy conversion. *Coastal Engineering Proceedings*, page 12, 6 2017.
- [66] Giuseppina Palma, Pasquale Contestabile, Barbara Zanuttigh, Sara Mizar Formentin, and Diego Vicinanza. Integrated assessment of the hydraulic and structural performance of the obrec device in the gulf of naples, italy. *Applied Ocean Research*, 101, 8 2020.
- [67] Diego Vicinanza, Lucia Margheritini, Jens Peter Kofoed, and Mariano Bucicino. The ssg wave energy converter: Performance, status and recent developments. *Energies*, 5:193–226, 2012.
- [68] Diego Vicinanza, Pasquale Contestabile, Jørgen Quvang Harck Nørgaard, and Thomas Lykke Andersen. Innovative rubble mound breakwaters for overtopping wave energy conversion. *Coastal Engineering*, 88:154–170, 2014.
- [69] Enrico Di Lauro, Javier L. Lara, Maria Maza, Inigo J. Losada, Pasquale Contestabile, and Diego Vicinanza. Stability analysis of a non-conventional breakwater for wave energy conversion. *Coastal Engineering*, 145:36–52, 3 2019.
- [70] Enrico Di Lauro, Maria Maza, Javier L. Lara, Inigo J. Losada, Pasquale Contestabile, and Diego Vicinanza. Advantages of an innovative vertical breakwater with an overtopping wave energy converter. *Coastal Engineering*, 159, 8 2020.
- [71] Akio Okayasu, Takayuki Suzuki, and Yuriko Matsubayashi. Laboratory experiment and three-dimensional large eddy simulation of wave overtopping on gentle slope seawalls. *Coastal Engineering Journal*, 47:71–89, 2005.
- [72] Sibel Kara, Thorsten Stoesser, Terry W. Sturm, and Saad Mulahasan. Flow dynamics through a submerged bridge opening with overtopping. *Journal of Hydraulic Research*, 53:186–195, 3 2015.

- [73] Zhihua Xie. A two-phase flow model for three-dimensional breaking waves over complex topography. *Proceedings of the Royal Society A: Mathematical, Physical and Engineering Sciences*, 471, 8 2015.
- [74] Zheyu Zhou, Tian Jian Hsu, Daniel Cox, and Xiaofeng Liu. Large-eddy simulation of wave-breaking induced turbulent coherent structures and suspended sediment transport on a barred beach. *Journal of Geophysical Research: Oceans*, 122:207–235, 1 2017.
- [75] N. N. Peng and K. W. Chow. A numerical wave tank with large eddy simulation for wave breaking. *Ocean Engineering*, 266, 12 2022.
- [76] Thorsten Stoesser, Richard McSherry, and Bruno Fraga. Secondary currents and turbulence over a non-uniformly roughened open-channel bed. *Water (Switzerland)*, 7:4896–4913, 2015.
- [77] Bruño Fraga, Thorsten Stoesser, Chris C.K. Lai, and Scott A. Socolofsky. A les-based eulerian-lagrangian approach to predict the dynamics of bubble plumes. *Ocean Modelling*, 97:27–36, 1 2016.
- [78] Pablo Ouro and Thorsten Stoesser. An immersed boundary-based large-eddy simulation approach to predict the performance of vertical axis tidal turbines. *Computers and Fluids*, 152:74–87, 7 2017.
- [79] Aristos Christou, Zhihua Xie, Thorsten Stoesser, and Pablo Ouro. Propagation of a solitary wave over a finite submerged thin plate. *Applied Ocean Research*, 106, 1 2021.
- [80] Santiago Martelo Lopez, Aristos Christou, Shunqi Pan, Thorsten Stoesser, and Zhihua Xie. A new ghost-cell/level-set method for three-dimensional flows. *Journal of Computational Physics*, 499:112710, 2 2024.
- [81] M. Cevheri, R. McSherry, and T. Stoesser. A local mesh refinement approach for large-eddy simulations of turbulent flows. *International Journal for Numerical Methods in Fluids*, 82:261–285, 10 2016.

- [82] M. F. Roslan, M. F. Ahmad, and M. A. Musa. Investigation on reflected wave by different geometrical ramp shape of overtopping break water for energy conversions using experimental and simulation. volume 676. IOP Publishing Ltd, 12 2019.
- [83] Alexandre Joel Chorin. Numerical solution of the Navier-Stokes equations. *Mathematics of Computation*, 22(104):745–745, 1968.
- [84] F. Nicoud and F. Ducros. Subgrid-scale stress modelling based on the square of the velocity gradient tensor. *Flow, Turbulence and Combustion*, 62(3):183–200, 1999.
- [85] Stanley Osher and James A. Sethian. Fronts propagating with curvature-dependent speed: Algorithms based on Hamilton-Jacobi formulations. *Journal of Computational Physics*, 79(1):12–49, 1988.
- [86] Chi-Wang Shu. High Order Weighted Essentially Nonoscillatory Schemes for Convection Dominated Problems. *SIAM Review*, 51(1):82–126, 2009.
- [87] S. Osher M. Sussman, P. Smereka. A level set approach for computing solutions to incompressible two-phase flow. *Journal of Computational Physics*, 114(1):146–159, sep 1994.
- [88] Ruidong An, Shengji Yu, Ching hao Yu, and Wenkang Meng. Numerical simulation of breaking wave propagation under various gate lifting speeds by a level set method. *Ocean Engineering*, 312, 11 2024.
- [89] A. Salih and S. Ghosh Moulic. A mass conservation scheme for level set method applied to multiphase incompressible flows. *International Journal for Computational Methods in Engineering Science and Mechanics*, 14:271–289, 6 2013.
- [90] Z. H. Gu, H. L. Wen, C. H. Yu, and Tony W.H. Sheu. Interface-preserving level set method for simulating dam-break flows. *Journal of Computational Physics*, 374:249–280, 12 2018.

- [91] Kaustubh Khedkar, Amirreza Charchi Mamaghani, Pieter Ghysels, Neelesh A. Patankar, and Amneet Pal Singh Bhalla. Preventing mass loss in the standard level set method: New insights from variational analyses. 4 2024.
- [92] William J Rider and Douglas B Kothe. Reconstructing volume tracking 1. Technical report, 1998.
- [93] Ruben Scardovelli and Stéphane Zaleski. Direct numerical simulation of free-surface and interfacial flow. *Annual Review of Fluid Mechanics*, 31:567–603, 1999.
- [94] Heebum Lee and Shin Hyung Rhee. A dynamic interface compression method for vof simulations of high-speed planing watercraft. *Journal of Mechanical Science and Technology*, 29:1849–1857, 5 2015.
- [95] Markus Uhlmann. An immersed boundary method with direct forcing for the simulation of particulate flows. *Journal of Computational Physics*, 209(2):448–476, nov 2005.
- [96] Alexandre M. Roma, Charles S. Peskin, and Marsha J. Berger. An Adaptive Version of the Immersed Boundary Method. *Journal of Computational Physics*, 153(2):509–534, aug 1999.
- [97] Xiaolei Yang, Xing Zhang, Zhilin Li, and Guo Wei He. A smoothing technique for discrete delta functions with application to immersed boundary method in moving boundary simulations. *Journal of Computational Physics*, 228:7821–7836, 11 2009.
- [98] Kensuke Yokoi, Ryo Onishi, Xiao-Long Deng, and Mark Sussman. Density-Scaled Balanced Continuum Surface Force Model with a Level Set Based Curvature Interpolation Technique. *International Journal of Computational Methods*, 13(4):1641004, 2016.

- [99] Niels G. Jacobsen, David R. Fuhrman, and Jørgen Fredsøe. A wave generation toolbox for the open-source cfd library: Openfoam®. *International Journal for Numerical Methods in Fluids*, 70:1073–1088, 11 2012.
- [100] Ibrahim Izzat Na’Im, Ab Razak Mohd Shahrizal, and Mat Desa Safari. A short review of submerged breakwaters. volume 203. EDP Sciences, 9 2018.
- [101] Cherdvong Saengsupavanich, Effi Helmy Ariffin, Lee Shin Yun, and Dunstan Anthony Pereira. Environmental impact of submerged and emerged breakwaters. *Heliyon*, 8, 12 2022.
- [102] J Dattatri, H Raman, and N Jothi Shankar. Performance characteristics of submerged breakwaters. page 2153–2171, 1978.
- [103] B. L. Davies and D. L. Kriebel. Model testing of wave transmission past low-crested breakwaters. pages 1115–1128, 1992.
- [104] S Beji and J A Battjes. Experimental investigation of wave propagation over a bar, 1993.
- [105] S Beji and J A Battjes. Coastal engineering numerical simulation of nonlinear wave propagation over a bar, 1994.
- [106] Roshanka Ranasinghe and Ian L. Turner. Shoreline response to submerged structures: A review. *Coastal Engineering*, 53:65–79, 2006.
- [107] Ping Wang, Kezhao Fang, Gang Wang, Zhongbo Liu, and Jiawen Sun. Experimental and numerical study of the nonlinear evolution of regular waves over a permeable submerged breakwater. *Journal of Marine Science and Engineering*, 11, 8 2023.
- [108] Ching Piao Tsai, Chun Han Ko, Han Chen Shih, Yueh Heng Chen, and Ying Chi Chen. Comparative study of wave height transformation: Bragg reflection versus wave breaking at submerged rectangular breakwaters. *Ocean Engineering*, 299, 5 2024.

- [109] L. Guo, K. Qu, X. Wang, and J. X. Huang. Numerical study on performance of submerged permeable breakwater under impacts of multi-directional focused wave groups. *Ocean Engineering*, 302, 6 2024.
- [110] Agnieszka Kubowicz-Grajewska. Morpholithodynamical changes of the beach and the nearshore zone under the impact of submerged breakwaters - a case study (orłowo cliff, the southern baltic). *Oceanologia*, 57:144–158, 4 2015.
- [111] Kees D’Angremond, Jentsje W Van Der Meer, and Rutger J De Jong. Wave transmission at low-crested structures, 1996.
- [112] Ikha Magdalena, Hany Q. Rif’atin, M. Syahril Badri Kusuma, and Dominic E. Reeve. A non-hydrostatic model for wave evolution on a submerged trapezoidal breakwater. *Results in Applied Mathematics*, 18, 5 2023.
- [113] Thorsten Stoesser. Large-eddy simulation in hydraulics: Quo vadis? *Journal of Hydraulic Research*, 52:441–452, 2014.
- [114] Francis C K Ting ’ and James T Kirby. Dynamics of surf-zone turbulence in a strong plunging breaker. *EISEVIER Coastal Engineering*, 24:177–204, 1995.
- [115] J. C. R. Hunt, A. A. Wray, and P. Moin. Eddies, streams, and convergence zones in turbulent flows. *Studying Turbulence Using Numerical Simulation Databases, 2. Proceedings of the 1988 Summer Program*, pages 193–208, 1988.
- [116] Jinhee JEong and Fazle Hussain. On the identification of a vortex. *Journal of Fluid Mechanics*, 285:69–94, 1995.
- [117] Gavin N Palmer and Colin D Christian. Design and construction of rubble mound breakwaters. *IPENZ Transactions*, 25, 1998.
- [118] Pierre Lubin, Olivier Kimmoun, Fabrice Véron, and Stéphane Glockner. Discussion on instabilities in breaking waves: Vortices, air-entrainment and

droplet generation. *European Journal of Mechanics, B/Fluids*, 73:144–156, 1 2019.